



HAL
open science

Optically addressed spatial light modulators as generic dynamical systems for novel computing substrates

Vladimir Semenov

► **To cite this version:**

Vladimir Semenov. Optically addressed spatial light modulators as generic dynamical systems for novel computing substrates. Neural and Evolutionary Computing [cs.NE]. Université Bourgogne Franche-Comté, 2022. English. NNT : 2022UBFCD005 . tel-03851539

HAL Id: tel-03851539

<https://theses.hal.science/tel-03851539>

Submitted on 14 Nov 2022

HAL is a multi-disciplinary open access archive for the deposit and dissemination of scientific research documents, whether they are published or not. The documents may come from teaching and research institutions in France or abroad, or from public or private research centers.

L'archive ouverte pluridisciplinaire **HAL**, est destinée au dépôt et à la diffusion de documents scientifiques de niveau recherche, publiés ou non, émanant des établissements d'enseignement et de recherche français ou étrangers, des laboratoires publics ou privés.

THÈSE DE DOCTORAT DE L'ÉTABLISSEMENT UNIVERSITÉ BOURGOGNE FRANCHE-COMTÉ

PRÉPARÉE À L'UNIVERSITÉ DE FRANCHE-COMTÉ

École doctorale n°37

Sciences Pour l'Ingénieur et Microtechniques

Doctorat d'Optique et Photonique

par

VLADIMIR SEMENOV

Modulateurs spatiaux de lumière tout-optique destinés à la conception de nouveaux processeurs basés sur des systèmes dynamiques complexes

Optically addressed spatial light modulators as generic dynamical systems for novel computing substrates

Thèse présentée et soutenue à Besançon, le 1 Avril 2022

Composition du Jury :

JACQUOT MAXIME	Professeur, Université de Bourgogne Franche-Comté	Président du jury
KAPITANIAK TOMASZ	Professeur, Université de technologie de Lodz	Rapporteur
LÜDGE KATHY	Professeure, Université technique d'Ilmenau	Rapporteuse
YANCHUK SERHIY	Chargé de Recherche, Institut de Potsdam pour la recherche sur l'impact climatique	Examineur
LARGER LAURENT	Professeur, Université de Bourgogne Franche-Comté	Co-directeur de thèse
BRUNNER DANIEL	Chargé de Recherche CNRS, l'Institut FEMTO-ST	Directeur de thèse

Title: Modulateurs spatiaux de lumière tout-optique destinés à la conception de nouveaux processeurs basés sur des systèmes dynamiques complexes

Keywords: Optical neural networks, spatial light modulation, bifurcations

Abstract:

In this thesis, we show that coherent and incoherent illumination of an optically addressed spatial light modulator (OASLM) subjected to optical feedback allows to implement a wide range of nonlinear oscillator networks exhibiting highly diverse yet tuneable bifurcation scenarios. We analytically derive the conditions for implementing pitchfork, transcritical and saddle-node bifurcations of steady states without modifying the systems under study, and by simply tuning the relative optical intensities of our two-color illumination.

Using an OASLM spatial model, we demonstrate that the pitchfork and saddle-node bifurcations allow to control the speed and direction of the wavefront propagation in bistable spatially-extended systems. In addition, the pitchfork bifurcation conditions provide for controlling the symmetry

of bistable systems and we use this to emulate spin-networks based on the autonomous OASLM's dynamics. In particular, leveraging experimental symmetries, we simplify the corresponding system equations and demonstrate that OASLM-based setups allow for the implementation of an Ising machine. Through experimental characterizations of a particular OASLM based on nematic liquid crystal and nano-scale amorphous arsenic trisulfide (α -As₂S₃) chalcogenide glassy films, we find that such a system is capable to implement up to 10⁴ nodes per mm², requiring illumination intensities as low as 10 nW/mm² at 450 nm. Thus, OASLMs appear as promising candidates for implementing autonomous photonic neural networks and novel next generation optical computing architectures with ultra-low energy consumption.

Titre : Modulateurs spatiaux de lumière tout-optique destinés à la conception de nouveaux processeurs basés sur des systèmes dynamiques complexes

Mots-clés : Réseau de neurones optique, modulation spatiale de la lumière, bifurcations

Résumé :

Dans cette thèse, nous montrons que l'illumination cohérente et incohérente d'un modulateur spatial de lumière à adressage optique (OASLM) soumis à une rétroaction optique permet d'implémenter une large gamme de réseaux d'oscillateurs non linéaires couplés présentant des scénarios de bifurcation très diversifiés mais ajustables. Nous dérivons analytiquement les conditions de mise en œuvre de bifurcations d'états stables, de type fourche, transcritiques ou nœud-col, sans modifier les systèmes étudiés et simplement en réglant les intensités optiques relatives de notre illumination bicolore à deux longueurs d'onde laser.

En utilisant un modèle spatial d'OASLM, nous démontrons que les bifurcations de type fourche et nœud-col permettent de contrôler la vitesse et la direction de la propagation du front d'onde dans les systèmes bistables étendus spatialement. En outre, les conditions de bifurcation fourche permettent de contrôler la symétrie des systèmes

bistables et nous les utilisons pour émuler des réseaux de spin basés sur la dynamique de l'OASLM autonome. En particulier, en exploitant les symétries expérimentales, nous simplifions les équations du système correspondant et nous démontrons qu'un tel système optique utilisant un OASLM permet de réaliser une machine d'Ising. A l'aide de caractérisations expérimentales d'un OASLM particulier basé sur des cristaux liquides nématiques et des films vitreux amorphes nanométriques de trisulfure d'arsenic (α -As₂S₃) chalcogénure, nous constatons qu'un tel système est capable de mettre en œuvre jusqu'à 10⁴ nœuds par mm² en ne nécessitant des intensités d'éclairage que de 10 nW/mm² à 450 nm. Avec de telles caractéristiques, les OASLM apparaissent comme des candidats très prometteurs pour la mise en œuvre de réseaux neuronaux photoniques autonomes réalisant de nouvelles architectures de calcul optique à très faible consommation d'énergie.

ACKNOWLEDGEMENTS

I would like to thank the administration of University Bourgogne Franche-Comté and Institute FEMTO-ST for this opportunity for studying in France. This gave me a unique chance to explore new areas of physics, mathematics and artificial intelligence as well as to learn about new cultures and make new friends. I would like to acknowledge the collective of FEMTO-ST for positive and pleasant atmosphere which additionally supported me during this time.

I would like to thank my supervisors Dr. Daniel Brunner, Dr. Xavier Porte and Prof. Laurent Larger for their consistent support and guidance during the running of this project. In addition, I am very grateful to Valérie Fauvez, Maxime Jacquot and Thérèse Leblois for their help with documents and bureaucratic issues.

And my biggest thanks to my family for all the support you have shown me through this research, the culmination of three years of learning. Especially for my wife Nadya and my parents Irina and Victor, thanks for all your support, without which I would have stopped these studies a long time ago or haven't even started.

LIST OF NOTATIONS

n_e	refractive index of the extraordinary wave
n_o	refractive index of the ordinary wave
Δn	birefringence (magnitude of the refractive index difference)
λ_b	wavelength of incident blue light
λ_g	wavelength of incident green light
Γ	phase retardation between the ordinary and extraordinary waves produced by OASLM's LC-layer
V_0	DC-voltage applied across the OASLM
i_s	current passing through the OASLM
j_s	electric current density
ψ	OASLM's rotation angle
$\Delta\varphi$	electric potential difference
d_{LC}	thickness of OASLM's LC-layer
G_0	PS-layer's conductance in the darkness
R_{LC}	LC-layer resistance
R_{PS}	PS-layer resistance
I_s	summary light intensity on the left and right PS-layers
$\vec{E}_{0,1,2,3}$	Jones vector for light waves characterised in terms of electro-magnetic fields
S	square of illuminated area
I_{in}	incident light intensity
P_{in}	incident light power
D_l	lateral diffusion coefficient
I_0	incident light intensity in the one-color OASLM model
I_{0b}	incident blue light intensity in the two-color OASLM model
I_{0g}	incident green light intensity in the two-color OASLM model
α_b	OASLM's sensitivity to blue illumination
α_g	OASLM's sensitivity to green illumination
β	OASLM's model parameter
γ	OASLM's model parameter
ε	OASLM's response time
R	reflection index
D	noise intensity
$\xi(x, y, t)$	correlated noise term
τ_c	correlation time of fluctuations

$n_a(x, y, t)$	source of additive white Gaussian noise
$n(x, y, t)$	source of correlated Gaussian noise
φ_0	constant retardation induced by the OASLM without illumination
φ_1	retardation accumulated in the external cavity round-trip
i	imaginary unit
$f(\Gamma)$	right-hand side function
$f_T(\Gamma)$	Taylor series expression
κ	OASLM's sensitivity to green illumination in the linearised OASLM model
Γ_*	linearised OASLM's model parameter characterising the response to green illumination
σ	medium electric conductivity or spatial resolution of OASLM-based system
$P_n(\Gamma)$	normalised probability density distribution
W and \tilde{W}	coupling matrices

LIST OF ACRONYMS

BS	beam splitter
PBS	polarizing beam splitter
MO	microscope objective
LC	liquid crystal
PS	photosensor
SLM	spatial light modulator
EASLM	electrically-addressed spatial light modulator
OASLM	optically-addressed spatial light modulator
NN	neural network
ANN	artificial neural network
BNN	biological neural network
FNN	feedforward neural network
RNN	recurrent neural network
PNN	photonic neural network
RC	reservoir computing
PDF	probability density function

CONTENTS

List of notations	vii
List of acronyms	ix
Introduction	1
1 Neural networks and bifurcations	5
1.1 Artificial Neural networks	5
1.1.1 Feedforward neural networks	6
1.1.2 Recurrent neural networks	7
1.1.3 Spin-networks and Ising machine	8
1.2 Hardware for neural networks	11
1.2.1 Spatially-extended systems and networks	12
1.2.2 Delay systems	13
1.3 Photonic neural networks	13
1.3.1 Spatial light modulation and neural networks	14
1.3.2 Optical Hopfield networks	15
1.3.3 Photonic Reservoir Computing	16
1.4 Dynamical systems and neural networks	17
1.4.1 Oscillator networks in OASLM	18
1.4.2 Taylor series	19
1.4.3 Normal forms and bifurcations	19
1.5 Summary	21
2 Optically-addressed spatial light modulator: physical processes and mathematical models	23
2.1 OASLM and Jones calculus	23

2.2	General description of the OASLM	25
2.3	Electric processes in the OASLM	26
2.4	From electric processes towards the optical response	31
2.5	Nonlinear spatial light transformation	33
2.6	Optical feedback	35
2.7	Incoherent illumination	36
2.8	Coherent illumination	39
2.8.1	OASLM for amplitude modulation	39
2.8.2	OASLM for phase modulation	41
2.9	OASLM under simultaneous two-color illumination	42
2.10	Linearization of retardation of the OASLM under two-color illumination	45
2.11	Potential modifications of the OASLM	46
2.11.1	OASLM with single PS-layer	47
2.12	Conclusion	49
3	OASLM-based nonlinear systems	51
3.1	OASLM under incoherent two-color illumination	51
3.1.1	Pitchfork bifurcation	52
3.1.2	Saddle-node bifurcation	55
3.1.3	Transcritical bifurcation	57
3.2	OASLM under coherent illumination with feedback: the amplitude modulation regime	59
3.2.1	Pitchfork bifurcation	60
3.2.2	Saddle-node bifurcation	63
3.2.3	Transcritical bifurcation	65
3.3	OASLM under coherent illumination with feedback: the phase modulation regime	67
3.4	Single-PS-layer OASLM under coherent illumination with feedback: the phase modulation regime	70
3.4.1	Pitchfork bifurcation	71
3.4.2	Saddle-node bifurcation	72
3.4.3	Transcritical bifurcation	73

3.5	Conclusion	74
4	Deterministic and stochastic control of coarsening	75
4.1	Introduction	75
4.1.1	Deterministic control of the front propagation in bistable reaction-diffusion models	76
4.1.2	Stochastic control of front propagation	80
4.2	Spatially-extended model of the feedback-driven OASLM	83
4.3	Deterministic coarsening control	85
4.3.1	Pitchfork bifurcation conditions	85
4.3.2	Saddle-node bifurcation conditions	86
4.4	Stochastic coarsening control	86
4.5	Conclusion	91
5	OASLM for Ising machine implementations	93
5.1	OASLM-based model under study	93
5.1.1	Single-oscillator model	94
5.1.2	Network model	96
5.1.2.1	Coherent illumination	96
5.1.2.2	Incoherent illumination	97
5.2	Pitchfork bifurcation conditions and spin-network dynamics	98
5.2.1	Incoherent illumination (full model)	98
5.2.2	Incoherent illumination (Linearised model)	101
5.2.3	Coherent illumination (Linearised model)	103
5.3	Conclusion	104
6	Conclusion	107
	List of figures	109
	Bibliography	116

INTRODUCTION

Dynamics exhibited by photonic nonlinear oscillator systems are very diverse and include regular and chaotic self-oscillatory behaviour [1], stochastic resonance [2], coherence resonance [3, 4], noise-induced transitions [5, 6] or complex spatial structures revealed in the temporal dynamics of delay-feedback oscillators [7–9]. An inherent asset of such optical systems is its high bandwidth, which makes them attractive for practical applications such as optical communication [10, 11] and signal processing [12]. However, an additional fundamental appeal of photonic architectures is their almost unlimited parallelism [13] combined with their unique potential for information transduction [14]. All these features make photonic architectures prime candidates for novel implementation and technological exploitation [15] of large scale systems, and for network-based concepts in particular [16–19].

One compelling strategy for large-scale optical system synthesis are spatial light modulators (SLMs). The excellent scalability of SLMs (commercial devices now enable up to 10^7 individual pixels) make them suitable for creating spatially-extended systems with large-scale ensembles of interacting oscillators [20]. Besides the importance associated with observing different families of complex dynamics in physical experiments, such systems are of practical relevance for applications, for example in novel information processing concepts [17]. Consequently, SLMs have been widely applied in the context of machine learning using photonic neural networks [16, 18, 21] as well as for the solution of combinatorial problems by the implementation of photonic Ising machines [22, 23].

However, the physical composition and construction principles of electrically (EASLMs) or optically (OASLM) addressed reflective SLMs result in constraints. Reflective illumination makes coherent interference between the optical state variable and coupling fields challenging, yet this can substantially enrich the range of dynamical behaviour accessible to the system. Such interference is straightforward with transmissive OASLMs. Furthermore, EASLMs require extensive control hardware. This implies additional energy consumption, which is a disadvantage for high energy efficient computing. Transmissive OASLMs are therefore a smart and powerful solution for a variety of fundamental and technological challenges.

It is demonstrated in the present PhD-project that a variety of single dynamical systems and networks can be implemented using transmissive OASLMs under two-colour illumination. We identify the corresponding bifurcation scenarios by deriving normal forms through the Taylor-expansion of the equations governing the system's dynamics.

These we then associate to the conditions specifically realizing pitchfork, transcritical and saddle-node bifurcations of steady states. However, intermediate configurations are possible. Simply by adjusting the relative intensities of the two-colored illumination allows to continuously transition between the different bifurcation scenarios. Here, one color encodes the system's dynamical state and its optical coupling, while the other color realizes a constant DC control parameter. Our OASLM model is inspired by I. Abdulhalim et al. [24], and we used one of their proof of concept devices for obtaining the device parameters used in analytical derivations and numerical modelling.

THESIS PLAN

This PhD thesis is divided into six chapters. In Chapter 1, we introduce the basic equations describing the optical system, the bifurcation theory and nonlinear dynamics, and focus towards relevant aspects that will be explored in the subsequent chapters. Moreover, we explain the main challenge to which this study is dedicated and discuss several hardware realizations of neural networks.

In Chapter 2, we experimentally study the electronic and optical responses of the OASLM to blue and green illumination and analyse the underlying electric and optical processes occurring in the OASLM. The obtained results are used to develop a detailed OASLM model. After experimental characterization of the OASLM we analyse which phenomena can occur in the presence of optical feedback implemented by a mirror and derive differential equation models for a couple of modifications to the system.

In Chapter 3, we analyse which bifurcation phenomena can be exhibited by the OASLM driven by optical feedback. For this purpose, we employ a methodology based on the Taylor-series expansion of the differential equations in order to obtain their representation in form of a polynomial series. After the derivation of bifurcation conditions that determine the particular relationship between the blue and green light intensities, we demonstrate on the examples of the pitchfork, saddle-node and transcritical bifurcations that the results of the numerical simulations and analytics are in perfect agreement.

In Chapter 4, we develop the OASLM's spatially-extended model and apply the bifurcation conditions derived in Chapter 3 to control its spatial dynamics related to the effects of wave front propagation and coarsening. In addition, we demonstrate the possibility to control the system behaviour by varying the intensity of an externally introduced noise source. Thus, the issues of, both, deterministic and stochastic control are discussed.

Finally, in Chapter 5 we apply the Taylor-series approach for the implementation of spin-networks. We analyse which modifications provide for simplification of the OASLM-based systems and further applying them for the solution of a combinatorial optimization problem.

The PhD thesis ends with Chapter 6 providing general conclusion and perspectives for future work.

PUBLICATIONS

- X. Porte, L. Andreoli, N. Semenova, V. Semenov, M. Jacquot, L. Larger and D. Brunner; "Noise and Consistency of Analogue Spatio-Temporal Photonic Neural Networks", IEEE 2019 Conference on Lasers and Electro-Optics Europe & European Quantum Electronics Conference (CLEO/Europe-EQEC), June 2019
- V. Semenov, X. Porte, M. Jacquot, L. Larger, I. Abdulhalim and D. Brunner; "Optically addressed spatial light modulators for photonic neural network implementations", Proc. SPIE, Emerging Topics in Artificial Intelligence (ETAI) 2020, vol. 11469, p. 1146905, August 2020
- V.V. Semenov, X. Porte, C. Conti, I. Abdulhalim, L. Larger, D. Brunner; "Optically-addressed spatial light modulator for the Ising machine implementation", 2021 Conference on Lasers and Electro-Optics Europe & European Quantum Electronics Conference (CLEO/Europe-EQEC), June 2021
- V. Semenov, X. Porte, I. Abdulhalim, L. Larger and D. Brunner; "Two-color optically-addressed spatial light modulator as a generic spatiotemporal system", Chaos **31**, 121104 (2021)
- V. Semenov, X. Porte, L. Larger and D. Brunner; "Deterministic and stochastic control of coarsening in a system based on optically-addressed spatial light modulator" [in progress]
- V. Semenov, X. Porte, L. Larger and D. Brunner; "Autonomous photonic Ising machine based on optically-addressed spatial light modulator" [in progress]

CONFERENCE PRESENTATIONS

- V. Semenov, X. Porte, M. Jacquot, L. Larger, I. Abdulhalim and D. Brunner; "Optically addressed spatial light modulators for photonic neural network implementations", SPIE Optics & Photonics - digital forum, August 2020, San-Diego, USA (online).
- V.V. Semenov, X. Porte, C. Conti, I. Abdulhalim, L. Larger, D. Brunner; "Optically-addressed spatial light modulator for the Ising machine implementation", 2021 Conference on Lasers and Electro-Optics Europe & European Quantum Electronics Conference (CLEO/Europe-EQEC), June 2021, Munich, Germany (online).

NEURAL NETWORKS AND BIFURCATIONS

1.1/ ARTIFICIAL NEURAL NETWORKS

The idea of computational neural network algorithm proposed by W. McCulloch and W. Pitts [25] has been transformed into the generalized concept of an artificial neural network (ANN) over time. The principal roots of the original work and further ideas are inspired by the most simplistic interpretation of the functioning principles of the human brain [26–30]. The most principal and distinct class of cells in the brain is a nerve cell, or a neuron. Neurons transfer and nonlinearly transform information between each other in the central nervous system and to other cells in the peripheral nervous system. Thus, the nervous system, and in particular the human brain, represents a biological neural network (BNN) which has billions of interconnections. As the brain learns, these connections are either formed, changed or removed.

Similarly to the BNNs, ANN consists of a large number of interacting elements called 'neurons' or 'nodes' and include the adjusting coupling weights that determine the interaction strength between neurons to account for a new training example. Despite the similarity between the BNNs and ANNs, the term 'neuron' can imply vastly different meanings. For specialists in fields addressing biological issues, the neuron is a morphological and physiological unit with various intrinsic peculiarities such as the sensitivity to external stimulus, response time, excitability, the ability for spiking, chaotic behaviour, just to name a few. There is a broad variety of mathematical models reflecting the properties of individual and collective neural dynamics [31, 32] and exhibiting typical phenomena such as regular self-sustained and noise-sustained spiking activity [33], chaotic bursting [34], synchronization [33, 35], propagation of neural impulses [33, 36, 37]. In the context of artificial intelligence, especially in the frameworks of software development, the term 'neuron' is mostly considered as an element for the summation of input signals and the functional nonlinear transformation of this input information. It therefore dominantly excludes aspects of the oscillatory dynamics. However, this does not mean that both methodologies

cannot be united in principle. For instance, both approaches are merged in the context of neuromorphic computing addressing applications of spiking neural networks [38–41].

For the last decades, ANNs have drawn attention as machine learning algorithms involved in a wide range of scientific and applied areas. These include computer vision [42, 43], language processing [44], speech processing and generation [45], robotics and self-driving cars [42]. Many problems which were previously reserved exclusively for humans suddenly became automatically solved with ANNs, often with equal or even better performance. A manifold of artificial neural networks is represented by several classes distinguished by input/output data properties and for example an ANN's coupling topology.

1.1.1/ FEEDFORWARD NEURAL NETWORKS

Feedforward neural networks (FNNs) consist of multiple layers: input and output layers (blue circles in Fig. 1.1) and optionally a number of hidden layers (red circles in Fig. 1.1). Coupling interactions are organized such that input signals propagate in only one direction: from input to output (schematically illustrated in Fig. 1.1). In such a case, the output of the i -th neuron in l -th layer, y_i^l , is a nonlinear transformation of the product of input signals from the previous layer $l-1$. The output signal of such an artificial neuron is defined as

$$y_i^l = f \left(\sum_{j=1}^{N_{l-1}} W_{i,j}^l y_j^{l-1} \right), \quad (1.1)$$

where N_{l-1} is the number of elements in the $(l-1)$ -th layer, $W_{i,j}^l$ is a matrix of weights which determines the unidirectional coupling strength between layers $l-1$ and l , and $f(\cdot)$ is a nonlinear function usually referred to the neuron's activation function. FNNs are effective tools for classification problems such as pattern recognition and computer vision as well

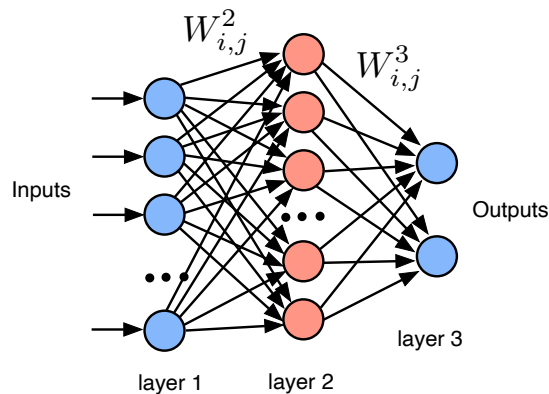


Figure 1.1: Schematic illustration of a feedforward neural network. Circles are the artificial neurons (blue circles form the input and output layers, the red ones belong to the hidden layer), while arrows are the connections described by matrices W^2 and W^3 .

as for the implementation of single-valued prediction systems (regression solvers) [46].

1.1.2/ RECURRENT NEURAL NETWORKS

Recurrent neural networks (RNNs) represent a class of ANNs which often are used to process sequential data or time series. These ANNs are commonly used for ordinal or temporal problems, such as language translation, natural language processing, speech recognition, and image captioning. Like FNNs, the RNNs utilize training data to learn. The principal difference between the FNNs and RNNs is the fact that the RNN topology provides for feedback connections, such that neurons' output signals can return back to the neurons creating self-feedback loops, see Fig. 1.2. This distinguishes RNNs from simple FNNs: feedback connection provide short term "memory" as they take information from prior inputs to interact with the current input and through that to modify the output in the context of past inputs. The output of recurrent neural networks depends on prior elements within the input sequence.

The progress in areas related to development and applications of the RNNs has given rise to the appearance of new concepts. One of these reservoir computing (RC) [47, 48] was developed at the beginning of 2000s and was independently introduced as the echo-state network [49] and the liquid-state machine [50]. In both cases the authors introduced a novel way of training using complex networks of nodes. After that the RC approach was quickly adopted due to its ease of use and its excellent performance. Furthermore, state-of-the-art results have been obtained in tasks that are considered computationally difficult, such as chaotic time series prediction [48], or speech recognition [51, 52].

The RC architecture is schematically illustrated in Fig. 1.3. The RC implies using a RNN

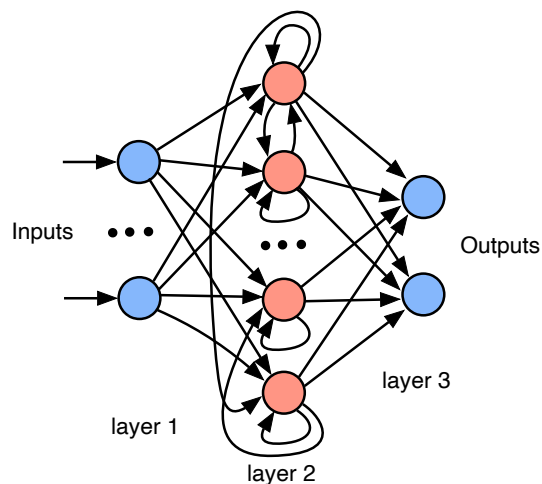


Figure 1.2: Schematic illustration of a recurrent neural network. Blue circles form the input and output layers, while the red ones belong to the hidden layer. Arrowed lines and curves are the connections.

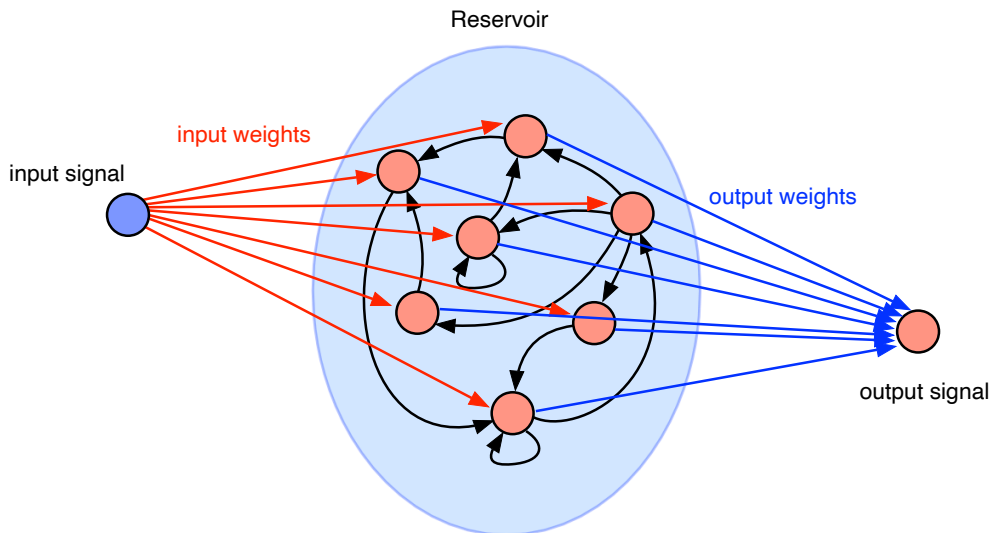


Figure 1.3: Schematic illustration of reservoir computing. In contrast to Fig. 1.2, only output connections (blue arrowed lines) are adjustable, while the input weights (red arrowed lines) and internal reservoir connections (black arrowed lines) are fixed.

with the following characteristics: a large and sparsely interconnected dynamical reservoir, that is driven by inputs and/or feedback of the outputs. The connection weights of the reservoir and from the input to the reservoir are not changed by the training, only weights from the reservoir to the output units are adapted (previous techniques tune all synaptic connections). Then, training becomes a linear regression task.

There exists a broad variety of physical systems which can be implemented for dynamical reservoir developments: from photonic systems discussed in Sec. 1.3.3 to electronic (see review [53]) and mechanical (for instance, see Ref. [54] where the reservoir is the water in a bucket) setups. For this reason the RC-architecture is especially attractive in the context of hardware implementation.

1.1.3/ SPIN-NETWORKS AND ISING MACHINE

In its initial sense, a spin network represents the states and interactions between particles and fields in quantum mechanics. Nowadays, however, spin networks, or spin glasses, represent a broad class of networks which have provided a canonical mathematical framework for understanding and analyzing properties of complex interacting systems across many disciplines including computational biology [55, 56], neuroscience [57], and data science [58, 59] and other fields. In the past decades, the hardware implementation of such spin-glass models have generated tremendous interest due to the prospects of solving NP-hard problems (problems with non-deterministic polynomial-time hardness). The spin-glass models are widely used for investigations of interacting systems in both science and engineering [60–66]. One of such models is the Hopfield network [67] com-

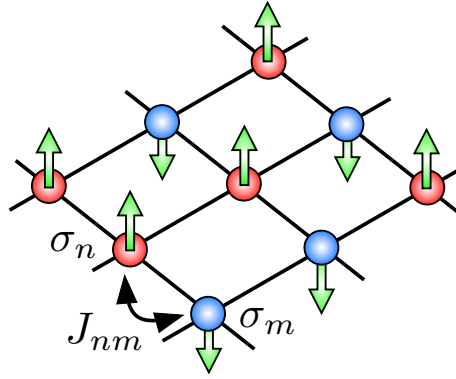


Figure 1.4: Schematic illustration of the Ising machine. Here, the spin-network elements possess either spin-up (red circles) or spin-down (blue circles) states.

only applied for combinatorial optimization [68, 69] as well as for image recognition, enhancement and restoration [70–72].

An important class of spin-glass models is the Ising machine, see Fig. 1.4, that can be applied for a wide range of NP-hard problems. A key observation behind these methods is that optimization problems can be efficiently mapped onto specific classical Ising models [73]. Solving the specific optimization problem then translates into finding the ground state of the corresponding Ising Hamiltonian [74]. The Ising model describes an ensemble of binary spins σ_n . In the simplified case the spin states are either in the spin up $\sigma_n = 1$ or the spin down $\sigma_n = -1$. Interaction between different spins is achieved by coupling them using the spin coupling topology J_{nm} . The energy function of an ensemble of N coupled spins is then given by the Ising Hamiltonian

$$H = - \sum_{n,m=1}^N J_{nm} \sigma_n \sigma_m - \mu \sum_{n=1}^N B_n \sigma_n, \quad (1.2)$$

where the first sum is over pairs of spins. The model has an external magnetic field B_n interacting with spin. Parameter μ is the magnetic moment. Generally, the second sum is optional and can be excluded from the consideration in the simplified modifications of the model. Under a given J_{nm} , spins take values $\sigma_n = \pm 1$ in order to minimize the system's total energy H .

One distinguishes two kinds of the spin interaction: ferromagnetic interaction at $J_{nm} > 0$ and antiferromagnetic one at $J_{nm} < 0$. The system is called ferromagnetic or antiferromagnetic if all interactions are either ferromagnetic or antiferromagnetic. The original Ising models were ferromagnetic, and it is still often assumed that 'Ising model' refers to the ferromagnetic Ising model. In a ferromagnetic Ising model, spins desire to be aligned with parallel orientation: the configurations in which adjacent spins are of the same sign have higher probability. In an antiferromagnetic model, adjacent spins tend to have opposite signs, i.e. directions.

In contrast to the Ising model, where the spin states possess two discrete values $\sigma_n = \pm 1$, the spin network model called XY-model [75] implies a continuous manifold of spin states. This can be interpreted as a network of spins lying on a unit circle: $\sigma_n = \cos(\Theta_n) + i \sin(\Theta_n)$. Then, for N spins, the classical Hamiltonians for these models can be rewritten as

$$H = - \sum_{n,m=1}^N J_{nm} \cos(\Theta_n - \Theta_m) - \mu \sum_{n=1}^N B_n \cos(\Theta_n). \quad (1.3)$$

For the continuous XY-model one therefore has dynamic spin variables with $\Theta_n \in [0, 2\pi)$, while for the Ising model $\Theta_n \in \{0, \pi\}$.

A basic way to develop an Ising spin system with polynomial transfer functions is the pitchfork normal form, which is often applied to describe various physical implementations of the Ising machine: degenerate optical parametric oscillators [76–78], Kerr-nonlinear microring resonators [79], nonlinear opto-electronic oscillators [22, 80] and polariton condensates [81]. The nonlinear transfer function of Ising machines based on the supercritical pitchfork normal form is given by

$$F_n(\vec{x}) = bx_n - dx_n^3 + \beta \sum_m J_{nm} x_m + \gamma \xi_n(t). \quad (1.4)$$

Spin systems can be generated by mimicking the shape of the transfer function which differs from polynomial form (1.4) [80, 82]. One of these approaches is based on sigmoid functions. While sigmoid functions have so far not been considered for Ising machines, they are widely used in the context of Hopfield-Tank-networks and other neuromorphic systems to mimic the activation function of neurons [83]. Efficient ways of implementing them have been reported for both optical systems and electronic systems [84–87]. Sigmoid functions are characterized by an s-shaped nonlinearity and can be modelled by a variety of functions such as the logistic function or the Gompertz function. In particular, a sigmoid based on the hyperbolic tangent function takes the form

$$F_n(\vec{x}) = -x_n + \tanh\left(\alpha x_n + \beta \sum_m J_{nm} x_m + \gamma \xi_n(t)\right). \quad (1.5)$$

Equation (1.5) can be expanded into the third-order Taylor series which allows to facilitate a simple comparison to the polynomial model of Eq. (1.4) [82].

Periodic transfer functions represent another set of nonlinearities that can be implemented with optical and electric systems [80, 88]. To generate an Ising spin system with periodic transfer functions, the general shape of the polynomial model (1.4) can be mimicked by appropriately shifting cosine or sine functions. For instance, a transfer function

based on \cos^2 -nonlinearity takes the form

$$F_n(\vec{x}) = -x_n + \cos^2 \left(\alpha x_n - \frac{\pi}{4} + \beta \sum_m J_{nm} x_m + \gamma \xi_n(t) \right) - \frac{1}{2}. \quad (1.6)$$

The \cos^2 nonlinearity models Ising machines based on optical intensity modulators [80] but is also equivalent to electronic oscillator-based Ising machines [88]. Similarly to sigmoid models, \cos^2 and \sin^2 transfer function can be expressed as the third-order Taylor series and represented in the form being similar to Eq. (1.4). However, the periodicity of \cos^2 and \sin^2 functions can induce problems for systems exhibiting inhomogeneous amplitude distributions [82].

1.2/ HARDWARE FOR NEURAL NETWORKS

These days, most ANNs are software simulations executed on electronic computers [89] based on the von Neumann architecture. Despite plenty of notable achievements that have been achieved using this strategy [90–92], its limitations are evident: first, as the transistor counts of central processing units (CPUs) and graphical processing units (GPUs) increase exponentially, current leakage in nanometric nodes becomes the major contribution to power consumption, inducing a halt to the growth of microprocessor clock rates at approximately 4 GHz [93]. Moreover, the breakdown of Dennard scaling [94] means that smaller transistors do not consume less power; thus, improvements in CPU or GPU performance may come at the expense of a substantial increase in energy consumption and heat generation. For instance, within the existing von Neumann framework, to achieve an ANN software simulation at the scale of the human brain in 100% real time, at least 500 MW of power will be consumed [95] and the required supercomputer would have to be enormous. The two mentioned limitations indicate that the problem of training a large ANN on a von Neumann machine that takes a lot of time and energy, and that this problem will not be significantly alleviated in the near future. Due to the mentioned facts, the development of alternative hardware-implemented neural networks becomes more and more important [96, 97].

ANNs can be implemented by means of electronics [98, 99]. Here, one can distinguish analog and digital circuit approaches. The class of digital electronic ANNs includes a broad variety of circuits which have the advantage of being easy to design and build. They rely on existing logic elements and can take full advantage of decades of development and optimization in digital circuits. Although adapting digital logic for ANNs leads to fairly simple designs, the result is inherently not power and area optimized. On the other hand, integrated circuit design is much more complicated in the case of analog circuits, especially in a case of scaling to large number of elements. The mentioned limitations force researchers to develop and evaluate fundamentally new operating princi-

ples. Field-Programmable Gate Arrays (FPGA) and application-specific integrated circuits (ASIC) [100] (including Google Tensor Processing Units - TPU - [101] and IBM TrueNorth [102]) have been specifically designed to implement ANN computations. In addition, one of the novel concept for electronic implementations of neuromorphic computing systems involves resistive elements with memory and memristors [103–105]. However, the main drawback of the memristors concerns the high power dissipation (being resistance-based), IR-drops (the voltage drop due to energy losses in a resistive element) in the array [106], the lack of accurate models for mainstream simulation tools, and the absence of process standards [107].

In recent years, hardware realizations of ANNs based on optical approaches [108] have attracted more and more attention due to the fact that optical information processing can inherently be massively parallel [13] and optical approaches provide for the implementation of scalable systems. Optical systems can have much larger bandwidths than electronic systems, which results in much faster response time. These characteristics make optical methods potentially applicable for the implementation of large-scale ANNs [15–19], which contain a large quantity of neurons and synapses. Furthermore, photonic neural networks (PNNs) can surpass electronic ANNs in computational efficiency. For example, at present, by using realistic optical devices, an energy consumption per multiply-accumulate (MAC) at the sub-fJ level should be feasible, which is two to three orders of magnitude smaller than the 1...10-pJ/MAC value for a state-of-the-art complementary CMOS circuit [109, 110]. Thus, the PNNs are considered to have bright prospects as the next generation of ANNs.

1.2.1/ SPATIALLY-EXTENDED SYSTEMS AND NETWORKS

Nonlinear spatio-temporal systems are the basis for countless phenomena in such diverse fields as ecology [111], biology [112], optics [113] and chemistry [114]. Experimentally realizing different types of dynamical systems, one extends a manifold of spatially-extended systems and ensembles of interacting oscillators which can be potentially used for the implementation of an ANN. Among these are optical systems such as spatial light modulators (discussed in Sec. 1.3.1) and vertical-cavity surface-emitting lasers [115, 116], optical fibers [117, 118], electronic SQUID metamaterials (Superconducting QUantum Interference Devices) [119, 120] and electronic transmission lines [121].

Mathematical describing a spatially-extended systems evolving in continuous time is often carried out through reaction-diffusion equations $\frac{du}{dt} = f(u) + g(u, \nabla u, \nabla^2 u, \vec{r})$ for continuous space \vec{r} which implies a mathematical solution in a functional form $u = u(t, \vec{r})$. Another approach consists in the space discretisation and rewriting equations in an ensemble form $\frac{u_i}{dt} = f(u_i) + g(\vec{u})$. The second form allows to distinguish particular elements u_i and to carry out numerical simulations of studied equations using standard integration methods,

and to implement spatially-complex interaction between different positions of the system. If, both, time and space are discretised, then the system is considered as an iterating map $u_i[n + 1] = f(u_i[n]) + g(\vec{u}[n])$, where $n \in \{1, 2, 3, \dots\}$ is a discrete set of time moments.

1.2.2/ DELAY SYSTEMS

Generally, time-delayed dynamical systems are described by $\frac{dx}{dt} = f(t, x(t), x(t - \tau))$. As was first mentioned in Refs. [122], there exists an analogy between the behavior of time-delayed systems and the dynamics of ensembles of coupled oscillators or spatially extended systems [123]. The similarity takes place when the delay time is much longer than system's response time, which allows the system to exhibit spatio-temporal phenomena (for example, coarsening [8], chimera states [7, 124, 125], soliton dynamics [9, 126]) in the purely temporal dynamics of a time-delay system. This time-space analogy can be obtained by implementing a space-time transformation of the delay-feedback system, where the purely temporal dynamics is mapped onto space-time (σ, n) by introducing the space-time map $t = n\tau + \sigma$ with an integer (slow) time variable n , and a pseudo-space variable $\sigma \in [0, \eta]$, where $\eta = \tau + \delta$ with a small quantity δ . For each set of parameters a unique value η can be chosen such that the oscillatory dynamics is periodic with the period η .

Using such a space-time representation allows to transform a single oscillator into a single-node reservoir with delayed feedback. Appeltant et al. [127] developed and successfully implemented the RC scheme onto a single nonlinear node with a delayed self-feedback. In the input layer, time-multiplexing is used to create temporally separated virtual nodes. The reservoir dynamics are hereby given by a delay differential equation, which exhibit rich high-dimensional dynamics. For the training, the temporally separated nodes are read out and weighted to solve a given task. The introduction of time-delay reservoir computing enabled simple optical, electronic and opto-electronic hardware implementations, which led to improvements of computation time scales for supervised learning [53, 128–131]. Moreover, deep-learning architectures have been adopted for RC [132–134]. The delay-based reservoirs were successfully applied to a wide range of tasks, such as chaotic time series forecasting or speech recognition [135].

1.3/ PHOTONIC NEURAL NETWORKS

Photonics has unmatched feats for interconnects and communications in terms of bandwidth, which can negate the bandwidth and interconnectivity trade-offs [136–138]. When PNNs were pioneered by D. Psaltis and N. Farhat [139], the at the time low level of photonic integration and packaging technologies hindered the practical applications of photonic neural networks. However, the emergence of large-scale photonic fabrication and

integration techniques [138, 140–142] has tremendously changed the situation. For instance, among such technologies is silicon photonics, which has significantly extended a manifold of large-scale and low-cost optical systems [142–144]. As a consequence, these changes have shed light on new opportunities and directions for photonic neural networks [145]. The variety of different technologies and solutions for PNNs implementations is extraordinary large, and particular approaches which have to do with the PhD-thesis topics are discussed below.

1.3.1/ SPATIAL LIGHT MODULATION AND NEURAL NETWORKS

A spatial light modulator (SLM) is an optical device that imposes some form of spatially varying modulation on a beam of light [146–148]. Spatial modification to a wavefront can be achieved by modulation of the spatial distribution of the light intensity or phase, or both of them at the same time. In most cases, spatial light transformation is caused by the action of a birefringent liquid crystal layer (LC) changing the polarization state of the transmitted or reflected light. The resulting light polarization state at each point of the LC's illuminated area is determined by a liquid crystal molecules state which is dictated by electric field strength at this point.

Generally, one can classify SLMs into two groups: electrically addressed SLMs (EASLMs) and optically addressed SLMs (OASLMs), see Fig. 1.5. For the OASLM, the image is created and changed by shining light encoded with an image on its front or back surface, see Fig. 1.5 (a,b), respectively. A photosensor layer (PS) allows the OASLM to sense the brightness at each point of the illuminated area and the PS's electric conductivity varies under illumination resulting in varying electric field spatial distribution. A derivation of the interaction between the local PS conductivity, the local voltage across a LC cell and the resulting local retardation can be found in Chapter 2 (see Sec. 2.4). A light beam illuminating the photosensitive layer is called 'write beam', while the processed light is mentioned as 'read beam'. OASLMs do not require pixels for the modulation as one can select PS materials with low lateral carrier mobility. This simplifies device fabrication, potentially reduces unwanted diffraction from pixels and improves the resolution when limited by diffusive processes in the PS and LC layers.

On the other hand, the image on an electrically addressed SLM is created and changed electronically, see Fig. 1.5 (c). Such devices require external hardware for controlling the electric field distribution. EASLMs usually receive input via a conventional interface such as USB, VGA or DVI input, and they are available at resolutions determined by the SLM's pixel matrix.

The OASLM and EASLM schemes depicted in Fig. 1.5 (a,c) are reflective, meaning that the information of the modulated light beams is encoded in the reflected optical signal. However, one can implement transmissive OASLMs, such as illustrated in Fig. 1.5 (b).

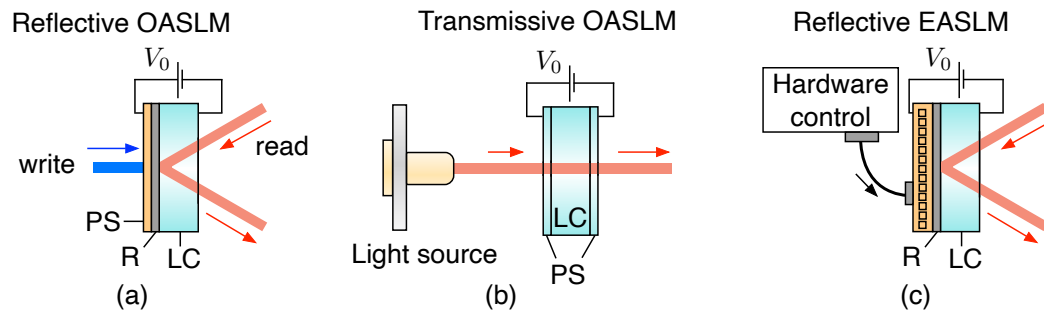


Figure 1.5: Schematic illustration of reflecting (panel (a)) and transmissive (panel (b)) OASLMs, and EASLM (panel (c)).

This is possible by using semi-transparent materials for the PS, such as $\alpha\text{-As}_2\text{S}_3$ [24], C-doped $\alpha\text{-Si:H}$ [149], ZnO [150]. Such devices allow using the same light beam for reading and writing functions.

SLMs provide for implementations of a wide range of spatially-extended dynamical systems described by reaction-diffusion models and ensembles of coupled oscillators [20] as well as in the form of interacting maps [16, 21]. A manifold of phenomena exhibited by such systems includes regular and chaotic pattern formation, propagating fronts and soliton structures [20, 151] as well as chimera states characterised by the coexistence of localized coherent and incoherent states [152].

SLMs are highly attractive in the context of PNN implementations and hardware solution of machine learning tasks [16, 21, 153, 154]. Different kinds of coupling elements such as diffractive optical elements [155] or scattering media [154], which can be easily introduced in such PNNs, complement a variety of systems and exhibited regimes. Moreover, the SLMs allow for implementations of photonic spin-networks and experimental solutions of combinatorial optimization problems [22, 23, 156–158].

1.3.2/ OPTICAL HOPFIELD NETWORKS

The first optical implementation of the Hopfield network was proposed by Psaltis et al. in 1985 [139, 159] which has stimulated the emergence of a new PNN class called optical associative memories [160, 161]. Such systems exhibit remarkable computational properties such as the ability for recognition from partial input, robustness, and error-correction capability. The first implementations were based on vector matrix multiplication with thresholding and feedback scheme, but applied physical phenomena include holographic storage [162], phase conjugate optics [163, 164], and wavefront modulation [165, 166] and mixing [167] were used to realize associative memory functions.

Associative memories provides for storing multiple patterns as local minima of an energy landscape. Moreover, recall of any individual memory is possible even if mistakes are

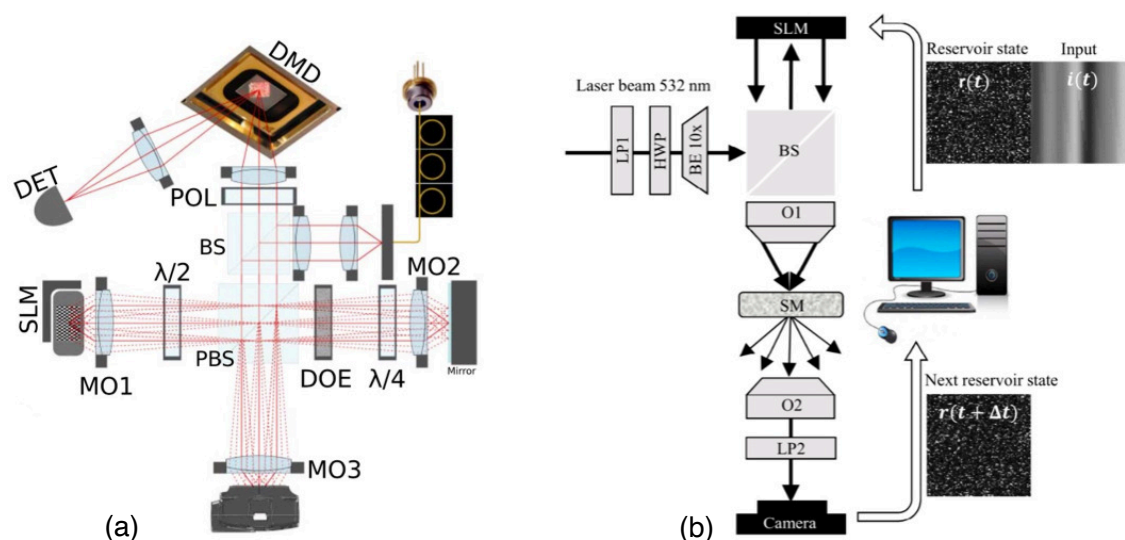


Figure 1.6: Photonic EASLM-based RC schemes applied in Ref. [16] (panel (a)) and in Ref. [21] (panel (b)).

made when addressing the memory to be recalled. Such networks exhibit a trade-off between capacity (number of memories stored) and robustness (the size of the basins of attraction of each memory under pattern completion). Once too many memories are stored, the basins of attraction cease to be extensive, and the model transitions to a spin glass regime with exponentially many spurious memories (with subextensive basins of attraction) that are nowhere near the desired memories [168]. Thus, the relevant directions in associative memories development is the creation of experimental platforms for simultaneously store much more memories in comparison with classical solutions. One of such perspective platforms is based on bosons coupled to a degenerate multimode optical cavity where the associative memory is realized by a confocal cavity QED (quantum electrodynamics) neural network [169], with the modes serving as the synapses, connecting a network of superradiant atomic spin ensembles, which serve as the neurons.

1.3.3/ PHOTONIC RESERVOIR COMPUTING

In principle, all photonic RC schemes are divided into RCs implemented in spatially extended and delay-feedback architectures [131]. The first approach is illustrated in Fig. 1.6 on an example of EASLM-based reservoirs [16, 21]. Here, the feedback loop being responsible for recurrent connections is implemented by a personal computer which controls the EASLM's state according to the system's state recorded by a camera. A difference between two such EALSM reservoirs consists in physical realization of internal connections: by a diffractive optical element in [16] as illustrated in Fig. 1.6 (a), and a scattering medium in [21], illustrated in Fig. 1.6 (b).

The second approach for photonic reservoir computing is based on long feedback loops

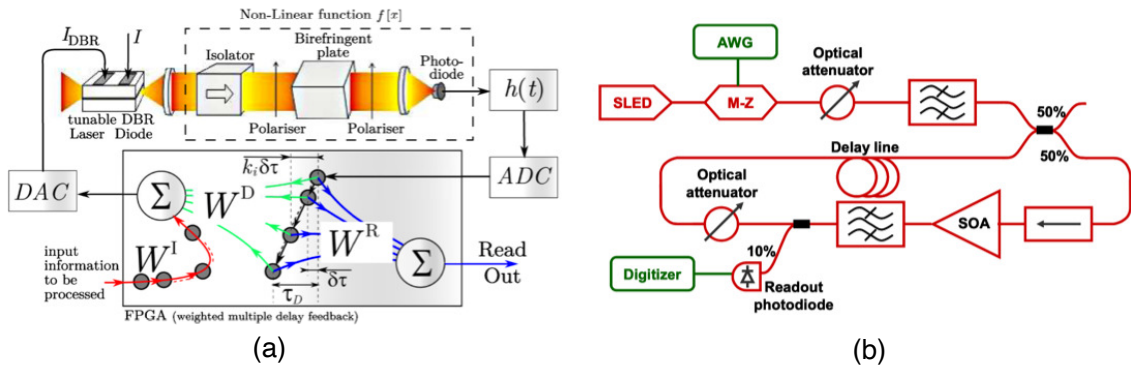


Figure 1.7: Opto-electronic delay-based RC architecture implemented in Ref. [128] and all-optical delay-oscillator scheme presented in Ref. [170].

and a single nonlinear node. To implement such a system one can use opto-electronic approaches, for instance, FPGA-based setups [128] as depicted in Fig. 1.7 (a). Here, time delay, injection of input signal and output response generation (adjusting output weights) are implemented by means of FPGA technology, while the system's nonlinearity is determined by photonic processes. This approach requires ADC- and DAC-converters. Meanwhile, all-optical RC schemes allow to implement pure analog reservoirs [170, 171]. For this purpose, one can use single-mode fibers as a delay line and integrated Lithium Niobate Mach-Zehnder intensity modulator or a semiconductor optical amplifier as depicted in Fig. 1.7 (b) for the nonlinearity implementation. In the case of delay-feedback-based reservoir the property of scalability persists due to the possibility to increase the time delay.

1.4/ DYNAMICAL SYSTEMS AND NEURAL NETWORKS

A dynamical system is any object or process evolving in accordance with a certain law, and described by a set of quantities uniquely identifying its state at a given time moment. The evolution law is a functional dependence, which describes the evolution of an initial state over time. Initially, the term 'Dynamical system' was introduced in the context of mechanical processes described by Newton's laws of dynamics. Nowadays, the definition of the dynamical system involves systems and processes of any nature (physical, biological, chemical, geological, climatic, economical, social, informational, etc.). Depending on the specifics of the evolution law, the dynamical system can be defined in a different manner. For example, the evolution law (evolution operator) can be determined using differential equations or discrete maps. The choice of a description establishes a concrete kind of a dynamical system model.

It is important to note that in most cases the term 'dynamical system' is used to refer to its mathematical model. A dynamical system is defined if the following elements are given:

- A set of states X forming system's phase space;
- A set of time moments Q ;
- An evolution operator $F_{t_0}^\tau$, which unambiguously transforms each state $\vec{x}_0 \in X$ at initial time moment $t_0 \in Q$ into state $\vec{x}_t \in X$ at time $t = t_0 + \Delta t \in Q$.

A classification of dynamical systems is based on the properties of the evolution operator and sets X and Q . If Q is a continuous manifold of real numbers $Q \in \mathbb{R}$, i.e. time is given by a continuous set of values, and the evolution operator is continuous, then the dynamical system is called a continuous system, a continuous-time system or a flow. If set Q is countable, then the dynamical system is called a discrete-time system, a cascade or an iterated map. For instance, dynamical systems with a countable manifold of time moments describe climate changes or changes in animal populations registered with a certain temporal resolution T . Then a functional dependence has the form $x(t_0 + (n+1)T) = f(x(t_0 + nT))$, where t_0 is the initial moment of observation.

Similarly to the set of time moments Q , the set of states X can be continuous or countable (finite). Typical examples of dynamical systems with the countable sets of states are cellular automata. Dynamical systems given by the continuous sets of time and states of dimension N ($X \in \mathbb{R}^N$) are systems of ordinary differential equations. Set X can be a functional space. In such a case, the dynamical system is described by partial differential equations, integro-differential equations or ordinary equations with time delay. Systems with a finite number of degrees of freedom are called lumped. Their phase space is finite-dimensional. If the system state is described by a function of spatial coordinates, then the system is called a distributed system or a medium. If spatial coordinates are defined on a continuous set, the number of degrees of freedom becomes infinite.

1.4.1/ OSCILLATOR NETWORKS IN OASLM

The current PhD-thesis is focused on the dynamics of OASLM-based dynamical systems. All equations are derived for the dynamical variable $\Gamma(t, \mathbf{x})$, which is the spatially distributed phase retardation. Derivations are carried out under the condition that light propagation occurs instantaneously compared to the slow timescales of LC and voltage dynamics (light beams propagate only in short distances and the finite light propagation speed is neglected). In such a case, the dynamical evolution time scales are dictated only by the OASLM response time ε . Then the OASLM state after transient time $\Delta t = \varepsilon$ denoted as $\Gamma_{\text{response}} = \Gamma(t_0 + \varepsilon)$ is determined by the initial state $\Gamma_{\text{initial}} = \Gamma(t_0)$ and can be mathematically expressed in the differential form $\Gamma_{\text{response}} = \Gamma_{\text{initial}} + \varepsilon \frac{d\Gamma}{dt}$ which leads to the expression $\varepsilon \frac{d\Gamma}{dt} = -\Gamma_{\text{initial}} + \Gamma_{\text{response}}$. This approach can be applied for low-pass

systems of any nature and gives rise to the following form of dynamical model

$$\varepsilon \frac{dx}{dt} = -x + f(x), \quad (1.7)$$

which represents a first-order ordinary differential equation. Equation (1.7) is a model of a single oscillator. If the the considered model is scalable or consists of a set of identical objects like EASLM's pixels, Eq. (1.7) is rewritten in the vector form for an array of interacting oscillators

$$\varepsilon \frac{dx_i}{dt} = -x_i + f(\vec{x}), \quad (1.8)$$

or in the reaction-diffusion form for a variable x evolving in time t and space \vec{r} , $x = x(t, \vec{r})$

$$\varepsilon \frac{dx}{dt} = -x + f(x) + g(x, \nabla x, \nabla^2 x, \dots, \nabla^n x). \quad (1.9)$$

1.4.2/ TAYLOR SERIES

The Taylor series of a function is an infinite sum of terms that contain function's derivatives at a single support point x_0 . For most common functions, the Taylor series can well approximate the original function near point x_0 for a limited number of terms. The Taylor series of a real or complex-valued function $f(x)$ that is infinitely differentiable at a real or complex number is the power series

$$f(x) = f(x_0) + \frac{f'(x_0)}{1!}(x-x_0) + \frac{f''(x_0)}{2!}(x-x_0)^2 + \frac{f'''(x_0)}{3!}(x-x_0)^3 + \dots + \frac{f^{(n)}(x_0)}{n!}(x-x_0)^n, \quad (1.10)$$

where $f^{(n)}(x_0)$ denotes the n -th derivative of $f(x)$ evaluated at point x_0 and $n!$ denotes the factorial of n .

In the framework of the PhD-thesis, the Taylor series expression is used to approximate the considered model equations in the nomenclature of steady-state bifurcation normal forms. All the expressed functions contain trigonometric dependencies such as \sin or \cos and are therefore infinitely differentiable.

1.4.3/ NORMAL FORMS AND BIFURCATIONS

Generally, the term 'bifurcation' means qualitative changes in the behaviour of dynamical systems caused by variation of parameters. In terms of qualitative theory of differential equations, the bifurcations are associated with transformations of limit sets in the phase space: appearance, disappearance or change of stability.

Bifurcations in deterministic dynamical systems are divided into local and nonlocal bifurcations. Local bifurcations are associated with the behaviour of phase trajectories in a local neighbourhood of limit sets (steady states and limit cycles). Local bifurcations are

related to transformations of certain limit sets and can be identified by means of linear stability analysis. Nonlocal bifurcations involve manifolds of saddle limit sets (separatrix loops, separatrix curves and surfaces, homoclinic and heteroclinic curves). Usually, a linear approach is insufficient for description of these bifurcations.

Mathematically, a normal form of a certain bifurcation is the simplest equation form that can exhibit this bifurcation. Such normal forms are often used for determining local bifurcations in a system. All systems exhibiting a certain type of bifurcation are locally (around the equilibrium) topologically equivalent to the normal form of the bifurcation. Three kinds of bifurcations can be observed in one-dimensional oscillators described by Eq. (1.7), and they are briefly discussed below on the example of the corresponding normal forms written in the form $\frac{dx}{dt} = f(x)$.

SADDLE-NODE BIFURCATION

The normal form of a saddle-node bifurcation of steady states is

$$\frac{dx}{dt} = m - x^2. \quad (1.11)$$

Equilibria, i.e. fixed points of Eq. (1.11) are $x_1^* = \sqrt{m}$ and $x_2^* = -\sqrt{m}$. It is evident that the points $x_{1,2}^*$ exist only in case $m > 0$, since coordinates of steady states are always real quantities. The stability of the fixed points $x_{1,2}^*$ is determined by a derivative of right-hand side of Eq. (1.11) $\frac{df}{dx} = -2x^*$ calculated at the points $x_{1,2}^*$. At the equilibrium x_1^* the derivative becomes $\frac{df}{dx} = -2\sqrt{m}$ and is always negative when steady state x_1^* exists. Steady state x_1^* is therefore stable for any $m > 0$. Similarly, a value of the derivative at the equilibrium x_2^* is $\frac{df}{dx} = 2\sqrt{m}$. It is always positive when steady state x_2^* exists, and consequently steady state x_2^* is unstable for any $m > 0$. In summary, the following bifurcation diagram is obtained for increasing parameter m [Fig. 1.8 (a)]: for $m < 0$ there exist no steady states, but two steady states, stable (solid line) and unstable (dashed line) appear at the bifurcation moment and exist after the bifurcation.

TRANSCRITICAL BIFURCATION

The transcritical bifurcation corresponds to an exchange of stability between two points of equilibrium. The normal form for this bifurcation is

$$\frac{dx}{dt} = mx - x^2. \quad (1.12)$$

Steady states of Eq. (1.12) are $x_1^* = 0$ and $x_2^* = m$, and they exist at any value of parameter m . The derivative $\frac{df}{dx}$ defining the stability becomes $\frac{df}{dx} = m$ for steady state x_1^* and $\frac{df}{dx} = -m$ for the steady state x_2^* . That means the fixed point $x_1^* = 0$ is stable for $m < 0$ and unstable

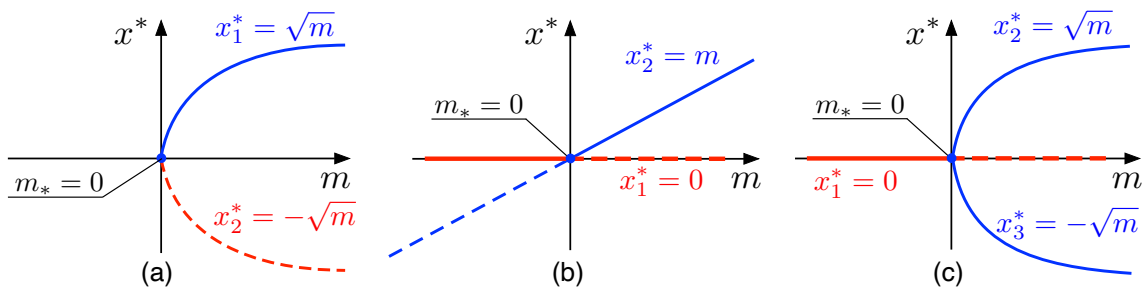


Figure 1.8: Phase-parametric diagram for the saddle-node bifurcation in Eq. (1.11) (panel (a)), the transcritical bifurcation in model (1.12) (panel (b)) and the pitchfork bifurcation in oscillator (1.13) (panel (c)). The solid lines indicate stable equilibria, while the dashed ones correspond to unstable fixed points.

for $m > 0$. At the same time steady state $x_2^* = m$ is stable for $m > 0$ and unstable for $m < 0$. In summary, two equilibria bifurcate at $m_* = 0$ and the stability exchange occurs, see Fig. 1.8 (b).

PITCHFORK BIFURCATION

The pitchfork bifurcation typically realizes transitions from monostability to bistability. It consists in the appearance of two stable states from the point of equilibrium, which was initially stable before the bifurcation, and is unstable afterwards. The normal form for this bifurcation takes a cubic form

$$\frac{dx}{dt} = mx - x^3. \quad (1.13)$$

The condition for steady state $\frac{dx}{dt} = 0$ leads to the cubic equation $mx - x^3 = 0$ which has one solution $x_1^* = 0$ for $m < 0$ and three solutions $x_1^* = 0$ and $x_{2,3}^* = \pm\sqrt{m}$ for $m > 0$. That means that before the bifurcation only one steady state x_1^* exists. After the bifurcation at $m_* = 0$, two new steady states $x_{2,3}^*$ appear in the vicinity of equilibrium point x_1^* . A derivative $\frac{df}{dx}$ takes the value $\frac{df}{dx} = m$ at steady state x_1^* and $\frac{df}{dx} = -2m$ for steady states $x_{2,3}^*$. That means fixed point $x_1^* = 0$ is stable for $m < 0$ and unstable for $m > 0$. At the same time, fixed points $x_{2,3}^*$ are stable over the whole area of the existence. One can plot a complete bifurcation diagram, Fig. 1.8 (c), which shows the pitchfork bifurcation at $m_* = 0$.

1.5/ SUMMARY

SLMs are prime candidates for implementations of large scale photonic systems including PNNs. OASLMs are especially attractive in this regard since they simplify the PNN construction and can potentially reduce the energy consumption. However, the development of OASLM-based PNNs requires preliminary experimental and theoretical studies. The first necessary steps are experimental exploration of the OASLM characteristics and

further development of OASLM-models including the relevant optical and electronic interactions. Analysis of the OASLM stability is also necessary to estimate the expected robustness of OASLM-based devices. Further work is to understand which kinds of OASLM-based dynamical systems can potentially be implemented, and which types of oscillatory dynamics and bifurcation transitions can be observed in such systems. In addition, it is significantly important to establish how one can simplify the device construction while preserving the required dynamics. The present PhD-thesis aims to answer these questions for further practical applications of the OASLMs in the context of PNN synthesis and beyond this issue.

OPTICALLY-ADDRESSED SPATIAL LIGHT MODULATOR: PHYSICAL PROCESSES AND MATHEMATICAL MODELS

In this chapter the optically-addressed spatial light modulator (OASLM) is introduced in detail, starting from a general description of its structure and action, followed by electric and optical processes occurring in the OASLM. The relevant aspects will be explored in detail and will be closely linked to device characterization on the base of the experimental study. Afterwards, a detailed and close to ab-initio mathematical model of the device is developed. Building on the description of a standalone OASLM, the possibility to implement optical feedback is discussed and included based on ordinary differential equations (ODEs). Furthermore, oscillatory regimes exhibited by the developed mathematical models are examined. Finally, it is analysed which OASLM's modifications can be introduced to simplify the OASLM construction and to tailor the device for interesting dynamical properties.

The research presented in the current chapter has the following goals:

- To discuss principle device characteristics such as the energy consumption, resolution, operating range of the incident light intensities.
- To discuss issues regarding temporal stability of the device.
- To develop the OASLM model and to estimate its parameter values.
- To establish which types of the single-oscillator dynamics can be realized.

2.1/ OASLM AND JONES CALCULUS

The OASLM discussed in this thesis was developed and fabricated by Ibrahim Abdulhalim and colleagues [24]. The OASLM is a light-transmissive device, and it is assumed in the

following that the OASLM fully transmits the incident light, i.e. has zero absorption. An OASLM operates as an optically controlled birefringent phase plate, the phase retardation of which is a varying quantity. Suppose that the OASLM, see Fig. 2.1, is illuminated by light with an polarization state defined by the Jones vector $\begin{bmatrix} E_{0x} \\ E_{0y} \end{bmatrix}$, where E_{0x} and E_{0y} are complex quantities. Then one can obtain the Jones vector \vec{E}_1 for the wave that has passed through the OASLM

$$\begin{aligned} \begin{bmatrix} E_{1x} \\ E_{1y} \end{bmatrix} &= \exp(i\phi_0) \begin{bmatrix} \cos(\psi) & -\sin(\psi) \\ \sin(\psi) & \cos(\psi) \end{bmatrix} \begin{bmatrix} \exp(i\Gamma) & 0 \\ 0 & \exp(-i\Gamma) \end{bmatrix} \begin{bmatrix} \cos(\psi) & \sin(\psi) \\ -\sin(\psi) & \cos(\psi) \end{bmatrix} \begin{bmatrix} E_{0x} \\ E_{0y} \end{bmatrix} \\ &= \exp(i\phi_0) \begin{bmatrix} \cos(\Gamma) + i \sin(\Gamma) \cos(2\psi) & i \sin(2\psi) \sin(\Gamma) \\ i \sin(2\psi) \sin(\Gamma) & \cos(\Gamma) - i \sin(\Gamma) \cos(2\psi) \end{bmatrix} \begin{bmatrix} E_{0x} \\ E_{0y} \end{bmatrix}, \quad (2.1) \end{aligned}$$

where ψ is the OASLM rotation angle of its fast slow (fast) axis relative to the x (y) axis, ϕ_0 is the constant offset phase retardation caused by the propagation through the liquid crystal (LC) layer, Γ is the varying phase retardation between the polarization components of the transmitted light, and i is the imaginary unit. Finally, the incident light intensity is $I_0 = |E_{0x}|^2 + |E_{0y}|^2$ while the transmitted light intensity is $I_1 = |E_{1x}|^2 + |E_{1y}|^2$. Since the OASLM is assumed to be fully transmissive, the input and output light intensities are equal, $I_0 = I_1$.

The Jones matrix approach is used for the OASLM characterization as well as for derivations of mathematical models of the OASLM.

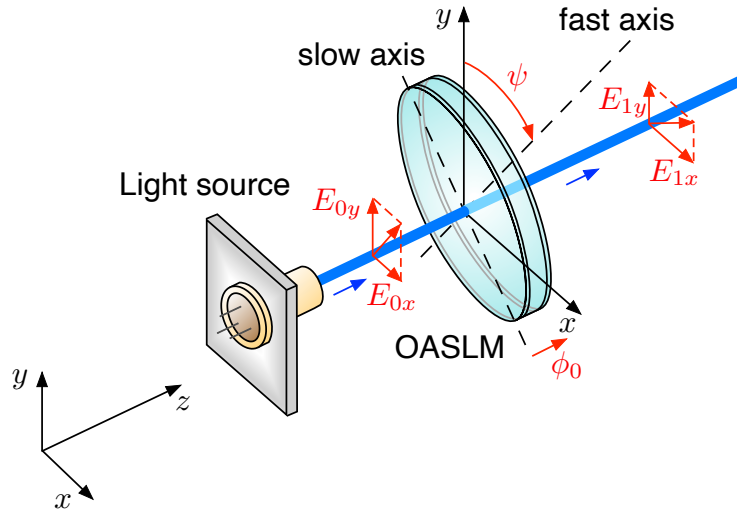


Figure 2.1: OASLM illuminated by a light source. Here, the Jones vector components of the incident and transmitted lights are schematically shown by red arrowed lines.

2.2/ GENERAL DESCRIPTION OF THE OASLM

Our particular OASLM and its dimensions are depicted on photos in Fig. 2.2. It contains two wires used for connecting the device to an electrical power source. Two metal plates on both sides provide the mechanical protection, and the OASLM's operating area is a circle with the diameter 10 mm.

The OASLM is based on a nematic liquid crystal (LC) layer, sandwiched between two a-As₂S₃ chalcogenide thin films with 60 nm thickness, which form two photosensitive (PS) layers [Fig. 2.3 (a)]. The PS layer responsivity depends on the incident light wavelength: a-As₂S₃ films are almost insensitive to red light while blue illumination induces a notable reaction by the OASLM even when the incident light intensity is below 10 nW/mm². We consider a PS with a thickness significantly smaller than the incident light's wavelength, which allows to avoid interference and reflection inside the OASLM.

As LC the devices uses Merck E44 that creates a homogeneous birefringent layer. It is characterized by refractive indices n_o and n_e of the ordinary and extraordinary axis, and the refractive index difference quantifies the birefringence, $\Delta n = n_e - n_o$. The relevant details of the processes regarding this birefringence are discussed in Sec. 2.4. The corresponding phase retardation is $\Gamma = \frac{2\pi d_{LC}}{\lambda} \Delta n$, where λ is the incident light wavelength, d_{LC} is the LC thickness.

The OASLM is connected to the DC-power source and operated when the applied DC-voltage is larger than the threshold value 4 V. The larger is the applied voltage, the stronger is the OASLM's response to incident light. The applied voltage produces an electric field distribution inside the layer, which is assumed to be uniform in darkness (see the electric field E_d in Fig. 2.3 (a)). Since only the central area of the OASLM is used, electric field effects occurring on the OASLM edge are excluded. To avoid the damage to the OASLM, the applied voltage did not exceed $V_{max} = 10$ V in all our experiments.

When a light source illuminates the OASLM, see Fig. 2.3 (b), the PS layer's conductivity locally increases in the illuminated area. This modifies the electric field distribution: the

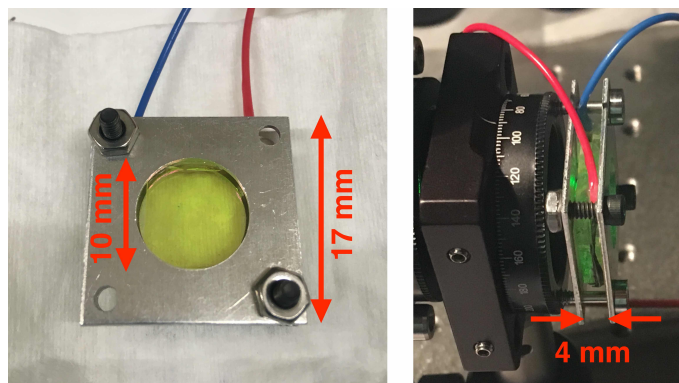


Figure 2.2: OASLM and its dimensions.

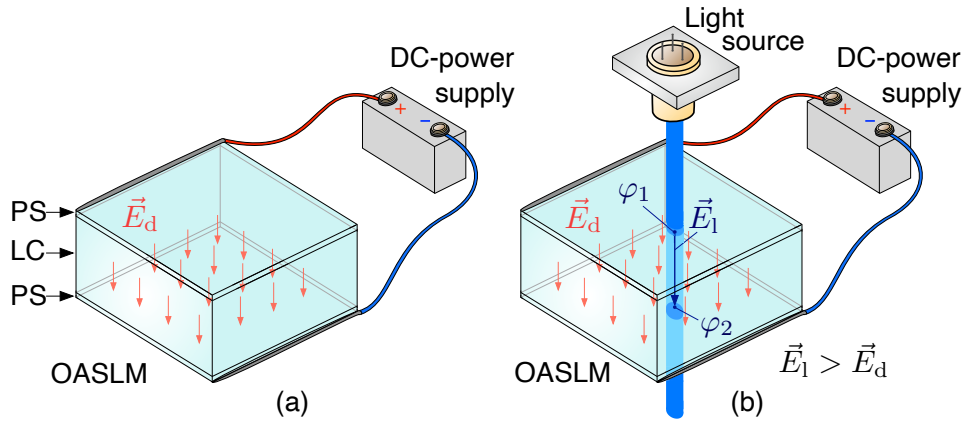


Figure 2.3: OASLM in darkness (panel (a)) and under illumination (panel (b)). Here, the red arrows indicate the electric field E_d in the areas where the illumination is absent, while the electric field at the illuminated point E_l is illustrated by the blue arrow.

electric field applied to the LC-layer at the illuminated area increases (see \vec{E}_l in Fig. 2.3 (b)). As a consequence, LC molecules in the illuminated areas are twisted, and this reorientation results in modifying retardation at the point of illumination. Thus, individual areas of the OASLM act as birefringent waveplates the retardation of which nonlinearly depends on the incident light intensity.

2.3/ ELECTRIC PROCESSES IN THE OASLM

To characterize the resistive properties of the OASLM, the device is approximated as three resistors connected in series, see Fig. 2.4 (a), where each resistor reflects the electric conductivity of a corresponding OASLM layer. It has been shown in [24] that the LC's conductivity is almost agnostic to the optical irradiation intensity, while the conductivity of the α -As₂S₃ PS layers strongly increases with the light intensity. The following assumption is used for the OASLM electronic-circuit model: $R_{LC} = \text{const}$, $R_{PS} = (G_0 + \alpha P_{in})^{-1}$, where G_0 is the PS layer conductance in darkness, α is the PS's conductivity dependence on the illumination, P_{in} is the incident light power on a PS layer. According to the circuit in Fig. 2.4 (a), the current passing through the spatial light modulator takes the form

$$i_S = \frac{V_0}{R_{LC} + 2R_{PS}} = \frac{V_0}{R_{LC} + 2(G_0 + \alpha P_{in})^{-1}}. \quad (2.2)$$

To experimentally determine the OASLM's opto-electronic properties, the optical setup depicted in Fig. 2.4 (b) was used. Here, the injected laser light passes through a lens in order to create a collimated optical beam. The incident light is produced by a laser diode Roithner SHD4580MG, $\lambda = 450$ nm, and collimated by the lens Thorlabs C240TMD-A. The beam then propagates through the block of 'Polarizer1 - $\lambda/2$ -plate - Polarizer2', and

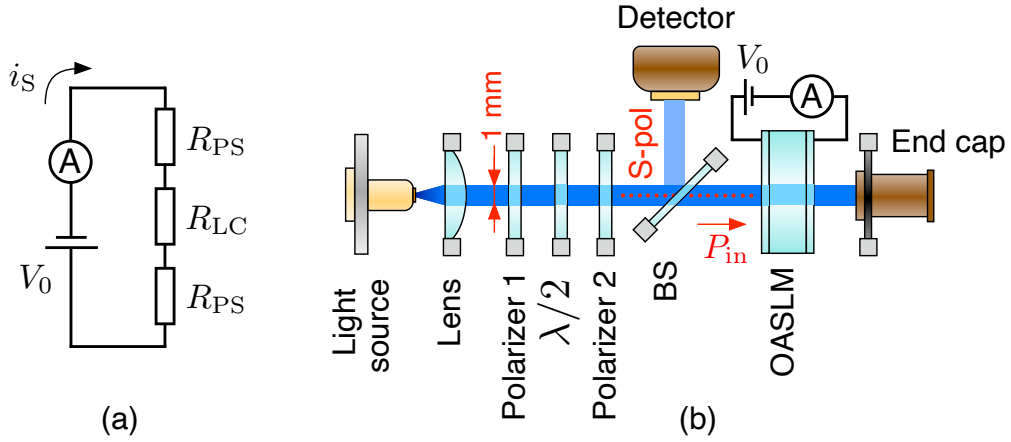


Figure 2.4: (a) Electronic circuit interpretation of the OASLM; (b) Experimental setup developed for the study of OASLM's electrical properties under blue illumination.

is hence linearly polarized. Rotating the $\lambda/2$ -plate, one can control P_{in} illuminating the OASLM surface without change of the laser's bias current. Polarizer 2 is rotated such that the transmitted light is S-polarized. The beamsplitter (BS) reflects 4% of the incident light to the detector, which allows to measure P_{in} . The light beam transmitted by the OASLM is discarded, since here the OASLM's optical response is not under study. The voltage applied across the OASLM is $V_0 = 9$ V.

The experimental setup allows to measure the current flowing through the OASLM as a function of the incident light power, red circles in Fig. 2.5 (a). Experimentally recording current $i_S(P_{in})$, one obtains the global OASLM resistance $R_S = V_0/i_S$, red circles in Fig. 2.5 (b). The parameters R_{LC} , G_0 , and α in Eq. (2.2) are obtained from a fit to the experimental data $i_S(P_{in})$ using the least squares method, blue solid curve in Fig. 2.5 (a), and from this we obtain the dependence $R_S(P_{in})$, blue solid curve in Fig. 2.5 (b). As can be seen from the excellent agreement, the experimental data is well-approximated by the simple electronic model within four orders of magnitude of the incident light power $P_{in}[10^{-8}; 6 \times 10^{-4}]$ W.

Interestingly, quantities i_S and P_{in} are integrals that describe the global resistive behaviour of the OASLM as a function of the global illumination power. To describe the action of the OASLM at any point of the surface (x,y) , quantities i_S and P_{in} are expressed in a surface integral form as

$$P_{in} = \iint_S I_{in} dS = \int_{-\infty}^{\infty} \int_{-\infty}^{\infty} I_{in}(x,y) dx dy, \quad i_S = \iint_S j_S dS = \int_{-\infty}^{\infty} \int_{-\infty}^{\infty} j_S(x,y) dx dy, \quad (2.3)$$

where $j_S(x,y)$ is an electric current density, $I_{in}(x,y)$ is the optical irradiance. Using Eqs.

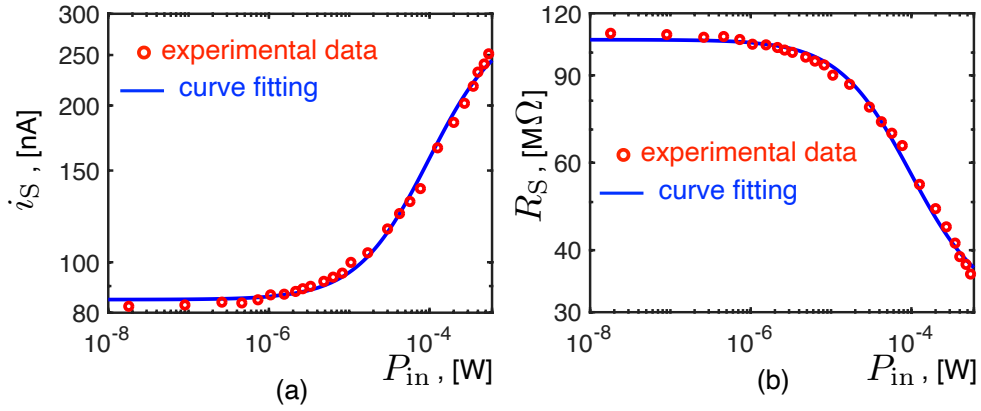


Figure 2.5: OASLM under blue laser illumination, $\lambda = 450$ nm.: (a) Experimentally measured dependences of the current through the OASLM, i_S , on the incident optical power, P_{in} (red circles), and the result of curve fitting (blue solid line) to Eq. (2.2). The obtained parameters are $R_{LC} = 3.08 \times 10^7$ [Ω], $G_0 = 2.65 \times 10^{-8}$ [Ω^{-1}], $\alpha = 5.03 \times 10^{-4}$ [$W^{-1}\Omega^{-1}$]; (b) Dependence of OASLM's resistance, R_S , on the incident light power, P_{in} , obtained from experimental data (red circles). The blue line corresponds to the parameters obtained through the fit in panel (a).

(2.3), Eq. (2.2) is transformed into

$$\int_{-\infty}^{\infty} \int_{-\infty}^{\infty} j_S(x, y) dx dy = \frac{V_0}{R_{LC} + 2 \left(G_0 + \alpha \int_{-\infty}^{\infty} \int_{-\infty}^{\infty} I_{in}(x, y) dx dy \right)^{-1}}. \quad (2.4)$$

Extracting the derivatives $\frac{d}{dx}$ and $\frac{d}{dy}$ from the left and right part of Eq. (2.4), one can derive the dependence of the electric current density on the optical irradiance. The calculation of the first derivative $\frac{d}{dx}$ results in

$$\int_{-\infty}^{\infty} j_S(x, y) dy = \frac{2V_0\alpha \int_{-\infty}^{\infty} I(x, y) dy}{\left(R_{LC} \left(G_0 + \alpha \int_{-\infty}^{\infty} \int_{-\infty}^{\infty} I_{in}(x, y) dx dy \right) + 2 \right)^2}, \quad (2.5)$$

while derivation against $\frac{d}{dy}$ gives

$$j_S(x, y) = \frac{2V_0\alpha I(x, y)}{\left(R_{LC} \left(G_0 + \alpha \int_{-\infty}^{\infty} \int_{-\infty}^{\infty} I_{in}(x, y) dx dy \right) + 2 \right)^2} - \frac{4V_0\alpha^2 R_{LC} \int_{-\infty}^{\infty} I_{in}(x, y) dx \int_{-\infty}^{\infty} I_{in}(x, y) dy}{\left(R_{LC} \left(G_0 + \alpha \int_{-\infty}^{\infty} \int_{-\infty}^{\infty} I_{in}(x, y) dx dy \right) + 2 \right)^3}. \quad (2.6)$$

During the experiment described above, the OASLM was illuminated by a Gaussian beam (schematically shown in Fig. 2.6 (a)) with irradiance according to $I_{in}(x, y) = \frac{P_{in}}{2\pi\sigma_1^2} \exp\left(-\frac{x^2}{2\sigma_1^2} - \frac{y^2}{2\sigma_1^2}\right)$, where σ_1 defines the width. The corresponding power

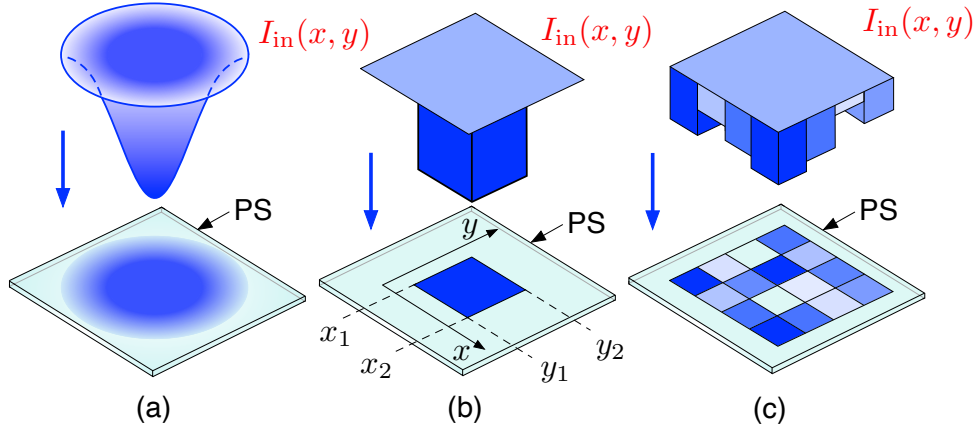


Figure 2.6: Different options for the OASLM illumination: Gaussian (panel (a)), uniform (panel (b)), partially-uniform (panel(c)).

is $\int_{-\infty}^{\infty} \int_{-\infty}^{\infty} \frac{P_{in}}{2\pi\sigma_1^2} \exp\left(-\frac{x^2}{2\sigma_1} - \frac{y^2}{2\sigma_1}\right) dx dy = P_{in}$, and the result of multiplying both integrals can be rewritten as

$$\begin{aligned} \int_{-\infty}^{\infty} I_{in}(x, y) dx \int_{-\infty}^{\infty} I_{in}(x, y) dy &= \frac{P_{in}}{\sqrt{2\pi\sigma_1}} \exp\left(-\frac{y^2}{2\sigma_1}\right) \frac{P_{in}}{\sqrt{2\pi\sigma_1}} \exp\left(-\frac{x^2}{2\sigma_1}\right) \\ &= \frac{P_{in}^2}{2\pi\sigma_1^2} \exp\left(-\frac{x^2}{2\sigma_1} - \frac{y^2}{2\sigma_1}\right) = P_{in} I_{in}(x, y). \end{aligned} \quad (2.7)$$

Consequently, Eq. (2.6) takes the form

$$\begin{aligned} j_S(x, y) &= K I_{in}(x, y), \text{ where} \\ K &= \frac{2V_0\alpha}{(R_{LC}(G_0 + \alpha P_{in}) + 2)^2} - \frac{4V_0\alpha^2 R_{LC} P_{in}}{(R_{LC}(G_0 + \alpha P_{in}) + 2)^3}. \end{aligned} \quad (2.8)$$

It results from Eq. (2.8) that $j_S(I_{in} = 0) = 0$. This contradicts the experimental results which showed a weak but non-zero current flowing through the OASLM in darkness. Since this range is out of consideration in the following, the mentioned difference between the experiment and model can be neglected.

Equation (2.8) highlights an important result: the electric current density is linearly proportional to the incident light intensity at any point of the illumination area. Thus, an increase of the optical intensity induces a proportional electric current density. In terms of electrodynamics, such an increase in current density growth correspondingly increases the local electric field \vec{E} which quantitatively is expressed by the differential Ohm's Law $\vec{j}_S = \sigma \vec{E}$, where σ is the medium's conductivity. As a consequence, the electric potential difference between two points on the opposite sides of the illuminated LC-layer (see the potentials φ_1 and φ_2 in Fig. 2.3) becomes $\varphi_1 - \varphi_2 = \Delta\varphi = d_{LC} E$. Summarising, one can

derive the dependence of the electric potential difference at any point of the illuminated area on the incident light irradiance according to $\Delta\varphi(x, y) = \frac{d_{LC}K}{\sigma} I_{in}(x, y)$.

Suppose that the OASLM is illuminated such that $I_{in}(x, y) = \text{const} = I_0$ inside the area $x \in [x_1; x_2]$, $y \in [y_1; y_2]$, and $I_{in}(x, y) = 0$ elsewhere [Fig. 2.6 (b)]. For this case Eq. (2.6) needs to be transformed to the new illumination profile, for which $\int_{-\infty}^{\infty} \int_{-\infty}^{\infty} I_{in}(x, y) dx dy = P_{in}$.

Particularly, power for uniform illumination is $P_{in} = I_0 S$, where S is the illuminated area, here a square, and one immediately obtained $\int_{-\infty}^{\infty} I_{in}(x, y) dx \int_{-\infty}^{\infty} I_{in}(x, y) dy = \int_{x_1}^{x_2} I_0 dx \int_{y_1}^{y_2} I_0 dy = I_0^2 \int_{x_1}^{x_2} dx \int_{y_1}^{y_2} dy = I_0^2 S$. The relationship between irradiance and the electric current density at any point of the illuminated area takes the final form

$$j_S = \frac{2V_0\alpha I_0}{(R_{LC}(G_0 + \alpha I_0 S) + 2)^2} - \frac{4V_0\alpha^2 R_{LC} I_0^2 S}{(R_{LC}(G_0 + \alpha I_0 S) + 2)^3}. \quad (2.9)$$

Nonlinear current dependencies only arise for large light intensities, $I > 10 \text{ W/m}^2$, which is outside the relevant range since for the retardation reaches saturation much before such intensities, see Chapter 2.5. As in the OASLM description presented in [24], the maximal illumination intensity did not exceed $I_{\max} = 1.5 \text{ W/m}^2$ (for $\lambda = 450 \text{ nm}$). Thus, it can be assumed in the following that $j_S = KI_0$. Applying the same reasoning on an electric field used for the Gaussian illumination, one obtains the same linear relationship for the electric potential difference at the illuminated area on the local irradiance $\Delta\varphi = \frac{d_{LC}K}{\sigma} I_0$.

If the distribution of the incident irradiance is partially uniform such that one can distinguish square areas of the uniform illumination, as in Fig. 2.6 (c), and the OASLM resolution allows to separate the areas well, then one can independently consider each area. In such a case, Eq. (2.9) is assumed to be valid for each particular uniformly illuminated area which means the applicability of the relationship $j_S(x, y) = KI_0(x, y)$.

The maximal number of such distinguishable areas on the OASLM is determined by the device's resolution. According to [24], OASLM's maximal spatial resolution is around 135 lp/mm (which corresponds to $\sigma_{\text{OASLM}} = 3.5 \mu\text{m}$). The spatial resolution is associated to processes occurring at the PS layers. The illumination of the PS-layers induces the internal photoelectric effect that increases the concentration of charge carriers at the illuminated area. Mobility of the charge carriers results in diffusion, and the quantitative characteristics of this carrier diffusion process is lateral diffusion coefficient D_l . It can be calculated using the Einstein relation $D_l = \mu k_B T$, where μ is the charge carrier mobility, k_B is Boltzmann's constant and T is the absolute temperature. Here, the PS-layer manifests p-type conductivity, where the charge carriers are positive holes whose lateral mobility is $\mu = 5.4 \times 10^{-2} [\text{cm}^2 / (\text{V} \times \text{s})]$ (see [24] for details). The lateral diffusion coefficient D_l for room temperature $T = 300 \text{ [K]}$ takes the value $D_l = 1.4 \times 10^{-3} [\text{cm}^2/\text{s}]$.

Since the spatial charge carrier distribution gradually changes along positions in (x, y)

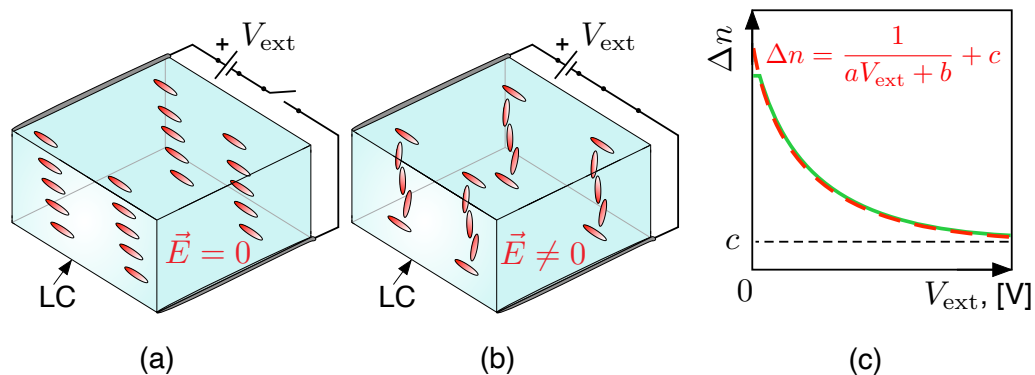


Figure 2.7: LC molecule orientation: a natural state (panel (a)) and the twisted one in the presence of an external voltage applied across the LC layer (panel (b)); (c) Dependence of the birefringence on the applied voltage being typical for many kinds of LC mixtures (green solid curve) and its approximation by the curve $\Delta n = \frac{1}{aV_{\text{ext}} + b} + c$ (red dashed curve).

due to carrier diffusion, the PS-layer conductivity varies accordingly. That means that the electric field inside the LC-layer also continuously varies in space, and hence so does the resulting electric potential difference $\varphi(x, y)$. That is the dominant factor limiting spatial resolution.

2.4/ FROM ELECTRIC PROCESSES TOWARDS THE OPTICAL RESPONSE

Nematic liquid crystal molecules are rod-shaped, and the molecule's refractive index is different along its short and long axis. While in general they can move with respect to each other, their long molecular axes usually remain aligned relative to each other [Fig. 2.7 (a)]. Furthermore, alignment layers on the front and backside of the LC cell induce a global orientation of the LC molecules. For that, the alignment layers exhibit small surface modulations, which result in a direction-aligned anchoring of the molecules to the surface [24]. When an external electric field is applied, changes in the molecule alignment occur [Fig. 2.7 (b)]. The LC molecule reorientation in turn causes a variation of the LC birefringence Δn . Panel (c) in Fig. 2.7 illustrates $\Delta n(V_{\text{ext}})$, which is typically obtained for many types of nematic liquid crystal mixtures. Neglecting the fact that the LC-response is observed for applied voltage values bigger than some threshold $V_{\text{ext}} > V_{\text{thr}}$, $\Delta n(V_{\text{ext}})$ usually follows the dependence $\Delta n(V_{\text{ext}}) = (aV_{\text{ext}} + b)^{-1} + c$. The phase retardation between the ordinary and extraordinary components of the transmitted light, $\Gamma = 2\pi d_{\text{LC}} \Delta n / \lambda$, can therefore be represented as a function of the applied voltage. Taking into account the fact that the applied voltage is equivalent to the electric potential difference between positions on the opposite sides of the LC cell (the electric field distribution is assumed to be uniform

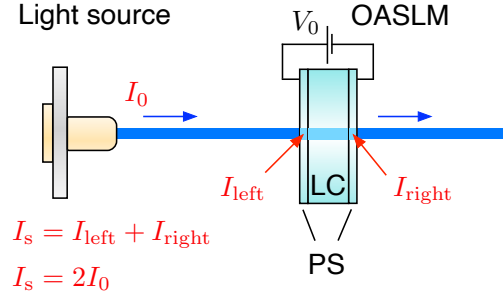


Figure 2.8: Simplified illustration of the OASLM illuminated by a light source and the relevant optical intensities.

at this moment), $V_{ext} = \Delta\varphi$, one can derive the dependence of the retardation Γ on the electric potential difference $\Delta\varphi$ in the form

$$\Gamma(\Delta\varphi) = \frac{2\pi d_{LC}}{\lambda} \left(\frac{1}{a\Delta\varphi + b} + c \right). \quad (2.10)$$

In the OASLM case, the electric potential difference at any point $\Delta\varphi(x, y)$ is linearly proportional on the incident irradiance $I(x, y)$ at this point (see the previous section), $\Delta\varphi(x, y) = K_0 I(x, y)$. The dependence of the retardation produced by the OASLM on the incident irradiance becomes

$$\Gamma(x, y) = \frac{2\pi d_{LC}}{\lambda} \left(\frac{1}{aK_0 I(x, y) + b} + c \right), \quad (2.11)$$

or simply

$$\Gamma(x, y) = \frac{1}{\alpha I(x, y) + \beta} + \gamma, \quad (2.12)$$

where $\alpha = \frac{\lambda a K_0}{2\pi d_{LC}}$, $\beta = \frac{\lambda b}{2\pi d_{LC}}$, $\gamma = \frac{2c\pi d_{LC}}{\lambda}$. The validity of Eq. (2.12) is experimentally examined in the next section.

Considering the individual responses of the left and right PS-layers to the illumination intensity [Fig.2.8], one can rewrite $\Gamma(I_0)$ in the form $\Gamma(I_s)$, where I_s is the summary light intensity on the left and right PS-layers, $I_s = I_{left} + I_{right}$. If the OASLM is studied in the transmissive regime, as in Fig. 2.8, then we ignore the low optical losses of the device and assume $I_{left} = I_{right} = I_0$ and $I_s = 2I_0$. Consequently, Eq. (2.12) takes the form

$$\Gamma(x, y) = \frac{1}{\alpha_s 2I_0(x, y) + \beta} + \gamma, \quad (2.13)$$

where $\alpha_s = \alpha/2$.

2.5/ NONLINEAR SPATIAL LIGHT TRANSFORMATION

To experimentally examine the optical action of the OASLM, the experimental setup in Fig. 2.4 (b) has been modified, see Fig. 2.9. Here, microscope objective MO (Olympus UPlan FL 4x/-0.13) and Lens 2 (Thorlabs AC127-100-A-ML) are used for imaging the OASLM's surface by a camera (IDS U3-3482LE-M). Polarizer 3 only transmits the p-polarized part of the optical field, and the OASLM's rotation angle is $\psi = \frac{\pi}{4}$ [Rad]. The applied voltage across the OASLM is $V_0 = 9$ [V]. The s-polarization state of the light illuminating the OASLM surface is described by the Jones vector $\begin{bmatrix} 0 \\ E_{0y} \end{bmatrix}$. Using the matrix expression of

Eq. (2.1), the polarization state after transmission through the OASLM becomes $\begin{bmatrix} E_{1x} \\ E_{1y} \end{bmatrix} = \begin{bmatrix} i \sin(\Gamma) E_{0y} \\ \cos(\Gamma) E_{0y} \end{bmatrix}$. Since polarizer 3 transmits only p-polarization, the optical field imaged on the camera surface takes the form $\begin{bmatrix} i \sin(\Gamma) E_{0y} \\ 0 \end{bmatrix}$, with corresponding irradiance $|i \sin(\Gamma) E_{0y}|^2 = E_{0y}^2 \sin^2(\Gamma)$. Thus, the relationship between the incident light intensity I_{in} and the detected irradiance is $I_{out} = I_{in} \sin^2(\Gamma)$.

The camera records the polarization filtered irradiance at the OASLM surface as a matrix of pixels, and the optical image resolution is limited by the size of these camera pixels. The pixel size for the used camera is $l_{\text{pixel}} = 2.2 \mu\text{m}$, then the pixel area is $S_{\text{pixel}} = l_{\text{pixel}}^2$. The overall power P_{in} is an integral quantity, $P_{in} = \sum P_{i,j}^{in}$. Taking into consideration the summary power P_{in} and the corresponding scanned irradiance distribution, the power at each camera pixel can be calculated. Then the transition from the light power to the light intensity can be carried out: $I_{i,j}^{in} = P_{i,j}^{in}/S_{\text{pixel}}$ and $I_{i,j}^{out} = P_{i,j}^{out}/S_{\text{pixel}}$. This allows to determine the retardation for each camera pixel by determining the irradiance distributions

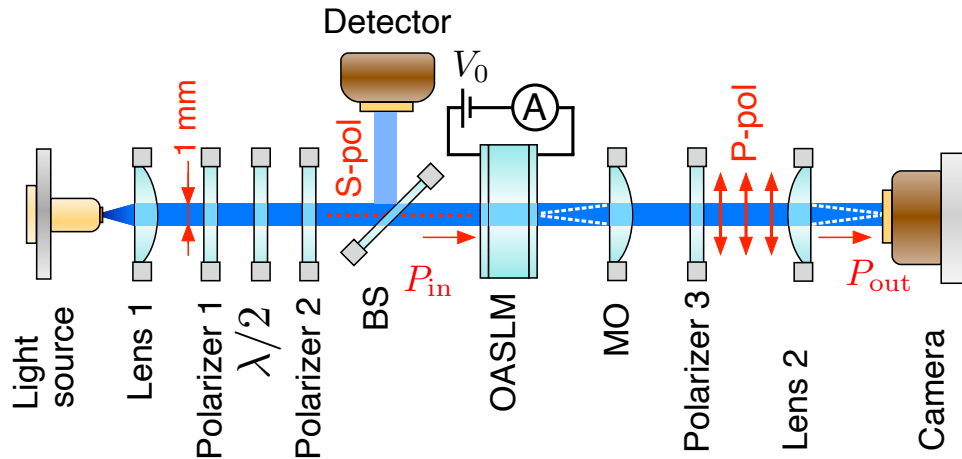


Figure 2.9: Experimental setup developed for the exploration of OASLM's optical response to the blue laser illumination.

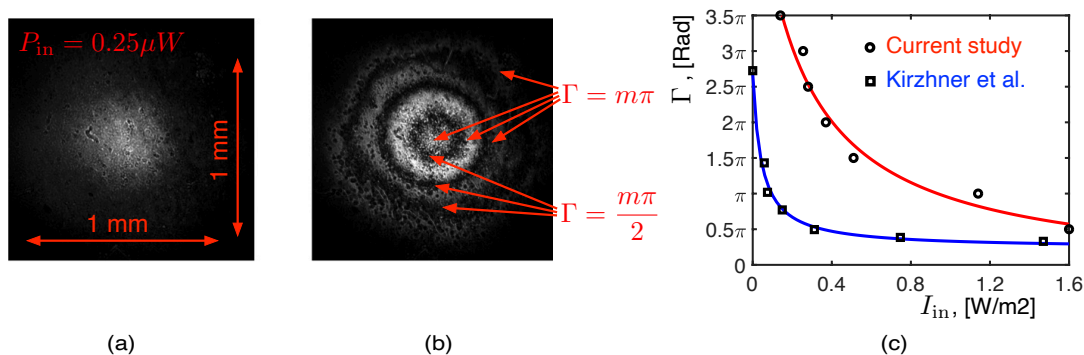


Figure 2.10: (a-b) Scanned by the camera brightness spatial distributions of the incident light beam in front of the OASLM (panel (a)) and of the processed light beam (panel (b)). Local maxima correspond to the retardation $\Gamma = \frac{m\pi}{2}$ while the retardations at the local minima are $\Gamma = m\pi$. (c) Experimentally established dependence of the retardation on the incident light intensity built on the base of local extrema in panel (b) (black circles) and the experimental data for $V_0 = 9$ [V] taken from the paper [24] (black squares). Both dependences are fitted using the function $\Gamma(I_{in}) = (\alpha I_{in} + \beta)^{-1} + \gamma$ (see Eq. (2.12)). The parameters estimated by means of curve-fitting are: $\alpha = 0.234$, $\beta = 0.052$, $\gamma = -0.55$ for the red solid line (curve-fitting of the current experiment), and $\alpha = 2.96$, $\beta = 0.13$, $\gamma = 0.72$ for the blue solid line (curve-fitting of the experiment in [24]).

of the incident and transmitted light beams, see Fig.2.10 (a,b). The incident light has a Gaussian distribution, while the output irradiance distribution possesses distinctive rings. The phase retardation is $\Gamma = \frac{m\pi}{2}$ in the points where the output light has local maxima ($\sin^2(\Gamma) = 1$ in these points). Similarly, $\Gamma = m\pi$ in the points of local minima. Calculating the incident light intensity in these points, the dependence of the retardation, Γ , on the incident light intensity, I_{in} , can be obtained, see Fig.2.10 (c).

The measured $\Gamma(I_{in})$ is similar to the results presented in [24]. However, quantitative difference are present. This is due to the fact that particular areas of the OASLM surface have similar but not exactly the same response to the light illumination.

Curve-fitting using the least squares method allows to estimate the applicability of OASLM model using Eq. (2.12). As can be seen in Fig. 2.10 (c), the experimental data is well approximated by Eq. (2.12).

Furthermore, the OASLM under green illumination was studied. For this purpose the light source and the collimation scheme of the experimental setup in Fig. 2.8 were modified (see Fig. 2.11 (a)). The experimental dependence $\Gamma(I_{in})$ was measured and fitted via the same approach as for the OASLM under blue illumination [Fig. 2.11 (b)]. The experiment revealed that the OASLM sensitivity to green light is much lower than for blue illumination. However, the functional dependence persists.

All results of the OASLM parameter estimation are summarized in table 2.1.

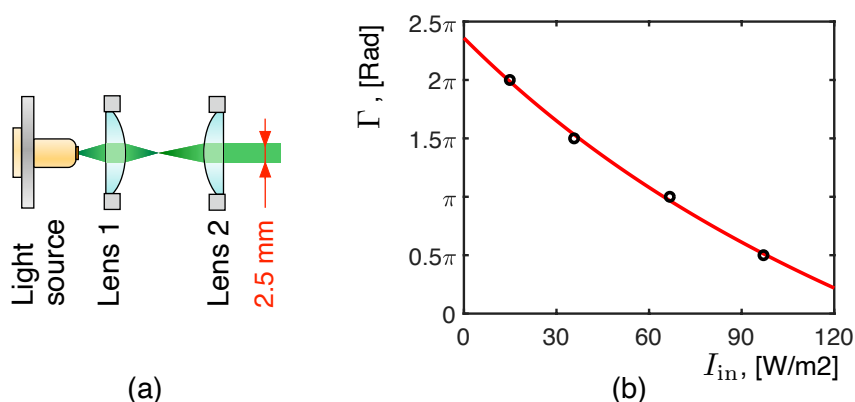


Figure 2.11: (a) Modified block of the experimental setup in Fig.2.9 used for the study of the OASLM under green illumination. This option involves the green laser diode DJ532-10 ($\lambda=532$ nm) and two lenses C110TMD-A (Lens1) and AC254-035-A-ML (Lens2) used for the light collimation. All the other setup elements are the same as in Fig.2.9; (b) Experimentally obtained dependence $\Gamma(I_{in})$ for the green illumination of the OASLM (black circles) and the result of curve-fitting using Eq. (2.12) (red solid curve). The parameters estimated by means of curve-fitting are: $\alpha = 1.97 \times 10^{-4}$, $\beta = 0.0486$, $\gamma = -13.17$.

	Dependence on the incident light intensity, I_{in} (see Eq. (2.12))
OASLM under blue light (experimental data taken from[24])	$\alpha_b = 2.96$, $\beta_b = 0.13$, $\gamma_b = 0.72$
OASLM under blue light (current experiment)	$\alpha_b = 0.234$, $\beta_b = 0.052$, $\gamma_b = -0.55$
OASLM under green light (current experiment)	$\alpha_g = 1.97 \times 10^{-4}$, $\beta_g = 0.0486$, $\gamma_g = -13.17$

Table 2.1: Summary results of the OASLM model parameter estimation

2.6/ OPTICAL FEEDBACK

In the previous sections, the OASLM is considered as a light-processing device. Next, the OASLM is discussed as an element for the implementation of autonomous dynamical systems. For this purpose, one can create a feedback loop through which the optical signal transmitted by the OASLM returns back and through that modifies the instantaneous OASLM state. A simple mirror can be used to realize such feedback, as schematically illustrated in Fig. 2.12. As before, the light source is characterized by the Jones vector $\vec{E}_0 = \begin{bmatrix} E_{0x} \\ E_{0y} \end{bmatrix}$. After passing through the OASLM it transforms into $\vec{E}_1 = \begin{bmatrix} E_{1x} \\ E_{1y} \end{bmatrix}$ at the right PS layer, and this optical field is reflected by the mirror and returns to the right PS layer,

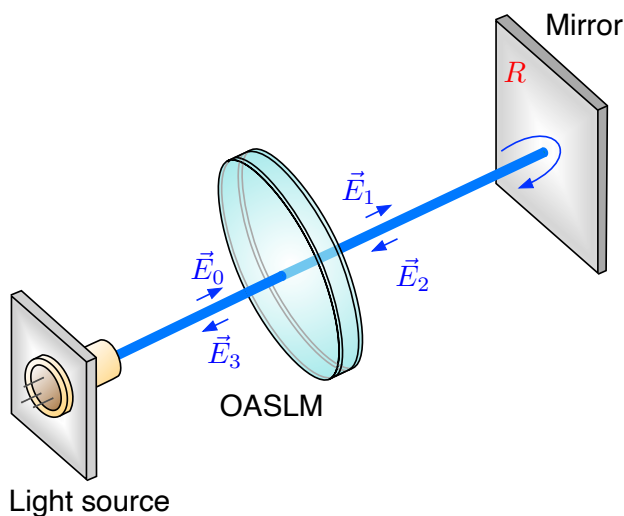


Figure 2.12: OASLM under illumination and optical feedback implemented through an external mirror. In contrast to Fig. 2.1, the system with feedback implies the presence of four optical fields $E_{0,1,2,3}$.

where it is described by $\vec{E}_2 = \begin{bmatrix} E_{2x} \\ E_{2y} \end{bmatrix}$. Finally, the optical wave passes through the OASLM again and is expressed by $\vec{E}_3 = \begin{bmatrix} E_{3x} \\ E_{3y} \end{bmatrix}$ at the left PS layer.

To avoid confusing between experimental studies and numerical simulations, all the mathematical models studied below are considered in the dimensionless form, where all the parameters and variables are normalized by the corresponding units. For this reason, all the quantities and parameters of mathematical models are mentioned later without dimensions.

2.7/ INCOHERENT ILLUMINATION

Suppose that the OASLM is illuminated by an incoherent light source, for instance, by a light-emitting diode (LED) [Fig. 2.13]. The OASLM feedback is implemented by a mirror whose field-reflectivity is R , and we assume that the incoherent light source's coherence time is small compared to the external cavities' roundtrip time. Consequently, interference between the incident light wave and the reflected one does not occur. Again, here we consider a PS with a thickness significantly smaller than the wavelength. If there is no additional selective element between the OASLM and mirror, the resulting light irradiance at the left and right PS-layers are $I_{\text{left}} = I_0(1 + R^2)$ and $I_{\text{right}} = I_0(1 + R^2)$ does not depend on the OASLM's retardation. For this reason the optical setup in [Fig. 2.13] includes a polarizer between the OASLM and mirror, which allows to create functional dependences $I_{\text{left}}(\Gamma)$ and $I_{\text{right}}(\Gamma)$.

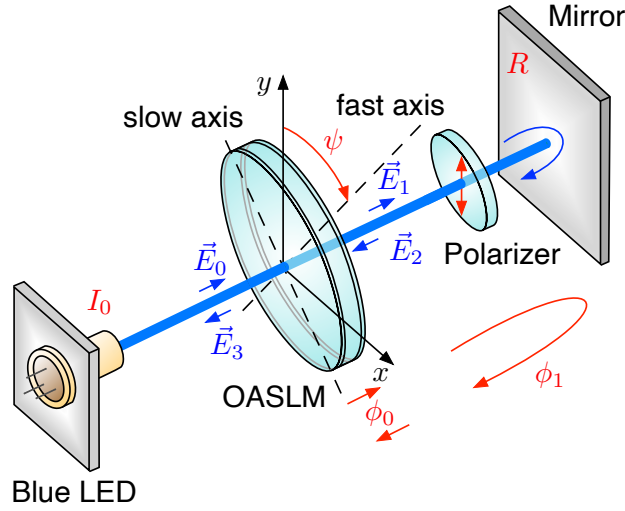


Figure 2.13: OASLM under incoherent illumination of a blue LED and feedback created by a mirror and a polarizer transmitting p-polarization.

The system in Fig.2.13 is investigated using a constant $\psi = \frac{\pi}{4} + \pi m$, where $m \in \mathbb{Z}$. The injected blue light field is s-polarized, $\vec{E}_0 = \begin{bmatrix} E_0 \\ 0 \end{bmatrix}$. When the light beam passes through the OASLM first time, its state becomes $\vec{E}_1 = E_0 \exp(i\phi_0) \begin{bmatrix} \cos(\Gamma) \\ i \sin(\Gamma) \end{bmatrix}$. After that, the polarizer transmits only s-polarization component, reaches the mirror and returns to the right PS-layer. The optical phase shift associated with the propagation along the external cavity is ϕ_1 , and the polarization state of light which returns to the right PS-layer is $\vec{E}_2 = RE_0 \exp(i(\phi_0 + \phi_1)) \begin{bmatrix} 0 \\ i \sin(\Gamma) \end{bmatrix}$. The light beam passes through the OASLM again and its Jones vector at the left PS-layer becomes $\vec{E}_3 = RE_0 \exp(i(2\phi_0 + \phi_1)) \begin{bmatrix} -\sin^2(\Gamma) \\ \frac{i}{2} \sin(2\Gamma) \end{bmatrix}$, and the intensities of the light fields are $|E_1|^2 = I_0$, $|E_2|^2 = |E_3|^2 = I_0 R^2 \sin^2(\Gamma)$. Since interference effect can be neglected, the intensities at the left and right PS-layers are $I_{\text{left}} = |E_0|^2 + |E_3|^2 = I_0 \{1 + R^2 \sin^2(\Gamma)\}$ and $I_{\text{right}} = |E_1|^2 + |E_2|^2 = I_0 \{1 + R^2 \sin^2(\Gamma)\}$, leading to an overall detected intensity of $I_s = I_{\text{left}} + I_{\text{right}} = 2I_0 \{1 + R^2 \sin^2(\Gamma)\}$.

Light wave propagation along the feedback loop is much faster than the OASLM's response time. That means the OASLM's temporal dynamics can be written in the differential form $\Gamma + \varepsilon \frac{d\Gamma}{dt} = \Gamma(I_s)$, where ε is OASLM's response time. The function $\Gamma(I_s)$ is determined according to Eq. (2.13), and the dynamical system equations are

$$\varepsilon \frac{d\Gamma}{dt} = -\Gamma + \frac{1}{\alpha I_s + \beta} + \gamma, \quad I_s = 2I_0 \{1 + R^2 \sin^2(\Gamma)\}. \quad (2.14)$$

Let's consider fixed parameters $\alpha = 0.117$, $\beta = 0.052$, $\gamma = -0.55$ (a set of OASLM's

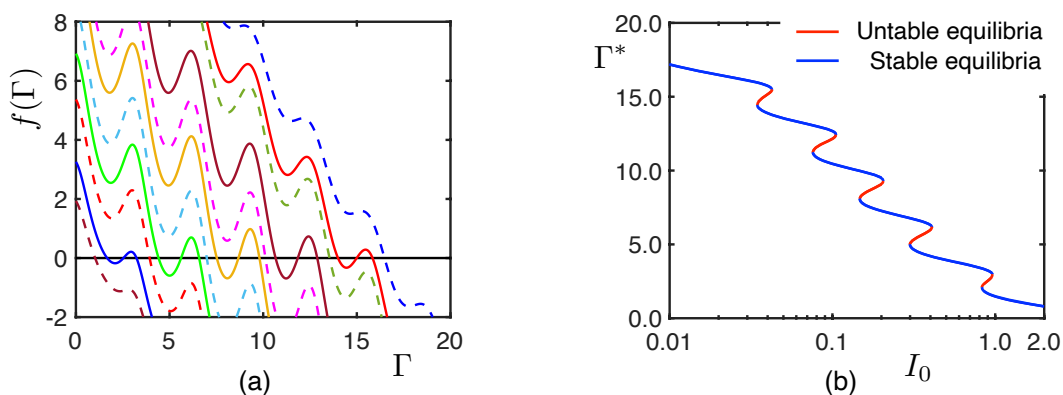


Figure 2.14: System (2.14): (a) The evolution of the right-hand side function $f(\Gamma)$ for Eq. (2.14) caused by the injected light intensity growth: $I_0 = 0.02$ (blue dashed curve), $I_0 = 0.038$ (red solid curve), $I_0 = 0.05$ (dark-green dashed curve), $I_0 = 0.088$ (brown solid curve), $I_0 = 0.13$ (magenta dashed curve), $I_0 = 0.17$ (orange solid curve), $I_0 = 0.25$ (cyan dashed curve), $I_0 = 0.35$ (green solid curve), $I_0 = 0.5$ (red dashed curve), $I_0 = 0.9$ (blue solid curve), $I_0 = 1.5$ (brown dashed curve); (b) Phase-parametric diagram reflecting the existence, appearance, disappearance and motion of steady states for increasing parameter I_0 . System parameters are: $\alpha = 0.117$, $\beta = 0.052$, $\gamma = -0.55$, $\varepsilon = 1$, $R = 0.95$.

parameters experimentally obtained in Sec. 2.5 for the blue illumination, see table 2.1), $R = 0.95$ and varying I_0 . Increasing I_0 gives rise to multiple transitions between monostable and bistable steady-state regimes occurring via the saddle-node bifurcation. This process is illustrated in the evolution of the right-hand side function $f(\Gamma) = -\Gamma + (2\alpha I_0(1 + R^2 \sin^2(\Gamma)) + \beta)^{-1} + \gamma$ for Eq. (2.14) [Fig. 2.13 (a)] and the corresponding phase-parametric diagram [Fig. 2.13 (b)]. There, different colors correspond to different I_0 . The transition from monostability to bistability manifests itself through the appearance of a pair of stable and unstable steady states, while the initially monostable fixed point does not bifurcate. The transition from bistability to monostability represents the opposite process when the unstable steady state approaches either fixed point, collides and finally disappears with it. The bistable dynamics of Eq. (2.14) is observed in the parameter ranges $I_0 \in [0.035 \ 0.042]$, $I_0 \in [0.076 \ 0.105]$, $I_0 \in [0.147 \ 0.2]$, $I_0 \in [0.3 \ 0.405]$, and $I_0 \in [0.85 \ 0.95]$, while the system is monostable elsewhere.

If the polarizer in Fig. 2.13 is horizontally oriented, the system equation becomes $\varepsilon \frac{d\Gamma}{dt} = -\Gamma + (2\alpha I_0(1 + R^2 \cos^2(\Gamma)) + \beta)^{-1} + \gamma$, yet the dynamics remains to be qualitatively the same: the saddle-node bifurcations of steady states are possible, but the bifurcation parameter values differ.

Crucially, here we talk about the OASLM as a single oscillator, i.e. without coupling between different spatial positions of the the device. For such a system, any other kinds of the oscillatory behaviour besides the existence of one stable steady state and the coexistence of two stable equilibria cannot be found for systems described by Eq. (2.14). To extend a manifold of oscillatory regimes demonstrated by the OASLM with the optical

feedback, one will need to rely on the interference effects provided by coherent light.

2.8/ COHERENT ILLUMINATION

Suppose that the OASLM is illuminated by laser light [Fig. 2.15], which usually has coherence lengths significantly larger than meters. This implies the injected light wave's initial phase is assumed to be constant during the time of propagation through the OASLM and between the OASLM and the mirror. Again, here we consider a PS with a thickness significantly smaller than the wavelength. In contrast to the incoherent illumination case, the optical setup in Fig. 2.15 does not contain the polarizer between the OASLM and the mirror. Due to the now present interference between coherent optical fields, the optical fields at the left and right PS layers are $\vec{E}_{\text{left}} = \vec{E}_0 + \vec{E}_3$ and $\vec{E}_{\text{right}} = \vec{E}_1 + \vec{E}_2$, respectively, with their corresponding overall intensity $I = I_{\text{left}} + I_{\text{right}} = |\vec{E}_{\text{left}}|^2 + |\vec{E}_{\text{right}}|^2$. Generally, the summary intensity is a function of the OASLM parameters including the rotation angle, of the feedback characteristics, and of the laser light intensity and polarization state. Concrete configurations are studied below.

2.8.1/ OASLM FOR AMPLITUDE MODULATION

Consider the model of the optical setup in Fig. 2.15 for the following assumptions: the OASLM's rotation angle is $\psi = \pi/4$, the injected light polarization state is $\vec{E}_0 = \begin{bmatrix} E_0 \\ 0 \end{bmatrix}$, and

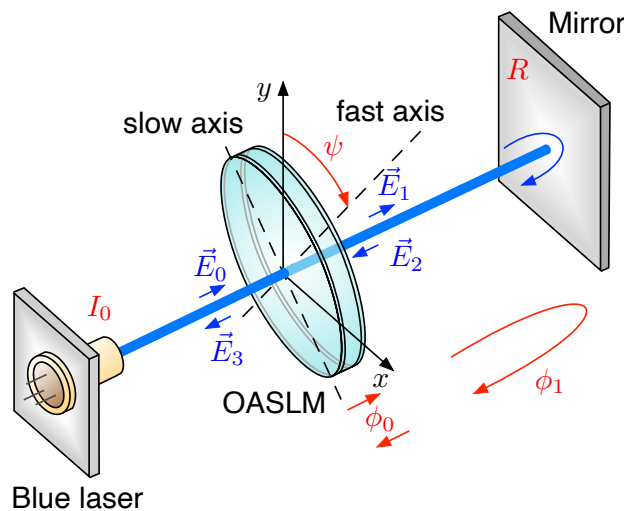


Figure 2.15: OASLM under coherent illumination of a blue laser and mirror feedback. In contrast to the system depicted in Fig. 2.14, the system with coherent illumination involves interference between fields $E_{0,3}$ on the left side of the OASLM, and between fields $E_{1,2}$ on the right side.

the Jones vectors for the light fields $\vec{E}_{1,2,3}$ are

$$\begin{aligned}\vec{E}_1 &= E_0 \exp(i\phi_0) \begin{bmatrix} \cos(\Gamma) \\ i \sin(\Gamma) \end{bmatrix}, & \vec{E}_2 &= RE_0 \exp(i(\phi_0 + \phi_1)) \begin{bmatrix} \cos(\Gamma) \\ i \sin(\Gamma) \end{bmatrix}, \\ \vec{E}_3 &= RE_0 \exp(i(2\phi_0 + \phi_1)) \begin{bmatrix} \cos(2\Gamma) \\ i \sin(2\Gamma) \end{bmatrix}.\end{aligned}\tag{2.15}$$

The phase retardation Γ appears in the expressions for the complex field amplitudes. The OASLM therefore is operated in the amplitude modulation configuration, and we obtain

$$\begin{aligned}\vec{E}_{\text{left}} = \vec{E}_0 + \vec{E}_3 &= E_0 \begin{bmatrix} 1 + R \exp(i(2\phi_0 + \phi_1)) \cos(2\Gamma) \\ iR \exp(i(2\phi_0 + \phi_1)) \sin(2\Gamma) \end{bmatrix}, \\ \vec{E}_{\text{right}} = \vec{E}_1 + \vec{E}_2 &= E_0 (\exp(i\phi_0) + R \exp(i(\phi_0 + \phi_1))) \begin{bmatrix} \cos(\Gamma) \\ i \sin(\Gamma) \end{bmatrix},\end{aligned}\tag{2.16}$$

with

$$\begin{aligned}I_{\text{left}} = |\vec{E}_{\text{left}}|^2 &= I_0 \{1 + R^2 + 2R \cos(2\phi_0 + \phi_1) \cos(2\Gamma)\}, \\ I_{\text{right}} = |\vec{E}_{\text{right}}|^2 &= I_0 \{1 + R^2 + 2R \cos(\phi_1)\}.\end{aligned}\tag{2.17}$$

Taking into account that the global optical intensity controlling the OASLM state is $I_s = I_{\text{left}} + I_{\text{right}}$, the model equations become

$$\begin{aligned}\varepsilon \frac{d\Gamma}{dt} &= -\Gamma + \frac{1}{\alpha I_s + \beta} + \gamma, \\ I_s &= 2I_0 \{1 + R^2 + R \cos(2\phi_0 + \phi_1) \cos(2\Gamma) + R \cos(\phi_1)\}.\end{aligned}\tag{2.18}$$

The nonlinearity of Eq. (2.18) is most pronounced at $\phi_1 = m\pi$, $\phi_0 = n(1 + 1/2)\pi$, where $m, n \in \mathbb{Z}$. In this case, the corresponding expression for the summary light irradiance takes the form $I_s = 2I_0 \{1 + R^2 - R + R \cos(2\Gamma)\}$, and we use $R = 0.95$, $\varepsilon = 1$, $\alpha = 0.117$, $\beta = 0.052$, $\gamma = -0.55$. In such a case, increasing I_0 gives rise to a cascade steady-state saddle-node bifurcations which is indicated in the evolution of the right-hand side function $f(\Gamma) = -\Gamma + (2\alpha I_0(1 + R^2 - R + R \cos(2\Gamma)) + \beta)^{-1} + \gamma$ for Eq. (2.18), see Fig. 2.16 (a), and the corresponding phase-parametric diagram in Fig. 2.16 (b). In contrast to the incoherent system described by Eq. (2.14), the saddle-node bifurcations in Eq. (2.18) realizes the transition from the monostability all the way to the coexistence of six steady states. The bifurcations occur at $I_0 \approx 0.0205$, $I_0 \approx 0.054$, $I_0 \approx 0.11$, $I_0 \approx 0.21$, $I_0 \approx 0.48$. In contrast to the case of incoherent illumination, the saddle-node bifurcations in Eq. (2.18) result only in the appearance of new steady states, and their associated basins of attraction.

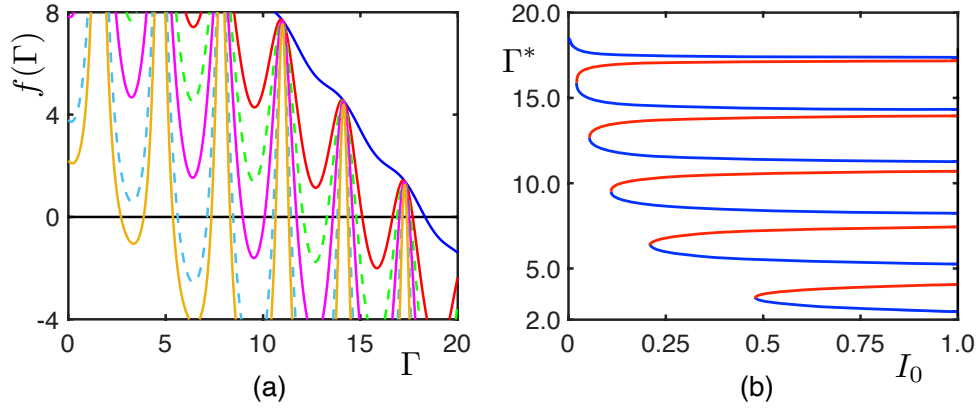


Figure 2.16: (a) The evolution of the right-hand side function $f(\Gamma)$ for Eqs. (2.18) and (2.22) caused by increasing the parameter I_0 : $I_0 = 0.003$ (blue solid line), $I_0 = 0.04$ (red solid line), $I_0 = 0.08$ (green dashed line), $I_0 = 0.15$ (magenta solid line), $I_0 = 0.4$ (cyan dashed line), $I_0 = 0.7$ (orange solid line); (b) Phase-parametric diagram reflecting the existence, appearance, disappearance and motion of steady states for increasing parameter I_0 (stable steady states are coloured in blue, the unstable ones are coloured in red). System parameters are: $\alpha = 0.117$, $\beta = 0.052$, $\gamma = -0.55$, $\varepsilon = 1$, $R = 0.95$, $\phi_0 = \pi$, $\phi_1 = \pi/2$.

2.8.2/ OASLM FOR PHASE MODULATION

Next, the system in Fig. 2.15 is studied for an OASLM rotation angle $\psi = m\pi$, $m \in \mathbb{Z}$, and the injected light Jones vector $\vec{E}_0 = \begin{bmatrix} E_0 \\ 0 \end{bmatrix}$. The Jones vectors for the light fields are

$$\vec{E}_1 = \exp(i\phi_0) \begin{bmatrix} E_0(\cos(\Gamma) + i \sin(\Gamma)) \\ 0 \end{bmatrix} = \exp(i(\phi_0 + \Gamma)) \begin{bmatrix} E_0 \\ 0 \end{bmatrix}, \quad (2.19)$$

$$\vec{E}_2 = R \exp(i(\phi_0 + \phi_1 + \Gamma)) \begin{bmatrix} E_0 \\ 0 \end{bmatrix}, \quad \vec{E}_3 = R \exp(i(2\phi_0 + \phi_1 + 2\Gamma)) \begin{bmatrix} E_0 \\ 0 \end{bmatrix}.$$

Here, phase retardation Γ is present only in the optical phase-term $\exp(i(\dots))$ which determines the light wave phase for, both, x - and y -components. Therefore, the explored configuration corresponds to the phase modulation configuration of the OASLM, for which the optical fields at the left and right PS layers are

$$\vec{E}_{\text{left}} = \vec{E}_0 + \vec{E}_3 = \begin{bmatrix} E_0 \{1 + R \exp(i(2\phi_0 + \phi_1 + 2\Gamma))\} \\ 0 \end{bmatrix}, \quad (2.20)$$

$$\vec{E}_{\text{right}} = \vec{E}_1 + \vec{E}_2 = \begin{bmatrix} E_0 \{ \exp(i(\phi_0 + \Gamma)) + \exp(i(\phi_0 + \phi_1 + \Gamma)) \} \\ 0 \end{bmatrix},$$

with the corresponding light intensities

$$\begin{aligned} I_{\text{left}} &= I_{0b} \{1 + R^2 + 2R \cos(2\phi_0 + \phi_1 + 2\Gamma)\}, \\ I_{\text{right}} &= I_{0b} \{1 + R^2 + 2R \cos(\phi_1)\}. \end{aligned} \quad (2.21)$$

The summary light intensity is $I_s = I_{\text{left}} + I_{\text{right}}$, and then the system's dynamical equation is

$$\varepsilon \frac{d\Gamma}{dt} = -\Gamma + \frac{1}{\alpha I_s + \beta} + \gamma, \quad (2.22)$$

$$I_s = 2I_0 \{1 + R^2 + R \cos(\phi_1) + R \cos(2\phi_0 + \phi_1 + 2\Gamma)\}.$$

When the system phase parameters are $\phi_1 = m\pi$, $\phi_0 = n(1 + 1/2)\pi$, where $m, n \in \mathbb{Z}$, the summary light intensity takes the form $I_s = 2I_0 \{1 + R^2 - R + R \cos(2\Gamma)\}$. In such a case, Eqs. (2.22) and (2.18) fully correspond and all bifurcation phenomena caused by increasing the parameter I_0 (see Fig. 2.16) are identical up to the degree of a direct quantitative correspondence.

2.9/ OASLM UNDER SIMULTANEOUS TWO-COLOR ILLUMINATION

Suppose that the OASLM is simultaneously illuminated by coherent blue and green light, as illustrated in Fig. 2.17. Again, here we consider a PS with a thickness significantly smaller than the wavelength. One can write the PS-layer resistance as a function on the corresponding incident light powers P_b^{in} and P_g^{in} as $R_{\text{PS}} = (G_0 + \alpha_b P_b^{\text{in}} + \alpha_g P_g^{\text{in}})^{-1}$. The expression for the current through the OASLM then takes the form (similar to Eq. (2.2)): $i_s = \frac{V_0}{R_{\text{LC}} + 2R_{\text{PS}}} = \frac{V_0}{R_{\text{LC}} + 2(G_0 + \alpha_b P_b^{\text{in}} + \alpha_g P_g^{\text{in}})^{-1}}$. Following to the same logic as in Secs. 2.3 and 2.4 and repeating all the procedures presented there, one obtains the following expressions for the retardation of the green and blue light produced by the OASLM at spatial position

$$\begin{aligned} \Gamma_b(x, y) &= \frac{1}{\alpha_b I_b(x, y) + \alpha_g^* I_g(x, y) + \beta_b} + \gamma_b, \\ \Gamma_g(x, y) &= \frac{1}{\alpha_b^* I_b(x, y) + \alpha_g I_g(x, y) + \beta_g} + \gamma_g, \end{aligned} \quad (2.23)$$

where I_b and I_g are the light combined irradiance at the left and right PS-layers of the blue and green lights at the left and right PS-layers, the expressions for α_g^* and α_b^* will be derived below. For the configuration in Fig. 2.17, the summary irradiances are $I_b = 2I_{0b}$ and $I_g = 2I_{0g}$.

Due to the different wavelengths, the same birefringence produces different retardations

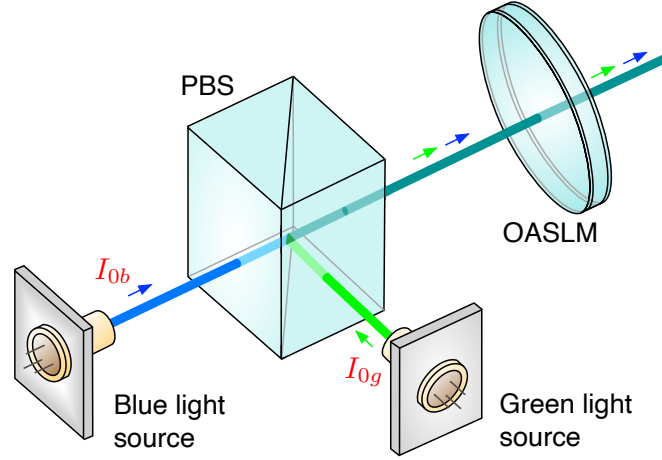


Figure 2.17: OASLM under simultaneous blue and green illumination.

for light with different colors according to

$$\begin{cases} \Gamma_b = \frac{2\pi d}{\lambda_b} \Delta n, \\ \Gamma_g = \frac{2\pi d}{\lambda_g} \Delta n, \end{cases} \Rightarrow \Gamma_g = \frac{\lambda_b}{\lambda_g} \Gamma_b. \quad (2.24)$$

If the OASLM operates in the saturation regime at $I_b \rightarrow \infty$ or $I_g \rightarrow \infty$, then the corresponding retardation of the blue light tends to the value $\Gamma_b \rightarrow \gamma_b$. Meanwhile, the same birefringence at the illuminated OASLM area corresponds to the green light retardation $\Gamma_g \rightarrow \gamma_g = \frac{\lambda_b}{\lambda_g} \gamma_b$. If the considered irradiance is negligibly small, $I_b \rightarrow 0$ and $I_g \rightarrow 0$, then the retardation values are $\Gamma_g \rightarrow \frac{1}{\beta_g} + \gamma_g$ and $\Gamma_b \rightarrow \frac{1}{\beta_b} + \gamma_b$. Taking into account that $\Gamma_g = \frac{\lambda_b}{\lambda_g} \Gamma_b$ and $\gamma_g = \frac{\lambda_b}{\lambda_g} \gamma_b$, one obtains that $\beta_g = \frac{\lambda_g}{\lambda_b} \beta_b$. Substituting the relationships for the parameters $\gamma_{b,g}$ and $\beta_{b,g}$ into Eq. (2.23), parameters $\alpha_{b,g}^*$ can be identified as $\alpha_g^* = \frac{\lambda_g}{\lambda_b} \alpha_b$, $\alpha_b^* = \frac{\lambda_b}{\lambda_g} \alpha_g$. Finally, the retardation accumulated upon transmission for the different wavelengths is

$$\Gamma_b(x, y) = \frac{1}{\alpha_b I_b(x, y) + \frac{\lambda_g}{\lambda_b} \alpha_g I_g(x, y) + \beta_b} + \gamma_b, \quad (2.25)$$

$$\Gamma_g(x, y) = \frac{1}{\frac{\lambda_b}{\lambda_g} \alpha_b I_b(x, y) + \alpha_g I_g(x, y) + \beta_g} + \gamma_g,$$

where parameters $\lambda_{b,g}$, $\beta_{b,g}$ and $\gamma_{b,g}$ can be established by experimental characterization in the same way as in Sec. 2.5.

Here, an important aspect should be noted. One cannot relate the parameter values for $\gamma_{b,g}$ and $\beta_{b,g}$ estimated in physical experiments (see Sec. 2.5) as $\gamma_g = \frac{\lambda_b}{\lambda_g} \gamma_b$ and $\beta_g = \frac{\lambda_g}{\lambda_b} \beta_b$. This is due to the fact that different OASLM's areas were illuminated in the experiments with the green and blue lasers. As noted in Sec. 2.5, the OASLM's response to the same

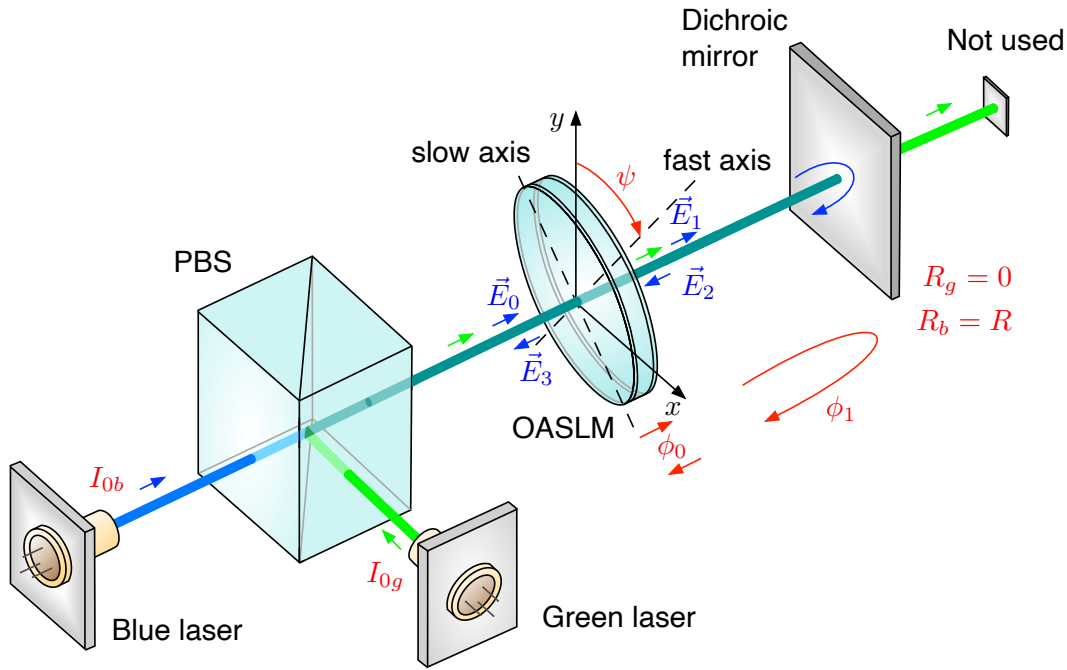


Figure 2.18: OASLM under simultaneous blue and green illumination when the blue light beam is reflected by the dichroic mirror and creates feedback.

illumination varies depending on the illuminated sector of the OASLM surface.

For the two-color illumination, the configuration study is the OASLM illuminated by blue and green lasers and blue light feedback [Fig. 2.18], and such wavelength discriminating feedback can be implemented using a dichroic mirror. Here it is assumed that the dichroic mirror fully transmits the green light beam and fully reflects the blue one. The same interference phenomenon as in the previous section occurs in the context of the blue light, while the green beam passes through the OASLM only once. Interference between blue and green light waves can be neglected, since the blue and green lasers are independent light sources and already less than a nanometer spectral detuning results in beat-frequencies beyond the detection range of standard electronics.

For blue laser illumination the Jones vector is $\vec{E}_0 = \begin{bmatrix} E_0 \\ 0 \end{bmatrix}$ and the OSALM operating in the amplitude modulation configuration ($\psi = \pi/4$), one obtains

$$\varepsilon \frac{d\Gamma_b}{dt} = -\Gamma_b + \frac{1}{\alpha_b I_b + 2 \frac{\lambda_g}{\lambda_b} \alpha_g I_{0g} + \beta_b} + \gamma_b. \quad (2.26)$$

$$I_b = 2I_{0b} \{ 1 + R^2 + R \cos(2\phi_0 + \phi_1) \cos(2\Gamma) + R \cos(\phi_1) \}.$$

The model corresponding to the OASLM in the phase modulation configuration takes the

form

$$\varepsilon \frac{d\Gamma_b}{dt} = -\Gamma_b + \frac{1}{\alpha_b I_b + 2 \frac{\lambda_g}{\lambda_b} \alpha_g I_{0g} + \beta_b} + \gamma_b, \quad (2.27)$$

$$I_b = 2I_{0b} \{1 + R^2 + R \cos(\phi_1) + R \cos(2\phi_0 + \phi_1 + 2\Gamma)\}.$$

The term $2 \frac{\lambda_g}{\lambda_b} \alpha_g I_{0g}$ plays the important role of an additional parameter that allows to vary a slope of the OASLM's response function $\Gamma(I_b)$, and I_{0g} is used in the next chapter to enable control over the precise nature of the bifurcation phenomena observed in the two-color OASLM-based system.

The equations for the OASLM under blue and green incoherent illumination are simpler than ones for the coherent case. To demonstrate this, we suppose that the light sources in Fig. 2.18 operate in the LED regime and the experimental setup contains a vertically oriented polarizer between the OASLM and the mirror, just as in Fig. 2.13. As in the previous sections, the injected blue light polarization state is assumed to be $\vec{E}_0 = \begin{bmatrix} E_0 \\ 0 \end{bmatrix}$.

Then the corresponding model equation becomes

$$\varepsilon \frac{d\Gamma_b}{dt} = -\Gamma_b + \frac{1}{\alpha_b I_b + 2 \frac{\lambda_g}{\lambda_b} \alpha_g I_{0g} + \beta_b} + \gamma_b, \quad (2.28)$$

$$I_b = 2I_{0b} \{1 + R^2 \sin^2(\Gamma)\}.$$

Thus, the model does not involve terms including the phases ϕ_0 and ϕ_1 .

2.10/ LINEARIZATION OF RETARDATION OF THE OASLM UNDER TWO-COLOR ILLUMINATION

Returning to Fig. 2.17 and considering a constant I_{0g} while I_b varies due to the OASLM's phase retardation and interference between illumination and feedback. In such a case the dependence of the blue light-wave's retardation on I_b has the distinctive shape (see blue curve in Fig. 2.19) given by the properties of function $\Gamma_b(I_b, I_g)$ in Eqs. (2.25). We can then simplify the OASLM's response $\Gamma_b(I_b)$ for a fixed I_{0g} if the dynamic variations for $\Gamma_b(I_b, I_g)$ is small compared to the retardation offset Γ_* by using the linearization $\Gamma_b(I_b) = \Gamma_* - \kappa I_b$ (red curve in Fig.2.19). In case $I_b \rightarrow 0$, the linear function tends to Γ_* . The linear model for the blue light retardation produced by the OASLM under simultaneous blue and green

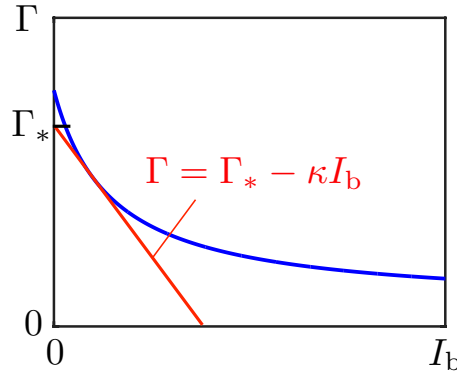


Figure 2.19: Schematic illustration to the linear approximation of the OASLM's response.

illumination takes the form

$$\Gamma_b = \Gamma_* - \kappa I_b, \quad \text{where} \quad \Gamma_* = \frac{1}{2 \frac{\lambda_g}{\lambda_b} \alpha_g I_{0g} + \beta_b} + \gamma_b. \quad (2.29)$$

The linearized two-color OASLM model with feedback as in Fig. 2.18 becomes $\varepsilon \frac{d\Gamma_b}{dt} = -\Gamma_b + \Gamma_* - \kappa I_b(I_{0b}, R, \phi_1, \phi_0, \Gamma_b)$. Specifically, for the OASLM in the amplitude modulation regime (see Eq. (2.26)) the dynamical model is

$$\varepsilon \frac{d\Gamma_b}{dt} = -\Gamma_b + \Gamma_* - 2\kappa I_{0b} \{1 + R^2 + R \cos(2\phi_0 + \phi_1) \cos(2\Gamma) + R \cos(\phi_1)\}. \quad (2.30)$$

Similarly, the linearized model corresponding to the phase modulation regime (see Eq. (2.27)) becomes

$$\varepsilon \frac{d\Gamma_b}{dt} = -\Gamma_b + \Gamma_* - 2\kappa I_{0b} \{1 + R^2 + R \cos(\phi_1) + R \cos(2\phi_0 + \phi_1 + 2\Gamma)\}. \quad (2.31)$$

In the limit case $R \rightarrow 1$, $\phi_0 = \pi/2$, $\phi_1 = \pi$, both, Eqs. (2.30) and (2.31) are transformed into the Ikeda-family oscillator $\varepsilon \frac{d\Gamma_b}{dt} = -\Gamma_b + \Gamma_* - 4\kappa I_{0b} \cos^2(\Gamma_b)$.

Applying the linear approximation to the case of incoherent illumination (see Eq. (2.28)), one obtains

$$\varepsilon \frac{d\Gamma_b}{dt} = -\Gamma_b + \Gamma_* - 2\kappa I_{0b} \{1 + R^2 \sin^2(\Gamma)\}. \quad (2.32)$$

2.11/ POTENTIAL MODIFICATIONS OF THE OASLM

An important question is how one can meaningfully modify, and how can one simplify the OASLM's construction without principal changing in the dynamics of OASLM-based devices. The first option implies the substitution of new photosensitive and birefringent materials. Using C-doped a-Si:H films as a photoconductor (see [149]) provides for an

OASLM spatial modulation resolution of the retardation up to 370 lp mm^{-1} . A resolution 527 lp mm^{-1} was achieved using a nematic LC with C_{60} -doped poly(N-vinylcarbazole) at an applied DC-voltage 80 V (see [172]). As reported in [150], the substitution of ZnO-based PS-layers allows to sufficiently increase the device resolution up to 825 lp mm^{-1} .

The second option for the OASLM-modification consists in changing the OASLM structure. As shown below, such an approach simplifies the ordinary differential equations of the OASLM under optical feedback without losing bifurcation transitions observed in the initial model.

2.11.1/ OASLM WITH SINGLE PS-LAYER

The nonlinearity of Eqs. (2.26) and (2.27) is most pronounced at $\phi_1 = m\pi$, $\phi_0 = n(1 + 1/2)\pi$, where $m, n \in \mathbb{Z}$. The second condition corresponds to the destructive interference of fields \vec{E}_1 and \vec{E}_2 (see Fig. 2.18). In this case, the action of the right OASLM PS-layer is suppressed. This fact suggests that the OASLM architecture for a dynamical system based on optical feedback can be further simplified without loss of bifurcation transitions by using only a single PS-layer, see Fig. 2.20 (a), and parameters α , β , and γ estimated before can be applied for the single-PS-layer model. The difference between the OASLMs with single- and double-PS-layer consists in the light intensity controlling the OASLM state. For the OASLM with two PS-layer the controlling intensity is a sum of two intensities, $I_s = I_{\text{left}} + I_{\text{right}}$, which gives $I_s = 2I_0$ for the the case without feedback (see Fig.

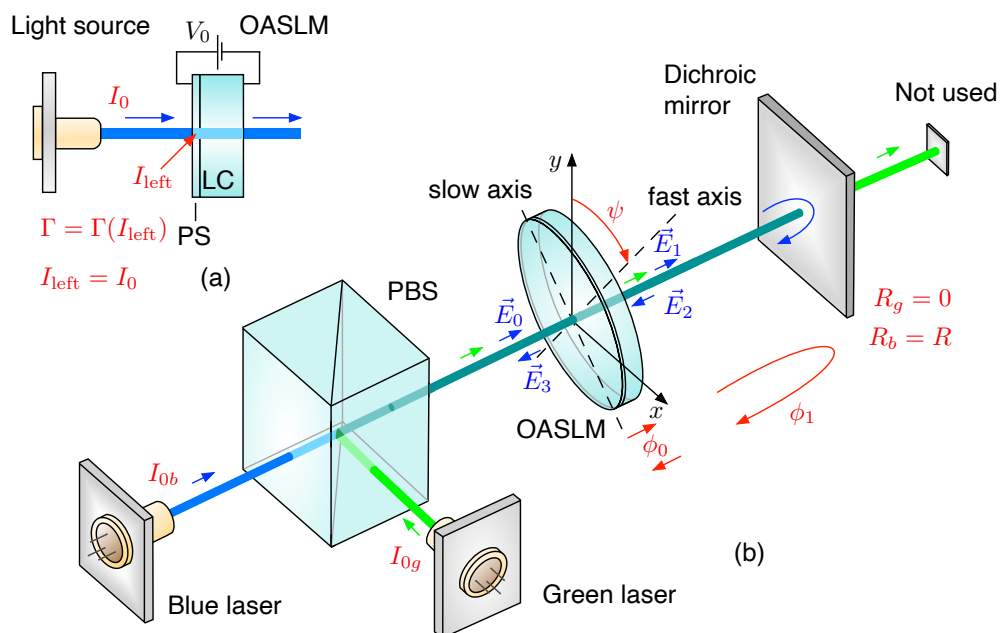


Figure 2.20: (a) Illustration of the single-PS-layer OASLM illuminated by a light source; (b) Single-PS-layer OASLM under simultaneous blue and green illumination when the blue light beam is reflected by the dichroic mirror and creates feedback.

2.8). In a case of the single PS-layer OASLM, the controlling intensity equals only to I_{left} or I_{right} .

Consider the single-PS-layer OASLM simultaneously illuminated by green and blue lasers with feedback got the blue light, see Fig. 2.20 (b). Suppose that the OASLM rotation angle is $\psi = m\pi$ (where $m \in \mathbb{Z}$), and the injected blue light Jones vector is $\vec{E}_0 = \begin{bmatrix} E_0 \\ 0 \end{bmatrix}$. The expressions for the optic fields are the same as in the case of the OASLM with two PS-layers (see Eqs. (2.19)) as well as the summary field at the PS-layer \vec{E}_{left} (see the expression for \vec{E}_{left} in Eqs. (2.20)). Considering the phase-modulation configuration, the blue light irradiance at the single PS-layer and the system equation become

$$\varepsilon \frac{d\Gamma_b}{dt} = -\Gamma_b + \frac{1}{\alpha_b I_b + \frac{\lambda_g}{\lambda_b} \alpha_g I_{0g} + \beta_b} + \gamma_b, \quad (2.33)$$

$$I_b = I_{0b} \{1 + R^2 + 2R \cos(2\phi_0 + \phi_1 + 2\Gamma)\}.$$

To simplify the system given by Eq. (2.33), the green light source is excluded from the setup in Fig. 2.20 (b), $I_{0g} = 0$. For $2\phi_0 + \phi_1 = 2m\pi$, where $m \in \mathbb{Z}$, and reflection R being close to unity, the system dynamics is very close to the one obtained from Eqs. (2.18) and (2.22). Qualitatively, the bifurcation transitions caused by increasing I_{0b} are the same: one observes the steady-state saddle-node bifurcations corresponding to the transition 'monostability-bistability-threestability'. Thus, at $R = 0.95$ the transformations of the right-hand side function $f(\Gamma_b) = -\Gamma_b + (\alpha_b I_{0b} (1 + R^2 + 2R \cos(2\phi_0 + \phi_1 + 2\Gamma)) + \beta_b)^{-1} + \gamma_b$ for Eq. (2.33), and the corresponding phase-parametric diagram are very close to the ones presented in Fig. 2.16 for Eqs. (2.18) and (2.22) at $\phi_0 = \pi/2$, $\phi_1 = \pi$, $R = 0.95$. The quantitative difference of bifurcation parameter values I_{0b} does not exceed 1–2 % as well as the difference in the steady state positions at fixed I_{0b} . Moreover, in the limit case $R \rightarrow 1$, $\phi_0 = \pi/2$, $\phi_1 = \pi$, Eqs. (2.18) and (2.22) and model (2.33) at $I_{0g} = 0$ fully coincide.

Thus, one can conclude that this simplification of the OASLM does not qualitatively change the bifurcation phenomena, and the corresponding dynamical regimes in the system with feedback and coherent illumination. For the system involving incoherent illumination (Eq. 2.28) this modification also does not principally transform the dynamics. In such a case, the equation for the single-PS-layer OASLM becomes

$$\varepsilon \frac{d\Gamma_b}{dt} = -\Gamma_b + \frac{1}{\alpha_b I_b + \frac{\lambda_g}{\lambda_b} \alpha_g I_{0g} + \beta_b} + \gamma_b, \quad (2.34)$$

$$I_b = I_{0b} \{1 + R^2 \sin^2(\Gamma)\}.$$

The only difference between Eqs. (2.28) and (2.34) is a factor of 2 in the terms for the combined optical irradiance.

2.12/ CONCLUSION

Based on the results presented in [24], the OASLM was considered as a birefringent wave plate the phase retardation of which nonlinearly depends on the incident light intensity. The exploration started from the characterization of the single OASLM under green and blue illumination. The carried out experiments have shown that the optical response of the particular OASLM areas depends only on the illumination irradiance, wavelength (the larger the incident light wavelength the weaker the OASLM sensitivity) and the OASLM rotation angle. The device sensitivity to the polarization state and to the coherent properties of the incident light has not been detected.

Based on the experimental study and further characterisation of the OASLM in terms of electronics and optics, the OASLM model has been developed and the OASLM parameter values have been estimated for the device under blue and green illumination. The resulting device model describes the electric and optical processes inside the OASLM well across a wide range of the incident light power.

After the development of single-OASLM model, a dynamical system for the OASLM with feedback formed by the reflected light beam has been derived. The first case under consideration implies the single-colour illumination. The second modification describes the OASLM under simultaneous illumination of two independent light sources with different wavelengths of the injected light. All the derived dynamical models exhibit the saddle-node bifurcations of steady states. If the OASLM driven by feedback is illuminated by incoherent light, the system exhibits only monostable and bistable regimes. In such a case, the saddle-node bifurcations result in appearance and disappearance of steady states. In contrast, for coherent illumination the each further saddle-node bifurcations gives rise to the appearance of a new attractor. Thus, the transition 'monostability-bistability-threestability-...-six-stability' occurs. Any other transitions except of the saddle-node bifurcations have not been revealed (the possibility to observe other bifurcations is analysed in the further chapter).

Finally, it was analysed how the OASLM could be modified to simplify its construction and to improve its characteristics. Excluding either PS-layer in most relevant cases mostly only decreases the OASLM's sensitivity in a transmissive regime (feedback is absent) and does not induce the significant changes in the dynamics of the system with feedback.

During all the experiments the OASLM's electrical power consumption did not exceed 1 μW , and the operating range of the incident light power did not exceed 0.25 μW for $\lambda = 450 \text{ nm}$ and 1 mW for $\lambda = 532 \text{ nm}$ in an area of 1 mm^2 . Moreover, increasing the incident light power of 150 nW for $\lambda = 450 \text{ nm}$ and of 40 μW for $\lambda = 532 \text{ nm}$ is enough for the light retardation change π in the area 1 $\text{mm} \times 1 \text{ mm}$. In contrast to electronically-addressed spatial light modulators, the OASLM does not need any supporting equipment except of the DC-power supply that could be provided by a 9 V-battery and is hence

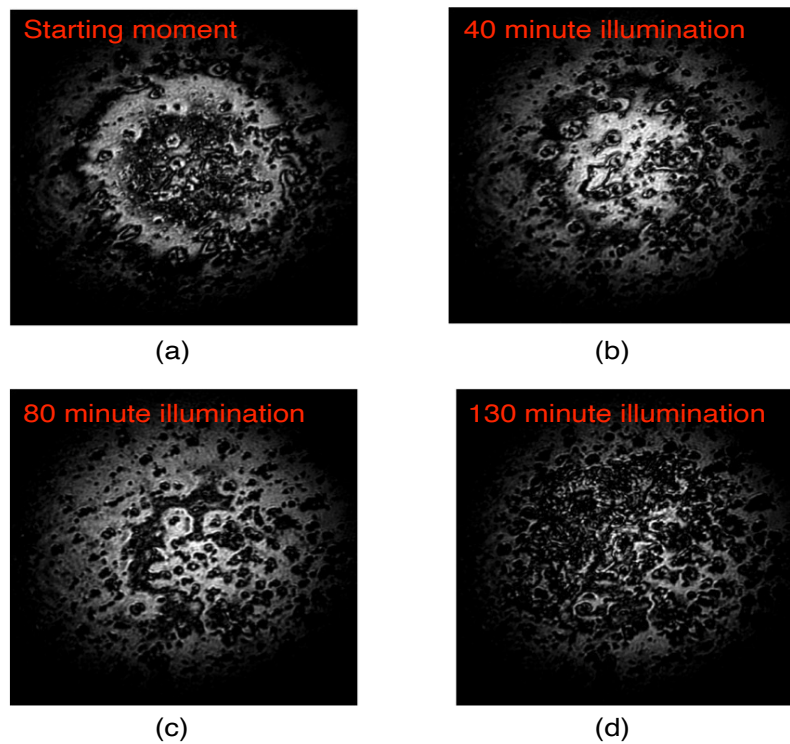


Figure 2.21: Evolution of the OASLM response to invariable Gaussian illumination (the corresponding experimental setup is depicted in Fig. 2.9): (a) initial moment; (b) after 40 minutes; (c) after 80 minutes; (d) after 130 minutes.

autonomous. Lateral carrier diffusion being responsible for local coupling determines the maximum possible number of nodes up to 10^4 nodes per mm^2 . Thus, such OASLMs are promising candidates for the implement of autonomous small-size PNNs with ultra low energy consumption. In particular, creating a cascade of several OASLMs is potentially useful for the feed-forward PNN implementation while the system with coherent feedback seems to be attractive in the context of recurrent PNNs.

However, the prospects for OASLM practical application are restrained by a destructive effect. The OASLM optical response to long-term irradiation unfortunately was not stable. After several hours of experiments, the spatial distribution of the retardation produced by OASLM becomes non-uniform and independent on the incident light intensity, see Fig.2.21. After that, the illuminated particular OASLM area cannot be used anymore. The reason for the observed OASLM response degradation consists in the ionic contamination, which occurs when a LC-based OASLM is driven by a DC-power supply [173, 174]. However, it is trivial to modify the OASLM's structure such that it has a shorter electrical response time, which in turn allows for operating the device in an AC mode. Under such conditions, this deteriorating effect is entirely avoided.

OASLM-BASED NONLINEAR SYSTEMS

It has been shown in Chap. 2 that OASLM-based systems with optical feedback can exhibit the saddle-node bifurcation of steady states. In the current chapter the objective is the identification of other bifurcations that occur in the studied systems, and which conditions must be fulfilled for that. Since the systems implying two-color illumination have one more parameter and hence are more flexible. The study therefore is focused on optical OASLM setups containing two light sources.

The models described in Chap. 2 are single oscillators governed by real variables. Three kinds of bifurcation transition can be observed in this class of dynamical systems: the pitchfork bifurcation, the saddle-node bifurcation and the transcritical bifurcation. All three bifurcations are characterised by their normal forms. The main question addressed in this chapter is whether one can implement the three possible bifurcations in OASLM-based optical oscillators such that the dynamical equations precisely correspond to the respective normal forms. To answer this question, the dynamical system's ODE's are developed as a Taylor series. After that, the conditions for concrete bifurcations are mathematically derived. Finally, the conclusions on the possibility to implement these bifurcations are drawn.

3.1/ OASLM UNDER INCOHERENT TWO-COLOR ILLUMINATION

Consider Eq. (2.28) for the OASLM with feedback in the presence of blue and green incoherent illumination. To simplify the following mathematical derivations the system's response time ε is set to unity. The system is described by the dynamical variable of the blue light retardation Γ_b , and for simplicity of the notations we use in the following $\Gamma_b = \Gamma$, as well as $\beta_b = \beta$ and $\gamma_b = \gamma$. The right-hand side function $f(\Gamma)$ is developed until the cubic function $f_T(\Gamma)$ using the Taylor series around some point Γ_0

$$f_T(\Gamma) = a + b(\Gamma - \Gamma_0) + c(\Gamma - \Gamma_0)^2 + d(\Gamma - \Gamma_0)^3. \quad (3.1)$$

The Taylor series coefficients are $a = f(\Gamma_0)$, $b = f'(\Gamma_0)$, $c = \frac{1}{2}f''(\Gamma_0)$, $d = \frac{1}{6}f'''(\Gamma_0)$, where $f' = \frac{df}{d\Gamma}$, $f'' = \frac{d^2f}{d\Gamma^2}$ and $f''' = \frac{d^3f}{d\Gamma^3}$. The right-hand side function of Eq. (2.28) takes the form $f(\Gamma) = -\Gamma + \left(\alpha_b I_b + 2\frac{\lambda_g}{\lambda_b}\alpha_g I_{0g} + \beta\right)^{-1} + \gamma$, where $I_b = 2I_{0b}\{1 + R^2 \sin^2(\Gamma)\}$. The corresponding Taylor series approximation becomes

$$\begin{aligned}
 f_T(\Gamma) &= a + b(\Gamma - \Gamma_0) + c(\Gamma - \Gamma_0)^2 + d(\Gamma - \Gamma_0)^3, & \text{with} \\
 a &= -\Gamma_0 + \left(\alpha_b I_b + 2\frac{\lambda_g}{\lambda_b}\alpha_g I_{0g} + \beta\right)^{-1} + \gamma, \\
 b &= -1 - 2\alpha_b I_{0b} R^2 \sin(2\Gamma_0) \left(\alpha_b I_b + 2\frac{\lambda_g}{\lambda_b}\alpha_g I_{0g} + \beta\right)^{-2}, \\
 c &= -2\alpha_b I_{0b} R^2 \cos(2\Gamma_0) \left(\alpha_b I_b + 2\frac{\lambda_g}{\lambda_b}\alpha_g I_{0g} + \beta\right)^{-2} \\
 &\quad + 4\alpha_b^2 I_{0b}^2 R^4 \sin^2(2\Gamma_0) \left(\alpha_b I_b + 2\frac{\lambda_g}{\lambda_b}\alpha_g I_{0g} + \beta\right)^{-3}, & (3.2) \\
 d &= \frac{4}{3}\alpha_b I_{0b} R^2 \sin(2\Gamma_0) \left(\alpha_b I_b + 2\frac{\lambda_g}{\lambda_b}\alpha_g I_{0g} + \beta\right)^{-2} \\
 &\quad + 4\alpha_b^2 I_{0b}^2 R^4 \sin(4\Gamma_0) \left(\alpha_b I_b + 2\frac{\lambda_g}{\lambda_b}\alpha_g I_{0g} + \beta\right)^{-3} \\
 &\quad - 8\alpha_b^3 I_{0b}^3 R^6 \sin^3(2\Gamma_0) \left(\alpha_b I_b + 2\frac{\lambda_g}{\lambda_b}\alpha_g I_{0g} + \beta\right)^{-4}, \\
 I_b &= 2I_{0b}\{1 + R^2 \sin^2(\Gamma_0)\}.
 \end{aligned}$$

Importantly, Γ_0 is not assumed to be fixed, but can be adjusted as a free parameter when the system parameters are correspondingly modified. Using the conditions that the necessary Taylor series coefficients are equal to zero, the function $f_T(\Gamma)$ is transformed into the normal form of a certain bifurcation. After that, the physical realizability of such conditions is analyzed.

3.1.1/ PITCHFORK BIFURCATION

The pitchfork bifurcation normal form is $\frac{dx}{dt} = bx - dx^3$, where $d > 0$. The approximation function $f_T(\Gamma)$ (see Eqs. 3.2) coincide with the pitchfork bifurcation normal form (except of horizontal shift caused by the term $(\Gamma - \Gamma_0)$) when the Taylor series coefficients a and c

equal to zero. Mathematically, this results in the following conditions

$$\begin{aligned}
 a = 0 &\Rightarrow \left(\alpha_b I_b + 2 \frac{\lambda_g}{\lambda_b} \alpha_g I_{0g} + \beta \right)^{-1} = \Gamma_0 - \gamma, \\
 c = 0 &\Rightarrow -2\alpha_b I_{0b} R^2 \cos(2\Gamma_0) \left(\alpha_b I_b + 2 \frac{\lambda_g}{\lambda_b} \alpha_g I_{0g} + \beta \right)^{-2} \\
 &+ 4\alpha_b^2 I_{0b}^2 R^4 \sin^2(2\Gamma_0) \left(\alpha_b I_b + 2 \frac{\lambda_g}{\lambda_b} \alpha_g I_{0g} + \beta \right)^{-3} = 0.
 \end{aligned} \tag{3.3}$$

Dividing the second expression by $2\alpha_b I_{0b} R^2$, which is always positive, and substituting the expression for $\left(\alpha_b I_b + 2 \frac{\lambda_g}{\lambda_b} \alpha_g I_{0g} + \beta \right)^{-1}$ from the first condition into the second one, one obtains the transformed condition corresponding to $c = 0$ as

$$-\cos(2\Gamma_0)(\Gamma_0 - \gamma)^2 + 2\alpha_b I_{0b} R^2 \sin^2(2\Gamma_0)(\Gamma_0 - \gamma)^3 = 0. \tag{3.4}$$

Since light intensities cannot be negative, the term $\left(\alpha_b I_b + 2 \frac{\lambda_g}{\lambda_b} \alpha_g I_{0g} + \beta \right)^{-1}$ is always positive, which is equivalent to $(\Gamma_0 - \gamma) > 0$. Then the second pitchfork condition finally transforms into

$$-\cos(2\Gamma_0) + 2\alpha_b I_{0b} R^2 \sin^2(2\Gamma_0)(\Gamma_0 - \gamma) = 0, \tag{3.5}$$

which allows to extract the incident blue light intensity

$$I_{0b} = \frac{\cos(2\Gamma_0)}{2\alpha_b R^2 \sin^2(2\Gamma_0)(\Gamma_0 - \gamma)}. \tag{3.6}$$

The green light intensity I_{0g} is expressed from the first pitchfork condition, $a = 0$ (see Eqs. (3.3))

$$\begin{aligned}
 I_{0g} &= \frac{\lambda_b}{\lambda_g} \frac{\frac{1}{\Gamma_0 - \gamma} - \alpha_b I_b - \beta}{2\alpha_g}, \\
 &\quad \downarrow \\
 I_{0g} &= \frac{\lambda_b}{\lambda_g} \frac{\frac{1}{\Gamma_0 - \gamma} - 2\alpha_b I_{0b} \{1 + R^2 \sin^2(\Gamma_0)\} - \beta}{2\alpha_g}.
 \end{aligned} \tag{3.7}$$

The expression for I_{0g} includes the parameter I_{0b} which is determined by Eq. (3.6) as a function of Γ_0 . Thus, the green light intensity is a function of Γ_0 according to Eq. (3.7).

Eqs. (3.6) and (3.7) define both light intensities as functions of Γ_0 . Thus, for each Γ_0 one can calculate concrete values I_{0b} and I_{0g} at which the Taylor series approximation corresponds to the pitchfork bifurcation normal form.

When the pitchfork bifurcation occurs, the Taylor series coefficient b equals to zero. Taking into account the condition for $a = 0$ (see Eqs. (3.3)), the Taylor series coefficient b can be

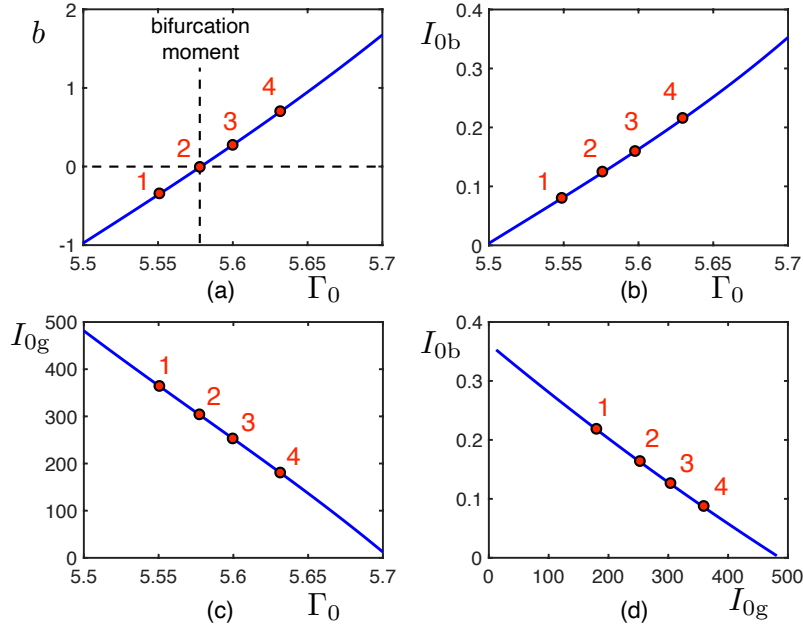


Figure 3.1: Pitchfork conditions determined by Eq. (2.28): (a) Taylor series coefficient b (Eq. (3.9)); (b-c) I_{0b} and I_{0g} according to Eqs. (3.6) and (3.7); (d) $I_{0b}(I_{0g})$ for I_{0b} and I_{0g} in panels (b) and (c) corresponding to the same argument Γ_0 . System parameters are: $\alpha_b = 0.117$, $\alpha_g = 0.985 \times 10^{-4}$, $\beta = 0.052$, $\gamma = -0.55$, $\lambda_b = 450 \times 10^{-9}$, $\lambda_g = 532 \times 10^{-9}$, $R = 0.95$.

presented as

$$b = -1 - 2\alpha_b I_{0b} R^2 \sin(2\Gamma_0)(\Gamma_0 - \Gamma)^2. \quad (3.8)$$

Substituting I_{0b} from Eq. (3.6), one obtains a simplified expression for the Taylor series coefficient b

$$b = -1 - \cot(2\Gamma_0)(\Gamma_0 - \gamma), \quad (3.9)$$

Equation (3.9) represents the Taylor series coefficient b as a function of Γ_0 and equals to zero at $\Gamma_0 \approx 7.13$, $\Gamma_0 \approx 5.58$, $\Gamma_0 \approx 4.0$, $\Gamma_0 \approx 2.5$, $\Gamma_0 \approx 1.02$.

Next, the discussion turns towards the neighbourhood of point $\Gamma_0 \approx 5.58$. The range $\Gamma_0 \in [5.5 : 5.7]$ is used in the following as a range for the analysis of $I_{0b}(\Gamma_0)$ and $I_{0g}(\Gamma_0)$ (Eqs. (3.6) and (3.7)). As can be seen in Fig. 3.1 (a), the Taylor series coefficient b changes its sign at $\Gamma_0^{\text{bif}} \approx 5.58$, which hence corresponds to a potential bifurcation point.

If both light intensities are tuned according to the curve in Fig. 3.1 (d), the dependence of I_{0b} and I_{0g} on Γ_0 disappears, and to bifurcate the system along the parameters always maintaining the system in conditions corresponding to the pitchfork normal form, I_{0b} and I_{0g} are tuned according to the curve in Fig. 3.1 (d). As shown before, $f(\Gamma)$ and its Taylor series approximation $f_T(\Gamma)$ evolve as a cubic function such that the central point Γ_0 shifts in the range $[5.5 : 5.7]$, see Fig. 3.2 (a). This assumption is examined by data shown in Fig. 3.2, which was determined using $f_i(\Gamma)$. These results confirm

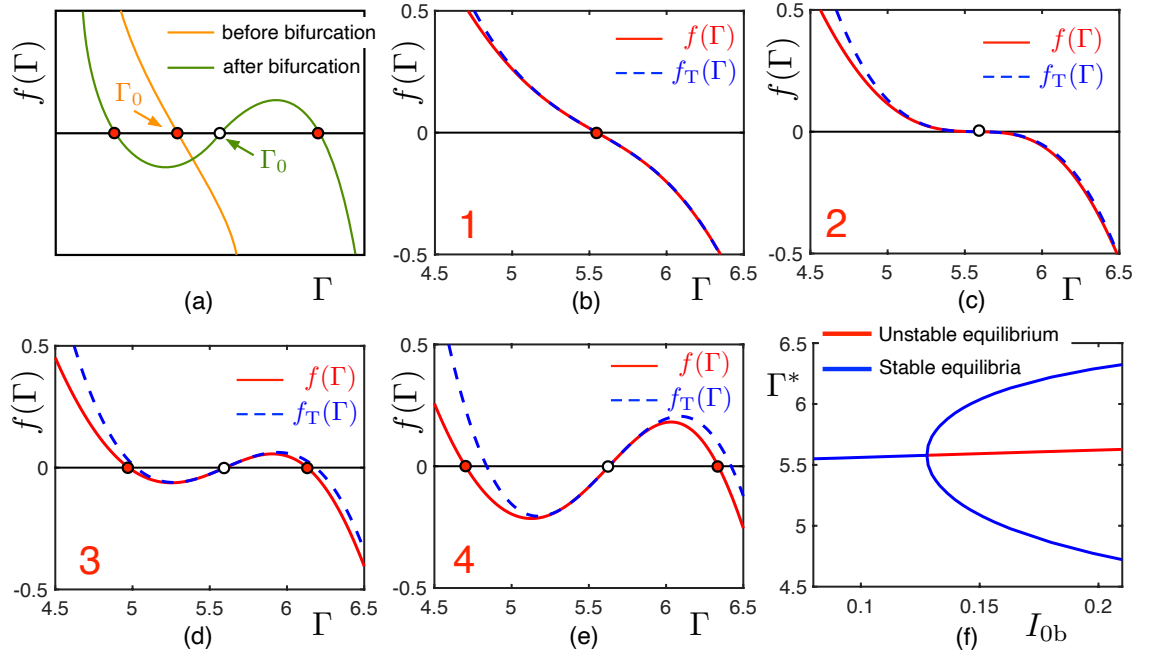


Figure 3.2: Pitchfork bifurcation in Eq. (2.28): (a) $f(\Gamma)$ for varying I_{0b} and I_{0g} according to Fig. 3.1 (d); (b-e) $f(\Gamma)$ (red solid curve) and $f_T(\Gamma)$ (blue dotted curve) at points 1-4 in Fig. 3.1: $I_{0b} = 0.0818$ and $I_{0g} = 365.2$ (point 1), $I_{0b} = 0.1267$ and $I_{0g} = 301.9$ (point 2), $I_{0b} = 0.163$ and $I_{0g} = 252.2$ (point 3), $I_{0b} = 0.2149$ and $I_{0g} = 183.6$ (point 4); (f) Phase-parametric diagram for I_{0b} and I_{0g} according to the curve in Fig. 3.1 (d). System parameters are: $\alpha_b = 0.117$, $\alpha_g = 0.985 \times 10^{-4}$, $\beta = 0.052$, $\gamma = -0.55$, $\lambda_b = 450 \times 10^{-9}$, $\lambda_g = 532 \times 10^{-9}$, $R = 0.95$.

- That the Taylor series approach allows to approximate the function $f(\Gamma)$ with high accuracy, except of well-developed bistability after the pitchfork bifurcation (see Fig. 3.2 (e)).
- That the pitchfork bifurcation can be observed in Eq. (2.28) when intensities I_{0b} and I_{0g} vary according to conditions determined by Eqs. (3.6) and (3.7).

The second result well illustrates the reason why the second laser with a different color was introduced into the optical setup: it is very convenient in physical experiments to adjust I_{0b} and I_{0g} with high accuracy, while continuous tuning OASLM parameters α_b , α_g , β , γ is near impossible, and tuning the OASLM rotation angle ψ is impractical as it commonly introduces misalignment.

3.1.2/ SADDLE-NODE BIFURCATION

As shown in Chap. 2, Eq. (2.28) exhibits multiple saddle-node bifurcations. The further issue discussed in this section is whether the saddle-node bifurcation in Eq. (2.28) can occur exactly as in the normal form $\frac{dx}{dt} = a + cx^2$. In terms of the Taylor series in Eq. (3.2),

the conditions for the saddle-node bifurcation in Eq. (2.28) are

$$\begin{aligned}
b = 0 &\Rightarrow \alpha_b I_{0b} R^2 \sin(2\Gamma_0) \left(\alpha_b I_b + 2 \frac{\lambda_g}{\lambda_b} \alpha_g I_{0g} + \beta \right)^{-2} = -\frac{1}{2}, \\
d = 0 &\Rightarrow \frac{4}{3} \left(\alpha_b I_{0b} R^2 \sin(2\Gamma_0) \left(\alpha_b I_b + 2 \frac{\lambda_g}{\lambda_b} \alpha_g I_{0g} + \beta \right)^{-2} \right) \\
&+ \frac{8}{3} \left(\left(\alpha_b I_b + 2 \frac{\lambda_g}{\lambda_b} \alpha_g I_{0g} + \beta \right)^{-2} \alpha_b I_{0b} R^2 \sin(2\Gamma_0) \right)^2 \cot(2\Gamma_0) \left(\alpha_b I_b + 2 \frac{\lambda_g}{\lambda_b} \alpha_g I_{0g} + \beta \right) \quad (3.10) \\
&- 8 \left(\left(\alpha_b I_b + 2 \frac{\lambda_g}{\lambda_b} \alpha_g I_{0g} + \beta \right)^{-2} \alpha_b I_{0b} R^2 \sin(2\Gamma_0) \right)^3 \left(\alpha_b I_b + 2 \frac{\lambda_g}{\lambda_b} \alpha_g I_{0g} + \beta \right)^2 = 0, \\
&\Downarrow \\
&-\frac{2}{3} + \frac{2}{3} \cot(2\Gamma_0) \left(\alpha_b I_b + 2 \frac{\lambda_g}{\lambda_b} \alpha_g I_{0g} + \beta \right) + \left(\alpha_b I_b + 2 \frac{\lambda_g}{\lambda_b} \alpha_g I_{0g} + \beta \right)^2 = 0.
\end{aligned}$$

The last expression results from the condition $d = 0$, which leads to a quadratic equation for $k = \left(\alpha_b I_b + 2 \frac{\lambda_g}{\lambda_b} \alpha_g I_{0g} + \beta \right)$ that is required to have only positive values. The corresponding solution is $k = -\frac{1}{3} \cot(2\Gamma_0) + \sqrt{\frac{1}{9} \cot^2(2\Gamma_0) + \frac{2}{3}}$. From condition $b = 0$ one then obtains

$$\sqrt{-2\alpha_b R^2 I_{0b} \sin(2\Gamma_0)} = \left(\alpha_b I_b + 2 \frac{\lambda_g}{\lambda_b} \alpha_g I_{0g} + \beta \right). \quad (3.11)$$

Then the incident blue light intensity needs to satisfy

$$I_{0b} = \frac{\left(-\frac{1}{3} \cot(2\Gamma_0) + \sqrt{\frac{1}{9} \cot^2(2\Gamma_0) + \frac{2}{3}} \right)^2}{-2\alpha_b R^2 \sin(2\Gamma_0)}, \quad (3.12)$$

which is a function of Γ_0 . After that, Eq. (3.11) allows to express the incident green light intensity as

$$I_{0g} = \frac{\lambda_b}{\lambda_g} \frac{\sqrt{-2\alpha_b R^2 I_{0b} \sin(2\Gamma_0)} - 2\alpha_b I_{0b} (1 + R^2 \sin^2(\Gamma_0)) - \beta}{2\alpha_g}, \quad (3.13)$$

where I_{0b} is a function of Γ_0 according to Eq. (3.12).

The substitution of Eq. (3.11) into the expression for Taylor series coefficient a allows to express it as a function of Γ_0

$$a = -\Gamma_0 + \frac{1}{\sqrt{-2\alpha_b R^2 I_{0b} \sin(2\Gamma_0)}} + \gamma, \quad (3.14)$$

where I_{0b} is a function of Γ_0 according to Eq. (3.12), and the results is illustrated in Fig. 3.3. Substituting Eq. (3.12) into Eq.(3.14), coefficient a is finally represented as a function of Γ_0

$$a = -\Gamma_0 + \gamma + \frac{1}{-\frac{1}{3} \cot(2\Gamma_0) + \sqrt{\frac{1}{9} \cot^2(2\Gamma_0) + \frac{2}{3}}}. \quad (3.15)$$

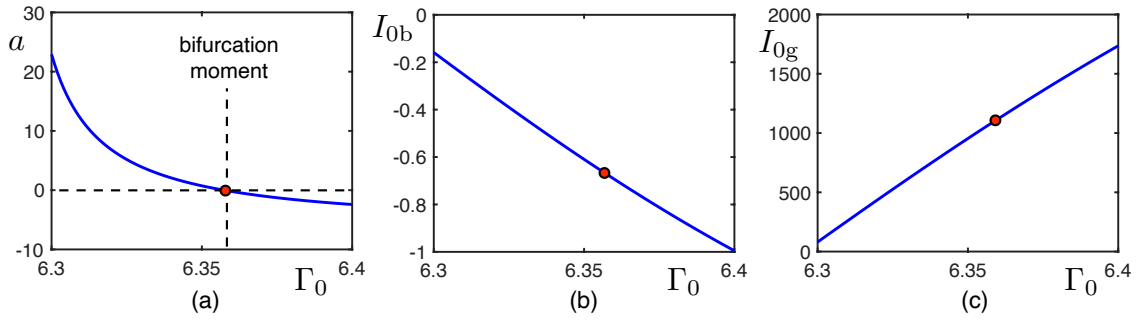


Figure 3.3: The dependence from the saddle-node bifurcation conditions for Eq. (2.28): (a) Taylor series coefficient a on Γ_0 ; (b-c) I_{0b} and I_{0g} according to Eqs. (3.12) and (3.13). System parameters are: $\alpha_b = 0.117$, $\alpha_g = 0.985 \times 10^{-4}$, $\beta = 0.052$, $\gamma = -0.55$, $\lambda_b = 450 \times 10^{-9}$, $\lambda_g = 532 \times 10^{-9}$, $R = 0.95$.

The saddle-node bifurcation point corresponds to $a = 0$, which is achieved at some points Γ_0^{bif} . However, in the neighbourhood of all points Γ_0^{bif} , either $I_{0b}(\Gamma_0)$ or $I_{0g}(\Gamma_0)$ take negative values. This situation is illustrated in Fig. 3.3 on the example of the range $\Gamma_0 \in [6.3 : 6.4]$. Coefficient a (see Eq. (3.15)) is zero in the point $\Gamma_0^{\text{bif}} \approx 6.357$ (see Fig. 3.3 (a)). However, $I_{0b}(\Gamma_0 \approx 6.357)$ is negative, which is unphysical and the saddle-node bifurcation in Eq. (2.28) cannot occur exactly as in the bifurcation normal form. However, this does not mean that the saddle-node bifurcation cannot be implemented in principle, and it also does not contradict the results presented in Chapter 2 where saddle-node bifurcations in Eq. (2.28) at $I_{0g} = 0$ are shown.

It follows from Eq. (3.15) that the position of bifurcation point Γ_0^{bif} and the ability to implement the saddle-node bifurcation can change when the parameter γ varies. However, the parameter γ estimated from the experimental characterization of the OASLM cannot be easily adjusted, as it is determined by the properties of the OASLM LC-layer.

3.1.3/ TRANSCRITICAL BIFURCATION

The transcritical bifurcation normal form is $\frac{dx}{dt} = bx + cx^2$. In terms of the Taylor series expressed by Eq. (3.2), the right-hand side function $f(\Gamma)$ of Eq. (2.28) can evolve as the transcritical bifurcation normal form in some neighbourhood of Γ_0 when two conditions

are obeyed as

$$\begin{aligned}
 a = 0 &\Rightarrow \left(\alpha_b I_b + 2 \frac{\lambda_g}{\lambda_b} \alpha_g I_{0g} + \beta \right)^{-1} = \Gamma_0 - \gamma, \\
 d = 0 &\Rightarrow \frac{4}{3} \alpha_b I_{0b} R^2 \sin(2\Gamma_0) + \frac{4}{3} \left(\alpha_b R^2 I_{0b} \right)^2 \sin(4\Gamma_0) \left(\alpha_b I_b + 2 \frac{\lambda_g}{\lambda_b} \alpha_g I_{0g} + \beta \right)^{-1} \\
 &\quad - 8 \left(\alpha_b I_{0b} R^2 \sin(2\Gamma_0) \right)^3 \left(\alpha_b I_b + 2 \frac{\lambda_g}{\lambda_b} \alpha_g I_{0g} + \beta \right)^{-2} = 0, \\
 &\quad \Downarrow \\
 &\quad 1 + 2 \cot(2\Gamma_0) (\Gamma_0 - \gamma) \left(\alpha_b R^2 I_{0b} \sin(2\Gamma_0) \right) - 6 (\Gamma_0 - \gamma)^2 \left(\alpha_b I_{0b} R^2 \sin(2\Gamma_0) \right)^2 = 0.
 \end{aligned} \tag{3.16}$$

The last expression follows from $d = 0$ and represents a quadratic equation for the variable $k = \alpha_b I_{0b} R^2 \sin(2\Gamma_0)$. It has two solutions $k = \left(\cot(2\Gamma_0) \pm \sqrt{\cot^2(2\Gamma_0) + 6} \right) / (6(\Gamma_0 - \gamma))$, which results in

$$I_{0b} = \frac{\cot(2\Gamma_0) + \sqrt{\cot^2(2\Gamma_0) + 6}}{6\alpha_b R^2 \sin(2\Gamma_0) (\Gamma_0 - \gamma)}, \tag{3.17}$$

$$I_{0b} = \frac{\cot(2\Gamma_0) - \sqrt{\cot^2(2\Gamma_0) + 6}}{6\alpha_b R^2 \sin(2\Gamma_0) (\Gamma_0 - \gamma)}. \tag{3.18}$$

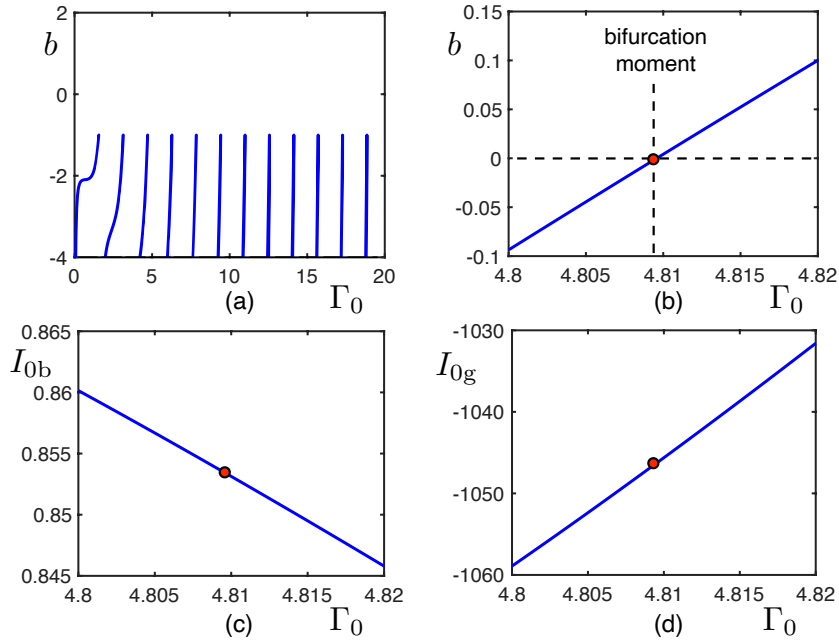


Figure 3.4: Transcritical bifurcation conditions for Eq. (2.28): (a-b) Taylor series coefficient b as a function of Γ_0 when I_{0b} varies according to Eq. (3.17) (panel (a)) and Eq. (3.18) (panel (b)); (c-d) I_{0b} and I_{0g} according to Eqs. (3.18) and (3.19). System parameters are: $\alpha_b = 0.117$, $\alpha_g = 0.985 \times 10^{-4}$, $\beta = 0.052$, $\gamma = -0.55$, $\lambda_b = 450 \times 10^{-9}$, $\lambda_g = 532 \times 10^{-9}$, $R = 0.95$.

Using $a = 0$, the expression for the incident green light intensity is

$$I_{0g} = \frac{\lambda_b}{\lambda_g} \frac{\frac{1}{\Gamma_0 - \gamma} - 2\alpha_b I_{0b} \{1 + R^2 \sin^2(\Gamma_0)\} - \beta}{2\alpha_g}, \quad (3.19)$$

where I_{0b} varies as a function of Γ_0 according to Eqs. (3.17) or (3.18). In addition, $a = 0$ allows to express coefficient b (see Eqs. (3.2)) as a function of Γ_0 illustrated in Fig. 3.4(a, b)

$$b = -1 - \frac{(\cot(2\Gamma_0) + \sqrt{\cot^2(2\Gamma_0) + 6})(\Gamma_0 - \gamma)}{3}, \quad (3.20)$$

$$b = -1 - \frac{(\cot(2\Gamma_0) - \sqrt{\cot^2(2\Gamma_0) + 6})(\Gamma_0 - \gamma)}{3}. \quad (3.21)$$

If $I_{0b}(\Gamma_0)$ varies according to Eq. (3.17), then coefficient b becomes a function of Γ_0 according to Eq. (3.20) and does not become zero at any Γ_0 (see Fig. 3.4 (a)). In such a case the transcritical bifurcation is impossible in principle.

If $I_{0b}(\Gamma_0)$ follows Eq. (3.18), then b takes the form corresponding to Eq. (3.21). In such a case $b(\Gamma_0)$ can become zero at certain values Γ_0^{bif} . However, in the neighbourhood of any Γ_0^{bif} , either I_{0b} or I_{0g} become negative, which is depicted in Fig. 3.4 (b-d) for $\Gamma_0^{\text{bif}} \approx 4.81$ where $b = 0$. As negative intensities are unphysical, the transcritical bifurcation cannot occur in an oscillator described by Eq. (2.28).

Analysis of Eqs. (3.20) and (3.21) allows to conclude that the position of bifurcation point Γ_0^{bif} and the ability to implement the transcritical bifurcation can change when the parameter γ varies. However, this would result in the same problem as in the case of the saddle-node bifurcation: parameter γ cannot be readily adjusted.

3.2/ OASLM UNDER COHERENT ILLUMINATION WITH FEEDBACK: THE AMPLITUDE MODULATION REGIME

Consider Eq. (2.26) for the OASLM with feedback corresponding to the amplitude modulation regime. Again, we set ε to unity. The system is described by Γ_b , and similarly to the previous section, this variable is mentioned without index, $\Gamma_b = \Gamma$, as well as $\beta_b = \beta$ and $\gamma_b = \gamma$. The system right-hand side function $f(\Gamma)$ is represented as a cubic function $f_{\Gamma}(\Gamma)$ using the Taylor series around some point Γ_0 . The right-hand side function of Eq. (2.26) takes the form

$$f(\Gamma) = -\Gamma + \left(\alpha_b I_b + 2 \frac{\lambda_g}{\lambda_b} \alpha_g I_{0g} + \beta \right)^{-1} + \gamma, \quad \text{where} \quad (3.22)$$

$$I_b = 2I_{0b} \{1 + R^2 + R \cos(2\phi_0 + \phi_1) \cos(2\Gamma) + R \cos(\phi_1)\}.$$

The corresponding Taylor series approximation becomes

$$\begin{aligned}
 f_{\Gamma}(\Gamma) &= a + b(\Gamma - \Gamma_0) + c(\Gamma - \Gamma_0)^2 + d(\Gamma - \Gamma_0)^3, \quad \text{where} \\
 a &= -\Gamma_0 + \left(\alpha_b I_b + 2 \frac{\lambda_g}{\lambda_b} \alpha_g I_{0g} + \beta \right)^{-1} + \gamma, \\
 b &= -1 + 4\alpha_b I_{0b} R \cos(2\phi_0 + \phi_1) \sin(2\Gamma_0) \left(\alpha_b I_b + 2 \frac{\lambda_g}{\lambda_b} \alpha_g I_{0g} + \beta \right)^{-2}, \\
 c &= 4\alpha_b I_{0b} R \cos(2\phi_0 + \phi_1) \cos(2\Gamma_0) \left(\alpha_b I_b + 2 \frac{\lambda_g}{\lambda_b} \alpha_g I_{0g} + \beta \right)^{-2} \\
 &\quad + 16\alpha_b^2 I_{0b}^2 R^2 \cos^2(2\phi_0 + \phi_1) \sin^2(2\Gamma_0) \left(\alpha_b I_b + 2 \frac{\lambda_g}{\lambda_b} \alpha_g I_{0g} + \beta \right)^{-3}, \quad (3.23) \\
 d &= -\frac{8}{3} \alpha_b I_{0b} R \cos(2\phi_0 + \phi_1) \sin(2\Gamma_0) \left(\alpha_b I_b + 2 \frac{\lambda_g}{\lambda_b} \alpha_g I_{0g} + \beta \right)^{-2} \\
 &\quad + 16\alpha_b^2 I_{0b}^2 R^2 \cos^2(2\phi_0 + \phi_1) \sin(4\Gamma_0) \left(\alpha_b I_b + 2 \frac{\lambda_g}{\lambda_b} \alpha_g I_{0g} + \beta \right)^{-3} \\
 &\quad + 64\alpha_b^3 I_{0b}^3 R^3 \cos^3(2\phi_0 + \phi_1) \sin^3(2\Gamma_0) \left(\alpha_b I_b + 2 \frac{\lambda_g}{\lambda_b} \alpha_g I_{0g} + \beta \right)^{-4}, \\
 I_b &= 2I_{0b} \left\{ 1 + R^2 + R \cos(2\phi_0 + \phi_1) \cos(2\Gamma_0) + R \cos(\phi_1) \right\}.
 \end{aligned}$$

In the further subsections the conditions for the transformation of $f_{\Gamma}(\Gamma_0)$ into the certain bifurcation normal form are mathematically analyzed.

3.2.1/ PITCHFORK BIFURCATION

Function $f_{\Gamma}(\Gamma)$ coincides with the pitchfork bifurcation normal form when coefficients a and c are zero. Taking into account Eqs. (3.23), two conditions take the form

$$\begin{aligned}
 a = 0 &\Rightarrow \left(\alpha_b I_b + 2 \frac{\lambda_g}{\lambda_b} \alpha_g I_{0g} + \beta \right)^{-1} = \Gamma_0 - \gamma, \\
 c = 0 &\Rightarrow 4\alpha_b I_{0b} R \cos(2\phi_0 + \phi_1) \cos(2\Gamma_0) \left(\alpha_b I_b + 2 \frac{\lambda_g}{\lambda_b} \alpha_g I_{0g} + \beta \right)^{-2} \\
 &\quad + 16\alpha_b^2 I_{0b}^2 R^2 \cos^2(2\phi_0 + \phi_1) \sin^2(2\Gamma_0) \left(\alpha_b I_b + 2 \frac{\lambda_g}{\lambda_b} \alpha_g I_{0g} + \beta \right)^{-3} = 0. \quad (3.24)
 \end{aligned}$$

Dividing the second expression by $4\alpha_b I_{0b} R$, which is always positive, and substituting the expression for $\left(\alpha_b I_b + 2 \frac{\lambda_g}{\lambda_b} \alpha_g I_{0g} + \beta \right)^{-1}$ from the first condition into the second, the

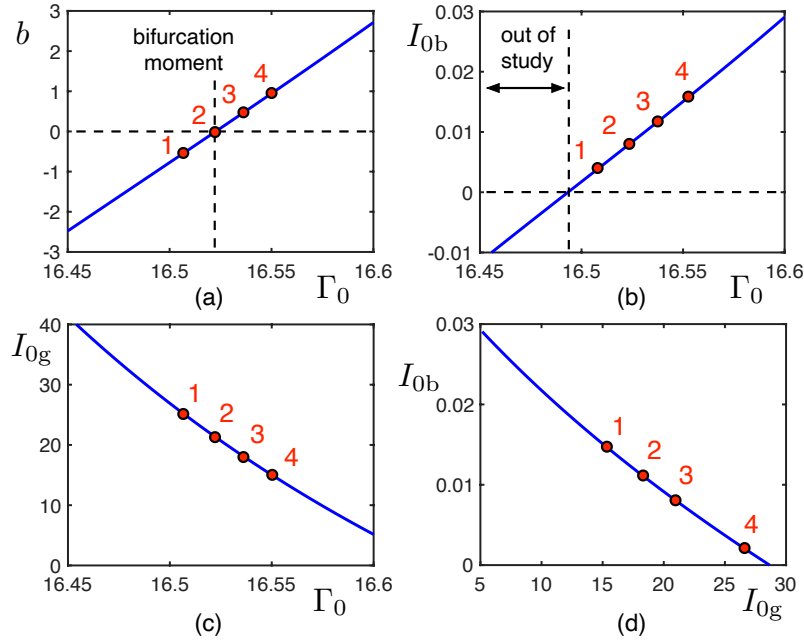


Figure 3.5: Pitchfork bifurcation conditions for Eq. (2.26): (a) Dependence of b on Γ_0 (Eq. (3.29)); (b-c) I_{0b} and I_{0g} according to Eqs. (3.27) and (3.28); (d) $I_{0b}(I_{0g})$ which consists of values I_{0b} and I_{0g} in panels (b) and (c) corresponding to the same argument Γ_0 . System parameters are: $\alpha_b = 0.117$, $\alpha_g = 0.985 \times 10^{-4}$, $\beta = 0.052$, $\gamma = -0.55$, $\phi_0 = \pi/2$, $\phi_1 = \pi$, $\lambda_b = 450 \times 10^{-9}$, $\lambda_g = 532 \times 10^{-9}$, $R = 0.95$.

transformed condition $c = 0$ becomes

$$\cos(2\phi_0 + \phi_1) \cos(2\Gamma_0)(\Gamma_0 - \gamma)^2 + 4\alpha_b I_{0b} R \cos^2(2\phi_0 + \phi_1) \sin^2(2\Gamma_0)(\Gamma_0 - \gamma)^3 = 0. \quad (3.25)$$

Since light intensities cannot be negative, $\left(\alpha_b I_b + 2\frac{\lambda_g}{\lambda_b} \alpha_g I_{0g} + \beta\right)^{-1}$ always needs to be positive and $(\Gamma_0 - \gamma) > 0$. Then the second pitchfork condition transforms into

$$\cos(2\phi_0 + \phi_1) \cos(2\Gamma_0) + 4\alpha_b I_{0b} R \cos^2(2\phi_0 + \phi_1) \sin^2(2\Gamma_0)(\Gamma_0 - \gamma) = 0, \quad (3.26)$$

which allows to extract the incident blue light intensity under the condition $\cos(2\phi_0 + \phi_1) \neq 0$

$$I_{0b} = -\frac{\cos(2\Gamma_0)}{4\alpha_b R \cos(2\phi_0 + \phi_1) \sin^2(2\Gamma_0)(\Gamma_0 - \gamma)}. \quad (3.27)$$

I_{0g} is expressed from the first pitchfork condition $a = 0$ (see Eq. (3.24))

$$I_{0g} = \frac{\lambda_b}{\lambda_g} \frac{\frac{1}{\Gamma_0 - \gamma} - \alpha_b I_b - \beta}{2\alpha_g}, \quad (3.28)$$

$$I_{0g} = \frac{\lambda_b}{\lambda_g} \frac{\frac{1}{\Gamma_0 - \gamma} - 2\alpha_b I_{0b} \{1 + R^2 + R \cos(2\phi_0 + \phi_1) \cos(2\Gamma_0) + R \cos(\phi_1)\} - \beta}{2\alpha_g}.$$

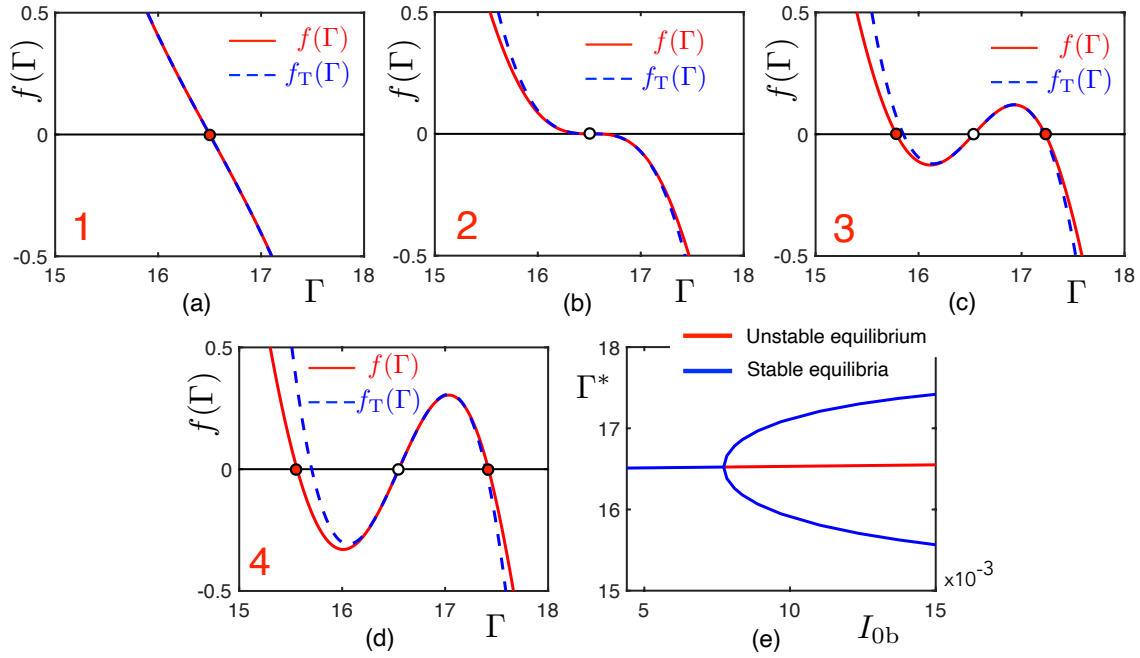


Figure 3.6: Pitchfork bifurcation in Eq. (2.26): (a-d) $f(\Gamma)$ (red solid curve) and its Taylor series approximation given by Eq.(3.23) (blue dotted curve) at points 1-4 in Fig. 3.5: $I_{0b} = 4.39 \times 10^{-3}$ and $I_{0g} = 24.35$ (point 1), $I_{0b} = 7.73 \times 10^{-3}$ and $I_{0g} = 21.26$ (point 2), $I_{0b} = 11.3 \times 10^{-3}$ and $I_{0g} = 18.14$ (point 3), $I_{0b} = 15.1 \times 10^{-3}$ and $I_{0g} = 15.03$ (point 4); (d) Phase-parametric diagram for I_{0b} and I_{0g} varying according to the curve in Fig. 3.5 (d). System parameters are: $\alpha_b = 0.117$, $\alpha_g = 0.985 \times 10^{-4}$, $\beta = 0.052$, $\gamma = -0.55$, $\phi_0 = \pi/2$, $\phi_1 = \pi$, $\lambda_b = 450 \times 10^{-9}$, $\lambda_g = 532 \times 10^{-9}$, $R = 0.95$.

I_{0g} includes I_{0b} , which is determined by Eq. (3.27) as a function of Γ_0 . Equations (3.27) and (3.28) represent I_{0b} and I_{0g} in order to match the pitchfork bifurcation conditions. Next, I_{0b} and I_{0g} are considered as functions of Γ_0 at fixed parameter values. Taking into account $a = 0$ (see Eqs. (3.24)), coefficient b takes the form

$$b = -1 - \cot(2\Gamma_0)(\Gamma_0 - \gamma). \quad (3.29)$$

$b(\Gamma_0)$ equals to zero at certain values Γ_0^{bif} , but in some cases, $\Gamma_0 = \Gamma_0^{\text{bif}}$ correspond to negative values I_{0b} or I_{0g} for which the pitchfork bifurcation cannot be realized. Meanwhile, $I_{0b}(\Gamma_0)$ (Eq. (3.27)) and $I_{0g}(\Gamma_0)$ (Eq. (3.28)) possess positive values at other $\Gamma_0 = \Gamma_0^{\text{bif}}$, and this situation is illustrated in Fig. 3.5. There, $b(\Gamma_0)$ passes through zero at $\Gamma_0 = 16.523$ [Fig. 3.5 (a)] and $I_{0b}(\Gamma_0)$ and $I_{0g}(\Gamma_0)$ take positive values [Fig. 3.5 (b,c)].

Similarly to the derivations presented in Sec. 3.1.1, Fig. 3.5 (b-c) are united and the consideration changes to the exploration of $I_{0b}(I_{0g})$, see Fig. 3.5 (d). When two intensities I_{0b} and I_{0g} varies according to the curve in Fig. 3.5 (d), one implements the pitchfork bifurcation, as can be seen comparing $f(\Gamma)$ and its Taylor series approximation $f_T(\Gamma)$ depicted in Fig. 3.6 (a-d). The corresponding phase-parametric diagram fully corresponds to the pitchfork bifurcation, see Fig. 3.6 (e).

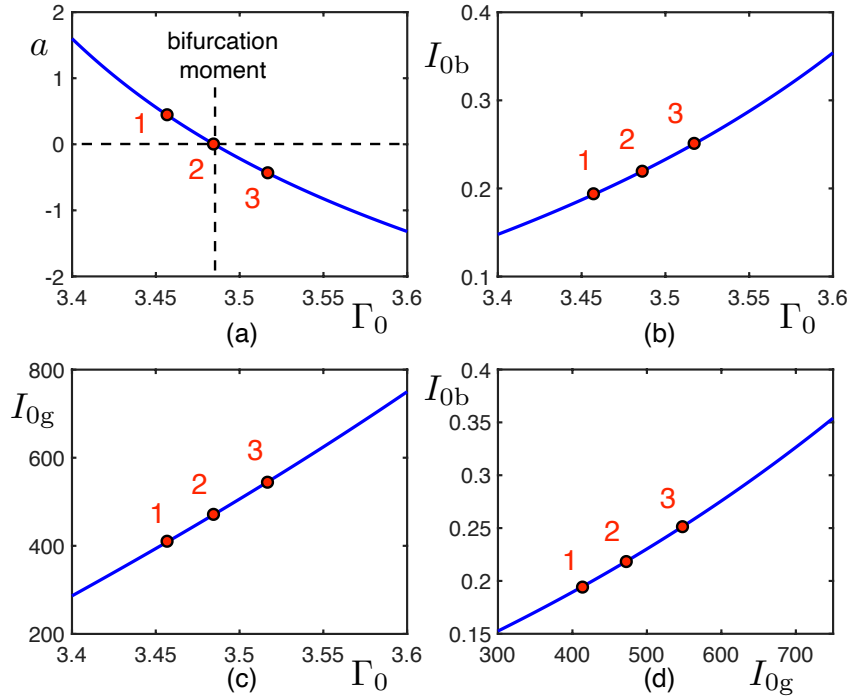


Figure 3.7: Saddle-node bifurcation conditions for Eq. (2.26): (a) Dependence of a on Γ_0 (Eq. (3.34)); (b-c) I_{0b} and I_{0g} according to Eqs. (3.32) and (3.33); (d) $I_{0b}(I_{0g})$ which consists of values I_{0b} and I_{0g} in panels (b) and (c) corresponding to the same argument Γ_0 . System parameters are: $\alpha_b = 0.117$, $\alpha_g = 0.985 \times 10^{-4}$, $\beta = 0.052$, $\gamma = -0.55$, $\phi_0 = \pi/2$, $\phi_1 = \pi$, $\lambda_b = 450 \times 10^{-9}$, $\lambda_g = 532 \times 10^{-9}$, $R = 0.95$.

3.2.2/ SADDLE-NODE BIFURCATION

The saddle-node normal form is $\frac{dx}{dt} = a + cx^2$. In terms of the Taylor series (see Eq.(3.23)), the conditions for the saddle-node bifurcation in Eq. (2.26) are

$$b = 0 \Rightarrow 4\alpha_b I_{0b} R \sin(2\Gamma_0) \cos(2\phi_0 + \phi_1) \left(\alpha_b I_b + 2 \frac{\lambda_g}{\lambda_b} \alpha_g I_{0g} + \beta \right)^{-2} = 1,$$

$$d = 0 \Rightarrow -\frac{2}{3} \left(4\alpha_b I_{0b} R \sin(2\Gamma_0) \cos(2\phi_0 + \phi_1) \left(\alpha_b I_b + 2 \frac{\lambda_g}{\lambda_b} \alpha_g I_{0g} + \beta \right)^{-2} \right) \\ + \left(\left(\alpha_b I_b + 2 \frac{\lambda_g}{\lambda_b} \alpha_g I_{0g} + \beta \right)^{-2} 4\alpha_b I_{0b} R \sin(2\Gamma_0) \cos(2\phi_0 + \phi_1) \right)^2 2 \cot(2\Gamma_0) \left(\alpha_b I_b + 2 \frac{\lambda_g}{\lambda_b} \alpha_g I_{0g} + \beta \right) \\ + \left(\left(\alpha_b I_b + 2 \frac{\lambda_g}{\lambda_b} \alpha_g I_{0g} + \beta \right)^{-2} \alpha_b I_{0b} R \sin(2\Gamma_0) \cos(2\phi_0 + \phi_1) \right)^3 \left(\alpha_b I_b + 2 \frac{\lambda_g}{\lambda_b} \alpha_g I_{0g} + \beta \right)^2 = 0,$$

$$\Downarrow \\ -\frac{2}{3} + 2 \cot(2\Gamma_0) \left(\alpha_b I_b + 2 \frac{\lambda_g}{\lambda_b} \alpha_g I_{0g} + \beta \right) + \left(\alpha_b I_b + 2 \frac{\lambda_g}{\lambda_b} \alpha_g I_{0g} + \beta \right)^2 = 0.$$

(3.30)

The last expression followed from $d = 0$, which is a quadratic equation for the variable

$k = \left(\alpha_b I_b + 2 \frac{\lambda_g}{\lambda_b} \alpha_g I_{0g} + \beta \right)$ which can possess only positive values. Then solution is $k = -\cot(2\Gamma_0) + \sqrt{\cot^2(2\Gamma_0) + \frac{2}{3}}$, and it follows from condition $b = 0$ that

$$\sqrt{4\alpha_b R I_{0b} \sin(2\Gamma_0) \cos(2\phi_0 + \phi_1)} = \left(\alpha_b I_b + 2 \frac{\lambda_g}{\lambda_b} \alpha_g I_{0g} + \beta \right). \quad (3.31)$$

Then the incident blue light intensity is

$$I_{0b} = \frac{\left(-\cot(2\Gamma_0) + \sqrt{\cot^2(2\Gamma_0) + \frac{2}{3}} \right)^2}{4\alpha_b R \sin(2\Gamma_0) \cos(2\phi_0 + \phi_1)}, \quad (3.32)$$

which is a function of Γ_0 . After that, the condition $b = 0$ allows to express the incident green light intensity as

$$I_{0g} = \frac{\lambda_b}{\lambda_g} \frac{\sqrt{\cot^2(2\Gamma_0) + \frac{2}{3}} - \cot(2\Gamma_0) - \alpha_b I_b - \beta}{2\alpha_g}, \quad (3.33)$$

where $I_b = 2I_{0b} \left\{ 1 + R^2 + R \cos(2\phi_0 + \phi_1) \cos(2\Gamma_0) + R \cos(\phi_1) \right\}$ (here I_{0b} is sought as a function of Γ_0 according to Eq. (3.32)).

Using equality $\left(\alpha_b I_b + 2 \frac{\lambda_g}{\lambda_b} \alpha_g I_{0g} + \beta \right) = -\cot(2\Gamma_0) + \sqrt{\cot^2(2\Gamma_0) + \frac{2}{3}}$, coefficient a (see Eqs. (3.23)) can be expressed as a function of Γ_0

$$a = -\Gamma_0 + \gamma + \frac{1}{-\cot(2\Gamma_0) + \sqrt{\cot^2(2\Gamma_0) + \frac{2}{3}}}. \quad (3.34)$$

The saddle-node bifurcation moment $a(\Gamma_0) = 0$ can be achieved at certain argument values $\Gamma_0 = \Gamma_0^{\text{bif}}$, some of which correspond to positive values of $I_{0b}(\Gamma_0^{\text{bif}})$ (see Eq. (3.32)) and $I_{0g}(\Gamma_0^{\text{bif}})$ (see Eq. (3.33)). Such a bifurcation transition is illustrated in Fig. 3.7. Coefficient a passes through zero in point $\Gamma \approx 3.4847$ where I_{0b} and I_{0g} are positive (see point 2 in Fig. 3.7).

Similarly to the derivations presented in the previous section, Fig. 3.7 (b-c) are merged and the consideration changes to the exploration of $I_{0b}(I_{0g})$, see Fig. 3.7 (d). When I_{0b} and I_{0g} vary according to Fig. 3.7 (d), one can implement the saddle-node bifurcation as in the normal form, as reflected in the evolution of the $f(\Gamma)$ and $f_{\Gamma}(\Gamma)$ depicted in Fig. 3.8 (a-c). The phase-parametric diagram corresponding to the saddle-node bifurcation is shown in Fig. 3.8 (d). It is important to note that the described saddle-node bifurcation is local and involves only one stable steady state, while the second stable equilibrium does not bifurcate.

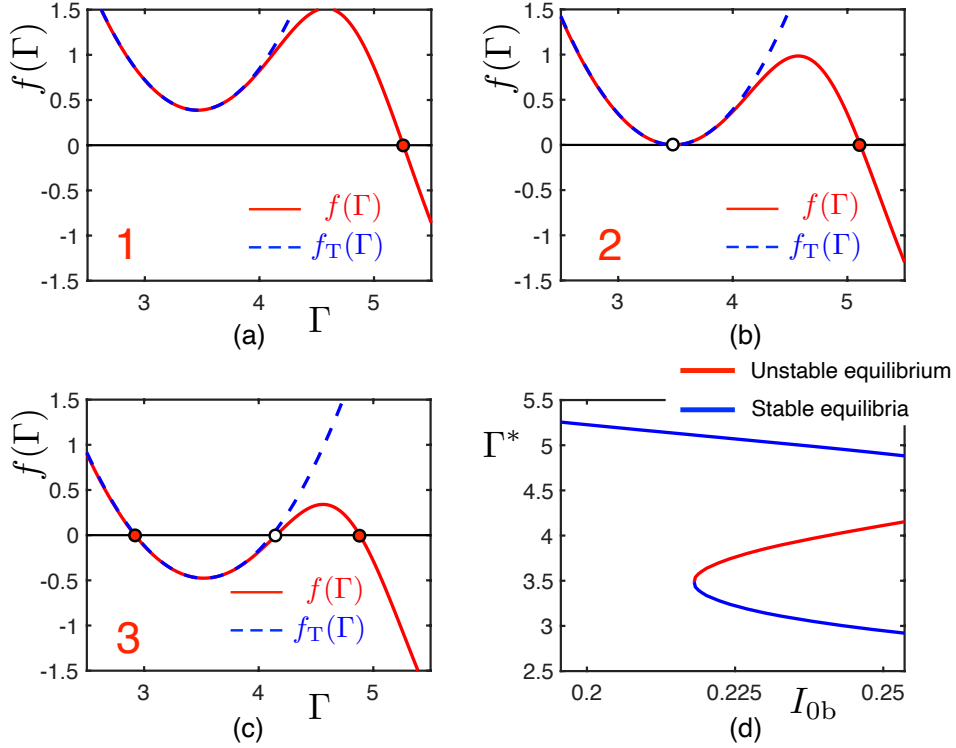


Figure 3.8: Saddle-node bifurcation in Eq. (2.26): (a-c) function $f(\Gamma)$ (red solid curve) and f_T of (3.23) (blue dotted curve) at points 1-3 in Fig. 3.7: $I_{0b} = 19.56 \times 10^{-2}$ and $I_{0g} = 415.8$ (point 1), $I_{0b} = 21.8 \times 10^{-2}$ and $I_{0g} = 471.2$ (point 2), $I_{0b} = 25.36 \times 10^{-2}$ and $I_{0g} = 552.7$ (point 3); (d) Phase-parametric diagram for I_{0b} and I_{0g} varying according to the curve in Fig. 3.7 (d). System parameters are: $\alpha_b = 0.117$, $\alpha_g = 0.985 \times 10^{-4}$, $\beta = 0.052$, $\gamma = -0.55$, $\phi_0 = \pi/2$, $\phi_1 = \pi$, $\lambda_b = 450 \times 10^{-9}$, $\lambda_g = 532 \times 10^{-9}$, $R = 0.95$.

3.2.3/ TRANSCRITICAL BIFURCATION

The transcritical bifurcation normal form is $\frac{dx}{dt} = bx + cx^2$. In terms of the Taylor series described by Eq. (3.23), function $f(\Gamma)$ of Eq. (2.26) can evolve as the transcritical bifurcation normal form in some neighbourhood of Γ_0 when two conditions are obeyed

$$\begin{aligned}
 a = 0 &\Rightarrow \left(\alpha_b I_b + 2 \frac{\lambda_g}{\lambda_b} \alpha_g I_{0g} + \beta \right)^{-1} = \Gamma_0 - \gamma, \\
 d = 0 &\Rightarrow -\frac{2}{3} (4\alpha_b I_{0b} R \sin(2\Gamma_0) \cos(2\phi_0 + \phi_1) (\Gamma_0 - \gamma)) \\
 &\quad + 2 \cot(2\Gamma_0) (4\alpha_b I_{0b} R \sin(2\Gamma_0) \cos(2\phi_0 + \phi_1) (\Gamma_0 - \gamma))^2 \\
 &\quad + (4\alpha_b I_{0b} R \sin(2\Gamma_0) \cos(2\phi_0 + \phi_1) (\Gamma_0 - \gamma))^3 = 0.
 \end{aligned} \tag{3.35}$$

Under the condition $4\alpha_b I_{0b} R \sin(2\Gamma_0) \cos(2\phi_0 + \phi_1) (\Gamma_0 - \gamma) \neq 0$ the expression $d = 0$ takes the form

$$\begin{aligned}
 -\frac{2}{3} + 2 \cot(2\Gamma_0) (4\alpha_b I_{0b} R \sin(2\Gamma_0) \cos(2\phi_0 + \phi_1) (\Gamma_0 - \gamma)) \\
 + (4\alpha_b I_{0b} R \sin(2\Gamma_0) \cos(2\phi_0 + \phi_1) (\Gamma_0 - \gamma))^2 = 0,
 \end{aligned} \tag{3.36}$$

which is a quadratic equation form for $k = 4\alpha_b I_{0b} R \sin(2\Gamma_0) \cos(2\phi_0 + \phi_1)(\Gamma_0 - \gamma)$. The equation has two solutions $k = -\cot(2\Gamma_0) \pm \sqrt{\cot^2(2\Gamma_0) + \frac{2}{3}}$, which allows to express two options for the incident blue light intensity

$$I_{0b} = \frac{-\cot(2\Gamma_0) - \sqrt{\cot^2(2\Gamma_0) + \frac{2}{3}}}{4\alpha_b R \sin(2\Gamma_0) \cos(2\phi_0 + \phi_1)(\Gamma_0 - \gamma)}, \quad (3.37)$$

$$I_{0b} = \frac{-\cot(2\Gamma_0) + \sqrt{\cot^2(2\Gamma_0) + \frac{2}{3}}}{4\alpha_b R \sin(2\Gamma_0) \cos(2\phi_0 + \phi_1)(\Gamma_0 - \gamma)}. \quad (3.38)$$

Using $a = 0$, the required incident green light intensity is

$$I_{0g} = \frac{\lambda_b}{\lambda_g} \frac{\frac{1}{\Gamma_0 - \gamma} - 2\alpha_b I_{0b} \{1 + R^2 + R \cos(2\phi_0 + \phi_1) \cos(2\Gamma_0) + R \cos(\phi_1)\} - \beta}{2\alpha_g}, \quad (3.39)$$

where I_{0b} varies as a function of Γ_0 according to Eq. (3.37) or Eq.(3.38). In addition, the condition $a = 0$ also allows to express coefficient b (see Eq. (3.23)) as a function of Γ_0 (illustrated in Fig. 3.9(a, b))

$$b = -1 + \left(-\cot(2\Gamma_0) - \sqrt{\cot^2(2\Gamma_0) + \frac{2}{3}} \right) (\Gamma_0 - \gamma), \quad (3.40)$$

$$b = -1 + \left(-\cot(2\Gamma_0) + \sqrt{\cot^2(2\Gamma_0) + \frac{2}{3}} \right) (\Gamma_0 - \gamma). \quad (3.41)$$

If the incident blue light intensity $I_{0b}(\Gamma_0)$ varies according to Eq. (3.37), then coefficient b becomes a function of Γ_0 according to Eq. (3.40) and does not possess zero value at any Γ_0 (see Fig. 3.9 (a)). In this case, the transcritical bifurcation is impossible in principle.

If the incident blue light intensity $I_{0b}(\Gamma_0)$ follows Eq. (3.38), then the Taylor series coefficient b takes the form given by Eq. (3.41). In such a case, $b(\Gamma_0)$ equals to zero at certain values Γ_0^{bif} , some of which correspond to positive values of $I_{0b}(\Gamma_0^{\text{bif}})$ (see Eq. (3.38)) and $I_{0g}(\Gamma_0^{\text{bif}})$ (see Eq. (3.39)) which means the transcritical bifurcation can occur in Eq. (2.26). The bifurcation transition is illustrated in Fig. 3.9 (b). Coefficient b passes through zero at $\Gamma \approx 3.4845$ where I_{0b} and I_{0g} are positive (see point 2 in Fig. 3.9).

Similarly to the derivations presented in the previous sections, two graphics in Fig. 3.9 (c-d) are merged and the consideration changes to the exploration of $I_{0b}(I_{0g})$, see Fig. 3.9 (e). When I_{0b} and I_{0g} vary according to Fig. 3.9 (e), one can implement the transcritical bifurcation as in the normal form, which can be seen by inspecting $f(\Gamma)$ and $f_{\Gamma}(\Gamma)$ depicted in Fig. 3.10 (a-c). The corresponding phase-parametric diagram corresponds to the bifurcation, see Fig. 3.10 (d). Similarly to the saddle-node bifurcation described in the

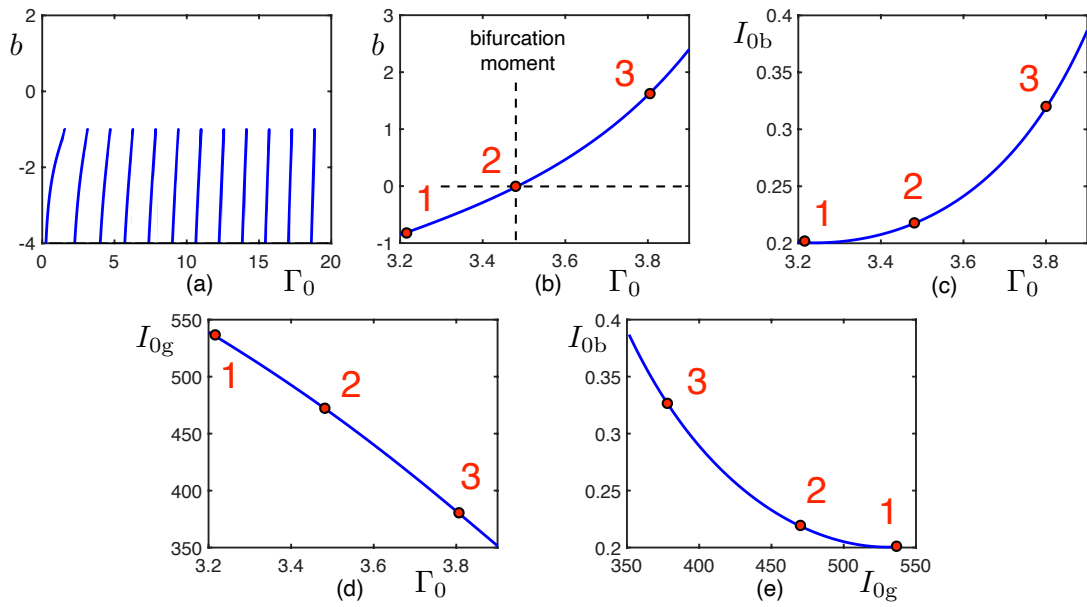


Figure 3.9: Transcritical bifurcation conditions for Eq. (2.26): (a-b) Dependences of coefficient b on Γ_0 (Eqs. (3.40) and (3.41)) when I_{0b} varies according to Eqs. (3.37) (panel (a)) and (3.38) (panel (b)); (c-d) I_{0b} and I_{0g} according to Eqs. (3.38) and (3.39); (e) $I_{0b}(I_{0g})$ which consists of values I_{0b} and I_{0g} in panels (c) and (d) corresponding to the same argument Γ_0 . System parameters are: $\alpha_b = 0.117$, $\alpha_g = 0.985 \times 10^{-4}$, $\beta = 0.052$, $\gamma = -0.55$, $\lambda_b = 450 \times 10^{-9}$, $\lambda_g = 532 \times 10^{-9}$, $R = 0.95$.

previous section, the transcritical bifurcation is local and involves only one stable steady state while the second stable equilibrium does not bifurcate.

3.3/ OASLM UNDER COHERENT ILLUMINATION WITH FEEDBACK: THE PHASE MODULATION REGIME

As mentioned in Chap. 2, Eqs. (2.26) and (2.27) that describe the OASLM driven by feedback in the amplitude and phase modulation regimes fully coincide at $\phi_0 = \pi/2 + n\pi$, $\phi_1 = \pi + 2m\pi$, where $n, m \in \mathbb{Z}$. Thus, for these values all conclusions on the possibility to implement the pitchfork bifurcation, the saddle-node bifurcation and the transcritical bifurcation in Eq. (2.26) can be extended to the system described by Eq. (2.27). In addition, all the dependence in Figs. 3.5-3.10 are also valid for the phase modulation regime at $\phi_0 = \pi/2 + n\pi$, $\phi_1 = \pi + 2m\pi$.

The results for the bifurcations in Eq. (2.27) are summarised below. The Taylor series

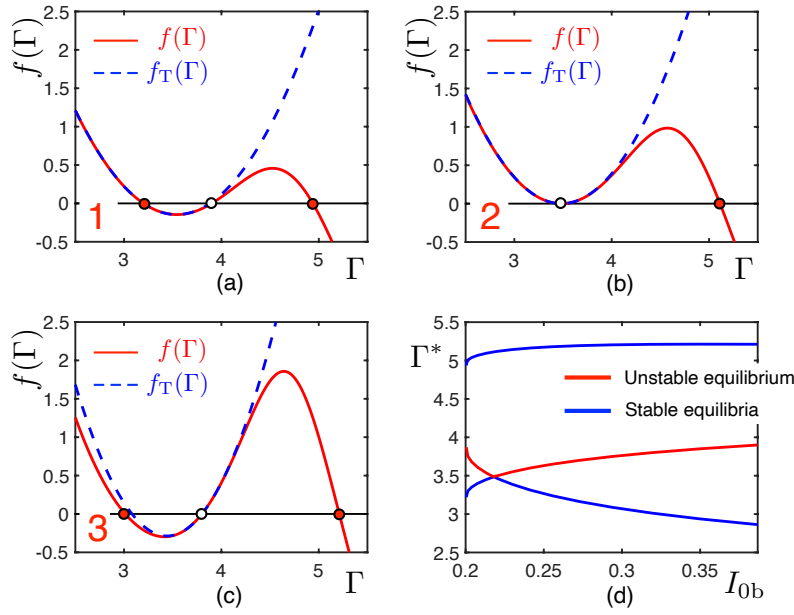


Figure 3.10: Transcritical bifurcation in Eq. (2.26): (a-c) $f(\Gamma)$ (red solid curve) and f_T according to Eq. (3.23) (blue dotted curve) at points 1-3 in Fig. 3.9: $I_{0b} = 20.1 \times 10^{-2}$ and $I_{0g} = 539.1$ (point 1), $I_{0b} = 21.8 \times 10^{-2}$ and $I_{0g} = 471.3$ (point 2), $I_{0b} = 31.9 \times 10^{-2}$ and $I_{0g} = 382$ (point 3); (d) Phase-parametric diagram for I_{0b} and I_{0g} varying according to the curve in Fig. 3.9 (e). System parameters are: $\alpha_b = 0.117$, $\alpha_g = 0.985 \times 10^{-4}$, $\beta = 0.052$, $\gamma = -0.55$, $\phi_0 = \pi/2$, $\phi_1 = \pi$, $\lambda_b = 450 \times 10^{-9}$, $\lambda_g = 532 \times 10^{-9}$, $R = 0.95$.

takes the form

$$\begin{aligned}
 f_T(\Gamma) &= a + b(\Gamma - \Gamma_0) + c(\Gamma - \Gamma_0)^2 + d(\Gamma - \Gamma_0)^3, \quad \text{where} \\
 a &= -\Gamma_0 + \left(\alpha_b I_b + 2 \frac{\lambda_g}{\lambda_b} \alpha_g I_{0g} + \beta \right)^{-1} + \gamma, \\
 b &= -1 + 4\alpha_b I_{0b} R \sin(2\phi_0 + \phi_1 + 2\Gamma_0) \left(\alpha_b I_b + 2 \frac{\lambda_g}{\lambda_b} \alpha_g I_{0g} + \beta \right)^{-2}, \\
 c &= 4\alpha_b I_{0b} R \cos(2\phi_0 + \phi_1 + 2\Gamma_0) \left(\alpha_b I_b + 2 \frac{\lambda_g}{\lambda_b} \alpha_g I_{0g} + \beta \right)^{-2} \\
 &\quad + 16\alpha_b^2 I_{0b}^2 R^2 \sin^2(2\phi_0 + \phi_1 + 2\Gamma_0) \left(\alpha_b I_b + 2 \frac{\lambda_g}{\lambda_b} \alpha_g I_{0g} + \beta \right)^{-3}, \\
 d &= -\frac{8}{3} \alpha_b I_{0b} R \sin(2\phi_0 + \phi_1 + 2\Gamma_0) \left(\alpha_b I_b + 2 \frac{\lambda_g}{\lambda_b} \alpha_g I_{0g} + \beta \right)^{-2} \\
 &\quad + 16\alpha_b^2 I_{0b}^2 R^2 \sin(4\phi_0 + 2\phi_1 + 4\Gamma_0) \left(\alpha_b I_b + 2 \frac{\lambda_g}{\lambda_b} \alpha_g I_{0g} + \beta \right)^{-3} \\
 &\quad + 64\alpha_b^3 I_{0b}^3 R^3 \sin^3(2\phi_0 + \phi_1 + 2\Gamma_0) \left(\alpha_b I_b + 2 \frac{\lambda_g}{\lambda_b} \alpha_g I_{0g} + \beta \right)^{-4}, \\
 I_b &= 2I_{0b} \left\{ 1 + R^2 + R \cos(2\phi_0 + \phi_1 + 2\Gamma_0) + R \cos(\phi_1) \right\}.
 \end{aligned} \tag{3.42}$$

3.3. OASLM UNDER COHERENT ILLUMINATION WITH FEEDBACK: THE PHASE MODULATION REGIME

Using the same approach as in Sec. 3.2, the expression for I_{0b} , I_{0g} and bifurcation parameters can be derived for all three bifurcations. For the pitchfork bifurcation the expressions are

$$I_{0b} = -\frac{\cos(2\phi_0 + \phi_1 + 2\Gamma_0)}{4\alpha_b R \sin^2(2\phi_0 + \phi_1 + 2\Gamma_0)(\Gamma_0 - \gamma)}, \quad (3.43)$$

$$I_{0g} = \frac{\lambda_b}{\lambda_g} \frac{\frac{1}{\Gamma_0 - \gamma} - 2\alpha_b I_{0b} \{1 + R^2 + R \cos(2\phi_0 + \phi_1 + 2\Gamma_0) + R \cos(\phi_1)\} - \beta}{2\alpha_g}, \quad (3.44)$$

$$b = -1 - \cot(2\phi_0 + \phi_1 + 2\Gamma_0)(\Gamma_0 - \gamma). \quad (3.45)$$

In contrast to dependence described by Eq. (3.29) for $b(\Gamma_0)$ in the amplitude modulation regime, the dependence $b(\Gamma_0)$ according to Eq. (3.45) contains parameters ϕ_0 and ϕ_1 . Thus, the phase modulation regime is more flexible, since the bifurcation point Γ_0^{bif} corresponding to $b(\Gamma_0) = 0$ can be shifted by adjusting ϕ_0 and ϕ_1 .

The dependences $I_{0b}(\Gamma_0)$, $I_{0g}(\Gamma_0)$ and $a(\Gamma_0)$ corresponding to the saddle-node bifurcation conditions $b = 0$ and $d = 0$ in Eq. (2.27) are

$$I_{0b} = \frac{\left(-\cot(2\phi_0 + \phi_1 + 2\Gamma_0) + \sqrt{\cot^2(2\phi_0 + \phi_1 + 2\Gamma_0) + \frac{2}{3}}\right)^2}{4\alpha_b R \sin(2\phi_0 + \phi_1 + 2\Gamma_0)}, \quad (3.46)$$

$$I_{0g} = \frac{\lambda_b}{\lambda_g} \frac{\sqrt{\cot^2(2\phi_0 + \phi_1 + 2\Gamma_0) + \frac{2}{3}} - \cot(2\phi_0 + \phi_1 + 2\Gamma_0) - \alpha_b I_b - \beta}{2\alpha_g}, \quad (3.47)$$

$$a = -\Gamma_0 + \gamma + \frac{1}{-\cot(2\phi_0 + \phi_1 + 2\Gamma_0) + \sqrt{\cot^2(2\phi_0 + \phi_1 + 2\Gamma_0) + \frac{2}{3}}}, \quad (3.48)$$

where $I_b = 2I_{0b} \{1 + R^2 + R \cos(2\phi_0 + \phi_1 + 2\Gamma_0) + R \cos(\phi_1)\}$. Equation (3.48) contains parameters ϕ_0 , ϕ_1 and γ . As discussed, it is difficult to vary γ , but ϕ_0 and ϕ_1 can be readily tuned in experiments. The principal difference between the saddle-node bifurcation conditions for the amplitude and phase modulation regimes therefore is that Γ_0^{bif} corresponding to $a(\Gamma_0) = 0$ in the phase modulation regime can be shifted by varying ϕ_0 and ϕ_1 .

The dependences $I_{0b}(\Gamma_0)$, $I_{0g}(\Gamma_0)$ and $b(\Gamma_0)$ following from the transcritical bifurcation conditions $a = 0$ and $d = 0$ in Eq. (2.27) take the form

$$I_{0b} = \frac{-\cot(2\phi_0 + \phi_1 + 2\Gamma_0) + \sqrt{\cot^2(2\phi_0 + \phi_1 + 2\Gamma_0) + \frac{2}{3}}}{4\alpha_b R \sin(2\phi_0 + \phi_1 + 2\Gamma_0)(\Gamma_0 - \gamma)}, \quad (3.49)$$

$$I_{0g} = \frac{\lambda_b}{\lambda_g} \frac{\frac{1}{\Gamma_0 - \gamma} - 2\alpha_b I_{0b} \{1 + R^2 + R \cos(2\phi_0 + \phi_1 + 2\Gamma_0) + R \cos(\phi_1)\} - \beta}{2\alpha_g}, \quad (3.50)$$

$$b = -1 + \left(-\cot(2\phi_0 + \phi_1 + 2\Gamma_0) + \sqrt{\cot^2(2\phi_0 + \phi_1 + 2\Gamma_0) + \frac{2}{3}} \right) (\Gamma_0 - \gamma). \quad (3.51)$$

As in the cases of the pitchfork and saddle-node bifurcations, the value Γ_0^{bif} corresponding to the transcritical bifurcation moment, $b(\Gamma_0^{\text{bif}}) = 0$, can be tuned by varying ϕ_0 and ϕ_1 in the phase modulation regime.

3.4/ SINGLE-PS-LAYER OASLM UNDER COHERENT ILLUMINATION WITH FEEDBACK: THE PHASE MODULATION REGIME

Suppose that the OASLM is modified as in Sec. 2.11.1 (single-PS-layer OASLM model) and is driven by feedback in the phase modulation regime. Then the system under study takes form of Eq. (2.33). As in the previous section, Eq. (2.33) is studied at $\varepsilon = 1$. To further simplify the equations, $\Gamma_b = \Gamma$, as well as $\gamma_b = \gamma$, $\beta_b = \beta$. The objective of this section is to identify a potential fundamental difference between the models implying single-PS and double-PS layer in terms of the bifurcation transitions. For that, right-hand side function $f(\Gamma)$ is represented using the Taylor series

$$\begin{aligned} f_{\Gamma}(\Gamma) &= a + b(\Gamma - \Gamma_0) + c(\Gamma - \Gamma_0)^2 + d(\Gamma - \Gamma_0)^3, \quad \text{where} \\ a &= -\Gamma_0 + \left(\alpha_b I_b + \frac{\lambda_g}{\lambda_b} \alpha_g I_{0g} + \beta \right)^{-1} + \gamma, \\ b &= -1 + 4\alpha_b I_{0b} R \sin(2\phi_0 + \phi_1 + 2\Gamma_0) \left(\alpha_b I_b + \frac{\lambda_g}{\lambda_b} \alpha_g I_{0g} + \beta \right)^{-2}, \\ c &= 4\alpha_b I_{0b} R \cos(2\phi_0 + \phi_1 + 2\Gamma_0) \left(\alpha_b I_b + \frac{\lambda_g}{\lambda_b} \alpha_g I_{0g} + \beta \right)^{-2} \\ &\quad + 16\alpha_b^2 I_{0b}^2 R^2 \sin^2(2\phi_0 + \phi_1 + 2\Gamma_0) \left(\alpha_b I_b + \frac{\lambda_g}{\lambda_b} \alpha_g I_{0g} + \beta \right)^{-3}, \\ d &= -\frac{8}{3} \alpha_b I_{0b} R \sin(2\phi_0 + \phi_1 + 2\Gamma_0) \left(\alpha_b I_b + \frac{\lambda_g}{\lambda_b} \alpha_g I_{0g} + \beta \right)^{-2} \\ &\quad + 16\alpha_b^2 I_{0b}^2 R^2 \sin(4\phi_0 + 2\phi_1 + 4\Gamma_0) \left(\alpha_b I_b + \frac{\lambda_g}{\lambda_b} \alpha_g I_{0g} + \beta \right)^{-3} \\ &\quad + 64\alpha_b^3 I_{0b}^3 R^3 \sin^3(2\phi_0 + \phi_1 + 2\Gamma_0) \left(\alpha_b I_b + \frac{\lambda_g}{\lambda_b} \alpha_g I_{0g} + \beta \right)^{-4}, \\ I_b &= I_{0b} \{ 1 + R^2 + 2R \cos(2\phi_0 + \phi_1 + 2\Gamma_0) \}. \end{aligned} \quad (3.52)$$

The Taylor series components for the double- (Eq. (3.42)) and single-PS-layer OASLM (Eq. (3.52)) in the phase modulation regime are similar, but the difference consists in the

expressions for I_b and the factor 2 in the term $\frac{\lambda_g}{\lambda_b} \alpha_g I_{0g}$ in Eq. (3.42).

3.4.1/ PITCHFORK BIFURCATION

To derive the dependences $I_{0b}(\Gamma_0)$, $I_{0g}(\Gamma_0)$, $b(\Gamma_0)$, the same approach as in the previous sections was used. The resulting equations are

$$I_{0b} = -\frac{\cos(2\phi_0 + \phi_1 + 2\Gamma_0)}{4\alpha_b R \sin^2(2\phi_0 + \phi_1 + 2\Gamma_0)(\Gamma_0 - \gamma)}, \quad (3.53)$$

$$I_{0g} = \frac{\lambda_b}{\lambda_g} \frac{\frac{1}{\Gamma_0 - \gamma} - \alpha_b I_{0b} \{1 + R^2 + 2R \cos(2\phi_0 + \phi_1 + 2\Gamma_0)\} - \beta}{\alpha_g}, \quad (3.54)$$

$$b = -1 - \cot(2\phi_0 + \phi_1 + 2\Gamma_0)(\Gamma_0 - \gamma). \quad (3.55)$$

The dependences $I_{0b}(\Gamma_0)$ and $b(\Gamma_0)$ for the single- and double-PS OASLM in the phase modulation regimes are identical (compare Eqs. (3.43),(3.45),(3.53),(3.55)) while the dependences for I_{0g} (see Eqs. (3.44) and (3.54)) differ. Moreover, for $\phi_0 = \pi/2 + n\pi$, $\phi_1 = \pi + 2m\pi$, where $n, m \in \mathbb{Z}$, $I_{0b}(\Gamma_0)$ for the amplitude and phase modulation regimes (Eqs. (3.27),(3.43) and (3.53)) fully coincide as well as for $b(\Gamma_0)$ (Eqs. (3.29), (3.45), (3.55)). The curves in Fig. 3.5(a-b) therefore also illustrate Eqs. (3.53) and (3.55). Then the pitchfork bifurcation in Eq. (2.33) can occur if $I_{0g}(\Gamma_0)$ takes a positive value at the bifurcation moment $\Gamma_0 = \Gamma_0^{\text{bif}} \approx 16.5256$. It is seen in Fig. 3.11 that $I_{0g}(\Gamma_0 \approx 16.5256)$ is positive, which indicates that the pitchfork bifurcation in Eq. (2.33) occurs exactly as in Fig. 3.6 when the intensities I_{0b} and I_{0g} are varied according to Eqs. (3.53) and (3.54).

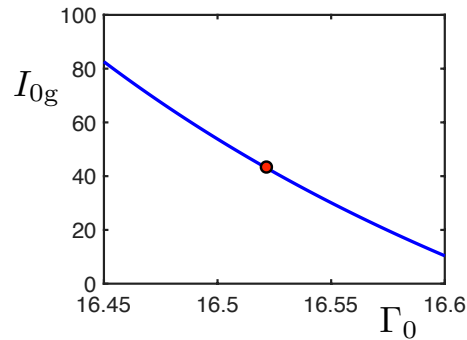


Figure 3.11: $I_{0g}(\Gamma_0)$ corresponding to Eq. (3.54), where $I_{0b}(\Gamma_0)$ varies according to Eq. (3.53). The red point corresponds to the pitchfork bifurcation moment $b(\Gamma_0 \approx 16.5256) = 0$. Parameters are: $\alpha_b = 0.117$, $\alpha_g = 0.985 \times 10^{-4}$, $\beta = 0.052$, $\gamma = -0.55$, $\phi_0 = \pi/2$, $\phi_1 = \pi$, $\lambda_b = 450 \times 10^{-9}$, $\lambda_g = 532 \times 10^{-9}$, $R = 0.95$.

3.4.2/ SADDLE-NODE BIFURCATION

The dependences $I_{0b}(\Gamma_0)$, $I_{0g}(\Gamma_0)$ and $a(\Gamma_0)$ corresponding to the saddle-node bifurcation conditions $b = 0$ and $d = 0$ in Eq. (2.33) are

$$I_{0b} = \frac{\left(-\cot(2\phi_0 + \phi_1 + 2\Gamma_0) + \sqrt{\cot^2(2\phi_0 + \phi_1 + 2\Gamma_0) + \frac{2}{3}} \right)^2}{4\alpha_b R \sin(2\phi_0 + \phi_1 + 2\Gamma_0)}, \quad (3.56)$$

$$I_{0g} = \frac{\lambda_b}{\lambda_g} \frac{\sqrt{\cot^2(2\phi_0 + \phi_1 + 2\Gamma_0) + \frac{2}{3}} - \cot(2\phi_0 + \phi_1 + 2\Gamma_0) - \alpha_b I_b - \beta}{\alpha_g}, \quad (3.57)$$

$$a = -\Gamma_0 + \gamma + \frac{1}{-\cot(2\phi_0 + \phi_1 + 2\Gamma_0) + \sqrt{\cot^2(2\phi_0 + \phi_1 + 2\Gamma_0) + \frac{2}{3}}}, \quad (3.58)$$

where $I_b = I_{0b} \{1 + R^2 + 2R \cos(2\phi_0 + \phi_1 + 2\Gamma_0)\}$.

In the phase modulation regime $I_{0b}(\Gamma_0)$ and $a(\Gamma_0)$ for the single- and double-PS-layer OASLM are identical. Moreover, for the particular values $\phi_0 = \pi/2 + n\pi$ and $\phi_1 = \pi + 2\pi m$ the expressions for I_{0b} (see Eqs. (3.32),(3.46) and (3.56)) and $a(\Gamma_0)$ (see Eqs. (3.34),(3.48) and (3.58)) corresponding to the amplitude and phase modulation regimes are identical. Thus, Fig. 3.7(a,b) describe Eqs. (3.58) and (3.56) for $\phi_0 = \pi/2$ and $\phi_1 = \pi$. Then the potential bifurcation point where $a(\Gamma_0) = 0$ is $\Gamma_0 = \Gamma_0^{\text{bif}} \approx 3.4847$. Figure 3.12 shows that $I_{0g}(\Gamma_0)$ (see Eq. 3.57) is positive in the neighbourhood of point Γ_0^{bif} . That means the saddle-node bifurcation can be implemented in Eq. (2.33) exactly as in the normal form. If I_{0b} and I_{0g} vary according to Eqs. (3.56) and (3.57), then the saddle-node bifurcation is observed as in Fig. 3.8.

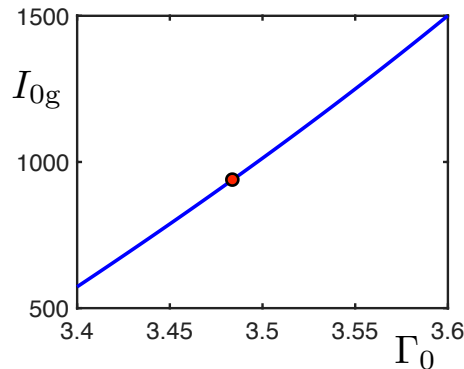


Figure 3.12: Dependence $I_{0g}(\Gamma_0)$ (Eq. (3.57) where $I_{0b}(\Gamma_0)$ varies according to Eq. (3.56)). The red point corresponds to the saddle-node bifurcation moment $b(\Gamma_0 \approx 3.4847) = 0$. Parameters are: $\alpha_b = 0.117$, $\alpha_g = 0.985 \times 10^{-4}$, $\beta = 0.052$, $\gamma = -0.55$, $\phi_0 = \pi/2$, $\phi_1 = \pi$, $\lambda_b = 450 \times 10^{-9}$, $\lambda_g = 532 \times 10^{-9}$, $R = 0.95$.

3.4.3/ TRANSCRITICAL BIFURCATION

The dependences $I_{0b}(\Gamma_0)$, $I_{0g}(\Gamma_0)$ and $a(\Gamma_0)$ corresponding to the transcritical bifurcation conditions $a = 0$ and $d = 0$ in Eq. (2.33) take the form

$$I_{0b} = \frac{-\cot(2\phi_0 + \phi_1 + 2\Gamma_0) + \sqrt{\cot^2(2\phi_0 + \phi_1 + 2\Gamma_0) + \frac{2}{3}}}{4\alpha_b R \sin(2\phi_0 + \phi_1 + 2\Gamma_0)(\Gamma_0 - \gamma)}, \quad (3.59)$$

$$I_{0g} = \frac{\lambda_b}{\lambda_g} \frac{\frac{1}{\Gamma_0 - \gamma} - \alpha_b I_{0b} \{1 + R^2 + 2R \cos(2\phi_0 + \phi_1 + 2\Gamma_0)\} - \beta}{\alpha_g}, \quad (3.60)$$

$$b = -1 + \left(-\cot(2\phi_0 + \phi_1 + 2\Gamma_0) + \sqrt{\cot^2(2\phi_0 + \phi_1 + 2\Gamma_0) + \frac{2}{3}} \right) (\Gamma_0 - \gamma). \quad (3.61)$$

In the phase modulation regime, the expressions for $I_{0b}(\Gamma_0)$ and $a(\Gamma_0)$ for transcritical bifurcation conditions in the systems with the single- and double-PS-layer OASLM are identical. Moreover, in case $\phi_0 = \pi/2 + n\pi$ and $\phi_1 = \pi + 2m\pi$ the expressions for I_{0b} (see Eqs. (3.38),(3.49) and (3.59)) and $a(\Gamma_0)$ (see Eqs. (3.41),(3.51) and (3.61)) corresponding to the amplitude and phase modulation regimes are identical. Thus, Fig. 3.9(b,c) describe dependences by Eqs. (3.61) and (3.59) for $\phi_0 = \pi/2$ and $\phi_1 = \pi$. Then the potential bifurcation point where $b(\Gamma_0) = 0$ is $\Gamma_0 = \Gamma_0^{\text{bif}} \approx 3.4845$. Figure 3.13 shows that $I_{0g}(\Gamma_0)$ (see Eq. 3.60) is positive in the neighbourhood of point Γ_0^{bif} . That means the transcritical bifurcation can be implemented in Eq. (2.33) exactly as in the normal form. If I_{0b} and I_{0g} vary according to Eqs. (3.59) and (3.60), then the transcritical bifurcation is observed as in Fig. 3.10.

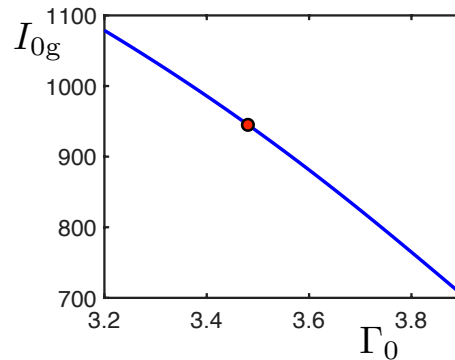


Figure 3.13: Dependence $I_{0g}(\Gamma_0)$ corresponding to Eq. (3.60) where $I_{0b}(\Gamma_0)$ varies according to Eq. (3.59). The red point corresponds to the transcritical bifurcation moment $b(\Gamma_0 \approx 3.4845) = 0$. Parameters are: $\alpha_b = 0.117$, $\alpha_g = 0.985 \times 10^{-4}$, $\beta = 0.052$, $\gamma = -0.55$, $\phi_0 = \pi/2$, $\phi_1 = \pi$, $\lambda_b = 450 \times 10^{-9}$, $\lambda_g = 532 \times 10^{-9}$, $R = 0.95$.

3.5/ CONCLUSION

The presented results shows that a manifold of the bifurcation transitions in OASLM-based systems is possible. In particular, incoherent illumination can create the pitchfork bifurcation in addition to the saddle-node bifurcations described in Chap. 2. To observe the pitchfork bifurcation, one must vary the incident light intensities according to the certain rule which was analytically derived.

The variety of bifurcation transitions which can be implemented in the OASLM-based systems under coherent illumination is even broader. Actually, coherent illumination enables any bifurcation possible with one dimensional real-valued dynamical systems: the pitchfork bifurcation, the saddle-node bifurcation and the transcritical bifurcation. The Hopf bifurcation is excluded since the corresponding normal form is written in complex form and hence is two-dimensional. To implement these bifurcations, one must adjust the incident light intensities according to analytically derived relationships. Generally, the phase modulation regime is more flexible in comparison with the amplitude modulation regime. This is due to the fact that the phase modulation regime additionally provides for the bifurcation moment to be shifted by adjusting ϕ_0 and ϕ_1 , which in an experiment readily can be changed by tuning of the wavelength and by moving the dichroic mirror.

The bifurcation conditions for the systems implying the single-PS-layer and double-PS-layer OASLM have no principal difference. For the concrete case $\phi_0 = \pi/2$ and $\phi_1 = \pi$ they are identical except of the expression for the incident green light intensity: in the case of the single-PS-layer OASLM the bifurcations occur at twice as high values of I_{0g} .

DETERMINISTIC AND STOCHASTIC CONTROL OF COARSENING

It is demonstrated in the fourth chapter how the bifurcation conditions established in Chap. 3 allow for controlling spatio-temporal dynamics based on the example of wavefront propagation and coarsening. It is important to note that the term 'wavefront' does not refer to the surface over which an optical wave has a constant phase. Here, a wavefront refers to the context of, for example, fluid dynamics and describes a boundary between domains corresponding to different quiescent steady state regimes in bistable reaction-diffusion systems. The effect of coarsening is considered as a particular case of propagating front phenomena in bistable spatially-extended systems, which can occur in two-dimensional space.

A spatial model of the OASLM with feedback is derived, based on which spatial dynamics is illustrated and explained. After that, the bifurcation normal form conditions are applied in order to control the front propagation's speed and direction based on tuning the system's parameters.

A second approach for front propagation control discussed in this chapter leverages different properties of noise. Here, the noise intensity is used as an additional system parameter. Varying the noise strength allows for tuning the wavefront propagation's speed, and in turn the dynamics of coarsening. First, this effect is described on the example of a phenomenological coarsening model. Then, it is demonstrated that identical phenomena occur in a stochastic spatial model of the OASLM with feedback. In this case, noise implies a fluctuating green illumination in the two-color illumination setup introduced in Chapter 2, which in an experiment can be readily controlled.

4.1/ INTRODUCTION

A reaction-diffusion system was naturally introduced in chemistry to represent substances reacting and diffusing over the spatial domain. Now, the definition of reaction-diffusion

systems refers to phenomena of any nature. Mathematically, reaction-diffusion systems take the form of partial differential equations. Besides the well-known Turing patterns, reaction-diffusion systems exhibit a big variety of spatio-temporal dynamics [175–178] including traveling fronts, solitary and periodic pulses, spiral turbulence, scroll waves and noise-induced pattern formation. In particular, bistable reaction-diffusion media can exhibit dynamics where for the case when two kinds of domains are formed and evolve in space, separating fronts between them are formed and propagate. Such propagating fronts are of frequent occurrence in chemistry, see, for instance, the Schlögl model [179–181] developed for the explanation of an autocatalytic reaction mechanism, as well as in electronics [182], flame propagation theory [183], just to name a few. In the simplest case, front propagation can be observed in 1D-space. If a studied bistable media evolves in 2D-space, then the peculiarities of front propagation is also determined by the shape of domains formed by such fronts. In such a case, one observes an effect often referred to as ‘coarsening’. It is characterised by identical manifestations when compared to front propagation, and coarsening consists in the expansion of domains which invade the entire space on the cost of other domains. Coarsening represents a fundamental phenomenon demonstrated in the context of different areas: physics of liquid crystals [184] and magnetism [185–188], physics and chemistry of materials [189–192], laser physics [193–195], electronics [196] and animal population statistics [197]. It can occur in bistable spatially-extended systems [185] and time-delay oscillators [193, 194, 196], and universal approaches to control such effects are proposed in the fourth chapter.

4.1.1/ DETERMINISTIC CONTROL OF THE FRONT PROPAGATION IN BISTABLE REACTION-DIFFUSION MODELS

Pitchfork bifurcation conditions imply asymmetry control in OASLM-based systems in terms of the right-hand side function $f(\Gamma)$: if the pitchfork bifurcation conditions are fulfilled, asymmetry in $f(\Gamma)$ in respect to its shape relative to a unstable fixed point disappears. It is well-known that the presence of asymmetry in bistable spatially-extended systems has a principal impact on the wavefront propagation speed, for instance, in bistable reaction-diffusion models [181, 198]: the bigger is the asymmetry, the faster is the wavefront propagation. Moreover, control of the system’s asymmetry allows to stop the wavefront propagation or to even invert its direction. Here, this fact is demonstrated on a concrete example.

The phenomenological model for the wavefront propagation in bistable systems takes the form

$$\frac{du}{dt} = k\nabla^2 u - u(u - a)(u + b), \quad (4.1)$$

where $a, b > 0$ are parameters defining the system nonlinearity, and parameter k is the diffusion strength. Equation (4.1) represents a particular modification of the Schlögl model

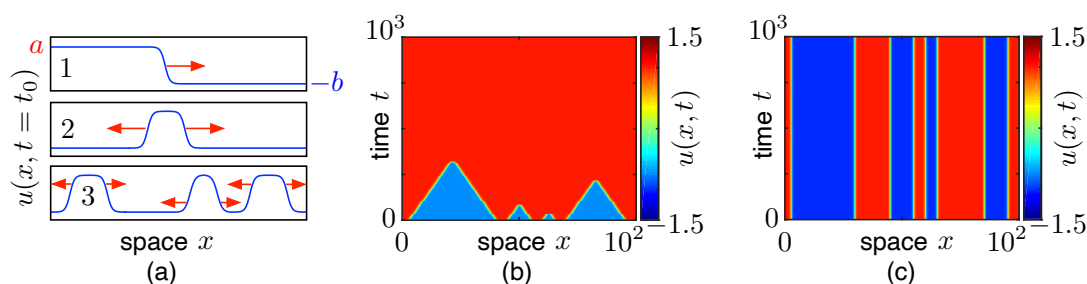


Figure 4.1: Eq. (4.2): (a-b) Schematic illustration of the profile evolution (panel (a1)) according to Eq. (4.3) and more complicated solutions (panels (a1) and (a2)) for $a = 1$, $b = 0.75$, $k = 0.1$. The space time plot corresponding to the solution in panel (a3) is depicted in panel (b). (c) Space-time plot illustrating a stationary wave front in a symmetric system for $a = b = 1$, $k = 0.1$.

[179, 180], but it was initially discussed in 1937 by Zel'dovich and Frank-Kamenetsky in connection with flame propagation [183]. The symmetry condition in Eq. (4.1) is $a = b$. In such a case, the reaction term $f(u) = -u(u - a)(u + b)$ fully coincides with the right-hand side function of the pitchfork bifurcation normal form.

Equation (4.1) possesses the two stable equilibrium states $u_1^* = a$, $u_2^* = -b$ and unstable steady state $u_3^* = 0$ located in between them. If the spatially-distributed initial state $u_0(\vec{r}) = u(\vec{r}, t = 0)$ is fully located inside the basin of attraction of either steady state u_1^* or u_2^* , then the system exhibits a quiescent steady state regime inside the corresponding equilibrium. However, the deterministic dynamics becomes more complex if the initial state $u_0(\vec{r}) = u(\vec{r}, t = 0)$ contains values from both basins of attraction. In this case, Eq. (4.1) can experience a non-equilibrium transition when the system evolves from its initial state distributed across the two basins of attraction towards its final state, where the system is exclusively located inside one basin. This process is accompanied by the growth of domains, the previously introduced coarsening, which results in extending domains of either equilibrium (phase) in space \vec{r} . The intrinsic peculiarities of this transition depend on the system's symmetry properties [181], and on the dimensionality of the system's phase space.

First, Eq. (4.1) is considered in the simplest case using one-dimensional space x . Then the equation takes the form

$$\frac{du}{dt} = k \frac{d^2u}{dx^2} - u(u - a)(u + b), \quad (4.2)$$

which has two quiescent steady state solutions $u(t, x) = a$ and $u(t, x) = -b$, and the third solution describing a propagating front profile [181, 198] in the form

$$u(x, t) = \frac{a - b}{2} - \frac{a + b}{2} \tanh\left(\frac{a + b}{2\sqrt{2k}}(x - ct)\right), \quad (4.3)$$

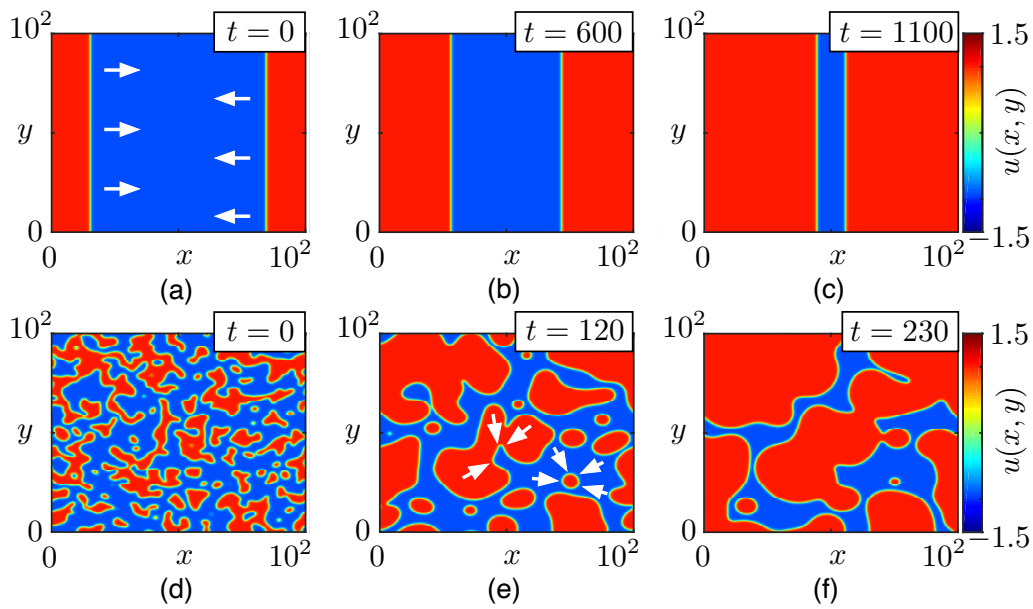


Figure 4.2: Spatial pattern evolution of Eq. (4.1) in 2D-space for $a = 1$, $b = 0.9$, $k = 0.1$: evolution of a plane-wave profile (panels (a-c)) and the effect of coarsening in the case of random initial conditions (panels (d-f)).

where $c = \sqrt{\frac{k}{2}}(a - b)$ is the front propagation speed. A solution to Eq. (4.3) is depicted in Fig. 4.1 (a1). The front velocity is nonzero for $a \neq b$. In such a case, the solution by Eq. (4.3) corresponds to the situation when a globally stable state tends to invade the entire available space, hence developing an expanding or retracting front that increasingly displaces a metastable domain. There exists a solution where the front moves to the left and to the right at the same velocity. Then the evolution of the symmetric u -profile including both fronts [Fig. 4.1 (a2)] exhibits a propagation with the same speed in opposite directions. More complicated profiles [Fig. 4.1 (a3)] evolve according to the same rule. Space-time plots illustrating such dynamics contain typical triangle patterns [Fig. 4.1 (b)].

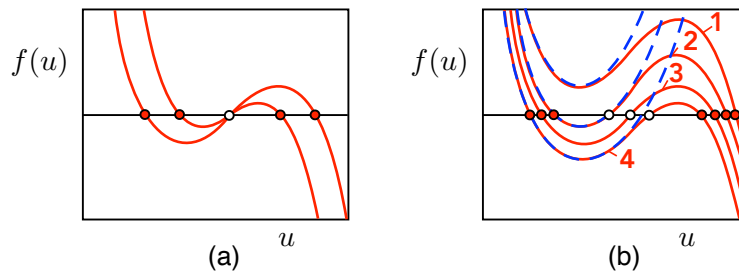


Figure 4.3: Evolution of the reaction-term function $f(u)$ (red solid curves) according to the pitchfork (panel (a)) and saddle-node (panel (b)) bifurcation and its Taylor series expansion using a quadratic function (blue dashed curves).

If Eq. (4.2) is symmetric ($a = b$), the wave front becomes stationary and the space-time plots consist of typical stripes corresponding to $u(x, t) = a$ and $u(x, t) = -b$ [Fig. 4.1 (c)].

The behaviour of Eq. (4.1) in 2D-space (x, y) depends on the initial pattern configuration and on the presence of asymmetry. In the simplest case, the initial state has a uniform structure [Fig. 4.2 (a)]. In such a case the asymmetry condition plays a principal role. If the system is symmetric, then the wavefront persists at a fixed position. If the system is asymmetric, then the wavefront moves in space at a constant speed [Fig. 4.2 (a-c)]. The direction of front propagation depends on the parameter values, and for case $a > b$ state $u(x, y, t) = a$ invades the whole space. If $a < b$, then the front propagation has the opposite direction and state $u(x, y, t) = b$ invades the whole space.

If the initial pattern $u(x, y, t = 0)$ is more complex (for example, see the state in Fig. 4.2 (d) obtained from random initial conditions), then the impact of diffusion is non-uniform, as it contracts domains in the areas that are fully or partially encircled (see white arrows Fig. 4.2 (e)). During some finite time, the spatial domains expand [Fig. 4.2 (d-f)], and either state $u(x, y, t) = a$ or $u(x, y, t) = b$ invades the entire space. If Eq. (4.1) is asymmetric, then this asymmetry can speed up or slow down the propagation of fronts. Moreover, large asymmetry can invert front propagation, and under such conditions even a fully encircled domain expands. The process illustrated in Fig. 4.2 (d-e) shows such domain growth in two-dimensional space. Despite the fact that such dynamics represent a particular case of front propagation, in most cases it is considered as a distinguished effect called 'coarsening'.

To adjust the front propagation (and coarsening) speed and direction in a bistable reaction-diffusion model, one must control the asymmetry in the reaction term of the model equation. The first approach is using the pitchfork bifurcation conditions as discussed in Chap. 3. Then the reaction-term takes the form as in Fig. 4.3 (a). The symmetric case provides for the slowest front propagation. The second proposed approach for coarsening control is associated with the saddle-node bifurcation of steady states. It consists in the adjustment of the vertical shift of some part of the reaction-term function. To achieve this, the function is developed until quadratic function $f_{\Gamma} = a + cu^2$ using the Taylor series around some point (blue dashed lines in Fig 4.3 (b)). Despite the saddle-node bifurcation conditions allow to modify only a part of the curve $f(u)$, controlling parameter a allows to induce the saddle-node bifurcation in the similar way as in Chap. 3 and to vary a distance between the steady states appeared after the bifurcation, as illustrated in Fig. 4.3 (b). The initial state in Fig. 4.3 (b) described by curve 1 corresponds to monostability. Coefficient a allows to shift the curve down and to induce the transition to bistability through the saddle-node bifurcation (curve 2 in Fig. 4.3 (b)). Further shift achieves a maximally symmetric configuration (curve 3 in Fig. 4.3 (b)), where the distances between the attractors and the unstable fixed point are almost identical, which corresponds to the slowest front propagation. Continuing in the same direction (curve 4 in Fig. 4.3 (b)) can produce the opposite asymmetry, and hence invert the front propagation. Both approaches of deterministic coarsening control are applied below on the example of a particular OASLM-based spatially-extended model with local interactions emulating

diffusion.

4.1.2/ STOCHASTIC CONTROL OF FRONT PROPAGATION

In order to investigate the interaction between noise and front propagation, the model of Eq. (4.1) is modified to include parametric noise sources according to

$$\frac{du}{dt} = k\nabla^2 u - u(u - a_0 + \sqrt{2D_a}n_a(\vec{r}, t))(u + b_0 + \sqrt{2D_b}n_b(\vec{r}, t)), \quad (4.4)$$

where $a_0, b_0 > 0$ are fixed parameters, $n_{a,b}$ are statistically independent spatially distributed sources of white Gaussian noise with intensities $D_{a,b}$. The term 'spatial white Gaussian noise' means that in any point \vec{r}_0 the mean value of the noise terms equals to zero, $\langle n_{a,b}(\vec{r}_0, t) \rangle = 0$, and that correlation between different values $n_{a,b}(\vec{r}_0, t)$ in time and space is absent. The function corresponding to zero correlation in space and time is the Delta-function described as $\langle n_a(\vec{r}_0, t)n_a(\vec{r}_0, t + \tau) \rangle = \delta(\tau)$, $\langle n_b(\vec{r}_0, t)n_b(\vec{r}_0, t + \tau) \rangle = \delta(\tau)$, $\langle n_a(\vec{r}_0, t)n_a(\vec{r}_0 + \vec{r}_d, t) \rangle = \delta(\vec{r}_d)$, $\langle n_b(\vec{r}_0, t)n_b(\vec{r}_0 + \vec{r}_d, t) \rangle = \delta(\vec{r}_d)$. In the case of one-dimensional space x , the stochastic equation becomes

$$\frac{du}{dt} = k\frac{d^2u}{dx^2} - u(u - a_0 + \sqrt{2D_a}n_a(x, t))(u + b_0 + \sqrt{2D_b}n_b(x, t)). \quad (4.5)$$

It has been shown by A. Engel in [198] that adjusting noise intensities allows to control the speed of front propagation in Eq. (4.4). This effect is illustrated in Fig. 4.4 for the evolution in one-dimensional space x . In the presence of asymmetry ($a = 1, b = 0.75$) and in the

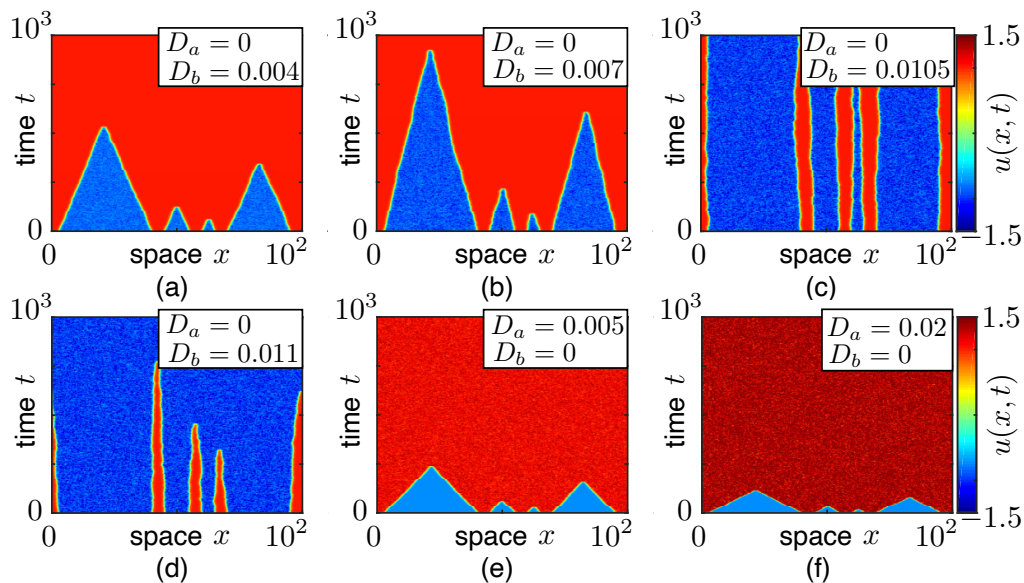


Figure 4.4: Stochastic control of coarsening in Eq. (4.5) by increasing the noise intensity D_b (panels (a-d)) and D_a (panels (e-f)). Other parameters are: $a = 1, b = 0.75, k = 0.1$.

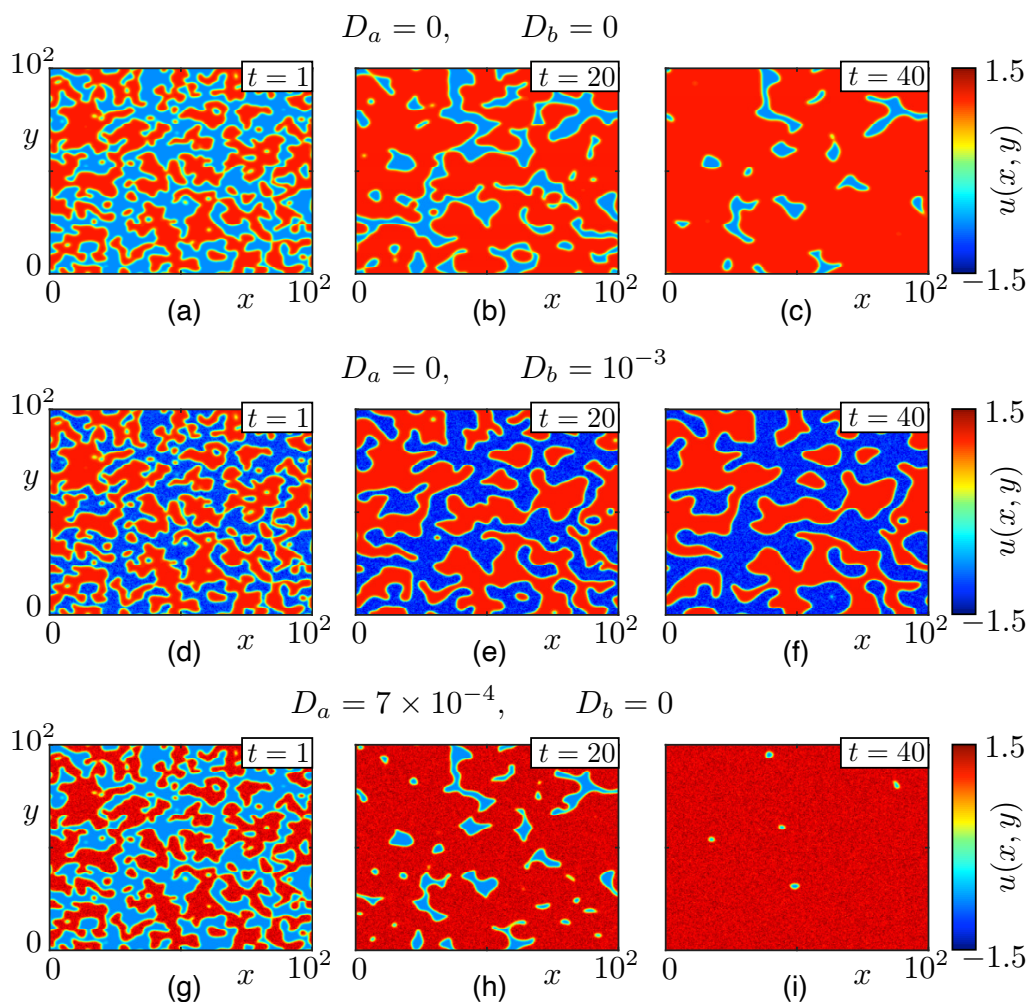


Figure 4.5: Spatial evolution of Eq. (4.4) in 2D-space (x,y) starting from the same initial conditions for $a = 1$, $b = 0.75$, $k = 0.1$ and varying noise intensities: $D_a = 0$, $D_b = 0$ (panels (a-c)), $D_a = 0$, $D_b = 10^{-3}$ (panels (d-f)), $D_a = 7 \times 10^{-4}$, $D_b = 0$ (panels (g-i)).

absence of noise, the system exhibits the effect of coarsening [Fig. 4.2 (b)]. Increasing the noise intensity D_b slows down the front propagation [Fig. 4.4 (a-b)], then it stops the front's motion [Fig. 4.4 (c)]. After that, the front propagation occurs in the opposite direction [Fig. 4.4 (d)]. At the same time, growth of intensity D_a results in the opposite effect: it accelerates front propagation along the original direction, i.e. the direction without noise [Fig. 4.4 (e-f)].

The same effects take place for Eq. (4.4) evolving in two-dimensional space (x,y) . Figure 4.5 illustrates the evolution of the same state, the domains in initial state at $t = 0$ shown in Fig. 4.5 (a,d,g) are identical. As in the one dimensional case, increasing noise intensity D_b slows down coarsening or inverts its direction, as can be seen by comparing the evolutions shown in Fig. 4.5 (a-c) and Fig. 4.5 (d-f). At the same time, increasing intensity D_a speeds up the process, as can be seen from the comparison of Fig. 4.5 (a-c) and Fig. 4.5 (g-i).

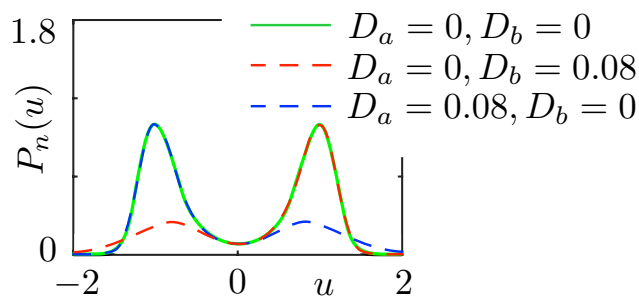


Figure 4.6: Evolution of the normalised probability density function $P_n(u)$ caused by varying noise intensities $D_{a,b}$ in Eq. (4.6). System parameters are $a_0 = b_0 = 1$, $D = 0.1$.

The stochastic control of front propagation in Eq. (4.4) has been explained by A. Engel in [198] based on the fact that multiplicative noise sources have an impact on the symmetry properties of the reaction-term. To demonstrate this in more detail, let us consider the system describing the reaction-term evolution

$$\frac{du}{dt} = -u(u - a_0 + \sqrt{2D_a}n_a(t))(u + b_0 + \sqrt{2D_b}n_b(t)) + \sqrt{2D}n(t). \quad (4.6)$$

In contrast to the full form given by Eq. (4.5), Eq. (4.6) contains only the reaction part and represents an ordinary differential equation. The oscillatory dynamics of Eq. (4.6) is explored by means of the evolution of a stationary probability density function (PDF), $P(u)$, in its normalized form $P_n(u) = P(u)/P_{\max}(u)$. The PDF is used to specify the probability of a dynamical variable falling within a particular range of values $u \in [u_1; u_2]$. This probability is given by the integral of this variable's PDF over that range, which is the area under the PDF function within the relevant range in u . The PDF is nonnegative everywhere, and its integral over the entire space $u \in (-\infty; +\infty)$ is unity. A set of values $u(t)$ was created by numerical simulations of Eq. (4.6). The obtained time realizations must be large and contain a big enough number of transitions between two coexisting attractors in the resulting stochastic phase trajectories to obtain a stationary PDF. However, Eq. (4.6) with multiplicative noise does not often exhibit transitions between the two attractors. To induce noise-sustained jumps between two stable steady states, and hence to obtain a stationary PDF, we introduced an additive source of white Gaussian noise, $\sqrt{2D}n(t)$, into Eq. (4.6), which has no impact on the PDF's symmetry properties [198].

For the symmetric case $a_0 = b_0 = 1$, fixed additive noise intensity $D = 0.1$, and without parametric noise, the distribution $P_n(u)$ is symmetric (the green solid curve in Fig. 4.6). The position of local maxima in $P_n(u)$ correspond to the stable equilibria $u_{1,2}^* = \pm 1$, while the local minimum of the distribution $P_n(u)$ indicates the unstable steady state $u_3^* = 0$. Increasing intensities D_a and D_b causes a transformation of the PDF-function such that $P(u)$ becomes asymmetric, see the red and blue dashed curves in Fig. 4.6. This corresponds to the stochastic dynamics of the asymmetric bistable system. The loss of symmetry under multiplicative noise is reflected in noise-induced front motion in the full reaction-

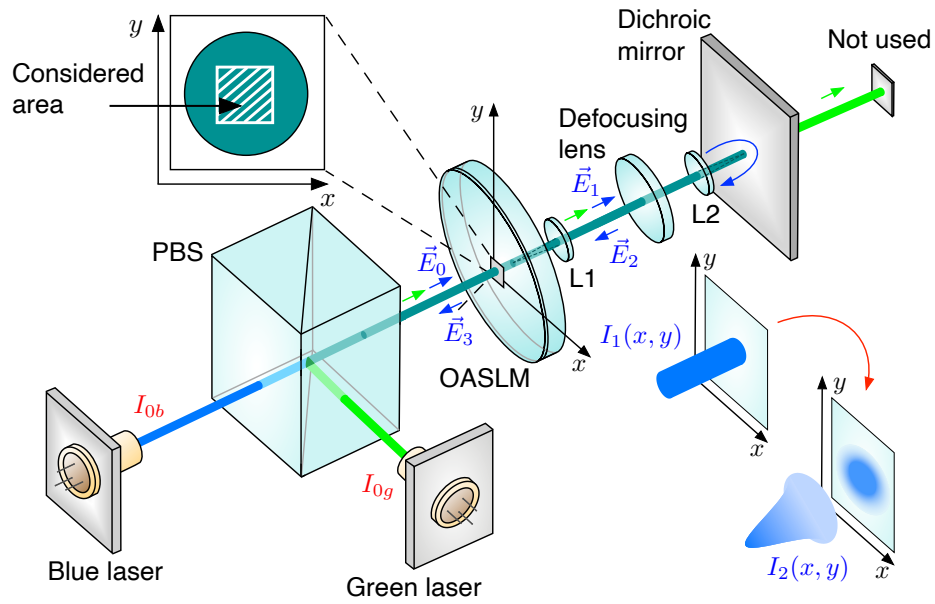


Figure 4.7: Single-PS-layer OASLM under simultaneous blue and green illumination when the blue light beam is reflected by the dichroic mirror and creates feedback. In contrast to Fig. 2.20, the system contains a defocusing lens to emulate local diffusion by spatially broadening the field distribution of the back-reflected optical field. Lenses L1 and L2 create 4f-imaging of the OASLM's state back on itself after reflection by the mirror.

diffusion model described by Eq. (4.4) for $a_0 = b_0 = 1$ and noise intensities $D_a \neq D_b$, which was called 'noise-induced front propagation' [198].

Rigorously speaking, the evolution of the PDF function does not explain noise-dependent front propagation, but it can be used as an indicator illustrating the symmetry property of the reaction term changes when varying $D_{a,b}$. The theoretical explanation of noise-controlled front propagation in bistable reaction-diffusion models is given in [178]. Using the 'Small-Noise-Expansion approach', the authors have shown that the multiplicative noise also influences the systematic part of the front dynamics. The same methodology has been used for the explanation of the front propagation in bistable population models [199].

4.2/ SPATIALLY-EXTENDED MODEL OF THE FEEDBACK-DRIVEN OASLM

Consider the model for the system depicted in Fig. 4.7. Here, the single-PS-layer OASLM operates in the phase modulation regime (OASLM rotation angle $\psi = m\pi$ where $m \in \mathbb{Z}$) under simultaneous blue and green laser illumination, and the blue light is reflected from the dichroic mirror (the corresponding reflective index is R) to form optical feedback and potentially coupling. It is assumed that the PS's thickness is significantly smaller than the

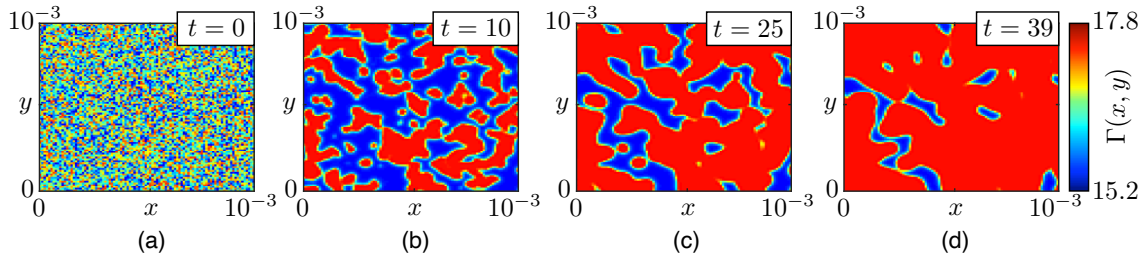


Figure 4.8: Coarsening in an OASLM as described by Eq. (4.8). The considered area is 1mm^2 . Parameters are: $\varepsilon = 1$, $\alpha_b = 0.117$, $\alpha_g = 0.985 \times 10^{-4}$, $\beta = 0.052$, $\gamma = -0.55$, $\phi_0 = \pi/2$, $\phi_1 = \pi$, $\lambda_b = 450 \times 10^{-9}$, $\lambda_g = 532 \times 10^{-9}$, $R = 0.95$, $I_{0b} = |\vec{E}_0|^2 = 0.01506$, $I_{0g} = 30.1$.

wavelength. In contrast to the model described by Eq. (2.33) and depicted in Fig. 2.20 (b), the spatial model of the setup in Fig. 4.7 contains two optical lenses to create 4f-imaging of the OASLM's state back on itself after reflection by the mirror, and a defocusing lens within the optical feedback path. Defocusing leads to blurred imaging, as illustrated in Fig. 4.7, and its impact can be mathematically described as a convolution with a Gaussian of controllable width. Applying this to the system in Fig. 4.7, one obtains a spatial distribution of the returned light Jones vector $\vec{E}_2(x, y)$ as

$$\vec{E}_2(x, y) = \left(R \exp(\phi_1) \vec{E}_1(x, y) \right) * \left(\frac{1}{2\pi\sigma^2} \exp\left(-\frac{x^2}{2\sigma^2} - \frac{y^2}{2\sigma^2}\right) \right), \quad (4.7)$$

where the symbol '*' means the convolution and Gaussian function plays a role of a point spread function widened from the normal imaging setup via the defocusing lens.

To simplify the model, diffusive processes inside the OASLM discussed in Chap. 2 are neglected and parameter σ in Eq. (4.7) is assumed to be several times greater than the OASLM resolution, $\sigma_{\text{OASLM}} = 3.5\mu\text{m}$ (see Sec. 2.3). In such a case, the model equations take the form

$$\begin{aligned} \vec{E}_0(x, y) &= \begin{bmatrix} E_0 \\ 0 \end{bmatrix}, & \vec{E}_1(x, y) &= \exp(i(\phi_0 + \Gamma(x, y))) \begin{bmatrix} E_0 \\ 0 \end{bmatrix}, \\ \vec{E}_2(x, y) &= \left(R \exp(\phi_1) \vec{E}_1(x, y) \right) * \left(\frac{1}{2\pi\sigma^2} \exp\left(-\frac{x^2}{2\sigma^2} - \frac{y^2}{2\sigma^2}\right) \right), \\ \vec{E}_3(x, y) &= R \exp(i(2\phi_0 + \phi_1 + 2\Gamma(x, y))) \begin{bmatrix} E_0 \\ 0 \end{bmatrix}, & I_b(x, y) &= \left| \vec{E}_0(x, y) + \vec{E}_3(x, y) \right|^2, \\ \varepsilon \frac{d\Gamma(x, y)}{dt} &= -\Gamma(x, y) + \frac{1}{\alpha_b I_b(x, y) + \frac{\lambda_g}{\lambda_b} \alpha_g I_{0g} + \beta} + \gamma. \end{aligned} \quad (4.8)$$

The action of the convolution operation is associated with homogenous coupling of the system state at any point on the plane (x, y) with its neighbour states in some range $x \in [x - \Delta x; x + \Delta x]$, $y \in [y - \Delta y; y + \Delta y]$. If the coupling radius does not exceed the

OASLM's linear pixel size, one deals with local coupling, whose impact is identical to the action of diffusion. Then one can expect to observe the effects of wave propagation and coarsening in Eq. (4.8), where the system parameters correspond to the regime of bistability. Moreover, the effects are expected to occur in a similar way as compared to the phenomenological model described by Eq. (4.1). These assumptions have been confirmed in numerical simulations starting from random initial conditions [Fig. 4.8]. It is discussed in the further sections how to control these effects.

4.3/ DETERMINISTIC COARSENING CONTROL

4.3.1/ PITCHFORK BIFURCATION CONDITIONS

Let us fix light intensities $I_{0g} = 22$, $I_{0b} = |\vec{E}_0|^2 = 0.01506$ in Eq. (4.8), while the other parameters are the same as in the previous section. This parameter set corresponds to the regime of bistability, but the pitchfork bifurcation conditions derived for the corresponding single-oscillator model (see Sec. 3.4) are not fulfilled and the right-hand side function of

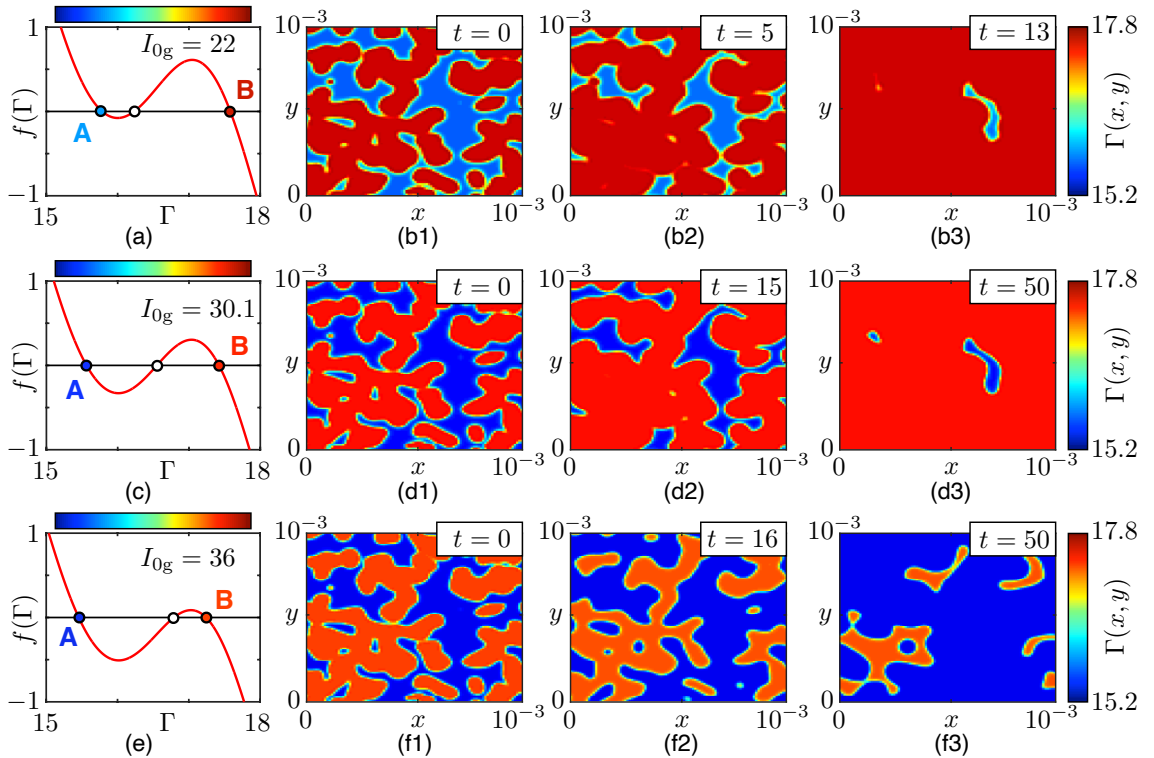


Figure 4.9: Evolution of the right-hand side function of Eq. (2.33) and coarsening in Eq. (4.8) for increasing green light intensity: $I_{0g} = 22$ (panels (a) and (b)), $I_{0g} = 30.1$ (panels (c) and (d)), $I_{0g} = 36$ (panels (e) and (f)). Other parameters are: $\varepsilon = 1$, $\alpha_b = 0.117$, $\alpha_g = 0.985 \times 10^{-4}$, $\beta = 0.052$, $\gamma = -0.55$, $\phi_0 = \pi/2$, $\phi_1 = \pi$, $\lambda_b = 450 \times 10^{-9}$, $\lambda_g = 532 \times 10^{-9}$, $R = 0.95$, $I_{0b} = 0.01506$, $\sigma = 10^{-5}$.

Eq. (2.33) is asymmetric, see Fig. 4.9 (a). In that case, the spatially extended model described by Eq. (4.8) exhibits the effect of coarsening, see Fig. 4.9 (b1-b3). The system asymmetry is reflected in the fact that the basin of attraction of state B is larger than the one of state A, and the unstable fixed point is closer to attractor A than to the stable steady state B. The domination of dynamics by state B results in the spatial evolution of Eq. (4.8) such that the red domains corresponding to state B extend and invade the whole space (x,y) , see Fig. 4.9 (b1-b3).

Increasing I_{0g} allows to fulfil the pitchfork bifurcation conditions at $I_{0g} \approx 30.1$, for which the asymmetry the right-hand side function $f(\Gamma)$ is removed, see Fig. 4.9 (c), and coarsening is substantially slower. Consequently, a longer time is necessary for the transformation of the same initial metastable state as in Fig. 4.9 (b1) (the initial spatial states in Fig. 4.9(b1,d1,f1) are identical) into the quiescent regime when either steady state A or B invades the whole space, see Fig. 4.9 (d1-d3). It must be noted that in the case of minimal asymmetry the probabilities to observe the final state $\Gamma(x,y) = A$ or $\Gamma(x,y) = B$ starting from random initial conditions is similar.

If one continues to increase the green light intensity, the phase space structure in comparison with the initial configuration is inverted, as can be seen from comparison of $f(\Gamma)$ in Fig. 4.9(a,e). The motion of fronts separating domains reverses, and coarsening has the opposite effect: steady state A invades the whole space, see Fig. 4.9(f1-f3).

4.3.2/ SADDLE-NODE BIFURCATION CONDITIONS

Varying I_{0b} and I_{0g} according to the curve obtained using the saddle-node bifurcation conditions, see Eqs. (3.56) and (3.57), allows to move the right-hand side function of Eq. (2.33) up and down, see Fig. 4.10 (a,c,e). A symmetric configuration of $f(\Gamma)$ can be achieved, see Fig. 4.10 (c), and the same effects as in the previous section can be observed. First, the system asymmetry is well-pronounced, as illustrated in Fig. 4.10 (a), and the state B rapidly invades the space (x,y) , see Fig. 4.10 (b1-b3). When I_{0b} and I_{0g} are adjusted such that the saddle-node bifurcation conditions are fulfilled, the system passes through the symmetric state [Fig. 4.10 (c)], and the coarsening effect maximally slows down, see Fig. 4.10 (d1-d3). Further changing I_{0b} and I_{0g} inverts the asymmetry [Fig. 4.10 (e)] and the motion of fronts separating blue and red domains reverses its direction, see Fig. 4.10 (f1-f3).

4.4/ STOCHASTIC COARSENING CONTROL

Consider a stochastic model of the optical setup in Fig. 4.7. For that purpose, it is assumed that the green light illumination contains a stochastic contribution according to $I_{0g}(x,y) = I_{0g} + \xi(x,y)$. Here, $\xi(x,y)$ represents a source of spatial coloured noise described

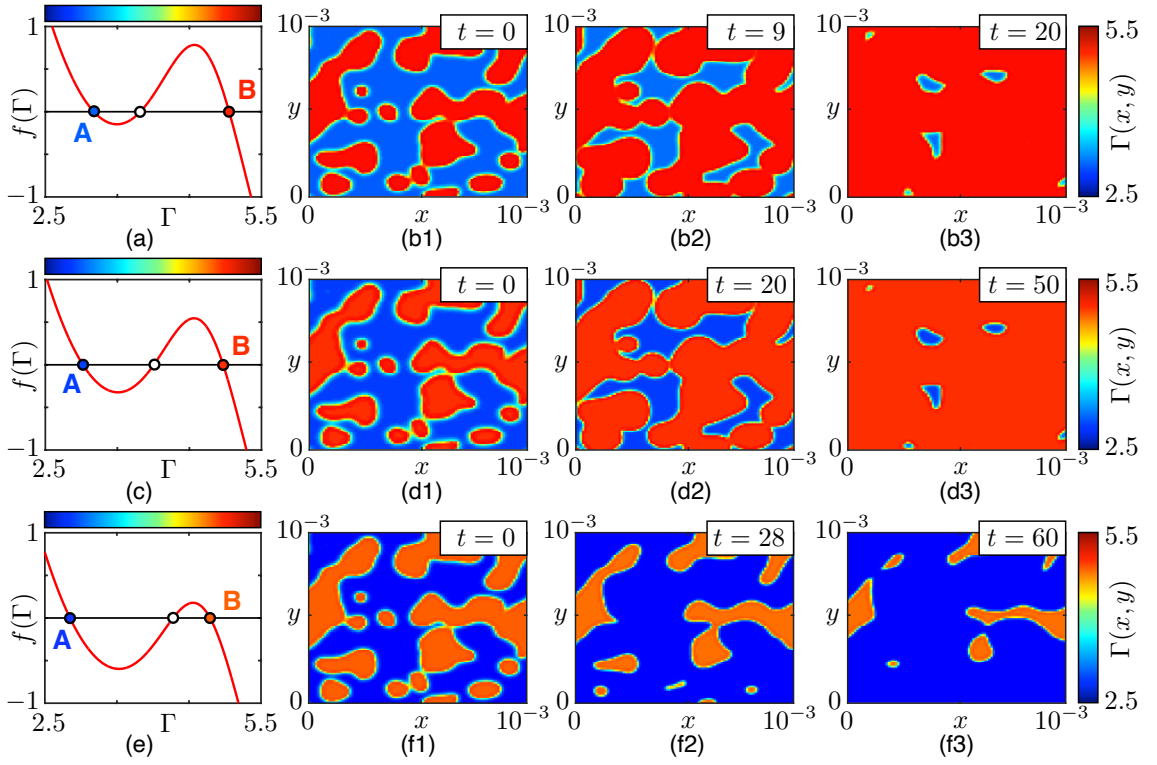


Figure 4.10: Evolution of the right-hand side function of Eq. (2.33) and coarsening in Eq. (4.8) when I_{0b} and I_{0g} vary according to the saddle-node bifurcation conditions for Eq. (2.33) (see Sec. 3.4): $I_{0b} = 0.228$, $I_{0g} = 990$ (panels (a) and (b)), $I_{0b} = 0.241$, $I_{0g} = 1050$ (panels (c) and (d)), $I_{0b} = 0.2645$, $I_{0g} = 1153$ (panels (e) and (f)). Other parameters are: $\varepsilon = 1$, $\alpha_b = 0.117$, $\alpha_g = 0.985 \times 10^{-4}$, $\beta = 0.052$, $\gamma = -0.55$, $\phi_0 = \pi/2$, $\phi_1 = \pi$, $\lambda_b = 450 \times 10^{-9}$, $\lambda_g = 532 \times 10^{-9}$, $R = 0.95$, $\sigma = 10^{-5}$.

by the first-order Ornstein-Uhlenbeck process

$$\tau_c \frac{d\xi(x, y)}{dt} = -\xi(x, y) + \sqrt{2D_g \tau_c} n(x, y, t), \quad (4.9)$$

where τ_c is the coloured noise correlation time, $n(x, y, t)$ is a normalized source of white Gaussian noise, D_g plays a role of the noise intensity. The temporal and spatial correlation properties of the noise source $n(x, y, t)$ at any point \vec{r}_0 are described by the delta function: $\langle n(\vec{r}_0, t) \rangle = 0$, $\langle n(\vec{r}_0, t) n(\vec{r}_0, t + \tau) \rangle = \delta(\tau)$, $\langle n(\vec{r}_0, t) n(\vec{r}_0 + \vec{r}_d, t) \rangle = \delta(\vec{r}_d)$ (here, the brackets $\langle \dots \rangle$ denote the mean value), which means that the correlation time of the source $n(x, y, t)$ equals zero and the noise signal values $n(x, y, t)$ at any different points (x_1, y_1) and (x_2, y_2) are statistically independent.

Similarly to the presence of a stochastic contribution in green light, one can consider the presence of random blue illumination: $I_{0b}(x, y) = I_{0b} + \xi(x, y)$ or $\vec{E}_0(x, y) = \begin{bmatrix} E_0 + \xi(x, y) \\ 0 \end{bmatrix}$. This case is more complicated, since the resulting blue light intensity at the OASLM PS-layer contains the stochastic component, which in turn depends on the instantaneous

state Γ , and as a consequence blue illumination noise becomes multiplicative. The third way to naturally introduce noise into the model under study is to suppose that the voltage applied across the OASLM comprises a constant DC-power signal and a noise generator signal. As the voltage equally addresses all spatial positions, all LC-layer molecules are driven by the same random forcing and the corresponding model describes the dynamics under common noise $\xi(t)$.

Physically, random spatial component $\xi(x, y)$ can be included into the green illumination by adding an electronically-addressed spatial light modulator that spatially modifies the green illumination. Regardless of technical implementation details, the spatial random illumination will be characterised by finite temporal correlation associated with finite response of the EASLMs and defined by the parameter τ_c . For this reason, the stochastic model of the setup in Fig. 4.7 implies the presence of coloured noise. It is assumed in the following that the noise correlation time τ_c is much smaller than the OASLM response time ε . In addition, all the instantaneous values $\xi(x, y, t) < -I_{0g}$ are changed to $\xi(x, y, t) = -I_{0g}$ since the summary green light intensity $I_{0g} + \xi(x, y, t)$ cannot be negative. Finally, the stochastic spatial model of the setup in Fig. 4.7 takes the form

$$\begin{aligned} \vec{E}_0(x, y) &= \begin{bmatrix} E_0 \\ 0 \end{bmatrix}, & \vec{E}_1(x, y) &= \exp(i(\phi_0 + \Gamma(x, y))) \begin{bmatrix} E_0 \\ 0 \end{bmatrix}, \\ \vec{E}_2(x, y) &= \left(R \exp(\phi_1) \vec{E}_1(x, y) \right) * \left(\frac{1}{2\pi\sigma^2} \exp\left(-\frac{x^2}{2\sigma^2} - \frac{y^2}{2\sigma^2}\right) \right), \\ \vec{E}_3(x, y) &= R \exp(i(2\phi_0 + \phi_1 + 2\Gamma(x, y))) \begin{bmatrix} E_0 \\ 0 \end{bmatrix}, & I_b(x, y) &= \left| \vec{E}_0(x, y) + \vec{E}_3(x, y) \right|^2, \quad (4.10) \\ \varepsilon \frac{d\Gamma(x, y)}{dt} &= -\Gamma(x, y) + \frac{1}{\alpha_b I_b(x, y) + \frac{\lambda_g}{\lambda_b} \alpha_g (I_{0g} + \xi(x, y)) + \beta} + \gamma, \\ \tau_c \frac{d\xi(x, y)}{dt} &= -\xi(x, y) + \sqrt{2D_g \tau_c} n(x, y, t). \end{aligned}$$

First, Eq. (4.10) is considered for a set of parameters corresponding to Fig. 4.9 (a) when the basin of attraction of steady state B is larger than the basin of state A. Then, Eq. (4.10) exhibits the effect of coarsening and the system state $\Gamma(x, y) = B$ invades the whole space in the absence of noise, $D_g = 0$ (see Fig. 4.11 (a-c)). Increasing noise intensity D_g , one slows down the effect of coarsening, see Fig. 4.11 (d-f), and above a threshold of $D \approx 3.7 \times 10^3$, noise inverts the front propagation dynamics and state A dominates, see Fig. 4.11 (g-i).

Similarly, if the system parameter set corresponds to Fig. 4.9 (e), one observes invading state A [Fig. 4.12 (a-c)]. In such a case increasing the noise intensity speeds up the

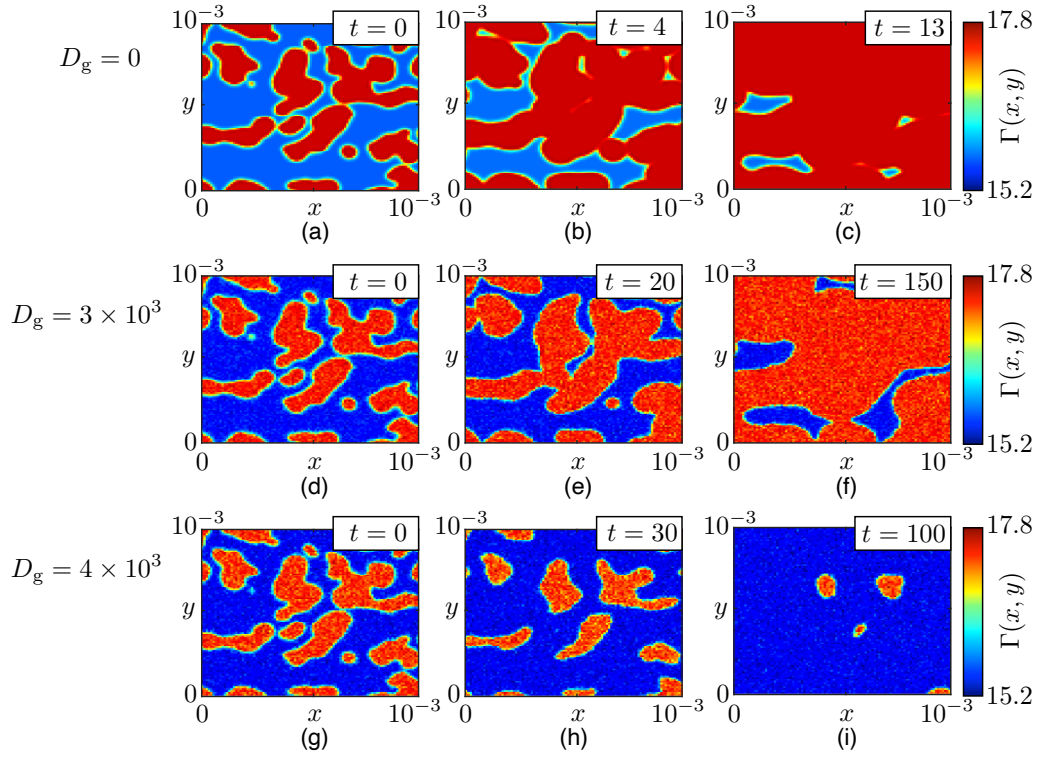


Figure 4.11: Coarsening in Eq. (4.10) for increasing noise intensity: $D_g = 0$ (panels (a-c)), $D_g = 3 \times 10^3$ (panels (d-f)), $D_g = 4 \times 10^3$ (panels (g-i)). Other parameters are: $\varepsilon = 1$, $\alpha_b = 0.117$, $\alpha_g = 0.985 \times 10^{-4}$, $\beta = 0.052$, $\gamma = -0.55$, $\phi_0 = \pi/2$, $\phi_1 = \pi$, $\lambda_b = 450 \times 10^{-9}$, $\lambda_g = 532 \times 10^{-9}$, $R = 0.95$, $I_{0b} = |\vec{E}_0|^2 = 0.01506$, $I_{0g} = 22$, $\sigma = 10^{-5}$, $\tau_c = 0.01$.

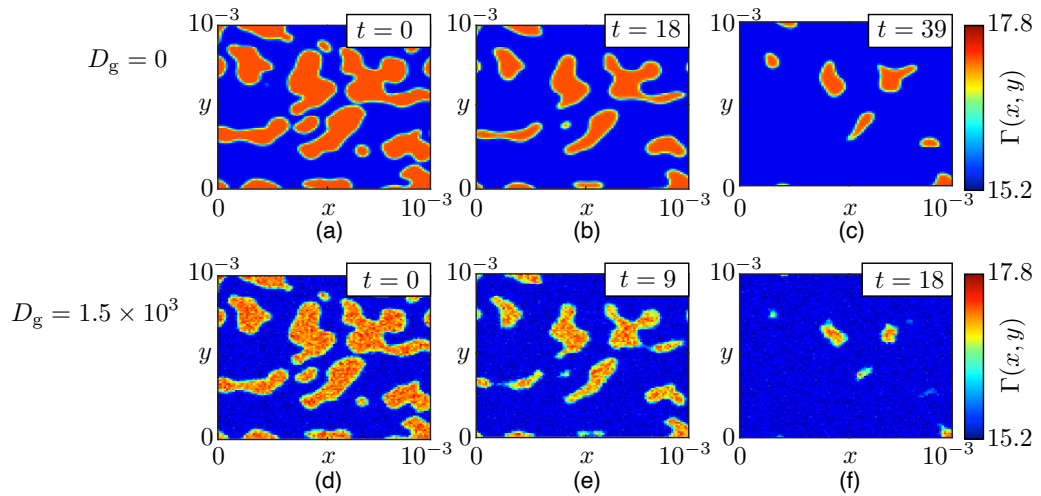


Figure 4.12: Coarsening in Eq. (4.10) for increasing noise intensity: $D_g = 0$ (panels (a-c)), $D_g = 1.5 \times 10^3$ (panels (d-f)). Other parameters are: $\varepsilon = 1$, $\alpha_b = 0.117$, $\alpha_g = 0.985 \times 10^{-4}$, $\beta = 0.052$, $\gamma = -0.55$, $\phi_0 = \pi/2$, $\phi_1 = \pi$, $\lambda_b = 450 \times 10^{-9}$, $\lambda_g = 532 \times 10^{-9}$, $R = 0.95$, $I_{0b} = |\vec{E}_0|^2 = 0.01506$, $I_{0g} = 36$, $\sigma = 10^{-5}$, $\tau_c = 0.01$.

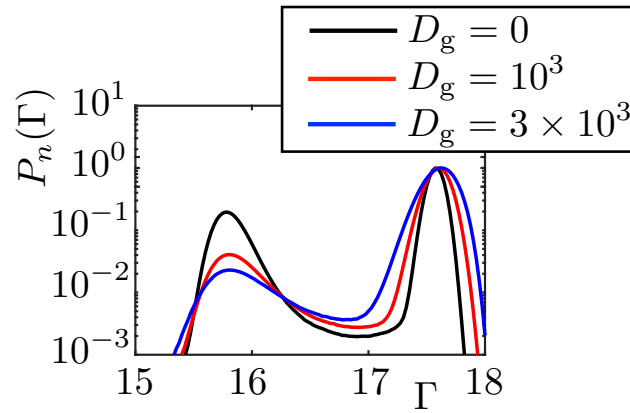


Figure 4.13: Evolution of the normalised probability density function $P_n(\Gamma)$ caused by the varying noise intensity D_g in Eq. (4.11). Parameters are: $\varepsilon = 1$, $\alpha_b = 0.117$, $\alpha_g = 0.985 \times 10^{-4}$, $\beta = 0.052$, $\gamma = -0.55$, $\phi_0 = \pi/2$, $\phi_1 = \pi$, $\lambda_b = 450 \times 10^{-9}$, $\lambda_g = 532 \times 10^{-9}$, $R = 0.95$, $I_{0b} = 0.01506$, $I_{0g} = 22$, $\tau_c = 0.01$.

process [Fig. 4.12 (d-f)]. Thus, it is demonstrated in Fig. 4.11 and Fig. 4.12 that, depending on the particular system configuration, noise can speed up coarsening, slow it down or to invert the process.

The theoretical explanation of the stochastic coarsening control in OASLM-based spatial models using the 'Small-Noise-Expansion approach' discussed in Sec. 4.1.2 seems to be significantly more difficult in comparison with the explanations presented in Refs. [178, 199] on the examples of basic reaction-diffusion models with multiplicative noise. This is due to the fact that any polynomial expression of Eq. (4.10) is challenging to obtain, and, will furthermore give rise to stochastic terms in all the polynomial components. Consequently, it becomes impossible to distinguish the systematic part of the noise influence. However, the similarity between the processes observed in the basic models used in references [178, 198, 199] and in OASLM-based spatial model described by Eq. (4.10) is evident. To visualise the fact that stochastic forcing has an asymmetric impact on Eq. (4.10), a single-oscillator stochastic model corresponding to Eq. (4.10) at $\sigma \rightarrow 0$ is taken into consideration. If $\sigma \rightarrow 0$, the spatial coupling is absent and the retardation Γ individually evolves according to Eq. (2.33) at each point of the illuminated area, but in the presence of the noise term ξ

$$\varepsilon \frac{d\Gamma}{dt} = -\Gamma + \frac{1}{\alpha_b I_b + \frac{\lambda_g}{\lambda_b} \alpha_g (I_{0g} + \xi) + \beta} + \gamma + \sqrt{0.02} n_a(t),$$

$$\tau_c \frac{d\xi}{dt} = -\xi + \sqrt{2D_g \tau_c} n(t),$$
(4.11)

$$I_b = I_{0b} \{1 + R^2 + 2R \cos(2\phi_0 + \phi_1 + 2\Gamma)\},$$

where the additive white Gaussian noise term $\sqrt{0.02} n_a(t)$ used to obtain the PDF has no

impact on the system's symmetry and is included to obtain a stationary distribution of the normalised probability density function for the dynamical variable, $P_n(\Gamma)$, in numerical simulations. The evolution of $P_n(\Gamma)$ caused by increasing noise intensity D_g illustrated in Fig. 4.13 indicates that the left peak gets smeared out faster than the right one. Thus, the action of noise $\xi(t)$ is significantly stronger in the vicinity of the left steady state $\Gamma_* = A$. This effect is similar to the noise-induced evolution of $P_n(u)$ in the phenomenological model defined by Eq. (4.6) (compare Fig. 4.6 and Fig. 4.13).

4.5/ CONCLUSION

The spatial model of the OASLM with mirror feedback takes into consideration the impact of a defocusing lens. Defocusing represents a natural physical approach for the homogeneous coupling implementation similarly to diffusive effects occurring inside the OASLM. But in contrast to the internal diffusive processes in the OASLM which were neglected, one can control the coupling radius by moving the defocusing lens of the dichroic mirror.

Bifurcation transitions to the bistable dynamics discussed in Chap. 2 and 3 in the context of single-oscillator models, are reflected in the behaviour of the corresponding spatially-extended systems, as for example in Eq. (4.8) or similar models corresponding to different OASLM's rotation angles or incident light polarization states, as formation of localized spatial domains corresponding to the attraction of two coexisting steady states. Then, if the system right-hand side function is asymmetric, the steady state characterized by the larger basin of attraction, invades the entire space. This process is accompanied by the effect of coarsening, which is determined by both asymmetry and the shape of evolving domains.

Applying the saddle-node or pitchfork bifurcation conditions derived in Chap. 3, one can remove the system asymmetry and then the dominating domain expansion is slowed down. Moreover, if the incident green and blue light intensities vary and obey the saddle-node bifurcation condition, one can controllably invert the front propagation direction. However, the saddle-node bifurcation conditions do not allow to rigorously define the absolutely symmetric state, while applying the pitchfork bifurcation conditions provide for mathematical derivation of appropriate parameter values.

The second approach to control coarsening is the introduction of noise into the system. In particular, the presence of parametric noise modulating the green light intensity gives rise to slowing down and inverting the effects of front propagation and coarsening. The ability to control the dynamics by increasing noise intensity strength is explained by the fact that fluctuation growth changes the system symmetry.

OASLM FOR ISING MACHINE IMPLEMENTATIONS

The spatial OASLM-based model considered in the previous chapters implies the action of homogenous coupling. Introducing additional optical devices in between the OASLM and the dichroic mirror, one can experimentally realize a wide range of coupling topologies. If the coupling element provides for the coupling weight control, it offers great opportunities for photonic neural network implementations, for example see the seminal work by Farhat et al. who implemented a Hopfield network [159]. A broad variety of potential applications includes classical machine learning tasks such as time series reconstruction and pattern recognition as well as combinatorial optimization problems. Particularly, the application to combinatorial problems is discussed in this chapter in the context of implementing a photonic Ising machine. Here, we address the question whether an OASLM can be used for the photonic Ising machine. In other words, the main discussed question is 'can the dynamical equations of an OASLM with optical feedback be transformed into the form of an Ising-model?'.

5.1/ OASLM-BASED MODEL UNDER STUDY

During the process of developing the OASLM-based model for any configuration in Chap. 2 it became clear that the resulting equations became very complex. For this reason, the first steps to derive an OASLM-based Ising machine are focused on identifying a experimental and hardware configuration which could significantly simplify the dynamical equations of the system. The most appropriate configuration is depicted in Fig. 5.1, where the OASLM operates in the amplitude modulation regime ($\psi = \pi/4$). In contrast to the previous hardware configurations, here a single PS-layer is situated on the right side of the OASLM. Again, here we consider a PS with a thickness being significantly smaller than the wavelength. Furthermore, we here assume that the PS-layer's conductivity depends on the polarization state of the resulting summary light, hence acts as a polariza-

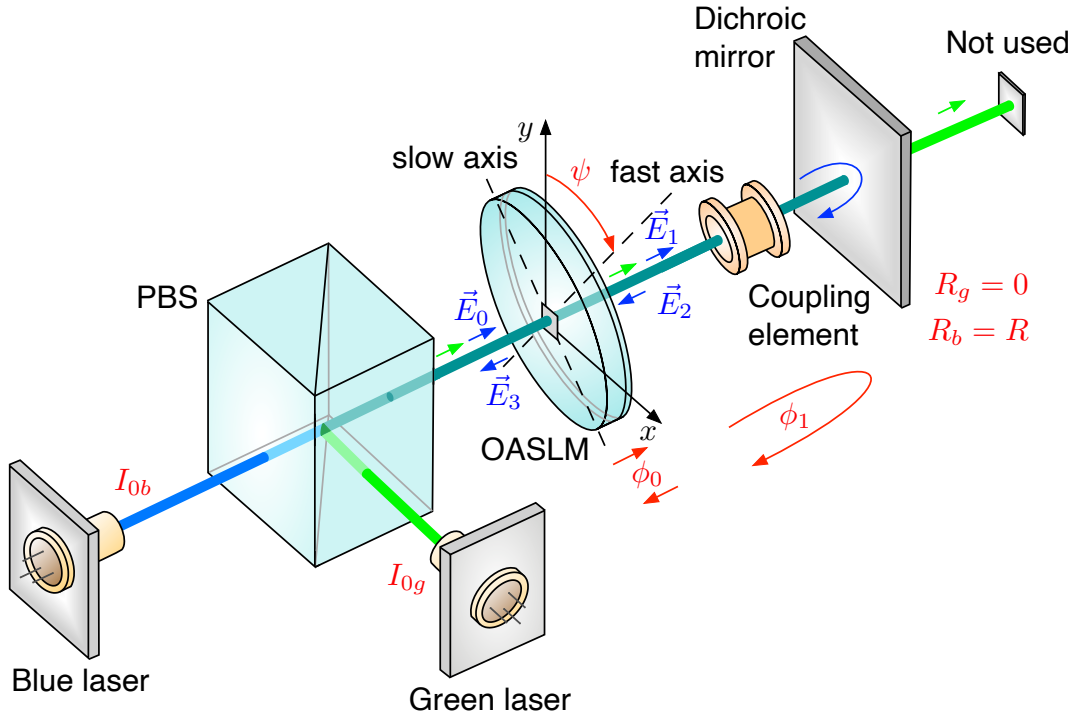


Figure 5.1: Single-PS-layer OASLM under simultaneous blue and green illumination when the blue light beam is reflected by the dichroic mirror and creates feedback. In contrast to Fig. 4.7, the PS-layer is polarization-sensitive and situated on the right side of the OASLM.

tion sensitive detector. Consequently, the retardation induced by the OASLM depends only on the vertical component of the optical intensity at the PS-layer. Such anisotropic photosensitive films, characterised by a periodic grating structure of their surface, have been recently demonstrated in Refs. [200–202], and we assume that for example similar nano-structuring of the chalcogenide PS layer could induce similar polarization sensitivity for our device. However, these are assumptions and need to be confirmed independently; the focus on this chapter is proposing an OASLM with particular properties and to demonstrate that it can serve as a simulator of an Ising model. Finally, we assume that the OASLM fully transmits the horizontally polarized light.

5.1.1/ SINGLE-OSCILLATOR MODEL

Consider the optical setup in Fig. 5.1 for the injected blue light polarization state $\vec{E}_0 = \begin{bmatrix} E_0 \\ 0 \end{bmatrix}$. For the single-oscillator mode, the Jones vectors for the blue light fields

$\vec{E}_{1,2,3}$ are

$$\begin{aligned}\vec{E}_1 &= E_0 \exp(i\phi_0) \begin{bmatrix} \cos(\Gamma) \\ i \sin(\Gamma) \end{bmatrix}, & \vec{E}_2 &= RE_0 \exp(i(\phi_0 + \phi_1)) \begin{bmatrix} \cos(\Gamma) \\ i \sin(\Gamma) \end{bmatrix}, \\ \vec{E}_3 &= RE_0 \exp(i(2\phi_0 + \phi_1)) \begin{bmatrix} \cos(2\Gamma) \\ i \sin(2\Gamma) \end{bmatrix}.\end{aligned}\quad (5.1)$$

If the blue light is coherent, the combined blue light field at the right PS layer takes the form

$$\vec{E}_{\text{right}} = \begin{bmatrix} E_x^{\text{right}} \\ E_y^{\text{right}} \end{bmatrix} = \vec{E}_1 + \vec{E}_2 = E_0(\exp(i\phi_0) + R \exp(i(\phi_0 + \phi_1))) \begin{bmatrix} \cos(\Gamma) \\ i \sin(\Gamma) \end{bmatrix}. \quad (5.2)$$

However, the blue light phase retardation is determined only by the vertical component, $\Gamma = \Gamma(|E_y^{\text{right}}|^2)$. Following the procedures described in the second chapter, one obtains the expression for the retardation $|E_y^{\text{right}}|^2 = I_{0b} \sin^2(\Gamma)(1 + R^2 + 2R \cos(\phi_1))$ and the dynamical system equation takes the form

$$\varepsilon \frac{d\Gamma}{dt} = -\Gamma + \frac{1}{\alpha_b |E_y^{\text{right}}|^2 + \frac{\lambda_g}{\lambda_b} \alpha_g I_{0g} + \beta} + \gamma, \quad (5.3)$$

$$|E_y^{\text{right}}|^2 = I_{0b} \sin^2(\Gamma) \{1 + R^2 + 2R \cos(\phi_1)\}.$$

Equations (5.3) can be simplified using the assumption that OASLM's response is linear as in Sec. 2.10: $\Gamma = \Gamma_* - \kappa |E_y^{\text{right}}|^2$, which for the case of coherent illumination results in

$$\begin{aligned}\varepsilon \frac{d\Gamma}{dt} &= -\Gamma + \Gamma_* - \kappa I_{0b} \sin^2(\Gamma) \{1 + R^2 + 2R \cos(\phi_1)\}, \\ \Gamma_* &= \left(\frac{\lambda_g}{\lambda_b} \alpha_g I_{0g} + \beta \right)^{-1} + \gamma.\end{aligned}\quad (5.4)$$

In such a case, the nonlinearity is fully determined by $\sin^2(\Gamma)$, and the model takes the Ikeda-like oscillator form.

Equation (5.4) describes the situation for coherent illumination, for which the intensity at the PS-layer is $|\vec{E}_1 + \vec{E}_2|^2$. If, however, the illumination is incoherent, then the overall light intensity is not determined by the coherent sum, but instead by $|\vec{E}_{1x}|^2 + |\vec{E}_{1y}|^2 + |\vec{E}_{2x}|^2 + |\vec{E}_{2y}|^2$. Since the OASLM PS-layer is sensitive only to the vertical polarization component of the illuminating light, the retardation becomes $\Gamma = \Gamma(|\vec{E}_{1y}|^2 + |\vec{E}_{2y}|^2)$ and the expression for the intensity controlling the OASLM state is $I_b = I_{0b} \sin^2(\Gamma) \{1 + R^2\}$. Then the model for linear

OASLM's response for the case of incoherent illumination becomes

$$\begin{aligned} \varepsilon \frac{d\Gamma}{dt} &= -\Gamma + \Gamma_* - \kappa I_{0b} \sin^2(\Gamma) \{1 + R^2\}, \\ \Gamma_* &= \left(\frac{\lambda_g}{\lambda_b} \alpha_g I_{0g} + \beta \right)^{-1} + \gamma. \end{aligned} \quad (5.5)$$

5.1.2/ NETWORK MODEL

5.1.2.1/ COHERENT ILLUMINATION

Suppose that a coherent light beam illuminating the OASLM (see Fig. 5.1) are spatially distributed. Under such conditions, the horizontally polarised incident blue light can be described via its spatially discretized field distribution on the PS's surface, using a set of N pixels, and its optical field at different positions can then be expressed in the form of the two n -dimensional vectors

$$\vec{E}_{0x} = \begin{bmatrix} E_0 \\ \vdots \\ E_0 \end{bmatrix}, \quad \vec{E}_{0y} = \begin{bmatrix} 0 \\ \vdots \\ 0 \end{bmatrix}. \quad (5.6)$$

It is assumed that the pixels are large enough such that the diffusive processes occurring inside the OASLM, see Chap. 2, can be excluded. Since the OASLM is operated in the amplitude modulation regime, the light passing through the OASLM at any pixel of the illuminated area is

$$\vec{E}_{1x} = E_0 \exp(i\phi_0) \cos(\vec{\Gamma}), \quad \vec{E}_{1y} = E_0 \exp(i\phi_0) i \sin(\vec{\Gamma}), \quad (5.7)$$

where $\vec{\Gamma}$ is a $1 \times N$ vector of local retardation values at particular pixels, i.e. $\vec{\Gamma}$ is the N -dimensional spatial birefringence distribution of the OASLM.

When placing a coupling element between OASLM and the dichroic mirror, the expressions for the optical feedback field \vec{E}_2 components become

$$\begin{aligned} \vec{E}_{2x} &= E_0 R \exp(i(\phi_0 + \phi_1)) \{W \times \cos(\vec{\Gamma})\}, \\ \vec{E}_{2y} &= i E_0 R \exp(i(\phi_0 + \phi_1)) \{W \times \sin(\vec{\Gamma})\}, \end{aligned} \quad (5.8)$$

where \mathbf{W} is a $N \times N$ coupling matrix without birefringence, $\sin(\vec{\Gamma})$ and $\cos(\vec{\Gamma})$ are $1 \times N$ vectors. The products $\{W \times \sin(\vec{\Gamma})\}$ and $\{W \times \cos(\vec{\Gamma})\}$ are $1 \times N$ vectors of elements $\{W \times \sin(\vec{\Gamma})\}_k = \sum_{l=1}^N W_{k,l} \sin(\Gamma_l)$ and $\{W \times \cos(\vec{\Gamma})\}_k = \sum_{l=1}^N W_{k,l} \cos(\Gamma_l)$, respectively. The resulting

light field components at the PS-layer $\vec{E}_s = \vec{E}_1 + \vec{E}_2$ therefore becomes

$$\begin{aligned}\vec{E}_{sx} &= E_0 \exp(i\phi_0) \left(\cos(\vec{\Gamma}) + R \exp(i\phi_1) \{W \times \cos(\vec{\Gamma})\} \right), \\ \vec{E}_{sy} &= iE_0 \exp(i\phi_0) \left(\sin(\vec{\Gamma}) + R \exp(i\phi_1) \{W \times \sin(\vec{\Gamma})\} \right).\end{aligned}\quad (5.9)$$

The phase retardation of the blue light is determined by the vertical component of the intensity at the PS, hence, $\Gamma = \Gamma \left(|E_{sy}|^2 \right)$, and finally the network's dynamical equation for oscillator k become

$$\begin{aligned}\varepsilon \frac{d\Gamma_k}{dt} &= -\Gamma_k + \frac{1}{\alpha_b I_k^b + \frac{\lambda_g}{\lambda_b} \alpha_g I_{0g} + \beta} + \gamma, \\ I_k^b &= I_{0b} \left(\sin^2(\Gamma_k) + R^2 \{W \times \sin(\vec{\Gamma})\}_k^2 + 2R \{W \times \sin(\vec{\Gamma})\}_k \sin(\Gamma_k) \cos(\phi_1) \right).\end{aligned}\quad (5.10)$$

For $\phi_1 = 0$ the model simplifies into

$$\begin{aligned}\varepsilon \frac{d\Gamma_k}{dt} &= -\Gamma_k + \frac{1}{\alpha_b I_k^b + \frac{\lambda_g}{\lambda_b} \alpha_g I_{0g} + \beta} + \gamma, \\ I_k^b &= I_{0b} \left(\sin(\Gamma_k) + R \left\{ \sum_{l=1}^N W_{k,l} \sin(\Gamma_l) \right\} \right)^2.\end{aligned}\quad (5.11)$$

Some further simplification can be achieved under the assumption of the linear OASLM response (similarly applied in the previous section for the single-oscillator model)

$$\begin{aligned}\varepsilon \frac{d\Gamma_k}{dt} &= -\Gamma_k + \Gamma_* - \kappa I_{0b} \left(\sin^2(\Gamma_k) + 2R \sin(\Gamma_k) \left\{ \sum_{l=1}^N W_{k,l} \sin(\Gamma_l) \right\} + R^2 \left\{ \sum_{l=1}^N W_{k,l} \sin(\Gamma_l) \right\}^2 \right), \\ \Gamma_* &= \left(\frac{\lambda_g}{\lambda_b} \alpha_g I_{0g} + \beta \right)^{-1} + \gamma.\end{aligned}\quad (5.12)$$

5.1.2.2/ INCOHERENT ILLUMINATION

Suppose that the blue illumination is incoherent. In such a case all the phase relationships inducing interference between the fields of different oscillators disappear. The expressions for intensities are transformed from the coherent-light form of squares-of-sums $\left| \sum_{k=1}^N \vec{E}_k \right|^2$ to the incoherent form of sum-of-squares $\sum_{k=1}^N |\vec{E}_k|^2$. The phase retardation becomes $\Gamma = \Gamma \left(|E_{1y}|^2 + |E_{2y}|^2 \right)$ and the network model takes the form

$$\begin{aligned}\varepsilon \frac{d\Gamma_k}{dt} &= -\Gamma_k + \frac{1}{\alpha_b I_k^b + \frac{\lambda_g}{\lambda_b} \alpha_g I_{0g} + \beta} + \gamma, \\ I_k^b &= I_{0b} \left(\sin^2(\Gamma_k) + R^2 \left\{ \sum_{l=1}^N W_{k,l}^2 \sin^2(\Gamma_l) \right\} \right),\end{aligned}\quad (5.13)$$

which can be rewritten for the linearized OASLM-response

$$\begin{aligned} \varepsilon \frac{d\Gamma_k}{dt} &= -\Gamma_k + \Gamma_* - \kappa I_{0b} \left(\sin^2(\Gamma_k) + R^2 \left\{ \sum_{l=1}^N W_{k,l}^2 \sin^2(\Gamma_l) \right\} \right), \\ \Gamma_* &= \left(\frac{\lambda_g}{\lambda_b} \alpha_g I_{0g} + \beta \right)^{-1} + \gamma, \end{aligned} \quad (5.14)$$

At this stage, the principal difference between given by Eqs. (5.12) and Eqs. (5.14) must be emphasized. Since the expression for the blue light intensity I_b in Eq. (5.12) is the square-of-sums of two terms, one obtains the additional term $2R \sin(\Gamma_k) \left\{ \sum_{l=1}^N W_{k,l} \sin(\Gamma_l) \right\}$, and crucially individual node dynamics according to, $\sin(\Gamma_k)$ are intertwined with the networks dynamics projected through the coupling matrix $\left\{ \sum_{l=1}^N W_{k,l} \sin(\Gamma_l) \right\}$. Thus, one cannot separate the terms determining the individual dynamics and network topology in Eq. (5.12). Meanwhile, the expression for the resulting intensity I_b in the coherent network model of Eqs. (5.14) is a sum of the local retardation value Γ_k and the coupling $R^2 \left\{ \sum_{l=1}^N W_{k,l}^2 \sin^2(\Gamma_l) \right\}$. That means the terms responsible for the individual dynamics and coupling in Eq. (5.14) can clearly be separated. This fact is important for the opportunity of photonic Ising machine implementations by using the OASLM, as the additional modifications appearing in the coherent network model can potentially modify the potential energy landscape of the system [80].

5.2/ PITCHFORK BIFURCATION CONDITIONS AND SPIN-NETWORK DYNAMICS

To represent the OASLM-based system as a network of interacting spins, the model equations are expressed in the form $\frac{dx_k}{dt} = bx_k + dx_k^3 + \sum_{k=1}^N J_{k,l} x_l$. The pitchfork bifurcation conditions derived by means of the Taylor series approximation are applied below for this purpose.

5.2.1/ INCOHERENT ILLUMINATION (FULL MODEL)

First, the pitchfork bifurcation conditions are derived for a single-oscillator model. For the incoherent illumination the model equations are

$$\varepsilon \frac{d\Gamma}{dt} = -\Gamma + \frac{1}{\alpha_b I_{0b} \sin^2(\Gamma) \{1 + R^2\} + \frac{\lambda_g}{\lambda_b} \alpha_g I_{0g} + \beta} + \gamma. \quad (5.15)$$

The equation right-hand side function $f(\Gamma)$ is represented by its Taylor series approximation $f_T(\Gamma)$ in the similar way as in Chap. 3

$$\begin{aligned}
 f(\Gamma) &= -\Gamma + \left(k \sin^2(\Gamma) + \frac{\lambda_g}{\lambda_b} \alpha_g I_{0g} + \beta \right)^{-1} + \gamma, \\
 f_T(\Gamma) &= a + b(\Gamma - \Gamma_0) + c(\Gamma - \Gamma_0)^2 + d(\Gamma - \Gamma_0)^3, \quad \text{where} \\
 a &= -\Gamma_0 + \left(k \sin^2(\Gamma_0) + \frac{\lambda_g}{\lambda_b} \alpha_g I_{0g} + \beta \right)^{-1} + \gamma, \\
 b &= -1 - k \sin(2\Gamma_0) \left(k \sin^2(\Gamma_0) + \frac{\lambda_g}{\lambda_b} \alpha_g I_{0g} + \beta \right)^{-2}, \\
 c &= -k \cos(2\Gamma_0) \left(k \sin^2(\Gamma_0) + \frac{\lambda_g}{\lambda_b} \alpha_g I_{0g} + \beta \right)^{-2} + k^2 \sin^2(2\Gamma_0) \left(k \sin^2(\Gamma_0) + \frac{\lambda_g}{\lambda_b} \alpha_g I_{0g} + \beta \right)^{-3}, \\
 d &= \frac{2}{3} k \sin(2\Gamma_0) \left(k \sin^2(\Gamma_0) + \frac{\lambda_g}{\lambda_b} \alpha_g I_{0g} + \beta \right)^{-2} + k^2 \sin(4\Gamma_0) \left(k \sin^2(\Gamma_0) + \frac{\lambda_g}{\lambda_b} \alpha_g I_{0g} + \beta \right)^{-3} \\
 &\quad - k^3 \sin^3(2\Gamma_0) \left(k \sin^2(\Gamma_0) + \frac{\lambda_g}{\lambda_b} \alpha_g I_{0g} + \beta \right)^{-4}, \\
 k &= \alpha_b I_{0b} \{1 + R^2\}.
 \end{aligned} \tag{5.16}$$

For further analysis one therefore obtains the pitchfork bifurcation conditions $a = 0$ and $c = 0$

$$a = 0 \Rightarrow \left(k \sin^2(\Gamma_0) + \frac{\lambda_g}{\lambda_b} \alpha_g I_{0g} + \beta \right)^{-1} = \Gamma_0 - \gamma, \tag{5.17}$$

$$c = 0 \Rightarrow -\cos(2\Gamma_0) + k \sin^2(2\Gamma_0)(\Gamma_0 - \gamma) = 0,$$

and the blue light intensity is expressed

$$I_{0b} = \frac{\cos(2\Gamma_0)}{\alpha_b \{1 + R^2\} \sin^2(2\Gamma_0)(\Gamma_0 - \gamma)}. \tag{5.18}$$

The green light intensity I_{0g} is expressed from the first pitchfork condition, $a = 0$

$$I_{0g} = \frac{\lambda_b}{\lambda_g} \frac{1}{\Gamma_0 - \gamma} - \frac{\alpha_b I_{0b} \{1 + R^2\} \sin^2(\Gamma_0) - \beta}{\alpha_g} \tag{5.19}$$

The expression for I_{0g} includes the parameter I_{0b} which is the one to be determined according to Eq. (5.18) as a function of Γ_0 . Thus, the green light intensity also is a function of Γ_0 . If the pitchfork bifurcation conditions are fulfilled, the Taylor series coefficient b takes the same form as for Eq. (2.28): $b = -1 - (\Gamma_0 - \gamma) \cot(2\Gamma_0)$. Following the same procedures as in Chap. (3) for different OASLM-based models, the curve $I_{0b}(I_{0g})$ corresponding to the pitchfork bifurcation conditions is obtained [Fig. 5.2 (a)]. If I_{0b} and I_{0g} vary according to the curve in Fig. 5.2 (a), one observes the pitchfork bifurcation [Fig. 5.2 (b-f)].

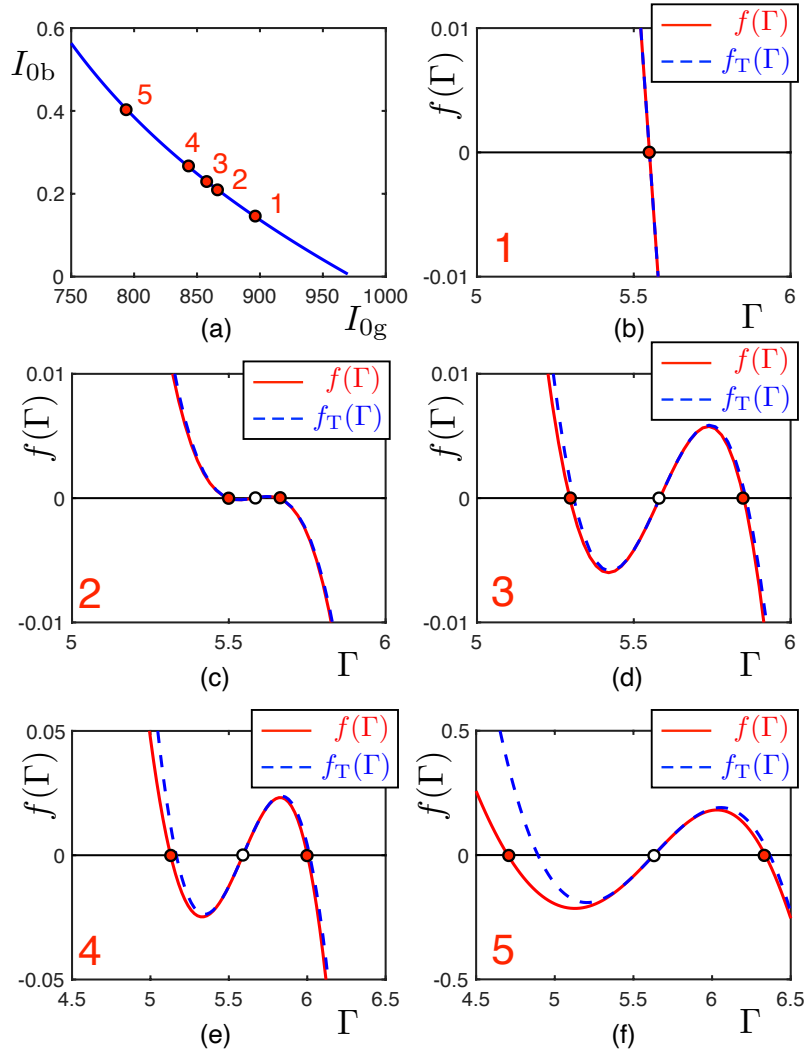


Figure 5.2: Pitchfork bifurcation in the incoherent network according to Eqs. (5.15) for the absence of the reflected feedback light ($R = 0$): (a) Dependence $I_{0b}(I_{0g})$ obtained from the pitchfork bifurcation conditions (see Exps. (5.18) and (5.19)); (b-f) Right-hand side function $f(\Gamma)$ (red solid curve) and its Taylor series approximation (5.16) (blue dashed curve) at control points 1-5 in panel (a): $I_{0b} = 0.1477$ and $I_{0g} = 894.8$ (point 1), $I_{0b} = 0.2316$ and $I_{0g} = 857$ (point 2), $I_{0b} = 0.2434$ and $I_{0g} = 852.1$ (point 3), $I_{0b} = 0.2642$ and $I_{0g} = 843.7$ (point 4), $I_{0b} = 0.388$ and $I_{0g} = 799$ (point 5). The system parameters are: $\alpha_b = 0.117$, $\alpha_g = 0.985 \times 10^{-4}$, $\beta = 0.052$, $\gamma = -0.55$, $\lambda_b = 450 \times 10^{-9}$, $\lambda_g = 532 \times 10^{-9}$.

Using the substitution $\tilde{W}_{k,l} = W_{k,l}^2$, network model of Eqs. (5.13) is rewritten as

$$\varepsilon \frac{d\Gamma_k}{dt} = -\Gamma_k + \frac{1}{\alpha_b I_k^b + \frac{\lambda_g}{\lambda_b} \alpha_g I_{0g} + \beta} + \gamma, \quad (5.20)$$

$$I_k^b = I_{0b} \left(\sin^2(\Gamma_k) + R^2 \left\{ \sum_{l=1}^N \tilde{W}_{k,l} \sin^2(\Gamma_l) \right\} \right),$$

To demonstrate that the model of Eqs. (5.20) can exhibit the basic properties of the the

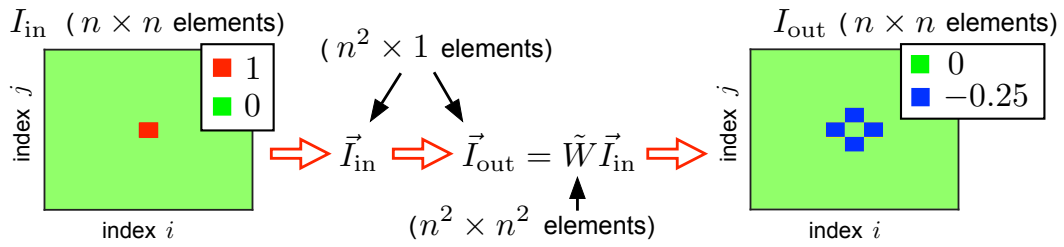


Figure 5.3: Illustration of the coupling matrix.

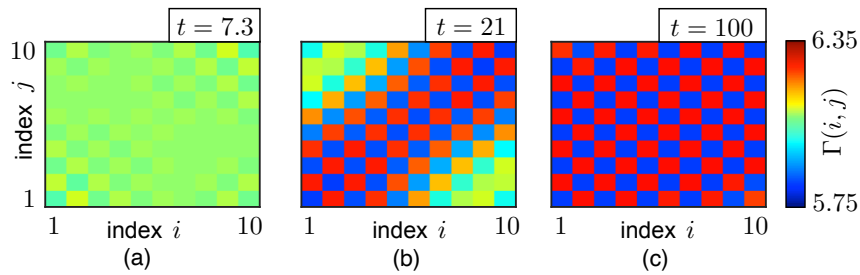


Figure 5.4: Antiferromagnetic interaction in the model of Eqs. (5.20). System parameters are: $\alpha_b = 0.117$, $\alpha_g = 0.985 \times 10^{-4}$, $\beta = 0.052$, $\gamma = -0.55$, $\lambda_b = 450 \times 10^{-9}$, $\lambda_g = 532 \times 10^{-9}$, $I_{0b} = 0.2434$ and $I_{0g} = 852.1$, $R = 0.95$. Parameters I_{0b} and I_{0g} correspond to the $f(\Gamma)$ configuration depicted in Fig. 5.2 (d).

Ising machine dynamics, the model is studied in the bistable regime close to the pitchfork bifurcation. The chosen pair of parameters I_{0b} and I_{0g} corresponds to the configuration $f(\Gamma)$ depicted in Fig. 5.2 (d). The action of this particular coupling matrix is illustrated in Fig. 5.3: it splits the input signal at any pixel into four and distributes it across the pixel's nearest neighbours according to negative coupling weights, and hence corresponds to the antiferromagnetic interactions model of a Ising spin system. Noteworthy, here we treat a network based on incoherent illumination, and diffractive optics hence cannot generally provide the required coupling mechanism, yet one would potentially need to consider difference in spatial and temporal coherence. If the initial conditions are initialized in the neighbourhood of the unstable fixed point, then Eqs. (5.20) exhibits the alternating-spin regime illustrated in Fig. 5.4 which in its final state and for this simple interaction topology corresponds to the solution of the Ising model [80].

5.2.2/ INCOHERENT ILLUMINATION (LINEARISED MODEL)

Consider the linearised model of Eqs. (5.5). To establish the conditions for the pitchfork bifurcation, the Taylor series is

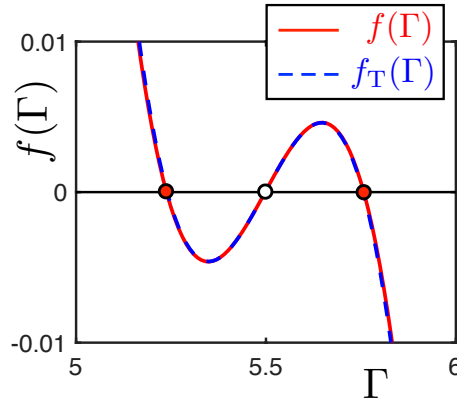


Figure 5.5: Right-hand side function $f(\Gamma)$ of Eq. (5.5) (red solid curve) and its Taylor series approximation (5.21) (blue dashed curve) for a set of parameters: $I_{0b} = 0.2434$ and $I_{0g} = 860.3$ (corresponds to $\Gamma_* = 6.021$), $\kappa = 4.3$, $R = 0$, $\alpha_b = 0.117$, $\alpha_g = 0.985 \times 10^{-4}$, $\beta = 0.052$, $\gamma = -0.55$, $\lambda_b = 450 \times 10^{-9}$, $\lambda_g = 532 \times 10^{-9}$.

$$\begin{aligned}
 f(\Gamma) &= -\Gamma + \Gamma_* - \kappa I_{0b} \sin^2(\Gamma_0) \{1 + R^2\}, \\
 f_T(\Gamma) &= a + b(\Gamma - \Gamma_0) + c(\Gamma - \Gamma_0)^2 + d(\Gamma - \Gamma_0)^3, \quad \text{where} \\
 a &= -\Gamma_0 + \Gamma_* - \kappa I_{0b} \sin^2(\Gamma_0) \{1 + R^2\}, \\
 b &= -1 - \kappa \{1 + R^2\} I_{0b} \sin(2\Gamma_0), \\
 c &= -\kappa \{1 + R^2\} I_{0b} \cos(2\Gamma_0), \\
 d &= \frac{2}{3} \kappa \{1 + R^2\} I_{0b} \sin(2\Gamma_0).
 \end{aligned} \tag{5.21}$$

The pitchfork bifurcation conditions $a = 0$ and $c = 0$ take the form

$$\begin{aligned}
 a = 0 &\Rightarrow \Gamma_* = \Gamma_0 + \kappa I_{0b} \sin^2(\Gamma_0) \{1 + R^2\}, \\
 c = 0 &\Rightarrow \cos(2\Gamma_0) = 0,
 \end{aligned} \tag{5.22}$$

which means that the symmetric cubic function $f_T(\Gamma) = b(\Gamma - \Gamma_0) + d(\Gamma - \Gamma_0)^3$ can be achieved only at $\Gamma_0 = \pm \frac{\pi}{4} + \frac{\pi n}{2}$ ($n \in \mathbb{Z}$). The linearised model is used below to reproduce the pattern formation dynamics illustrated in Fig. 5.4. Then the further assumptions are applied for the reconstruction of the curve $f(\Gamma)$ in Fig. 5.2 (d) for the case of linearised model given by Eq. (5.5). The nearest point Γ_0 corresponding to the symmetric bistable regime in the neighbourhood of the point $\Gamma_0 \approx 5.579$, which corresponds to $n = 3$, hence $\Gamma_0 = \frac{\pi}{4} + \frac{3\pi}{2}$. The chosen parameter values $I_{0b} = 0.2434$ and $R = 0$ are the same as for Fig. 5.2 (d). The main aim is therefore to estimate values κ and Γ_* such that the cubic form of the right-hand side function is similar to the original one in Fig. 5.2 (d) and the conditions according to Eqs. 5.22 are fulfilled, which is the case at $\kappa = 4.3$. The corresponding value $\Gamma_* = 6.021$ is calculated according to the condition $a = 0$ (see Eq. (5.22)). The resulting right-hand side function $f(\Gamma)$ is depicted in Fig. 5.5. It is important to note that in contrast to the full model of Eq. (5.15) where the pitchfork bifurcation conditions are fulfilled at $I_{0b} = 0.2434$ and

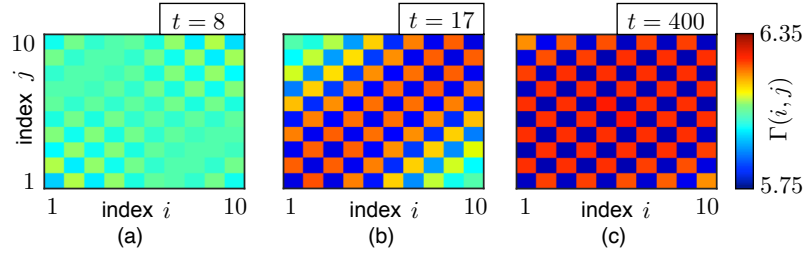


Figure 5.6: Antiferromagnetic interaction in Eq. (5.14). System parameters are: $\alpha_b = 0.117$, $\alpha_g = 0.985 \times 10^{-4}$, $\beta = 0.052$, $\gamma = -0.55$, $\lambda_b = 450 \times 10^{-9}$, $\lambda_g = 532 \times 10^{-9}$, $I_{0b} = 0.2434$ and $I_{0g} = 860.3$ (corresponds to $\Gamma_* = 6.021$), $\kappa = 4.3$, $R = 0.95$. The chosen set of parameters corresponds to the $f(\Gamma)$ configuration depicted in Fig. 5.5.

$I_{0g} = 852.1$ (see Fig. 5.2 (d)), the pitchfork bifurcation conditions in Eq. (5.5) are fulfilled at the same $I_{0b} = 0.2434$ and a slightly different $I_{0g} = \frac{\lambda_b}{\lambda_g \alpha_g} ((\Gamma_* - \gamma)^{-1} - \beta) = 860.3$.

After all parameter values corresponding to the symmetric cubic configuration $f(\Gamma)$ have been identified, this set of parameters is used for modelling network model according to Eqs. (5.14) with the same antiferromagnetic coupling matrix elements $\tilde{W}_{k,l} = W_{k,l}^2$ as in the full model by Eq. (see Fig. 5.3). The resulting patterns obtained from random initial conditions in the vicinity of the point $\Gamma_0 = \frac{\pi}{4} + \frac{3\pi}{2}$ are shown in Fig. 5.6. Similarly to the patterns observed in the full model [Fig. 5.4], the system state in Fig. 5.6 corresponds to the antiferromagnetic interaction.

5.2.3/ COHERENT ILLUMINATION (LINEARISED MODEL)

As demonstrated in Sec. 5.1.2, the model equations corresponding to coherent illumination are more complex. In such a case the system under study cannot be represented as the canonic model for the Ising machine. To demonstrate this fact, the system is considered for the linearised case (see Eqs. (5.12)) chosen as the simplest equation form. Substituting the coupling matrix as being

$$\tilde{W} = \begin{bmatrix} W_{1,1} + \frac{1}{R} & W_{1,2} & \dots & W_{1,N} \\ W_{2,1} & W_{2,2} + \frac{1}{R} & \dots & W_{2,N} \\ \vdots & \vdots & \vdots & \vdots \\ W_{N,1} & W_{N,2} & \dots & W_{N,N} + \frac{1}{R} \end{bmatrix} \quad (5.23)$$

one can rewrite Eqs. (5.12) as

$$\begin{aligned} \varepsilon \frac{d\Gamma_k}{dt} &= -\Gamma_k + \Gamma_* - \kappa I_{0b} R^2 \left\{ \sum_{l=1}^N \tilde{W}_{k,l} \sin(\Gamma_l) \right\}^2, \\ \Gamma_* &= \left(\frac{\lambda_g}{\lambda_b} \alpha_g I_{0g} + \beta \right)^{-1} + \gamma. \end{aligned} \quad (5.24)$$

Expressing the square of the sum in the brackets, the final equation form is obtained

$$\varepsilon \frac{d\Gamma_k}{dt} = -\Gamma_k + \Gamma_* - \kappa I_{0b} R^2 \left\{ \sum_{l=1}^N \tilde{W}_{k,l}^2 \sin^2(\Gamma_l) + \sum_{\substack{l=1 \\ k \neq l}}^N \tilde{W}_{k,l} \tilde{W}_{k,h} \sin(\Gamma_l) \sin(\Gamma_h) \right\}, \quad (5.25)$$

$$\Gamma_* = \left(\frac{\lambda_g}{\lambda_b} \alpha_g I_{0g} + \beta \right)^{-1} + \gamma.$$

The second sum complicates the equations and presents a deviation of the pure Ising model's form. Furthermore, one cannot explicitly distinguish the terms describing the individual dynamics of the k -th oscillator, and then represent them using the Taylor series approximation for further pitchfork bifurcation condition derivations. Any of our attempts to apply the Taylor series approach give rise to the presence of the coupling terms in the expressions for $a(\Gamma_0)$, $b(\Gamma_0)$, $c(\Gamma_0)$, $d(\Gamma_0)$. The possibility to implement symmetric spin dynamics at $a(\Gamma_0) = c(\Gamma_0) = 0$ for each partial oscillator depends, both, on individual dynamics determined by parameter values, on the coupling topology and the global state of the whole system (the retardation at other pixels).

The carried out simulations have shown that the antiferromagnetic interaction states can be exhibited by other configurations of the OASLM with optical feedback. In particular, such states can be achieved by the OASLM with a PS-layer being not polarization-sensitive. However, the corresponding model equations for these systems are more complex and cannot be reduced to the classical Ising model. In some cases the difference can be minimized by choosing special kinds of the coupling matrices, but the rigorous mathematical similarity cannot be reached. These complex systems are interesting in the context of further studies.

5.3/ CONCLUSION

It has been demonstrated that modifying the OASLM-design allows simplifying the system's nonlinear model equations. In particular, the introduction of the OASLM with a single polarization-sensitive PS-layer provides for the implementation of a \sin^2 -nonlinearity. In such a case, the model implying incoherent illumination is most simplified and can be represented as a particular manifestation of the Ising model. The advantage of incoherent illumination is the fact that the corresponding system equation can be represented as a sum of two separated functions: $\varepsilon \frac{d\Gamma_k}{dt} = f(\Gamma_k) + g(W \times \sin(\vec{\Gamma}))$, where the function f is responsible for the individual dynamics, while function g consists of the coupling terms (here, the symbol \times corresponds to matrix multiplication). Thus, applying the Taylor series approach and deriving the pitchfork bifurcation conditions, one can transform the model equations as being $\varepsilon \frac{d\Gamma_k}{dt} = b(\Gamma - \Gamma_0) + d(\Gamma - \Gamma_0)^3 + g(W \times \sin(\vec{\Gamma}))$, which represents a particular manifestation of the Ising model. It has been shown by means of numerical simulations

that the studied model can relax into a final state corresponding to the antiferromagnetic interaction of an Ising model. As a consequence, OASLMs are potentially promising for the implementation of spin-networks for solution of combinatorial optimisation problems [73].

In contrast to the incoherent illumination model, the dynamical system equations for coherent illumination are more complicated since the phase terms due to the interference between the field of coupled oscillators. The generalised form for the model equations takes the form $\varepsilon \frac{d\Gamma_k}{dt} = f(\Gamma_k) + q(\sin(\Gamma_k), W \times \sin(\vec{\Gamma})) + g(W \times \sin(\vec{\Gamma}))$. Thus, the representation of the right-hand side function as $b(\Gamma - \Gamma_0) + d(\Gamma - \Gamma_0)^3 + g(W \times \sin(\vec{\Gamma}))$ is impossible. However, this does not mean that the system cannot exhibit the distinguishable stable states of the Ising model such as the case of the antiferromagnetic interaction, but the rigorous mathematical correspondence could not be achieved within the framework of this thesis. This is due to the fact that for the case of coherent illumination the pitchfork bifurcation condition fulfilment is dictated by, both, the individual dynamics parameters and by the coupling weights.

CONCLUSION

In this thesis, we experimentally explored a nematic liquid crystal OASLM using nano-dimensional dichalcogenide (α -As₂S₃) glassy thin-films as photo sensors and alignment layers OASLM. We used device parameters obtained from experimental characterization to develop the general nonlinear-dynamical model of the OASLM and various OASLM-based optical systems. Numerical simulations of the different developed models revealed fundamental properties of their dynamics, which is of major importance for the growing field of special purpose hardware implementations of novel computing concepts.

The first part of this thesis is focused on experimental characterizations of OASLM parameters and its energy consumption. The carried out experiments demonstrated that the OASLM is characterized by a very low energy consumption and is able to operate at very low powers of incident light. However, during characterizations it was also found that the device response is not stable in the case of long-term illumination, since the studied OASLMs can only be operated using a DC-power supply, which in turn induced destructive effects inside the LC-layer of the OASLM.

Next, it was analysed which kinds of the dynamics can be realized in OASLM-based systems by the implementation of optical feedback loops. One of the simplest ways to achieve such feedbacks is using mirrors. This option was examined by means of numerical simulations of single-oscillator models corresponding to OASLM-based setups. It has been shown that transitions from monostability to multistability of steady-state regimes are typical for such systems. In particular, transitions from monostability to bistability were observed in a case of incoherent illumination, while the coherent illumination allows to achieve the coexistence of up to six stable equilibrium points.

Besides the consideration of single-colour models of OASLM-based setups, a manifold of models implying instantaneous two-colour (here blue and green) illumination of the OASLM has been analysed. The two-colour model contains an additional parameter and hence is more flexible. This was used to achieve the occurrence of different bifurcation scenarios in two-colour models of the OASLM. A Taylor series expansion-based technique allows deriving mathematical conditions for the observation of the pitchfork, transcritical and saddle-node bifurcations of steady states. The successful demonstration of

the different bifurcation conditions in numerical experiments has enabled us to emphasize the universality of OASLM-based models described by one dynamical variable: all three bifurcations which can occur in such systems were demonstrated in numerical experiments simply by varying the two different light intensities. Furthermore, simplification of the OASLM from two PS layers to a single-PS layer does not result in principal changes in the dynamics, and the possibility to observe the discussed bifurcation persists.

Besides the achievement of particular bifurcation transitions, adjusting the incident light intensities enables controlling the spatial dynamics. In particular, the established pitchfork bifurcation conditions provide for controlling the system symmetry. We use this to control the effect of coarsening in a spatially-extended model of the OASLM with optical feedback.

Finally, we showed that one can apply OASLMs for the emulation of dynamics highly similar or identical to networks of spin $1/2$ particles in the context of Ising machines. To achieve maximal correspondence with the Ising model, the OASLM must be transformed to a single PS-layer, where PS-layer's photosensitivity depends on a resulting light polarization state, i.e. a polarization selective PS layer. Such PS can be achieved, for example using nano-structuring of the PS layer similar to a wire-grid polarizer.

In summary, the obtained results indicate that OASLMs offer great opportunities for PNN implementations due to a wide spectrum of coupling elements state the OASLMs potential for further modifications. Using a series of OASLMs without feedback connections provides for development of FNNs, while the introduction of additional optical elements for feedback connections, such as mirrors, could establish RNNs. In particular, using the pitchfork bifurcation conditions one can achieve a system state being very close the the bifurcation point where transients are maximally long. Such states could be applied for transient computing architectures such as reservoir computing. In addition, OASLMs are promising in the context of synthesis of photonic spin-networks. Thus, a variety of practical applications of OASLM-based PNNs is not limited by typical machine learning tasks, such as pattern recognition or time series reconstruction, but also includes combinatorial optimization problems.

Concerning further researches addressing OASLMs, the most relevant one is transition from numerical modelling of OASLM-based setup models to creation of real PNNs for further study in physical experiments. For this purpose, one must use OASLMs with a thicker PS layer in order to enable sufficient response times allowing for an operation using a AC-power supply. In addition, one can simplify OASLMs construction as the two PS-layers are not necessary: all the dynamical regimes and occurred bifurcation transitions are also observed in a case of the OASLM with a single PS-layer. If one need to create a photonic Ising machine and a full correspondence with the theoretical model is principally important, then OASLM must be equipped with a PS-layer being sensitive to a polarization state of the incident light.

LIST OF FIGURES

1.1	Schematic illustration of a feedforward neural network. Circles are the artificial neurons (blue circles form the input and output layers, the red ones belong to the hidden layer), while arrows are the connections described by matrices W^2 and W^3	6
1.2	Schematic illustration of a recurrent neural network. Blue circles form the input and output layers, while the red ones belong to the hidden layer. Arrowed lines and curves are the connections.	7
1.3	Schematic illustration of reservoir computing. In contrast to Fig. 1.2, only output connections (blue arrowed lines) are adjustable, while the input weights (red arrowed lines) and internal reservoir connections (black arrowed lines) are fixed.	8
1.4	Schematic illustration of the Ising machine. Here, the spin-network elements possess either spin-up (red circles) or spin-down (blue circles) states.	9
1.5	Schematic illustration of reflecting (panel (a)) and transmissive (panel (b)) OASLMs, and EASLM (panel (c)).	15
1.6	Photonic EASLM-based RC schemes applied in Ref. [16] (panel (a)) and in Ref. [21] (panel (b)).	16
1.7	Opto-electronic delay-based RC architecture implemented in Ref. [128] and all-optical delay-oscillator scheme presented in Ref. [170].	17
1.8	Phase-parametric diagram for the saddle-node bifurcation in Eq. (1.11) (panel (a)), the transcritical bifurcation in model (1.12) (panel (b)) and the pitchfork bifurcation in oscillator (1.13) (panel (c)). The solid lines indicate stable equilibria, while the dashed ones correspond to unstable fixed points.	21
2.1	OASLM illuminated by a light source. Here, the Jones vector components of the incident and transmitted lights are schematically shown by red arrowed lines.	24
2.2	OASLM and its dimensions.	25

- 2.3 OASLM in darkness (panel (a)) and under illumination (panel (b)). Here, the red arrows indicate the electric field E_d in the areas where the illumination is absent, while the electric field at the illuminated point E_l is illustrated by the blue arrow. 26
- 2.4 (a) Electronic circuit interpretation of the OASLM; (b) Experimental setup developed for the study of OASLM's electrical properties under blue illumination. 27
- 2.5 OASLM under blue laser illumination, $\lambda = 450$ nm.: (a) Experimentally measured dependences of the current through the OASLM, i_S , on the incident optical power, P_{in} (red circles), and the result of curve fitting (blue solid line) to Eq. (2.2). The obtained parameters are $R_{LC} = 3.08 \times 10^7$ [Ω], $G_0 = 2.65 \times 10^{-8}$ [Ω^{-1}], $\alpha = 5.03 \times 10^{-4}$ [$W^{-1}\Omega^{-1}$]; (b) Dependence of OASLM's resistance, R_S , on the incident light power, P_{in} , obtained from experimental data (red circles). The blue line corresponds to the parameters obtained through the fit in panel (a). 28
- 2.6 Different options for the OASLM illumination: Gaussian (panel (a)), uniform (panel (b)), partially-uniform (panel(c)). 29
- 2.7 LC molecule orientation: a natural state (panel (a)) and the twisted one in the presence of an external voltage applied across the LC layer (panel (b)); (c) Dependence of the birefringence on the applied voltage being typical for many kinds of LC mixtures (green solid curve) and its approximation by the curve $\Delta n = \frac{1}{aV_{ext} + b} + c$ (red dashed curve). 31
- 2.8 Simplified illustration of the OASLM illuminated by a light source and the relevant optical intensities. 32
- 2.9 Experimental setup developed for the exploration of OASLM's optical response to the blue laser illumination. 33
- 2.10 (a-b) Scanned by the camera brightness spatial distributions of the incident light beam in front of the OASLM (panel (a)) and of the processed light beam (panel (b)). Local maxima correspond to the retardation $\Gamma = \frac{m\pi}{2}$ while the retardations at the local minima are $\Gamma = m\pi$. (c) Experimentally established dependence of the retardation on the incident light intensity built on the base of local extrema in panel (b) (black circles) and the experimental data for $V_0 = 9$ [V] taken from the paper [24] (black squares). Both dependences are fitted using the function $\Gamma(I_{in}) = (\alpha I_{in} + \beta)^{-1} + \gamma$ (see Eq. (2.12)). The parameters estimated by means of curve-fitting are: $\alpha = 0.234$, $\beta = 0.052$, $\gamma = -0.55$ for the red solid line (curve-fitting of the current experiment), and $\alpha = 2.96$, $\beta = 0.13$, $\gamma = 0.72$ for the blue solid line (curve-fitting of the experiment in [24]). 34

2.11 (a) Modified block of the experimental setup in Fig.2.9 used for the study of the OASLM under green illumination. This option involves the green laser diode DJ532-10 ($\lambda=532$ nm) and two lenses C110TMD-A (Lens1) and AC254-035-A-ML (Lens2) used for the light collimation. All the other setup elements are the same as in Fig.2.9; (b) Experimentally obtained dependence $\Gamma(I_{in})$ for the green illumination of the OASLM (black circles) and the result of curve-fitting using Eq. (2.12) (red solid curve). The parameters estimated by means of curve-fitting are: $\alpha = 1.97 \times 10^{-4}$, $\beta = 0.0486$, $\gamma = -13.17$ 35

2.12 OASLM under illumination and optical feedback implemented through an external mirror. In contrast to Fig. 2.1, the system with feedback implies the presence of four optical fields $E_{0,1,2,3}$ 36

2.13 OASLM under incoherent illumination of a blue LED and feedback created by a mirror and a polarizer transmitting p-polarization. 37

2.14 System (2.14): (a) The evolution of the right-hand side function $f(\Gamma)$ for Eq. (2.14) caused by the injected light intensity growth: $I_0 = 0.02$ (blue dashed curve), $I_0 = 0.038$ (red solid curve), $I_0 = 0.05$ (dark-green dashed curve), $I_0 = 0.088$ (brown solid curve), $I_0 = 0.13$ (magenta dashed curve), $I_0 = 0.17$ (orange solid curve), $I_0 = 0.25$ (cyan dashed curve), $I_0 = 0.35$ (green solid curve), $I_0 = 0.5$ (red dashed curve), $I_0 = 0.9$ (blue solid curve), $I_0 = 1.5$ (brown dashed curve); (b) Phase-parametric diagram reflecting the existence, appearance, disappearance and motion of steady states for increasing parameter I_0 . System parameters are: $\alpha = 0.117$, $\beta = 0.052$, $\gamma = -0.55$, $\varepsilon = 1$, $R = 0.95$ 38

2.15 OASLM under coherent illumination of a blue laser and mirror feedback. In contrast to the system depicted in Fig. 2.14, the system with coherent illumination involves interference between fields $E_{0,3}$ on the left side of the OASLM, and between fields $E_{1,2}$ on the right side. 39

2.16 (a) The evolution of the right-hand side function $f(\Gamma)$ for Eqs. (2.18) and (2.22) caused by increasing the parameter I_0 : $I_0 = 0.003$ (blue solid line), $I_0 = 0.04$ (red solid line), $I_0 = 0.08$ (green dashed line), $I_0 = 0.15$ (magenta solid line), $I_0 = 0.4$ (cyan dashed line), $I_0 = 0.7$ (orange solid line); (b) Phase-parametric diagram reflecting the existence, appearance, disappearance and motion of steady states for increasing parameter I_0 (stable steady states are coloured in blue, the unstable ones are coloured in red). System parameters are: $\alpha = 0.117$, $\beta = 0.052$, $\gamma = -0.55$, $\varepsilon = 1$, $R = 0.95$, $\phi_0 = \pi$, $\phi_0 = \pi/2$ 41

2.17 OASLM under simultaneous blue and green illumination. 43

- 2.18 OASLM under simultaneous blue and green illumination when the blue light beam is reflected by the dichroic mirror and creates feedback. 44
- 2.19 Schematic illustration to the linear approximation of the OASLM's response. 46
- 2.20 (a) Illustration of the single-PS-layer OASLM illuminated by a light source; (b) Single-PS-layer OASLM under simultaneous blue and green illumination when the blue light beam is reflected by the dichroic mirror and creates feedback. 47
- 2.21 Evolution of the OASLM response to invariable Gaussian illumination (the corresponding experimental setup is depicted in Fig. 2.9): (a) initial moment; (b) after 40 minutes; (c) after 80 minutes; (d) after 130 minutes. . . . 50
- 3.1 Pitchfork conditions determined by Eq. (2.28): (a) Taylor series coefficient b (Eq. (3.9)); (b-c) I_{0b} and I_{0g} according to Eqs. (3.6) and (3.7); (d) $I_{0b}(I_{0g})$ for I_{0b} and I_{0g} in panels (b) and (c) corresponding to the same argument Γ_0 . System parameters are: $\alpha_b = 0.117$, $\alpha_g = 0.985 \times 10^{-4}$, $\beta = 0.052$, $\gamma = -0.55$, $\lambda_b = 450 \times 10^{-9}$, $\lambda_g = 532 \times 10^{-9}$, $R = 0.95$ 54
- 3.2 Pitchfork bifurcation in Eq. (2.28): (a) $f(\Gamma)$ for varying I_{0b} and I_{0g} according to Fig. 3.1 (d); (b-e) $f(\Gamma)$ (red solid curve) and $f_{\Gamma}(\Gamma)$ (blue dotted curve) at points 1-4 in Fig. 3.1: $I_{0b} = 0.0818$ and $I_{0g} = 365.2$ (point 1), $I_{0b} = 0.1267$ and $I_{0g} = 301.9$ (point 2), $I_{0b} = 0.163$ and $I_{0g} = 252.2$ (point 3), $I_{0b} = 0.2149$ and $I_{0g} = 183.6$ (point 4); (f) Phase-parametric diagram for I_{0b} and I_{0g} according to the curve in Fig. 3.1 (d). System parameters are: $\alpha_b = 0.117$, $\alpha_g = 0.985 \times 10^{-4}$, $\beta = 0.052$, $\gamma = -0.55$, $\lambda_b = 450 \times 10^{-9}$, $\lambda_g = 532 \times 10^{-9}$, $R = 0.95$. 55
- 3.3 The dependence from the saddle-node bifurcation conditions for Eq. (2.28): (a) Taylor series coefficient a on Γ_0 ; (b-c) I_{0b} and I_{0g} according to Eqs. (3.12) and (3.13). System parameters are: $\alpha_b = 0.117$, $\alpha_g = 0.985 \times 10^{-4}$, $\beta = 0.052$, $\gamma = -0.55$, $\lambda_b = 450 \times 10^{-9}$, $\lambda_g = 532 \times 10^{-9}$, $R = 0.95$ 57
- 3.4 Transcritical bifurcation conditions for Eq. (2.28): (a-b) Taylor series coefficient b as a function of Γ_0 when I_{0b} varies according to Eq. (3.17) (panel (a)) and Eq. (3.18) (panel (b)); (c-d) I_{0b} and I_{0g} according to Eqs. (3.18) and (3.19). System parameters are: $\alpha_b = 0.117$, $\alpha_g = 0.985 \times 10^{-4}$, $\beta = 0.052$, $\gamma = -0.55$, $\lambda_b = 450 \times 10^{-9}$, $\lambda_g = 532 \times 10^{-9}$, $R = 0.95$ 58

- 3.5 Pitchfork bifurcation conditions for Eq. (2.26): (a) Dependence of b on Γ_0 (Eq. (3.29)); (b-c) I_{0b} and I_{0g} according to Eqs. (3.27) and (3.28); (d) $I_{0b}(I_{0g})$ which consists of values I_{0b} and I_{0g} in panels (b) and (c) corresponding to the same argument Γ_0 . System parameters are: $\alpha_b = 0.117$, $\alpha_g = 0.985 \times 10^{-4}$, $\beta = 0.052$, $\gamma = -0.55$, $\phi_0 = \pi/2$, $\phi_1 = \pi$, $\lambda_b = 450 \times 10^{-9}$, $\lambda_g = 532 \times 10^{-9}$, $R = 0.95$ 61
- 3.6 Pitchfork bifurcation in Eq. (2.26): (a-d) $f(\Gamma)$ (red solid curve) and its Taylor series approximation given by Eq.(3.23) (blue dotted curve) at points 1-4 in Fig. 3.5: $I_{0b} = 4.39 \times 10^{-3}$ and $I_{0g} = 24.35$ (point 1), $I_{0b} = 7.73 \times 10^{-3}$ and $I_{0g} = 21.26$ (point 2), $I_{0b} = 11.3 \times 10^{-3}$ and $I_{0g} = 18.14$ (point 3), $I_{0b} = 15.1 \times 10^{-3}$ and $I_{0g} = 15.03$ (point 4); (d) Phase-parametric diagram for I_{0b} and I_{0g} varying according to the curve in Fig. 3.5 (d). System parameters are: $\alpha_b = 0.117$, $\alpha_g = 0.985 \times 10^{-4}$, $\beta = 0.052$, $\gamma = -0.55$, $\phi_0 = \pi/2$, $\phi_1 = \pi$, $\lambda_b = 450 \times 10^{-9}$, $\lambda_g = 532 \times 10^{-9}$, $R = 0.95$ 62
- 3.7 Saddle-node bifurcation conditions for Eq. (2.26): (a) Dependence of a on Γ_0 (Eq. (3.34)); (b-c) I_{0b} and I_{0g} according to Eqs. (3.32) and (3.33); (d) $I_{0b}(I_{0g})$ which consists of values I_{0b} and I_{0g} in panels (b) and (c) corresponding to the same argument Γ_0 . System parameters are: $\alpha_b = 0.117$, $\alpha_g = 0.985 \times 10^{-4}$, $\beta = 0.052$, $\gamma = -0.55$, $\phi_0 = \pi/2$, $\phi_1 = \pi$, $\lambda_b = 450 \times 10^{-9}$, $\lambda_g = 532 \times 10^{-9}$, $R = 0.95$ 63
- 3.8 Saddle-node bifurcation in Eq. (2.26): (a-c) function $f(\Gamma)$ (red solid curve) and f_T of (3.23) (blue dotted curve) at points 1-3 in Fig. 3.7: $I_{0b} = 19.56 \times 10^{-2}$ and $I_{0g} = 415.8$ (point 1), $I_{0b} = 21.8 \times 10^{-2}$ and $I_{0g} = 471.2$ (point 2), $I_{0b} = 25.36 \times 10^{-2}$ and $I_{0g} = 552.7$ (point 3); (d) Phase-parametric diagram for I_{0b} and I_{0g} varying according to the curve in Fig. 3.7 (d). System parameters are: $\alpha_b = 0.117$, $\alpha_g = 0.985 \times 10^{-4}$, $\beta = 0.052$, $\gamma = -0.55$, $\phi_0 = \pi/2$, $\phi_1 = \pi$, $\lambda_b = 450 \times 10^{-9}$, $\lambda_g = 532 \times 10^{-9}$, $R = 0.95$ 65
- 3.9 Transcritical bifurcation conditions for Eq. (2.26): (a-b) Dependences of coefficient b on Γ_0 (Eqs. (3.40) and (3.41)) when I_{0b} varies according to Eqs. (3.37) (panel (a)) and (3.38) (panel (b)); (c-d) I_{0b} and I_{0g} according to Eqs. (3.38) and (3.39); (e) $I_{0b}(I_{0g})$ which consists of values I_{0b} and I_{0g} in panels (c) and (d) corresponding to the same argument Γ_0 . System parameters are: $\alpha_b = 0.117$, $\alpha_g = 0.985 \times 10^{-4}$, $\beta = 0.052$, $\gamma = -0.55$, $\lambda_b = 450 \times 10^{-9}$, $\lambda_g = 532 \times 10^{-9}$, $R = 0.95$ 67

- 3.10 Transcritical bifurcation in Eq. (2.26): (a-c) $f(\Gamma)$ (red solid curve) and f_{Γ} according to Eq. (3.23) (blue dotted curve) at points 1-3 in Fig. 3.9: $I_{0b} = 20.1 \times 10^{-2}$ and $I_{0g} = 539.1$ (point 1), $I_{0b} = 21.8 \times 10^{-2}$ and $I_{0g} = 471.3$ (point 2), $I_{0b} = 31.9 \times 10^{-2}$ and $I_{0g} = 382$ (point 3); (d) Phase-parametric diagram for I_{0b} and I_{0g} varying according to the curve in Fig. 3.9 (e). System parameters are: $\alpha_b = 0.117$, $\alpha_g = 0.985 \times 10^{-4}$, $\beta = 0.052$, $\gamma = -0.55$, $\phi_0 = \pi/2$, $\phi_1 = \pi$, $\lambda_b = 450 \times 10^{-9}$, $\lambda_g = 532 \times 10^{-9}$, $R = 0.95$ 68
- 3.11 $I_{0g}(\Gamma_0)$ corresponding to Eq. (3.54), where $I_{0b}(\Gamma_0)$ varies according to Eq. (3.53). The red point corresponds to the pitchfork bifurcation moment $b(\Gamma_0 \approx 16.5256) = 0$. Parameters are: $\alpha_b = 0.117$, $\alpha_g = 0.985 \times 10^{-4}$, $\beta = 0.052$, $\gamma = -0.55$, $\phi_0 = \pi/2$, $\phi_1 = \pi$, $\lambda_b = 450 \times 10^{-9}$, $\lambda_g = 532 \times 10^{-9}$, $R = 0.95$ 71
- 3.12 Dependence $I_{0g}(\Gamma_0)$ (Eq. (3.57) where $I_{0b}(\Gamma_0)$ varies according to Eq. (3.56)). The red point corresponds to the saddle-node bifurcation moment $b(\Gamma_0 \approx 3.4847) = 0$. Parameters are: $\alpha_b = 0.117$, $\alpha_g = 0.985 \times 10^{-4}$, $\beta = 0.052$, $\gamma = -0.55$, $\phi_0 = \pi/2$, $\phi_1 = \pi$, $\lambda_b = 450 \times 10^{-9}$, $\lambda_g = 532 \times 10^{-9}$, $R = 0.95$ 72
- 3.13 Dependence $I_{0g}(\Gamma_0)$ corresponding to Eq. (3.60) where $I_{0b}(\Gamma_0)$ varies according to Eq. (3.59)). The red point corresponds to the transcritical bifurcation moment $b(\Gamma_0 \approx 3.4845) = 0$. Parameters are: $\alpha_b = 0.117$, $\alpha_g = 0.985 \times 10^{-4}$, $\beta = 0.052$, $\gamma = -0.55$, $\phi_0 = \pi/2$, $\phi_1 = \pi$, $\lambda_b = 450 \times 10^{-9}$, $\lambda_g = 532 \times 10^{-9}$, $R = 0.95$ 73
- 4.1 Eq. (4.2): (a-b) Schematic illustration of the profile evolution (panel (a1)) according to Eq. (4.3) and more complicated solutions (panels (a1) and (a2)) for $a = 1$, $b = 0.75$, $k = 0.1$. The space time plot corresponding to the solution in panel (a3) is depicted in panel (b). (c) Space-time plot illustrating a stationary wave front in a symmetric system for $a = b = 1$, $k = 0.1$ 77
- 4.2 Spatial pattern evolution of Eq. (4.1) in 2D-space for $a = 1$, $b = 0.9$, $k = 0.1$: evolution of a plane-wave profile (panels (a-c)) and the effect of coarsening in the case of random initial conditions (panels (d-f)). 78
- 4.3 Evolution of the reaction-term function $f(u)$ (red solid curves) according to the pitchfork (panel (a)) and saddle-node (panel (b)) bifurcation and its Taylor series expansion using a quadratic function (blue dashed curves). 78
- 4.4 Stochastic control of coarsening in Eq. (4.5) by increasing the noise intensity D_b (panels (a-d)) and D_a (panels (e-f)). Other parameters are: $a = 1$, $b = 0.75$, $k = 0.1$ 80

- 4.5 Spatial evolution of Eq. (4.4) in 2D-space (x,y) starting from the same initial conditions for $a = 1$, $b = 0.75$, $k = 0.1$ and varying noise intensities: $D_a = 0$, $D_b = 0$ (panels (a-c)), $D_a = 0$, $D_b = 10^{-3}$ (panels (d-f)), $D_a = 7 \times 10^{-4}$, $D_b = 0$ (panels (g-i)). 81
- 4.6 Evolution of the normalised probability density function $P_n(u)$ caused by varying noise intensities $D_{a,b}$ in Eq. (4.6). System parameters are $a_0 = b_0 = 1$, $D = 0.1$ 82
- 4.7 Single-PS-layer OASLM under simultaneous blue and green illumination when the blue light beam is reflected by the dichroic mirror and creates feedback. In contrast to Fig. 2.20, the system contains a defocusing lens to emulate local diffusion by spatially broadening the field distribution of the back-reflected optical field. Lenses L1 and L2 create 4f-imaging of the OASLM's state back on itself after reflection by the mirror. 83
- 4.8 Coarsening in an OASLM as described by Eq. (4.8). The considered area is 1mm^2 . Parameters are: $\varepsilon = 1$, $\alpha_b = 0.117$, $\alpha_g = 0.985 \times 10^{-4}$, $\beta = 0.052$, $\gamma = -0.55$, $\phi_0 = \pi/2$, $\phi_1 = \pi$, $\lambda_b = 450 \times 10^{-9}$, $\lambda_g = 532 \times 10^{-9}$, $R = 0.95$, $I_{0b} = |\vec{E}_0|^2 = 0.01506$, $I_{0g} = 30.1$ 84
- 4.9 Evolution of the right-hand side function of Eq. (2.33) and coarsening in Eq. (4.8) for increasing green light intensity: $I_{0g} = 22$ (panels (a) and (b)), $I_{0g} = 30.1$ (panels (c) and (d)), $I_{0g} = 36$ (panels (e) and (f)). Other parameters are: $\varepsilon = 1$, $\alpha_b = 0.117$, $\alpha_g = 0.985 \times 10^{-4}$, $\beta = 0.052$, $\gamma = -0.55$, $\phi_0 = \pi/2$, $\phi_1 = \pi$, $\lambda_b = 450 \times 10^{-9}$, $\lambda_g = 532 \times 10^{-9}$, $R = 0.95$, $I_{0b} = 0.01506$, $\sigma = 10^{-5}$ 85
- 4.10 Evolution of the right-hand side function of Eq. (2.33) and coarsening in Eq. (4.8) when I_{0b} and I_{0g} vary according to the saddle-node bifurcation conditions for Eq. (2.33) (see Sec. 3.4): $I_{0b} = 0.228$, $I_{0g} = 990$ (panels (a) and (b)), $I_{0b} = 0.241$, $I_{0g} = 1050$ (panels (c) and (d)), $I_{0b} = 0.2645$, $I_{0g} = 1153$ (panels (e) and (f)). Other parameters are: $\varepsilon = 1$, $\alpha_b = 0.117$, $\alpha_g = 0.985 \times 10^{-4}$, $\beta = 0.052$, $\gamma = -0.55$, $\phi_0 = \pi/2$, $\phi_1 = \pi$, $\lambda_b = 450 \times 10^{-9}$, $\lambda_g = 532 \times 10^{-9}$, $R = 0.95$, $\sigma = 10^{-5}$ 87
- 4.11 Coarsening in Eq. (4.10) for increasing noise intensity: $D_g = 0$ (panels (a-c)), $D_g = 3 \times 10^3$ (panels (d-f)), $D_g = 4 \times 10^3$ (panels (g-i)). Other parameters are: $\varepsilon = 1$, $\alpha_b = 0.117$, $\alpha_g = 0.985 \times 10^{-4}$, $\beta = 0.052$, $\gamma = -0.55$, $\phi_0 = \pi/2$, $\phi_1 = \pi$, $\lambda_b = 450 \times 10^{-9}$, $\lambda_g = 532 \times 10^{-9}$, $R = 0.95$, $I_{0b} = |\vec{E}_0|^2 = 0.01506$, $I_{0g} = 22$, $\sigma = 10^{-5}$, $\tau_c = 0.01$ 89

- 4.12 Coarsening in Eq. (4.10) for increasing noise intensity: $D_g = 0$ (panels (a-c)), $D_g = 1.5 \times 10^3$ (panels (d-f)). Other parameters are: $\varepsilon = 1$, $\alpha_b = 0.117$, $\alpha_g = 0.985 \times 10^{-4}$, $\beta = 0.052$, $\gamma = -0.55$, $\phi_0 = \pi/2$, $\phi_1 = \pi$, $\lambda_b = 450 \times 10^{-9}$, $\lambda_g = 532 \times 10^{-9}$, $R = 0.95$, $I_{0b} = |\vec{E}_0|^2 = 0.01506$, $I_{0g} = 36$, $\sigma = 10^{-5}$, $\tau_c = 0.01$ 89
- 4.13 Evolution of the normalised probability density function $P_n(\Gamma)$ caused by the varying noise intensity D_g in Eq. (4.11). Parameters are: $\varepsilon = 1$, $\alpha_b = 0.117$, $\alpha_g = 0.985 \times 10^{-4}$, $\beta = 0.052$, $\gamma = -0.55$, $\phi_0 = \pi/2$, $\phi_1 = \pi$, $\lambda_b = 450 \times 10^{-9}$, $\lambda_g = 532 \times 10^{-9}$, $R = 0.95$, $I_{0b} = 0.01506$, $I_{0g} = 22$, $\tau_c = 0.01$ 90
- 5.1 Single-PS-layer OASLM under simultaneous blue and green illumination when the blue light beam is reflected by the dichroic mirror and creates feedback. In contrast to Fig. 4.7, the PS-layer is polarization-sensitive and situated on the right side of the OASLM. 94
- 5.2 Pitchfork bifurcation in the incoherent network according to Eqs. (5.15) for the absence of the reflected feedback light ($R = 0$): (a) Dependence $I_{0b}(I_{0g})$ obtained from the pitchfork bifurcation conditions (see Exps. (5.18) and (5.19)); (b-f) Right-hand side function $f(\Gamma)$ (red solid curve) and its Taylor series approximation (5.16) (blue dashed curve) at control points 1-5 in panel (a): $I_{0b} = 0.1477$ and $I_{0g} = 894.8$ (point 1), $I_{0b} = 0.2316$ and $I_{0g} = 857$ (point 2), $I_{0b} = 0.2434$ and $I_{0g} = 852.1$ (point 3), $I_{0b} = 0.2642$ and $I_{0g} = 843.7$ (point 4), $I_{0b} = 0.388$ and $I_{0g} = 799$ (point 5). The system parameters are: $\alpha_b = 0.117$, $\alpha_g = 0.985 \times 10^{-4}$, $\beta = 0.052$, $\gamma = -0.55$, $\lambda_b = 450 \times 10^{-9}$, $\lambda_g = 532 \times 10^{-9}$ 100
- 5.3 Illustration of the coupling matrix. 101
- 5.4 Antiferromagnetic interaction in the model of Eqs. (5.20). System parameters are: $\alpha_b = 0.117$, $\alpha_g = 0.985 \times 10^{-4}$, $\beta = 0.052$, $\gamma = -0.55$, $\lambda_b = 450 \times 10^{-9}$, $\lambda_g = 532 \times 10^{-9}$, $I_{0b} = 0.2434$ and $I_{0g} = 852.1$, $R = 0.95$. Parameters I_{0b} and I_{0g} correspond to the $f(\Gamma)$ configuration depicted in Fig. 5.2 (d). 101
- 5.5 Right-hand side function $f(\Gamma)$ of Eq. (5.5) (red solid curve) and its Taylor series approximation (5.21) (blue dashed curve) for a set of parameters: $I_{0b} = 0.2434$ and $I_{0g} = 860.3$ (corresponds to $\Gamma_* = 6.021$), $\kappa = 4.3$, $R = 0$, $\alpha_b = 0.117$, $\alpha_g = 0.985 \times 10^{-4}$, $\beta = 0.052$, $\gamma = -0.55$, $\lambda_b = 450 \times 10^{-9}$, $\lambda_g = 532 \times 10^{-9}$ 102
- 5.6 Antiferromagnetic interaction in Eq. (5.14). System parameters are: $\alpha_b = 0.117$, $\alpha_g = 0.985 \times 10^{-4}$, $\beta = 0.052$, $\gamma = -0.55$, $\lambda_b = 450 \times 10^{-9}$, $\lambda_g = 532 \times 10^{-9}$, $I_{0b} = 0.2434$ and $I_{0g} = 860.3$ (corresponds to $\Gamma_* = 6.021$), $\kappa = 4.3$, $R = 0.95$. The chosen set of parameters corresponds to the $f(\Gamma)$ configuration depicted in Fig. 5.5. 103

BIBLIOGRAPHY

- [1] BOWDEN, C., GIBBS, H., AND MCCALL, S., Eds. **Optical Bistability 2**. Springer, Boston, MA, 1984.
- [2] GAMMAITONI, L., HÄNGGI, P., JUNG, P., AND MARCHESONI, F. **Stochastic resonance**. *Rev. Mod. Phys.* 70, 1 (1998), 223–287.
- [3] GIACOMELLI, G., GUIDICI, M., BALLE, S., AND TREDICCE, J. **Experimental evidence of coherence resonance in an optical system**. *Phys. Rev. Lett.* 84, 15 (2000), 3298–3301.
- [4] KÖSTER, F., LINGNAU, B., KRIMLOWSKI, A., HÖVEL, P., AND LÜDGE, K. **Collective coherence resonance in networks of optical neurons**. *Physica Status Solidi (b)* (2021), 2100345.
- [5] NASERI, T., AND SADIGHI-BONABI, R. **Investigating the impact of correlated white noises on the bistability behavior in an optical three-level bistable system**. *Journal of the Optical Society of America B* 32, 1 (2015), 76–82.
- [6] BARBÉROSHIE, A., GONTSYA, I., NIKA, Y., AND ROTARY, A. K. **Noise-induced optical multistability**. *Zh. Eksp. Teor. Fiz.* 104 (1993), 2655–2667.
- [7] LARGER, L., PENKOVSKY, B., AND MAISTRENKO, Y. **Virtual chimera states for delayed-feedback systems**. *Phys. Rev. Lett.* 111, 5 (2013), 054103.
- [8] GIACOMELLI, G., MARINO, F., ZAKS, M., AND YANCHUK, S. **Coarsening in a bistable system with long-delayed feedback**. *Europhys. Lett.* 99, 5 (2012), 58005.
- [9] BRUNNER, D., PENKOVSKY, B., LEVCHENKO, R., SCHÖLL, E., LARGER, L., AND MAISTRENKO, Y. **Two-dimensional spatiotemporal complexity in dual-delayed nonlinear feedback systems: Chimeras and dissipative solitons**. *Chaos* 28, 10 (2018), 103106.
- [10] LAVROV, R., JACQUOT, M., AND LARGER, L. **Nonlocal nonlinear electro-optic phase dynamics demonstrating 10 gb/s chaos communications**. *IEEE Journal of Quantum Electronics* 46, 10 (2010), 1430–1435.
- [11] ARGYRIS, A., SYVRIDIS, D., LARGER, L., ANNOVAZZI-LODI, V., COLET, P., FISHER, I., GARCIA-OJALVO, J., MIRASSO, C., PESQUERA, L., AND SHORE, K.

- Chaos-based communications at high bit rates using commercial fibre-optic links.** *Nature* 438, 7066 (2005), 343–346.
- [12] WILLNER, A., KHALEGHI, S., CHITGARHA, M., AND YILMAZ, O. **All-optical signal processing.** *Journal of Lightwave Technology* 32, 4 (2014), 660–680.
- [13] PSALTIS, D., BRADY, D., GU, X.-G., AND LIN, S. **Holography in artificial neural networks.** *Nature* 343, 6256 (1990), 325–330.
- [14] LOHMANN, A. W. **Principles of optical computing.** In *Nonlinear Optics and Optical Computing*. Springer US, 1990, pp. 151–157.
- [15] GENTY, G., SALMELA, L., DUDLEY, J., BRUNNER, D., KOKHANOVSKIY, A., KOBTSEV, S., AND TURITSYN, S. **Machine learning and applications in ultrafast photonics.** *Nature Photonics* 15, 2 (2021), 91–101.
- [16] BUENO, J., MAKTOOBI, S., FROEHLI, L., FISHER, I., JACQUOT, M., LARGER, L., AND BRUNNER, D. **Reinforcement learning in a large-scale photonic recurrent neural network.** *Optica* 5, 6 (2018), 756–760.
- [17] WETZSTEIN, G., OZCAN, A., GIGAN, S., FAN, S., ENGLUND, D., SOLJAČIĆ, M., DENZ, C., MILLER, D., AND PSALTIS, D. **Inference in artificial intelligence with deep optics and photonics.** *Nature* 588, 7836 (2020), 39–47.
- [18] ZHOU, T., LIN, X., WU, J., CHEN, Y., XIE, H., LI, Y., FAN, J., WU, H., FANG, L., AND DAI, Q. **Large-scale neuromorphic optoelectronic computing with a reconfigurable diffractive processing unit.** *Nature Photonics* 15, 5 (2021), 367–373.
- [19] PORTE, X., SKALLI, A., HAGHIGHI, N., REITZENSTEIN, S., LOTT, J., AND BRUNNER, D. **A complete, parallel and autonomous photonic neural network in a semiconductor multimode laser.** *Journal of Physics: Photonics* 3, 2 (2021), 024017.
- [20] RESIDORI, S. **Patterns, fronts and structures in a liquid-crystal-light-valve with optical feedback.** *Physics Reports* 416, 5-6 (2005), 201–272.
- [21] RAFAYELIAN, M., DONG, J., TAN, Y., KRZAKALA, F., AND GIGAN, S. **Large-scale optical reservoir computing for spatiotemporal chaotic systems prediction.** *Phys. Rev. X* 10, 4 (2020), 041037.
- [22] PIERANGELI, D., MARCUCCI, G., AND CONTI, C. **Large-scale photonic ising machine by spatial light modulation.** *Phys. Rev. Lett.* 122, 21 (2019), 213902.
- [23] PIERANGELI, D., MARCUCCI, G., BRUNNER, D., AND CONTI, C. **Noise-enhanced spatial-photonic ising machine.** *Nanophotonics* 9, 13 (2020), 4109–4116.

- [24] KIRZHNER, M., KLEBANOV, M., LYUBIN, V., COLLINGS, N., AND ABDULHALIM, I. **Liquid crystal high-resolution optically addressed spatial light modulator using a nanodimensional chalcogenide photosensor.** *Optics Letters* 39, 7 (2014), 2048–2051.
- [25] McCULLOCH, W., AND PITTS, W. **A logical calculus of the ideas immanent in nervous activity.** *The bulletin of mathematical biophysics volume 5*, 4 (1943), 115–133.
- [26] FAUSETT, L. **Fundamentals of Neural Networks.** Pearson, 1993.
- [27] MIRA, J., AND SANDOVAL, F., Eds. **From Natural to Artificial Neural Computation.** Springer, 1995.
- [28] HASSOUN, M. **Fundamentals of Artificial Neural Networks.** MIT Press, 1995.
- [29] SCHALKOFF, R. **Artificial Neural Networks.** McGraw-Hill College, 1997.
- [30] AMUNTS, K., GRANDINETTI, L., LIPPERT, T., AND PETKOV, N., Eds. **Brain-Inspired Computing.** Springer, 2021.
- [31] HAKEN, H. **Principles of Brain Functioning.** Springer, 1996.
- [32] IZHIKEVICH, E. **Dynamical Systems in Neuroscience.** MIT Press, 2007.
- [33] LINDNER, B., GARCÍA-OJALVO, J., NEIMAN, A., AND SCHIMANSKY-GEYER, L. **Effects of noise in excitable systems.** *Physics Reports* 392, 6 (2004), 321–424.
- [34] SHILNIKOV, A., AND KOLOMIETS, M. **Methods of the qualitative theory for the hindmarsh–rose model: A case study – a tutorial.** *International Journal of Bifurcation and Chaos* 18, 8 (2008), 2141–2168.
- [35] NEIMAN, A., PEI, X., RUSSELL, D., WOJTENEK, W., WILKENS, L., MOSS, F., BRAUN, H., HUBER, M., AND VOIGT, K. **Synchronization of the noisy electro-sensitive cells in the paddlefish.** *Phys. Rev. Lett.* 82, 3 (1999), 660–663.
- [36] NAGUMO, J., ARIMOTO, S., AND YOSHIZAWA, S. **An active pulse transmission line simulating nerve axon.** *Proceedings of the IRE* 50, 10 (1962), 2061–2070.
- [37] GARCÍA-OJALVO, J., AND SCHIMANSKY-GEYER, L. **Excitable structures in stochastic bistable media.** *Journal of Statistical Physics* 101, 1 (2000), 473–481.
- [38] WU, Y., DENG, L., LI, G. ZHU, J., AND SHI, L. **Spatio-temporal backpropagation for training high-performance spiking neural networks.** *Frontiers in Neuroscience* 12 (2018), 331.
- [39] PFEIFFER, M., AND PFEIL, T. **Deep learning with spiking neurons: Opportunities and challenges.** *Frontiers in Neuroscience* 12 (2018), 774.

- [40] KASABOV, N. **Time-Space, Spiking Neural Networks and Brain-Inspired Artificial Intelligence**. Springer Series on Bio- and Neurosystems 7. Springer, 2019.
- [41] BELLEC, G., SCHERR, F., SUBRAMONEY, A., HAJEK, E., SALAJ, D., LEGENSTEIN, R., AND MAASS, W. **A solution to the learning dilemma for recurrent networks of spiking neurons**. *Nature communications* 11, 1 (2020), 3625.
- [42] RANJAN, S., AND SENTHAMILARASU, S. **Applied Deep Learning and Computer Vision for Self-Driving Cars**. Packt Publishing, 2020.
- [43] ANSARI, S. **Building Computer Vision Applications Using Artificial Neural Networks**. Springer, 2020.
- [44] GOLDBERG, Y. **Neural Network Methods in Natural Language Processing**. Morgan & Claypool Publishers, 2017.
- [45] CHOLLET, G., DI BENEDETTO, M., ESPOSITO, A., AND MARINARO, M., Eds. **Speech Processing, Recognition and Artificial Neural Networks**. Springer, 1999.
- [46] TOH, K.-A., AND YAN, W.-Y., Eds. **Global Feedforward Neural Network Learning for Classification and Regression**. Springer, 2001.
- [47] VERSTRAETEN, D., SCHRAUWEN, B., D'HAENE, M., AND STROOBANDT, D. **An experimental unification of reservoir computing methods**. *Neural Networks* 20, 3 (2007), 391–403.
- [48] JAEGER, H., AND HAAS, H. **Harnessing nonlinearity: Predicting chaotic systems and saving energy in wireless communication**. *Science* 304, 5667 (2004), 78–80.
- [49] JAEGER, H. **The 'echo state' approach to analysing and training recurrent neural networks-with an erratum note**. Tech. Rep. 148:34, Bonn, Germany: German National Research Center for Information Technology GMD, 2001.
- [50] MAASS, W., NATSCHLÄGER, T., AND MARKRAM, H. **Real-time computing without stable states: A new framework for neural computation based on perturbations**. *Neural computation* 14, 11 (2002), 2531–2560.
- [51] ARAUJO, F., RIOU, M., TORREJON, J., TSUNEGI, S., QUERLIOZ, D., YAKUSHIJI, K., FUKUSHIMA, A., KUBOTA, H., YUASA, S., STILES, M., AND GROLLIER, J. **Role of non-linear data processing on speech recognition task in the framework of reservoir computing**. *Scientific Reports* 10, 1 (2020), 328.
- [52] SMERIERI, A., DUPOUR, F., PAQUOT, Y., HAELTERMAN, M., SCHRAUWEN, B., AND MASSAR, S. **Towards fully analog hardware reservoir computing for speech recognition**. *AIP Conf. Proc.* 1479, 1 (2012), 1892.

- [53] TANAKA, G., YAMANE, T., HÉROUX, J., NAKANE, R., KANAZAWA, N., TAKEDA, S., NUMATA, H., NAKANO, D., AND HIROSE, A. **Recent advances in physical reservoir computing: A review.** *Neural Networks* 115 (2019), 100–123.
- [54] FERNANDO, C., AND SOJAKKA, S. **Pattern recognition in a bucket.** In *ECAL2003: Advances in Artificial Life* (2003), pp. 588–597.
- [55] MARKS, D., COLWELL, L., SHERIDAN, R., HOPF, T., PAGNANI, A., ZECCHINA, R., AND SANDER, C. **Protein 3d structure computed from evolutionary sequence variation.** *PLOS ONE* 6, 12 (2011), e28766.
- [56] LEZON, T., BANAVAR, J., CIEPLAK, M. ABD MARITAN, A., AND FEDOROFF, N. **Using the principle of entropy maximization to infer genetic interaction networks from gene expression patterns.** *Proceedings of the National Academy of Sciences* 103, 50 (2006), 19033–19038.
- [57] COCCO, S., LEIBLER, S., AND MONASSON, R. **Neuronal couplings between retinal ganglion cells inferred by efficient inverse statistical physics methods.** *Proceedings of the National Academy of Sciences* 106, 33 (2009), 14058–14062.
- [58] NGUYEN, H., ZECCHINA, R., AND BERG, J. **Inverse statistical problems: from the inverse ising problem to data science.** *Advances in Physics* 66, 3 (2017), 197–261.
- [59] HINTON, G., OSINDERO, S., AND TEH, Y. **A fast learning algorithm for deep belief nets.** *Neural computation* 18, 7 (2006), 1527–1554.
- [60] BINDER, K., AND YOUNG, A. **Spin glasses: Experimental facts, theoretical concepts, and open questions.** *Rev. Mod. Phys.* 58, 4 (1986), 801–976.
- [61] SHERRINGTON, D., AND KIRKPATRICK, S. **Solvable model of a spin-glass.** *Phys. Rev. Lett.* 35, 26 (1975), 1792–1796.
- [62] GABAY, M., AND TOULOUSE, G. **Coexistence of spin-glass and ferromagnetic orderings.** *Phys. Rev. Lett.* 47, 3 (1981), 201–204.
- [63] DE LAS CUEVAS, G., DÜR, W., BRIEGEL, H. J., AND MARTIN-DELGADO, M. A. **Unifying all classical spin models in a lattice gauge theory.** *Phys. Rev. Lett.* 102, 23 (2009), 230502.
- [64] AMIT, D. J., GUTFREUND, H., AND SOMPOLINSKY, H. **Spin-glass models of neural networks.** *Phys. Rev. A* 32, 2 (1985), 1007–1018.
- [65] SOURLAS, N. **Spin-glass models as error-correcting codes.** *Nature* 339, 6227 (1989), 693–695.

- [66] NISHIMORI, H. **Nishimori, H. Statistical Physics of Spin Glasses and Information Processing: an Introduction.** No. 111 in International Series of Monographs on Physics. Oxford University Press, 2001.
- [67] HOPFIELD, J. **Neural networks and physical systems with emergent collective computational abilities.** *Proceedings of the National Academy of Sciences* 79, 8 (1982), 2554–2558.
- [68] REKLAITIS, G., TSIRUKIS, A., AND TENORIO, M. **Generalized hopfield networks and nonlinear optimization.** In *Advances in Neural Information Processing Systems* (1990), D. Touretzky, Ed., vol. 2, Morgan-Kaufmann.
- [69] SMITH, K. **Neural networks for combinatorial optimization: A review of more than a decade of research.** *INFORMS Journal on Computing* 11, 1 (1999), 15–34.
- [70] PAIK, J., AND KATSAGGELOS, A. **Image restoration using a modified hopfield network.** *IEEE TRANSACTIONS ON IMAGE PROCESSING* 1, 1 (1992), 49–63.
- [71] SUN, Y. **Hopfield neural network based algorithms for image restoration and reconstruction. i. algorithms and simulations.** *IEEE TRANSACTIONS ON SIGNAL PROCESSING* 48, 7 (2000), 2105–2118.
- [72] SUN, Y. **Hopfield neural network based algorithms for image restoration and reconstruction. ii. performance analysis.** *IEEE TRANSACTIONS ON SIGNAL PROCESSING* 48, 7 (2000), 2119–2131.
- [73] LUCAS, A. **Ising formulations of many np problems.** *Frontiers in Physics* 2 (2014), 5.
- [74] BARAHONA, F. **On the computational complexity of ising spin glass models.** *J. Phys. A: Math. Gen.* 15, 10 (1982), 3241.
- [75] LIEB, E., SCHULTZ, T., AND MATTIS, D. **Two soluble models of an antiferromagnetic chain.** *Annals of Physics* 16, 3 (1961), 407–466.
- [76] WANG, Z., MARANDI, A., WEN, K., BYER, R., AND YAMAMOTO, Y. **Coherent ising machine based on degenerate optical parametric oscillators.** *Phys. Rev. A* 88, 6 (2013), 063853.
- [77] HARIBARA, Y., UTSUNOMIYA, S., AND YAMAMOTO, Y. **Computational principle and performance evaluation of coherent ising machine based on degenerate optical parametric oscillator network.** *Entropy* 18, 4 (2016), 151.
- [78] OKAWACHI, Y., YU, M., JANG, J., JI, X., ZHAO, Y., KIM, B., LIPSON, M., AND GAETA, A. **Demonstration of chip-based coupled degenerate optical parametric oscillators for realizing a nanophotonic spin-glass.** *Nature Communications* 11, 1 (2020), 4119.

- [79] TEZAK, N., VAN VAERENBERGH, T., PELC, J. S., MENDOZA, G. J., KIPLINSKI, D., MABUCHI, H., AND BEAUSOLEIL, R. **Integrated coherent ising machines based on self-phase modulation in microring resonators.** *IEEE Journal of Selected Topics in Quantum Electronics* 26, 1 (2020), 1–15.
- [80] BÖHM, F., VERSCHAFFELT, G., AND VAN DER SANDE, G. **A poor man’s coherent ising machine based on opto-electronic feedback systems for solving optimization problems.** *Nature Communications* 10, 1 (2019), 3538.
- [81] KALININ, K., AND BERLOFF, N. **Global optimization of spin hamiltonians with gain-dissipative systems.** *Scientific Reports* 8, 1 (2018), 17791.
- [82] BÖHM, F., VAN VAERENBERGH, T., VERSCHAFFELT, G., AND VAN DER SANDE, G. **Order-of-magnitude differences in computational performance of analog ising machines induced by the choice of nonlinearity.** *arXiv:2012.10430* (2021).
- [83] HOPFIELD, J., AND TANK, D. **“neural” computation of decisions in optimization problems.** *Biological Cybernetics* 52, 3 (1985), 141–152.
- [84] MISCUGLIO, M., MEHRABIAN, A., HU, Z., AZZAM, S., GEORGE, J., KILDISHEV, A., PELTON, M., AND SORGER, V. **All-optical nonlinear activation function for photonic neural networks.** *Optical Materials Express* 8, 12 (2018), 3851–3863.
- [85] WILLIAMSON, I. A. D., HUGHES, T. W., MINKOV, M., BARTLETT, B., PAI, S., AND FAN, S. **Reprogrammable electro-optic nonlinear activation functions for optical neural networks.** *IEEE Journal of Selected Topics in Quantum Electronics* 26, 1 (2020), 1–12.
- [86] JHA, A., HUANG, C., AND PRUCNAL, P. **Reconfigurable all-optical nonlinear activation functions for neuromorphic photonics.** *Optics Letters* 45, 17 (2020), 4819–4822.
- [87] MOURGIAS-ALEXANDRIS, G., TSAKYRIDIS, A., PASSALIS, N., TEFAS, A., VYRSOKINOS, K., AND PLEROS, N. **An all-optical neuron with sigmoid activation function.** *Optics Express* 27, 7 (2019), 9620–9630.
- [88] CHOU, J., BRAMHAVAR, S., GHOST, S., AND HERZOG, W. **Analog coupled oscillator based weighted ising machine.** *Scientific Reports* 9, 1 (2019), 14786.
- [89] HINES, M. L., AND CARNEVALE, N. T. **The neuron simulation environment.** *Neural Computation* 9, 6 (1997), 1179–1209.
- [90] KRIZHEVSKY, A., SUTSKEVER, I., AND HINTON, G. **Imagenet classification with deep convolutional neural networks.** In *Advances in Neural Information Processing Systems* (2012), F. Pereira, C. Burges, L. Bottou, and K. Weinberger, Eds., vol. 25, Curran Associates, Inc.

- [91] YOUNG, T., HAZARIKA, D., PORIA, S., AND CAMBRIA, E. **Recent trends in deep learning based natural language processing.** *IEEE Computational Intelligence Magazine* 13, 3 (2018), 55–75.
- [92] SILVER, D., HUBERT, T., SCHRIITWIESER, J., ANTONOGLU, I., LAI, M., GUEZ, A., LANCTOT, M., SIFRE, L., KUMARAN, D., GRAEPEL, T., LILICRAP, T., SIMONYAN, K., AND HASSABIS, D. **A general reinforcement learning algorithm that masters chess, shogi, and go through self-play.** *Science* 7, 362 (1140-1144 2018), 6419.
- [93] KIM, N., AUSTIN, T., BAAUW, D., MUDGE, T., FLAUTNER, K., HU, J., IRWIN, M., KANDEMIR, M., AND NARAYANAN, V. **Leakage current: Moore’s law meets static power.** *Computer* 36, 12 (2003), 68–75.
- [94] DENNARD, R., GAENSSLEN, F., YU, H.-N., RIDEOUT, V., BASSOUS, E., AND LEBLANC, A. **Design of ion-implanted mosfet’s with very small physical dimensions.** *IEEE Journal of Solid-State Circuits* 9, 5 (1974), 256–268.
- [95] MARKRAM, H., MULLER, E., RAMASWAMY, S., REIMANN, M., ABDELLAH, M., SANCHEZ, C., AILAMAKI, A., ALONSO-NANCLARES, L., ANTILLE, N., ARSEVER, S., KAHOU, G., BERGER, T. K., BILGILI, A., BUNCIC, N., CHALIMOURDA, A., CHINDEMI, G., COURCOL, J.-D., DELALONDRE, F., DELATTRE, V., DRUCKMANN, S., DUMUSC, R., DYNES, J., EILEMANN, S., GAL, E., GEVAERT, M., GHOBRIL, J.-P., GIDON, A., GRAHAM, J., GUPTA, A., HAENEL, V., HAY, E., HEINIS, T., HERNANDO, J., HINES, M., KANARI, L., KELLER, D., KENYON, J., KHAZEN, G., KIM, Y., KING, J., KISVARDAY, Z., KUMBHAR, P., LASSERRE, S., LE BÉ, J.-V., MAGALHÃES, B., MERCHÁN-PÉREZ, A., MEYSTRE, J., MORRICE, B. R., M., J., MUÑOZ-CÉSPEDES, A., MURALIDHAR, S., MUTHURASA, K., NACHBAUR, D., NEWTON, T. H., NOLTE, M., OVCHARENKO, A., PALACIOS, J., PASTOR, L., PERIN, R., RANJAN, R., RIACHI, I., RODRÍGUEZ, J.-R., RIQUELME, J. L., RÖSSERT, C., SFYRAKIS, K., SHI, Y., SHILLCOCK, J., SILBERBERG, G., SILVA, R., TAUHEED, F., TELEFONT, M., TOLEDO-RODRIGUEZ, M., TRÄNKLER, T., VAN GEIT, W., DÍAZ, J., WALKER, R., WANG, Y., ZANINETTA, S. M., DEFELIPE, J., HILL, S., SEGEV, I., AND SCHÜRMAN, F. **Reconstruction and simulation of neocortical microcircuitry.** *Cell* 163, 2 (2015), 456–492.
- [96] LIU, J., WU, Q., SUI, X., CHEN, Q., GU, G., WANG, L., AND LI, S. **Research progress in optical neural networks: theory, applications and developments.** *Photonix* 2, 1 (2021), 5.
- [97] XU, R., LV, P., XU, F., AND Y., S. **A survey of approaches for implementing optical neural networks.** *Optics & Laser Technology* 136 (2021), 106787.
- [98] MEAD, C. **Neuromorphic electronic systems.** *Proceedings of the IEEE* 78, 10 (1990), 1629–1636.

- [99] GROLLIER, J., QUERLIOZ, D., CAMSARI, K. Y., EVERSCHOR-SITTE, K., FUKAMI, S., AND STILES, M. D. **Neuromorphic spintronics**. *Nature Electronics* 3, 7 (2020), 360–370.
- [100] MISRA, J., AND SAHA, I. **Artificial neural networks in hardware: A survey of two decades of progress**. *Neurocomputing* 74, 1-3 (2010), 239–255.
- [101] GRAVES, A., WAYNE, G., REYNOLDS, M., HARLEY, T., DANIHELKA, I., GRABSKA-BARWINSKA, A., COLMENAREJO, S., GREFENSTETTE, E., RAMALHO, T., AGAPIOU, J., BADIA, A., HERMANN, K., ZWOLS, Y., OSTROVSKI, G., CAIN, A., KING, H., SUMMERFIELD, C., BLUNSOM, P., KAVUKCUOGLU, K., AND HASSABIS, D. **Hybrid computing using a neural network with dynamic external memory**. *Nature* 538, 7626 (2016), 471–476.
- [102] ESSER, S., MEROLLA, P., ARTHUR, J., CASSIDY, A., APPUSWAMY, R., ANDREOPOULOS, A., BERG, D., MCKINSTRY, J., MELANO, T., BARCH, D., DI NOLFO, C., DATTA, P., AMIR, A., TABA, B., FLICKNER, M., AND MODHA, D. **Convolutional networks for fast, energy-efficient neuromorphic computing**. *Proc. Nat. Acad. Sci. USA* 113, 41 (2016), 11441–11446.
- [103] ADAMATZKY, A., AND CHUA, L., Eds. **Memristor Networks**. Springer, 2014.
- [104] JAMES, A., Ed. **Deep Learning Classifiers with Memristive Networks**. Springer, 2020.
- [105] XU, W., WANG, J., AND YAN, X. **Advances in memristor-based neural networks**. *Front. Nanotechnol.* 3 (2021), 20.
- [106] LIU, B., LI, H., CHEN, Y., LI, X., HUANG, T., WU, Q., AND BARNELL, M. **Reduction and ir-drop compensations techniques for reliable neuromorphic computing systems**. In *IEEE/ACM Internat. Conf. Comput.-Aided Design (ICCAD)* (2014), pp. 63–70.
- [107] MAAN, A., JAYADEVI, D., AND JAMES, A. **A survey of memristive threshold logic circuits**. *IEEE Trans. Neural Netw. Learn. Syst.* 28, 8 (2017), 1734–1746.
- [108] DE MARINIS, L., COCOCCIONI, M., CASTOLDI, P., AND ANDRIOLLI, N. **Photonic neural networks: A survey**. *IEEE Access* 7 (2019), 175827–175841.
- [109] KECKLER, S., DALLY, W., KHAILANY, B., GARLAND, M., AND GLASCO, D. **Gpus and the future of parallel computing**. *IEEE Micro* 31, 5 (2011), 7–17.
- [110] HAMERLY, R., BERNSTEIN, L., SLUDDS, A., SOLJAČIĆ, M., AND ENGLUND, D. **Large-scale optical neural networks based on photoelectric multiplication**. *Phys. Rev. X* 9, 2 (2019), 021032.

- [111] TILMAN, D., AND KAREIVA, P., Eds. **Spatial Ecology: The Role of Space in Population Dynamics and Interspecific Interactions**. Princeton University Press, 2018.
- [112] MCLACHLAN, J. **On Growth and Form: Spatio-temporal Pattern Formation in Biology**. Wiley, 2000.
- [113] HESS, O., AND KUHN, T. **Spatio-temporal dynamics of semiconductor lasers: Theory, modelling and analysis**. *Prog. Quant. Electr.* 20, 2 (1996), 85–179.
- [114] ERBAN, R., AND CHAPMAN, S. J. **Stochastic Modelling of Reaction–Diffusion Processes**. Cambridge University Press, 2020.
- [115] CHANG-HASNAIN, C., ORENSTEIN, M., VON LEHMEN, A., FLOREZ, L., HARBISSON, J., AND STOFFEL, N. **Transverse mode characteristics of vertical cavity surface-emitting lasers**. *Applied Physics Letters* 57, 3 (1990), 218–220.
- [116] BUCCAFUSCA, O., CHILLA, J., ROCCA, J., WILMSEN, C., AND FELD, S. **Ultra-high frequency oscillations and multimode dynamics in vertical cavity surface emitting lasers**. *Appl. Phys. Lett.* 67, 2 (1995), 185–187.
- [117] DUDLEY, J., AND TAYLOR, J. **Ten years of nonlinear optics in photonic crystal fibre**. *Nature Photonics* 3, 2 (2009), 85–90.
- [118] DUDLEY, J. M., AND TAYLOR, J. **Supercontinuum Generation in Optical Fibers**. Cambridge University Press, 2010.
- [119] HIZANIDIS, J., LAZARIDES, N., NEOFOTISTOS, G., AND TSIRONIS, G. **Chimera states and synchronization in magnetically driven squid metamaterials**. *European Physical Journal Special Topics volume 225*, 6 (2016), 1231–1243.
- [120] HIZANIDIS, J., LAZARIDES, N., AND TSIRONIS, G. **Pattern formation and chimera states in 2d squid metamaterials**. *Chaos* 30, 1 (2020), 013115.
- [121] RICKETTS, D., AND HAM, D. **Electrical Solitons: Theory, Design, and Applications**. CRC Press, 2011.
- [122] ARECCHI, F., GIACOMELLI, G., LAPUCCI, A., AND MEUCCI, R. **Two-dimensional representation of a delayed dynamical system**. *Phys. Rev. A* 45, 7 (1992).
- [123] GIACOMELLI, G., AND POLITI, A. **Relationship between delayed and spatially extended dynamical systems**. *Phys. Rev. Lett.* 76, 15 (1996), 2686–2689.
- [124] SEMENOV, V., ZAKHAROVA, A., MAISTRENKO, Y., AND SCHÖLL, E. **Delayed-feedback chimera states: Forced multiclusters and stochastic resonance**. *Europhys. Lett.* 115, 1 (2016), 10005.

- [125] LARGER, L., PENKOVSKY, B., AND MAISTRENKO, Y. **Laser chimeras as a paradigm for multistable patterns in complex systems.** *Nature Communications* 6, 1 (2015), 7752.
- [126] YANCHUK, S., RUSCHEL, S., SIEBER, J., AND WOLFRUM, M. **Temporal dissipative solitons in time-delay feedback systems.** *Phys. Rev. Lett.* 123, 5 (2019), 053901.
- [127] APPELTANT, L., SORIANO, M. C., VAN DER SANDE, G., DANCKAERT, J., MASSAR, S., DAMBRE, J., SCHRAUWEN, B., MIRASSO, C. R., AND FISCHER, I. **Information processing using a single dynamical node as complex system.** *Nature Communications* 2, 1 (2011), 468.
- [128] MARTINENGI, R., RYBALKO, S., JACQUOT, M., CHEMBO, Y., AND LARGER, L. **Photonic nonlinear transient computing with multiple-delay wavelength dynamics.** *Phys. Rev. Lett.* 108, 24 (2012), 244101.
- [129] BRUNNER, D., PENKOVSKY, B., MARQUEZ, B., JACQUOT, M., FISCHER, I., AND LARGER, L. **Tutorial: Photonic neural networks in delay systems.** *Journal of Applied Physics* 124, 15 (2018), 152004.
- [130] LARGER, L., BAYLÓN-FUENTES, A., MARTINENGI, R., UDALTSOV, V., CHEMBO, Y., AND JACQUOT, M. **High-speed photonic reservoir computing using a time-delay-based architecture: Million words per second classification.** *Phys. Rev. X* 7, 1 (2017), 011015.
- [131] BRUNNER, D., SORIANO, M. C., AND VAN DER SANDE, G., Eds. **Photonic Reservoir Computing.** De Gruyter, 2019.
- [132] PENKOVSKY, B., PORTE, X., JACQUOT, M., LARGER, L., AND BRUNNER, D. **Coupled nonlinear delay systems as deep convolutional neural networks.** *Phys. Rev. Lett.* 123, 5 (2019), 054101.
- [133] GOLDMANN, M., KÖSTER, F., LÜDGE, K., AND YANCHUK, S. **Deep time-delay reservoir computing: Dynamics and memory capacity.** *Chaos* 30, 9 (2020), 093124.
- [134] STELZER, F., RÖHM, A., VICENTE, R., FISCHER, I., AND YANCHUK, S. **Deep neural networks using a single neuron: folded-in-time architecture using feedback-modulated delay loops.** *Nature Communications* 12, 1 (2021), 5164.
- [135] VAN DER SANDE, G. A. **Advances in photonic reservoir computing.** *Nanophotonics* 6, 3 (2017), 561–576.

- [136] AHMED, A. H., SHARKIA, A., CASPER, B., MIRABBASI, S., AND SHEKHAR, S. **Silicon-photonics microring links for datacenters-challenges and opportunities.** *IEEE Journal of Selected Topics in Quantum Electronics* 22, 6 (2016), 194–203.
- [137] AHMED, A. H., EL MOZNINE, A., LIM, D., MA, Y., RYLYAKOV, A., AND SHEKHAR, S. **A dual-polarization silicon-photonic coherent transmitter supporting 552 gb/s/wavelength.** *IEEE Journal of Solid-State Circuits* 55, 9 (2020), 2597–2608.
- [138] SHASTRI, B. J., TAIT, A. N., DE LIMA, T. F., PERNICE, W. H., BHASKARAN, H., WRIGHT, C. D., AND PRUCNAL, P. R. **Photonics for artificial intelligence and neuromorphic computing.** *Nature Photonics* 15, 2 (2021), 102–114.
- [139] PSALTIS, D., AND FARHAT, N. **Optical information processing based on an associative-memory model of neural nets with thresholding and feedback.** *Optics Letters* 10, 2 (1985), 98–100.
- [140] FELDMANN, J., YOUNGBLOOD, N., WRIGHT, C. D., BHASKARAN, H., AND PERNICE, W. **All-optical spiking neurosynaptic networks with self-learning capabilities.** *Nature* 569, 7755 (2019), 208–214.
- [141] LIN, X., RIVENSON, Y., YARDIMCI, N. T., VELI, M., LUO, Y., JARRAHI, M., AND OZCAN, A. **All-optical machine learning using diffractive deep neural networks.** *Science* 361, 6406 (2018), 1004–1008.
- [142] THOMSON, D., ZILKIE, A., BOWERS, J., KOMLJENOVIC, T., REED, G., VIVIEN, L., MARRIS-MORINI, D., CASSAN, E., VIROT, L., FÉDÉLI, J.-M., HARTMANN, J., SCHMID, J., XU, D., BOEUF, F., O'BRIEN, P., MASHANOVICH, G., AND NEDELJKOVIC, M. **Roadmap on silicon photonics.** *Journal of Optics* 18, 7 (2016), 073003.
- [143] SHEKHAR, S. **Tutorial: Silicon photonics - from basics to asics.** In *IEEE international solid-state circuits conference (ISSCC)* (2021).
- [144] SUN, J., TIMURDOGAN, E., YAACOBI, A., HOSSEINI, E. S., AND WATTS, M. R. **Large-scale nanophotonic phased array.** *Nature* 493, 7431 (2013), 195–199.
- [145] PRUCNAL, P., AND SHASTRI, B. J. **Neuromorphic photonics.** CRC Press, 2017.
- [146] EFRON, U., Ed. **Spatial Light Modulator Technology: Materials, Devices, and Applications.** CRC Press, 1994.
- [147] JUNG, I. **Spatial Light Modulators and Applications: Spatial Light Modulators for Applications in Coherent Communication, Adaptive Optics and Maskless Lithography.** VDM Verlag, 2009.

- [148] ROSALES-GUMÁN, C., AND FORBES, A. **How to Shape Light with Spatial Light Modulators**. SPIE PRESS, 2017.
- [149] WICK, D., MARTINEZ, T., WOOD, M., WILKES, J., GRUNEISEN, M., BERENBERG, V., VASIL'EV, M., ONOKHOV, A., AND BERESNEV, L. **Deformed-helix ferroelectric liquid-crystal spatial light modulator that demonstrates high diffraction efficiency and 370-line pairs/mm resolution**. *Applied Optics* 38, 17 (1999), 3798–3803.
- [150] SHRESTHA, P., CHUN, Y., AND CHU, D. **A high-resolution optically addressed spatial light modulator based on zno nanoparticles**. *Light: Science & Applications* 4, 3 (2015), e259.
- [151] PICCARDI, A., BORTOLOZZO, U., RESIDORI, S., AND ASSANTO, G. **Spatial solitons in liquid-crystal light valves**. *Optics Letters* 34, 6 (2009), 737–739.
- [152] VERSCHUEREN, N., BORTOLOZZO, U., CLERC, M., AND RESIDORI, S. **Spatiotemporal chaotic localized state in liquid crystal light valve experiments with optical feedback**. *Phys. Rev. Lett.* 110, 10 (2013), 104101.
- [153] ZUO, Y., ZHAO, Y., CHEN, Y.-C., DU, S., AND LIU, J. **Scalability of all-optical neural networks based on spatial light modulators**. *Phys. Rev. Applied* 15, 5 (2021), 054034.
- [154] DONG, J., RAFAYELIAN, M., KRZAKALA, F., AND GIGAN, S. **Optical reservoir computing using multiple light scattering for chaotic systems prediction**. *IEEE Journal of Selected Topics in Quantum Electronics* 26, 1 (2020), 1–12.
- [155] BRUNNER, D., AND FISHER, I. **Reconfigurable semiconductor laser networks based on diffractive coupling**. *Optics Letters* 40, 16 (2015), 3854–3857.
- [156] MARCUCCI, G., PIERANGELI, D., AND CONTI, C. **Adiabatic evolution on a spatial-photonic ising machine**. *Optica* 7, 11 (2020), 1535–1543.
- [157] STRINATI, M., PIERANGELI, D., AND CONTI, C. **All-optical scalable spatial coherent ising machine**. *Phys. Rev. Applied* 16, 5 (2021), 054022.
- [158] JACUCCI, G., DELLOYE, L., PIERANGELI, D., RAFAYELIAN, M., CONTI, C., AND GIGAN, S. **Tuneable spin-glass optical simulator based on multiple light scattering**. *arXiv:2111.07893* (2021).
- [159] FARHAT, N., PSALTIS, D., PRATA, A., AND PAEK, E. **Optical implementation of the hopfield model**. *Applied Optics* 24, 10 (1985), 1469–1475.
- [160] FARHAT, N. **Optical associative memories**. *Optics & Photonics News* 13 (1987), 15–16.

- [161] KUMAR, B., AND WONG, P. **Optical associative memories**. *Machine Intelligence and Pattern Recognition 11* (1991), 219–241.
- [162] WHITE, H., AND WRIGHT, W. **Holographic implementation of a hopfield model with discrete weightings**. *Applied Optics 27*, 2 (1988), 331–338.
- [163] SOFFER, B., DUNNING, G., OWECHKO, Y., AND MAROM, E. **Associative holographic memory with feedback using phase-conjugate mirrors**. *Optics Letters 11*, 2 (1986), 118–120.
- [164] DECUSATIS, C., DAS, P., AND LITYNSKI, D. **Integrated optical implementation of the hopfield neural network model**. In *Proc.SPIE* (1988), vol. 0963.
- [165] ABU-MOSTAFA, Y. S., AND PSALTIS, D. **Optical neural computers**. *Scientific American 256*, 3 (1987), 88–95.
- [166] YEH, S., LO, R., AND C.Y., S. **Optical implementation of the hopfield neural network with matrix gratings**. *Applied Optics 43*, 4 (2004), 858–865.
- [167] BELOV, M., AND MANYKIN, E. **Optical associative memories based on time-delayed four-wave mixing**. In *Optical Memory and Neural Networks* (1991), vol. 1621, pp. 268–279.
- [168] AMIT, D., GUTFREUND, H., AND SOMPOLINSKY, H. **Storing infinite numbers of patterns in a spin-glass model of neural networks**. *Phys. Rev. Lett. 55*, 14 (1985), 1530–1533.
- [169] MARSH, B., GUO, Y., KROEZE, R., GOPALAKRISHNAN, S., GANGULI, S., KEELING, J., AND LEV, B. **Enhancing associative memory recall and storage capacity using confocal cavity qed**. *Phys. Rev. X 11*, 2 (2021), 021048.
- [170] DUPORT, F., SCHNEIDER, B., SMERIERI, A., HAELTERMAN, M., AND MASSAR, S. **All-optical reservoir computing**. *Optics Express 20*, 20 (2012), 22783–22795.
- [171] NAKAJIMA, M., TANAKA, K., AND HASHIMOTO, T. **Scalable reservoir computing on coherent linear photonic processor**. *Communications Physics 4*, 1 (2021), 20.
- [172] YAO, F., PEI, Y., ZHANG, Y., HOU, C., AND SUN, X. **High-resolution photorefractive gratings in nematic liquid crystals sandwiched with photoconductive polymer film**. *Appl. Phys. B 92*, 4 (2008), 573.
- [173] PERLMUTTER, S., DOROSKI, D., AND MODDEL, G. **Degradation of liquid crystal device performance due to selective adsorption of ions**. *Appl. Phys. Lett. 69*, 9 (1996), 1182–1184.

- [174] REGRETTIER, T. **Optically addressed light modulators using an organic photo-voltaic layer**. PhD thesis, Micro and nanotechnologies/Microelectronics. Université de Strasbourg, 2017.
- [175] KURAMOTO, Y. **Chemical Oscillations, Waves and Turbulence**. Springer-Verlag, Berlin, 1984.
- [176] MIKHAILOV, A. **Foundations of Synergetics I: Distributed Active Systems**. Springer-Verlag, New York, 1990.
- [177] KAPRAL, R., AND SHOWALTER, K. **Chemical Waves and Patterns**. Kluwer, Dordrecht, 1995.
- [178] GARCIA-OJALVO, J., AND SANCHO, J. **Noise in Spatially Extended Systems**. Springer, 1999.
- [179] SCHLÖGL, F. **Chemical reaction models for non-equilibrium phase transitions**. *Zeitschrift für Physik* 253, 2 (1972), 147–161.
- [180] SCHLÖGL, F., ESCHER, C., AND BERRY, R. **Fluctuations in the interface between two phases**. *Phys. Rev. A* 27, 5 (1983), 2698–2704.
- [181] MIKHAILOV, A., AND ERTL, G., Eds. **Engineering of Chemical Complexity II**. World Scientific Lecture Notes in Complex Systems. World Scientific, 2014, ch. Control of Chemical Wave Propagation, pp. 185–207.
- [182] SCHÖLL, E. **Nonlinear Spatio-Temporal Dynamics and Chaos in Semiconductors**, vol. 10 of *Nonlinear Science Series*. Cambridge University Press, 2001.
- [183] ZEL'DOVICH, Y., AND FRANK-KAMENETSKII, D. **Theory of uniform flame propagation**. *Dokl. Akad. Nauk SSSR* 19 (1938), 693–798.
- [184] YURKE, B., PAGELLIS, A., CHUANG, I., AND TUROK, N. **Coarsening in nematic liquid crystals**. *Physica B* 178, 1-4 (1992), 56–72.
- [185] BRAY, A. **Theory of phase-ordering kinetics**. *Advances in Physics* 43, 3 (1994), 357–459.
- [186] CUGLIANDOLO, L. **Topics in coarsening phenomena**. *Physica A* 389, 20 (2010), 4360–4373.
- [187] CACCIOLI, F., FRANZ, S., AND MARSILI, M. **Ising model with memory: coarsening and persistence properties**. *Journal of Statistical Mechanics: Theory and Experiment* 2008, 7 (2008), P07006.
- [188] DENHOLM, J., AND REDNER, S. **Topology-controlled potts coarsening**. *Phys. Rev. E* 99, 6 (2019), 062142.

- [189] GOH, Y., AND JACOBS, R. **Coarsening dynamics of granular heaplets in tapped granular layers.** *New Journal of Physics* 4 (2002), 81.1–81.9.
- [190] ZHANG, C., YU, L., AND WANG, H. **Kinetic analysis for high-temperature coarsening of γ'' phase in ni-based superalloy gh4169.** *Materials* 12, 13 (2019), 2096.
- [191] ZHANG, L., LIU, Q., AND CROZIER, P. **Light induced coarsening of metal nanoparticles.** *J. Mater. Chem. A* 7, 19 (2019), 11756–11763.
- [192] GESLIN, P., BUCHET, M., WADA, T., AND KATO, H. **Phase-field investigation of the coarsening of porous structures by surface diffusion.** *Phys. Rev. Materials* 3, 8 (2019), 083401.
- [193] GIACOMELLI, G., MARINO, F., ZAKS, M., AND YANCHUK, S. **Coarsening in a bistable system with long-delayed feedback.** *Europhys. Lett.* 99, 5 (2012), 58005.
- [194] MARINO, F., GIACOMELLI, G., AND BARLAND, S. **Front pinning and localized states analogues in long-delayed bistable systems.** *Phys. Rev. Lett.* 112, 10 (2014), 103901.
- [195] JAVALOYES, J., ACKEMANN, T., AND HURTADO, A. **Arrest of domain coarsening via antiperiodic regimes in delay systems.** *Phys. Rev. Lett.* 115, 20 (2015), 203901.
- [196] SEMENOV, V., AND MAISTRENKO, Y. **Dissipative solitons for bistable delayed-feedback systems.** *Chaos* 28, 10 (2018), 101103.
- [197] DOBRAMYSL, U., MOBILIA, M., PLEIMLING, M., AND TÄUBER, U. **Stochastic population dynamics in spatially extended predator–prey systems.** *Journal of Physics A* 51, 6 (2018), 063001.
- [198] ENGEL, A. **Noise-induced front propagation in a bistable system.** *Phys. Lett. A* 113, 3 (1985), 139–142.
- [199] MÉNDEZ, V., LLOPIS, I., CAMPOS, D., AND HORSTHEMKE, W. **Effect of environmental fluctuations on invasion fronts.** *J. Theor. Biol.* 281, 1 (2011), 31–38.
- [200] WU, D., GUO, J., DU, J., XIA, C., ZENG, L., TIAN, Y., SHI, Z., TIAN, Y., LI, X., TSANG, Y., AND JIE, J. **Highly polarization-sensitive, broadband, self-powered photodetector based on graphene/pdse₂/germanium heterojunction.** *ACS Nano* 13, 9 (2019), 9907–9917.
- [201] XIN, Y., WANG, X., CHEN, Z., WELLER, D., WANG, Y., SHI, L., MA, X., DING, C., LI, W., GUO, S., AND LIU, R. **Polarization-sensitive self-powered type-ii gese/mos₂ van der waals heterojunction photodetector.** *ACS Appl. Mater. Interfaces* 12, 13 (2020), 15406–15413.

- [202] LI, Z., XU, B., LIANG, D., AND PAN, A. **Polarization-dependent optical properties and optoelectronic devices of 2d materials.** *Research 2020*, 5464258 (2020).

